UKD Universitätsklinikum Düsseldorf

hhu Heinrich Heine Universität Düsseldorf

Modelling neurological diseases using induced pluripotent stem cells

Inaugural-Dissertation

Zur Erlangung des Doktorgrades
der mathematisch-naturwissenschaftliche Fakultät
der Heinrich-Heine Universität Düsseldorf

vorgelegt von
Leon-Phillip Szepanowski
aus Krefeld

Düsseldorf, Oktober 2024

Aus dem Institut für Stammzellforschung und Regenerative Medizin der Heinrich-Heine Universität Düsseldorf

Gedruckt mit der Genehmigung der Mathematisch-Naturwissenschaftlichen Fakultät der Heinrich-Heine Universität Düsseldorf

Berichterstatter:

1. Prof. Dr. James Adjaye

2. Prof. Dr. Henrike Heise

Tag der mündlichen Prüfung: 26.06.2025

Die vorliegende Arbeit ist eine kumulative Dissertation gemäß § 6 (3) der Promotionsordnung der Mathematisch-Naturwissenschaftlichen Fakultät der Heinrich-Heine-Universität Düsseldorf vom 15.08.2018 zur Verleihung des Grades „Doctor rerum naturalium“

Acknowledgements

Firstly, I am immensely grateful to my supervisor, Prof. Dr. James Adjaye, whose guidance, insightful feedback, and unwavering support have been pivotal in shaping my research.

I am also deeply indebted to Prof. Dr. Henrike Heise for her willingness to take over this mentorship. I am truly fortunate to have had her guidance.

A special thank you goes to the incredible postdoctoral researchers, PD Dr. Nina Graffmann and Dr. Wasco Wruck. Their expertise, collaborative spirit, and readiness to assist have greatly enriched my research experience. Especially Dr. Wrucks bioinformatical expertise has been invaluable, and I am sincerely thankful for both their support.

I would also like to express my gratitude to my fellow PhD students: Lisa Nguyen, Abida Islam Pranty, Christiane Loerch, and Vanessa Christina de Meira Amorim. I truly appreciated their camaraderie, the intellectual exchanges, and the mutual support through often less than fortunate times. I especially want to thank Lisa Nguyen for organising the lab and always finding the right tone while doing so.

My appreciation extends to the outstanding technical assistants, Silke Wehrmeyer and Martina Bohndorf. Their dedication, patience, and assistance in various aspects of my research have significantly facilitated my progress. Special thanks of course go to my neighbour Silke Wehrmeyer for always having an open ear. You can always call me for technical assistance.

I am profoundly grateful to my girlfriend, Anna-Lisa Böttcher, for her unwavering love and support, especially towards the end of this journey.

Finally, I would like to thank my friends and family. Their unconditional love, encouragement, and faith in my abilities have been a source of immense strength and motivation. Especially my families support has been instrumental, if not indispensable in helping me navigate the challenges and celebrate the successes of my PhD journey. This achievement would not have been possible without you.

Table of Contents

Table of Figures

Abbreviations

2D	Two dimensional
3D	Three dimensional
aIP	Apical intermediate progenitor
aRGC	Apical radial glia cells
ATM	ATM Serine/Threonine Kinase
ATR	ATR Serine/Threonine Kinase
BBB	Blood-brain barrier
BDNF	Brain-derived growth factor
BER/mtBER	(Mitochondrial) base excision repair
bIP	Basal intermediate progenitor
BMP	Bone morphogenic protein
BP	Basal progenitor
bRGC	Basal radial glia cell
CCL	C-C Motif Chemokine Ligand
CM	Cerebral Malaria
CNS	Central Nervous System
COFS	Cerebro-oculo-fascio-skeletal syndrome
CP	Cortical plate
CRISPR/Cas9	Clustered regularly interspaced short palindromic repeats/CRISPR-associated nuclease 9
CS	Cockayne Syndrom/e
CSA/CSA	Cockayne Syndrome A/B Protein
CXCL	C-X-C Motif Chemokine
DSB	Double-strand break
EB	Embryoid Bodies
ER	Endoplasmatic reticulum
ERCC6/ERCC8	Excision repair cross-complementing protein group 6/8
ESC	Embryonic stem cells
GDNF	Glia-derived growth factor
GG-NER	Global genome nucleotide excision repair
GH	Growth hormone
GW	Gestational week
HDAC	Histone deacetylase

HMZ	Hemozoin/Hämozoin
HR	Homologous recombination
ICAM-1	Intercellular Adhesion Molecule 1
ICM	Inner cell mass
ICL	Interstrand crosslinks
ICR	Interstrand crosslinks repair
IGF-1	Insulin-like growth factor 1
IFN-γ	Interferon Gamma
IL	Interleukin
iPS	Induzierte pluripotente Stammzellen
iPSC	Induced pluripotent stem cells
iSVZ/OSVZ	Inner/outer subventricular zone
MAPK	Mitogen-activated protein kinase
MDM2	MDM2 Proto-Oncogene
MSC	Mesenchymal stem cells
MZ	Marginal zone
NEC	Neuroepithelial cell
NHEJ	Non-homologous end joining
NLRP3	NLR Family Pyrin Domain Containing 3
NPC	Neural progenitor cell
NR	Neural rosette
NS	Neurosphere
NT-3	Neurotrophin 3
OSKM	Oct3/4, Sox2, Klf4 and c-Myc
P.	Plasmodium
PAX6	Paired Box 6
PECAM-1	Platelet Endothelial Cell Adhesion Molecule
PfEMP-1	P. falciparum erythrocyte membrane protein-1
PGD	Preimplantation genetic diagnostics
PSC	Pluripotent stem cells
RNAPI/RNAPII	RNA Polymerase I/II
ROS	Reactive oxygen species
SAP	Subapical progenitor
SHH	Sonic Hedgehog

SP	Subplate
SVZ	Subventricular zone
TC-NER	Transcription-coupled nucleotide excision repair
TNFα	Tumor necrosis factor-α
UV	Ultraviolet
UVSS	UV-sensitive syndrome
VCAM-1	Vascular Cell Adhesion Molecule 1
VEGFA	Vascular Endothelial Growth Factor A
VEGFR2	Vascular Endothelial Growth Factor Receptor 2
VZ	Ventricular zone
WNT	WNT family member
ZM	Zerebrale Malaria

Abstract

Neurological diseases affect millions globally, leading to diminished quality of life due to progressive cognitive, motor, and sensory impairments. Research into these conditions is crucial, but often impeded by a lack of accurate disease models. The advent of induced pluripotent stem cells (iPSCs) in 2006 has partially addressed this limitation by enabling researchers to create patient-specific neural cells capable of modelling genetic and phenotypic characteristics of many previously inaccessible neurological diseases.

The work in hand leverages iPSCs to model two diseases with significant neurological involvement: Cockayne Syndrome (CS) and Cerebral Malaria (CM). For Cockayne Syndrome, iPSC-derived 3D neural models were established from patients with distinct severity grades of CS to identify pathways driving the neurological symptoms. For Cerebral Malaria, an iPSC-derived 2D neural model was developed to assess the impact of Hemozoin (HMZ) and provide a tool for researchers to explore the pathomechanisms underlying this severe potential complication of malaria.

In our CS research, transcriptome analysis of neurospheres and cerebral organoids derived from two CS patients revealed common pathways potentially driving CS neurological symptoms. These include dysregulation of RNA Polymerase I (RNAPI) transcription, protein processing in endoplasmic reticulum, and ribosome function in neural progenitor cells, indicating disrupted protein biosynthesis and overall proteome instability at early developmental stages. Dysregulation of intracellular protein transport and vesicle-mediated transport pathways was also identified, potentially due to microtubule network disruption. Development of neuronal projections was found to be severely dysregulated in cerebral organoids, as well as several other pathways essential for neuronal development, function and maintenance. Additionally, dysregulated cholesterol biosynthesis was observed at both investigated timepoints, implicating changes in lipid metabolism in the pathogenesis of CS neurological symptoms.

For Cerebral Malaria, iPSC-based 2D neuronal networks were established. Exposure to HMZ activated inflammation-associated pathways and altered the secretome of the investigated neuronal networks. Known CM-associated pro-inflammatory cytokines, such as IL-1β, IL-8, and IFN-γ, were elevated, while the anti-inflammatory cytokines IL-4 and IL-13 were reduced. DNA damage-associated gene expression was significantly elevated, seemingly independent of p53 activation. The p38 MAPK

pathway, a secondary pathway for cellular stress response to DNA damage and inflammation, was upregulated in HMZ-exposed neurons, suggesting a role in CM pathology and potential as a therapeutic target. The established iPSC-derived model thus mirrors CM inflammatory profiles and might offer insights into CM disease mechanisms and potential treatment strategies.

Overall, the work in hand strengthens the understanding of the underlying pathomechanisms of both CS and CM and highlights potential therapeutic targets, emphasizing the value of iPSC-based models in neurological disease research.

Zusammenfassung

Neurologische Erkrankungen betreffen weltweit Millionen Menschen und führen aufgrund fortschreitender kognitiver, motorischer und sensorischer Einschränkungen zu verminderter Lebensqualität. Die Erforschung dieser Krankheiten ist essenziell, wird jedoch durch einen Mangel an geeigneten Krankheitsmodellen behindert. Die Einführung induzierter pluripotenter Stammzellen (iPS) im Jahr 2006 hat geholfen diese Einschränkung teilweise zu überwinden, indem sie Forschern ermöglichte patientenspezifische neurale Zellen herzustellen, welche genetische und phänotypische Merkmale vieler zuvor unzugänglicher neurologischer Erkrankungen abbilden können.

Die vorliegende Arbeit nutzt iPS, um zwei Erkrankungen mit erheblicher neurologischer Beteiligung zu modellieren: Cockayne-Syndrom (CS) und zerebrale Malaria (ZM). Für das CS wurden iPS-basierte neurale 3D-Modelle von Patienten mit unterschiedlichen CS-Schweregraden erstellt, um die für die neurologischen Symptome verantwortlichen Signalwege zu identifizieren. Für die ZM wurde ein iPS-basiertes 2D-Neuralmodell entwickelt, um die Auswirkungen von Hämozoin (HMZ) zu untersuchen und Wissenschaftlern ein Instrument zur Erforschung der Pathomechanismen, die dieser schwerwiegenden potenziellen Malaria-Komplikation zugrunde liegen, zu verschaffen.

In unserer CS-Forschung hat die Transkriptomanalyse von Neurosphären und zerebralen Organoiden, die aus zwei CS-Patienten generiert wurden, sich überschneidende Signalwege aufgezeigt, die möglicherweise für die neurologischen Symptome des CS verantwortlich sind. Dazu gehören die Dysregulation der RNAPI-Transkription, der Proteinverarbeitung im endoplasmatischen Retikulum und der Ribosomenfunktion in neuralen Vorläuferzellen, was auf eine gestörte Proteinbiosynthese und eine allgemeine Proteominstabilität in den frühen Entwicklungsphasen hinweist. Es wurde auch eine Dysregulation des intrazellulären Proteintransports und des Vesikel-mediierten Transports festgestellt, die möglicherweise auf eine Störung des Mikrotubuli-Netzwerks zurückzuführen ist. Es wurde festgestellt, dass die Entwicklung der Neuronenprojektionen stark gestört ist, ebenso wie mehrere andere Signalwege, die für die Entwicklung, Funktion und Erhaltung von Neuronen essenziell sind. Darüber hinaus wurde an beiden untersuchten Zeitpunkten eine gestörte Cholesterinbiosynthese beobachtet, was auf

Veränderungen im Lipidstoffwechsel in der Pathogenese der CS-assoziierten neurologischen Symptome hindeutet.

Für die zerebrale Malaria wurden iPS-basierte neuronale 2D-Netzwerke etabliert. HMZ Exposition aktivierte entzündungsassoziierte Signalwege und veränderte das Sekretom der untersuchten neuronalen Netzwerke. Bekannte ZM-assoziierte pro-inflammatorische Zytokine, wie IL-1β, IL-8 und IFN-γ, waren erhöht, während die entzündungshemmenden Zytokine IL-4 und IL-13 reduziert waren. Die Expression von Genen, die mit DNA-Schäden assoziiert werden, war signifikant erhöht, anscheinend unabhängig von der Aktivierung von p53. Der p38-MAPK-Signalweg, ein sekundärer Signalweg für die zelluläre Reaktion auf Stress wie DNA-Schäden und Entzündungen, war in HMZ-ausgesetzten Neuronen hochreguliert, was auf eine Rolle in der Pathologie von ZM und ein potenzielles therapeutisches Ziel hinweist.

Das etablierte iPS-Modell spiegelt somit die Entzündungsprofile der ZM wider und könnte Einblicke in die Krankheitsmechanismen und potenzielle Behandlungsstrategien bieten.

Insgesamt stärkt die vorliegende Arbeit das Verständnis der zugrundeliegenden Pathomechanismen sowohl von CS als auch von ZM und weist auf potenzielle therapeutische Ziele hin, was den Wert von iPS-basierten Modellen in der Erforschung neurologischer Erkrankungen unterstreicht.

I. Structure of this thesis

This thesis compiles two publications that explore the potential of induced pluripotent stem cells (iPSCs) to model distinct degenerative and developmental diseases of the central nervous system (CNS). The publications are presented in chronological order:

1. Szepanowski, L. P., Wruck, W., Kapr, J., Rossi, A., Fritsche, E., Krutmann, J., & Adjaye, J. (2024). **Cockayne Syndrome Patient iPSC-Derived Brain Organoids and Neurospheres Show Early Transcriptional Dysregulation of Biological Processes Associated with Brain Development and Metabolism.** *Cells*, *13*(7), 591.
2. Pranty, A. I., Szepanowski, L. P., Wruck, W., Karikari, A. A., & Adjaye, J. (2024). **Hemozoin induces malaria via activation of DNA damage, p38 MAPK and neurodegenerative pathways in a human iPSC-derived neuronal model of cerebral malaria.** *Scientific Reports, 14*(1), 24959.

As the presented publications provide necessary background and methodological information by themselves, a brief general introduction into iPSCs, developmental mechanisms of the central nervous system and pathophysiological features of the modelled diseases is given first to enable a broader understanding of the topic. Following the presentation of the publications, the manuscripts will be summarized and set into scientific context.

II. Introduction

II.I. Stem cells

II.I.I. Introduction to stem cells

Mammalian development requires the specification and continuation of over 200 unique cell types from a single totipotent cell[1]. Stem cells, first described in 1961 by Till and McCulloch[2], are the undifferentiated cells from which these cell types derive at all stages of life – be it embryonic, fetal or adult. While these traits differ between distinct stem cell types, their major characteristics are the ability to extensively proliferate (self-renewal), origination from a single cell (clonality) and the ability to differentiate into diverse cell types (potency). Generally, developmentally younger stem cells have greater self-renewal and potency than developmentally older stem cells[3].

Stem cells are classified by their potency from most potent to least potent – totipotent, pluripotent, multipotent, oligopotent and unipotent. Totipotency as a concept was first described by Tarkowski in 1959[4], whose work showed that a single blastomere isolated from a 2-cell stage mouse embryo was able to generate a whole adult mouse. Totipotent cells can only be found at the very beginning of development and have the potential to form all tissues of an organism as well as extraembryonic tissues[5]. Pluripotent stem cells (PSCs) can most prominently be found in the inner cell mass (ICM) of a developing blastocyst and have the potential to develop into cells of all three germ layers – ectoderm, mesoderm and endoderm[6]. Multipotent stem cells are found in most organs and tissues. They have the ability to differentiate into cells from a single germ layer. The best characterized multipotent stem cells are mesenchymal stem cells (MSCs), which were first isolated from guinea-pig bone marrow and spleen by Friedenstein and colleagues in 1970[7]. MSCs can be found in all vascularized tissues and organs and are able to differentiate into adipose tissue, bone, cartilage and muscle cells. Due to their simplicity of isolation and cultivation, MSCs have been one of the major focal points of stem cell research in the last two decades and are currently being tested in clinical trials for various diseases[8,9]. Oligopotent stem cells are even more restricted and can differentiate into two or more distinct cell types. They can be found e.g. in the cornea of the eye, were they give rise to corneal and conjunctival cells[3,10]. Unipotent stem cells, as the name implies, can only differentiate into one type of cell. Unipotent stem cells can be found e.g. in skeletal muscle, where a subset of myogenic stem cells only develops into muscle cells (Figure 1)[3,11].

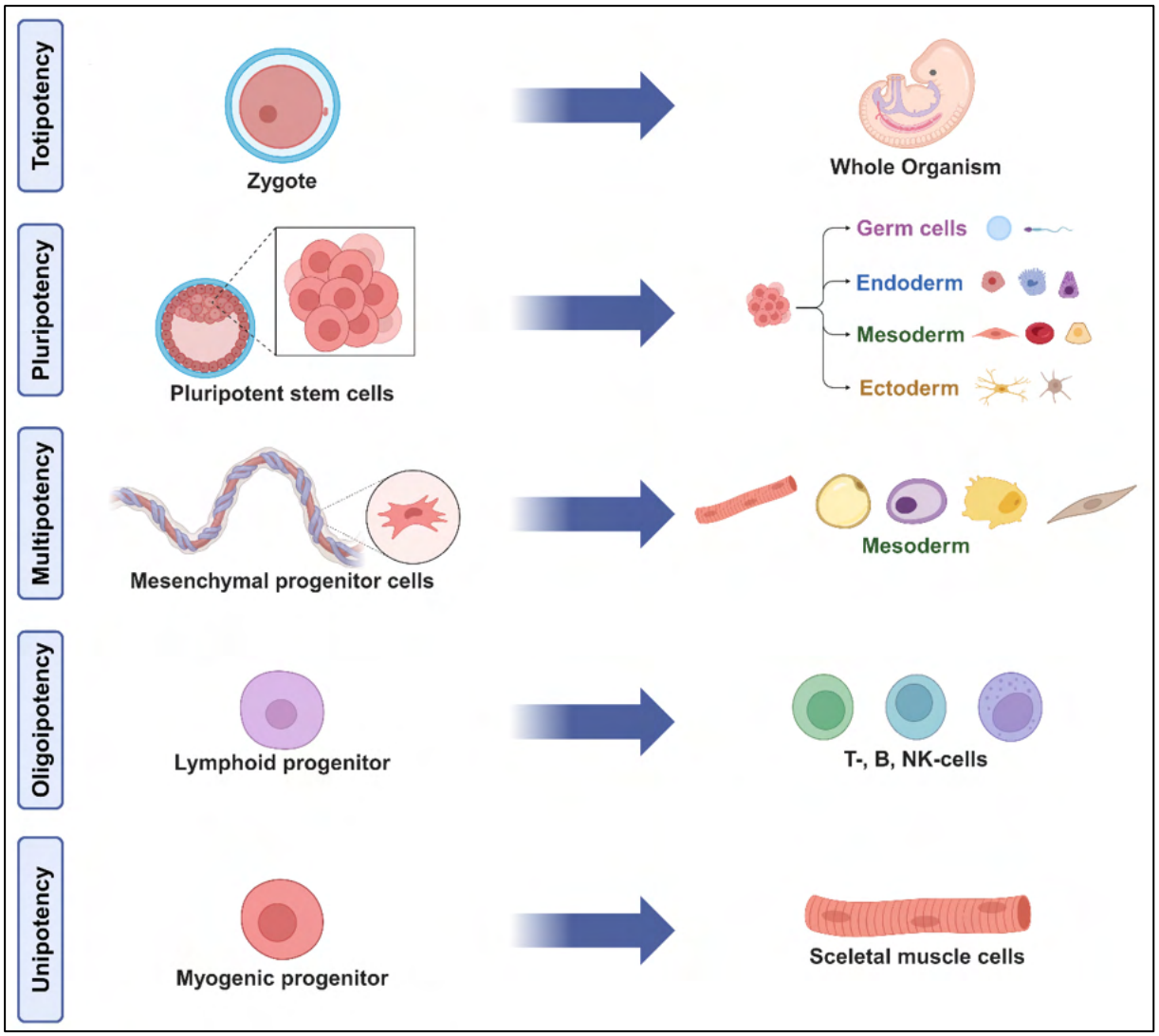

Figure 1: Schematic illustration introducing the distinct stem cell types. Stem cells are classified according to their potency. Totipotent cells (e.g. zygotes) can form all tissues of an organism as well as extraembryonic tissues. Pluripotent cells can differentiate into cells of all three germ layers. Multipotent stem cells (e.g. mesenchymal stem cells) can differentiate into cell types belonging to a single germ layer. Oligopotent stem cells (e.g. lymphoid progenitors) can differentiate into two or more distinct cell types. Lastly, unipotent stem cells (e.g. certain myogenic progenitors) can differentiate into a single cell type. Figure created with BioRender.com.

As true, stable culture of totipotent cells has not been achieved *in-vitro* and would introduce a host of severe ethical concerns if serially used for research, PSCs are the stem cells with the highest developmental potential frequently used in research[12].

II.I.II. Genesis of human induced pluripotent stem cells

Embryonic stem cells (ESCs), derived from the ICM of a developing blastocyst, are generally believed to have the potential to differentiate into all cells of an organism. Their pluripotent differentiation capabilities give them enormous potential in a wide

array of applications, such as developmental research, disease modelling, drug discovery screening, as well as regenerative and transplantation medicine[13]. However, even before the first establishment of mouse ESC cultures in 1981[14,15] and the subsequent derivation of human ESC cultures in 1998 by James Thomson[16], work with human zygotes and embryos raised severe ethical questions.

To avoid these ethical concerns and overwhelming bureaucracy, researchers needed a reliable way to fabricate human stem cell lines without introducing major damage to their source. The potential of achieving this was first indicated in 1962 by the work of Sir John Gurdon, who transferred the nuclei of differentiated *Xenopus* small intestinal epithelial cells into enucleated unfertilized eggs and obtained tadpoles[17]. This demonstrated that the differentiated nuclei still contain all the necessary information for the development of whole organisms. The established technique - somatic nuclear transfer – has since been used to clone several other animals, e.g. the famous Dolly the sheep as first mammal in 1997[18] and macaques as first primates in 2018[19]. Among other vital information, these experiments implied the existence of factors in the oocyte which reset – or reprogram – the differentiated nuclei into a totipotent state.

Further indicators for the possibility of producing human stem cell lines were provided by studies in which human embryonal carcinoma cells, ESCs and embryonic germ cells were fused with somatic cells. All fusions resulted in the reprogramming of the hybrid cell into a pluripotent state[20-22]. Thorough investigation of these cell types yielded a comprehensive list of pluripotency-associated genes[23-25]. Researchers speculated that utilizing this list and overexpressing select pluripotency-associated factors in somatic cells would reprogram these cells to a developmentally younger age. The first to succeed in this endeavour were Yamanaka and colleagues in 2006[26]. They selected 24 candidate genes that had been shown to be highly expressed in ESCs, as well as estimated to be important for the maintenance of ESC identity and retrovirally transduced them into *Fbx15*$^{\beta geo/\beta geo}$ mouse embryonic fibroblasts[27]. *Fbx15,* while specifically expressed in mouse ESCs, early embryos and testis tissue, has been shown to be dispensable for the maintenance of pluripotency, mouse embryonal development and fertility[28]. The inserted *βgeo* cassette, a fusion of the β-galactosidase and neomycin resistance genes, induced a strong resistance to Geneticin (G418) in mouse ESCs, which was lost upon differentiation. Reprogramming these cells to an ESC-like state was expected to reinstate this resistance[26].

The 24 candidate genes – *Ecat1, Dppa5, Fbxo15, Nanog, ERas, Dnmt31, Ecat8, Gdf3, Sox15, Dppa4, Dppa2, Fthl17, Sall4, Oct3/4, Sox2, Zfp42, Utf1, Tcl1, Dppa3, Klf4, β-catenin, c-Myc, Stat3* and *Grb2* – were inserted into mouse embryonic fibroblasts individually and as cocktail. Expectedly, transduction of singular genes failed to produce G418-resistant colonies. However, transduction of all 24 genes together produced G418-resistant clones, some of which exhibited ESC-like morphology, proliferation properties and gene expression. Subsequently, they reduced the gene cocktail from 24 to 10 genes via withdrawal of singular genes. Withdrawal of one of these 10 genes from the 24 gene cocktail resulted in no colony formation. Following this, they repeated the withdrawal experiments with the 10 gene cocktail. Again, they individually omitted each of the 10 genes, which lead them to the establishment of the final 4 gene cocktail – Oct3/4, Sox2, Klf4 and c-Myc (OSKM), later called the Yamanaka cocktail. In the 10 gene transduction experiments, omission of Oct3/4 or Klf4 resulted in no colony formation, omission of Sox2 severely reduced colony formation and altered colony morphology and removal of c-Myc resulted in flatter, non-ESC-like morphology of the colonies. In terms of efficiency, OSKM was found to be on par with the 10 gene cocktail. Cells produced by transduction of OSKM were termed induced pluripotent stem cells (iPSCs), as they were subsequently shown to be transcriptionally similar to ESCs and able to differentiate into cells of all three germ layers. In the same work, Yamanaka and colleagues introduced OSKM to adult male and female mouse tail-tip fibroblasts and were able to generate multiple iPSC lines. Rigorous testing revealed these cells to be similar to ESCs in morphology, proliferation, gene expression and teratoma formation, as well as able to contribute to the development of embryos via microinjection into mouse blastocysts. This demonstrated that OSKM could not only reprogram developmentally young cells into iPSCs, but also adult cells, an important feature for a prospective use in regenerative medicine[26].

Only one year later, in 2007, Yamanaka and colleagues demonstrated that OSKM can also be utilized to reprogram human cells. They derived iPSCs lines from human neonate fibroblast, adult human dermal fibroblasts from a 36-year-old Caucasian female and fibroblast-like synoviocytes donated by a 69-year-old Caucasian male, showcasing the utility of OSKM for the derivation of iPSCs from donors at all stages of life[29]. Since then, other reprogramming methods, delivery systems, as well as reprogramming protocols for various human cell types have been established and

further refined[13]. However, OSKM remains the gold standard of human cell reprogramming to date.

On a side note, in addition to mouse and human cells, iPSCs have successfully been established from pig, rabbit, monkey, goat, horse, cattle, chicken and fish cells[30].

II.I.III. Application of human embryonic and induced pluripotent stem cells

The advent of iPSCs enabled massive progress in regenerative medicine, disease modelling, drug screening, toxicity testing and human developmental biology. All these field are hampered either by extremely high ethical hurdles, scarce access to essential human samples, or both. The rapidly developing field of stem cell research alleviated both ethical concerns and scarcity of certain cell types and tissues, as iPSCs have been differentiated into a plethora of cells representing most human tissues[30].

Human developmental biology using iPSCs is essentially a feed-forward-loop. Due to their potential to generate every human cell type, basic research into lineage commitment and tissue patterning utilizing this rapid and cost-effective *in-vitro* platform can help answer key questions in human developmental biology, which in return can be used to establish or enhance *in-vitro* differentiation protocols[31].

Genetic screens and loss- and gain-of-function studies conducted in mice and other model organisms have revealed numerous genes and signalling pathways that regulate diverse developmental processes. These findings have been used to establish defined conditions to direct PSCs to specific fates, which supports the general conclusion that most developmental mechanisms are conserved. However, human-specific developmental regulation has also been uncovered, demonstrating the need for human developmental models to reveal which mechanisms are conserved or non-conserved. To give an example, neuroectoderm formation is one of the most studied developmental processes and the function of Paired Box 6 (*PAX6*) in this process is well investigated. However, only through the use of PSCs it became evident, that PAX6 is a sufficient cell fate determinant for differentiating human PSCs into neuroectoderm, but not mouse PSCs[31,32].

Under the right conditions, PSCs also form spherical aggregates known as embryoid bodies (EBs). These densely packed cells can be directed towards specific cell lineages, utilizing the right differentiation cues. Despite being far from replicating the exact patterning found in embryos and organs, the three-dimensional (3D) structure of

EBs offers the benefit of partially recapitulating complex cell and tissue interactions, such as cell polarization[33,34]. So, while not perfect, EBs present a second valuable PSC-derived model system for studying both conserved and non-conserved mechanisms of early embryo- and organogenesis.

Apart from studying normal developmental processes, human PSCs enable researchers to replicate abnormal development and investigate the pathogenesis of human diseases. Certain disease-relevant tissues and cell types, e.g. neurons, are often challenging to obtain directly from patients, especially in early stages of the disease. As a result, researchers have relied on model systems, particularly mice, to dissect the pathomechanisms underlying human diseases. Albeit, mouse models frequently fail to fully mimic the disease phenotypes observed in humans. These limitations can potentially be avoided by utilizing PSCs carrying disease-associated genetic variants, as they offer a potentially infinite source of all disease-relevant human cell types[31,35].

Various methods can be employed to create disease-relevant PSCs. The first described method was the derivation of ESC cultures from human embryos with genetic defects identified by preimplantation genetic diagnostics (PGD)[35]. However, the number of diseases covered by PGD-derived ESCs is restricted by the limited availability of PGD embryos for select, typically monogenic, human diseases e.g. Huntington´s disease and Marfan syndrome[36,37]. Additionally, due to their origin, PGD-ESCs lack any associated clinical history. This complicates result interpretation, as many genetic diseases exhibit incomplete penetrance[35].

While they introduce other challenges, the emergence of iPSC reprogramming attenuated these complications. Reprogramming allowed for the use of easily accessible and storable human samples, e.g. skin-derived fibroblasts, for the establishment of iPSC cultures from patients with known disease severity and clinical history. Therefore, iPSCs from donors with specified disease characteristics also allow for the more precise modelling of complex diseases like Parkinson´s disease[38,39]. The discovery of reprogramming thus led to the creation of *in-vitro* models for many diseases for which previously there were none.

As mentioned before, iPSCs introduce other limitations to disease modelling than ESCs. The most prominent challenges are the variations among human iPSC cell lines and the fact that iPSCs are only ESC-like, not identical. Variations can even be found between iPSC lines derived from the same donor and cell type. These variations may

derive from interclonal genetic variation, the source of the cell line, the presence of residual transgenes, epigenetic modifications which can be partially retained during the reprogramming process, thus e.g. priming the iPSC line for preferential differentiation into a specific germ layer, and in female lines, the status of X chromosome inactivation[40-43]. However, direct comparison with disease-variant carrying ESCs validated the effectiveness of patient-derived iPSCs for disease modelling, as similar phenotypes have been reported in most cases[44,45].

A solution to the variation problem is incidentally also the third way to derive disease-relevant PSCs. To reduce variation between disease and control line, genetically matched, isogenic cell lines that differ only in the disease-causing genetic modifications, can be generated employing genome editing technologies. This has been done as early as 2003, when Urbach and colleagues induced a *HPRT1* mutation in ESCs using homologous recombination to model Lesch-Nyhan disease[46]. However, the advent of another Nobel prize winning technology, Clustered regularly interspaced short palindromic repeats/CRISPR-associated nuclease 9 (CRISPR/Cas9) in 2013 streamlined this process enormously[47-49]. CRISPR/Cas9, which is part of an adaptive immune system in a range of prokaryotes, can be used to efficiently induce the formation of DNA double-strand breaks in a specified area of the genome and thus be used to either repair or induce specific mutations in target cells. The established isogenic controls will be particularly crucial for modelling sporadic or polygenic diseases, where only minor phenotypic variations are anticipated[50].

Thus, these disease-phenotypic PSC models can be used to recapitulate and decipher cellular, molecular and physiological mechanisms, which is interconnected with the ultimate goal of stem cell technology: the use of stem cells in regenerative and precision medicine, as well as the establishment of new pharmaceutical treatment options. In the last decades, drug screening approaches largely focused on targets believed to be relevant to disease mechanisms. However, the low success rates in the search for compounds via target-based screening have diverted attention towards phenotypic screening methodologies[51]. iPSCs are exceedingly suitable for phenotypic screening, due to their production scalability, which facilitates assay development, and their pluripotency, which enables them to differentiate into all disease-relevant cell types. The first iPSC-based large-scale drug screen was performed for familial dysautonomia, a monogenic early-onset disease characterized by degeneration of neurons in the sensory and autonomic nervous systems. Neural crest precursors for

autonomic neurons were sorted, purified, and ultimately screened utilizing using 6,912 compounds, identifying new potential drugs[52]. Since then, iPSC-based drug screening has been used to evaluate compounds for various diseases, identifying several clinical candidates[45].

Another application advanced by disease-specific iPSCs is drug-repositioning, which means screening of drugs already approved for specific diseases to find new applications for other diseases. Utilizing such a screen, e.g. the anti-epileptic drug ezogabine was found to be effective in an iPSC model of the motor neuron disease amyotrophic lateral sclerosis and underwent a phase 2 clinical trial[53,54].

Another focus of stem cell-based medical research are cellular therapies. Theoretically, PSCs can be used to promote endogenous regenerative processes or to replace damaged tissues through cellular transplantation. However, before PSC-based therapy can be routinely applied, several obstacles need to be eliminated. Firstly, due to their prolonged expansion in culture, pluripotent cells have the potential to accumulate karyotypic abnormalities and need to be carefully screened for potentially risky genetic alterations before use[55]. Secondly, while the differentiated products derived from iPSCs have not demonstrated teratoma formation before, it is imperative to verify that the final product does not contain undifferentiated cells, as they possess the potential to give rise to teratomas. Thirdly, an effective method of inducing immune tolerance is needed at least for allogenic PSC-derived transplantation products. The last part can potentially be avoided by precision medicine utilizing autologous patient iPSCs or iPSCs of matched donors. However, due to the high cost and long timeframe needed for full validation of each cell line, autologous iPSC therapy is not feasible especially for acute diseases[45]. Another workaround might be the establishment auf a universal donor PSC utilizing the already mentioned advances in genome editing[56].

Astonishingly, several clinical studies using ESC and iPSC-derived cellular products are already underway. The first clinical trial utilizing iPSCs already started in 2014 in Japan, which is the leading nation in PSC-based therapeutic clinical studies[57]. In this first study, autologous iPSC-derived retinal pigment epithelial cell sheets were transplanted into a patient with macular degeneration, which causes the progressive deterioration of light-sensing photoreceptors in the eye. The transplantation effectively stopped the progression of the patients macular degeneration and improved the vision of the patient[58,59]. Currently, the most advanced clinical trial is a phase 3 trial by Cynata

Therapeutics, which utilizes Cynata's iPSC-derived iMSC therapeutic, CYP-004, in 440 patients with osteoarthritis[60].

On a different note, stem cell technology can not only benefit human populations, but can also be used for animal preservation efforts. iPSCs have been derived from critically endangered animals with few reproductively capable representatives, like the drill or the northern white rhinoceros[61]. These iPSC can be used for enhancing genetic variability in the remaining populations and may be used for reintroducing extinct species in the future. The potential applications of PSC are summarized again in Figure 2.

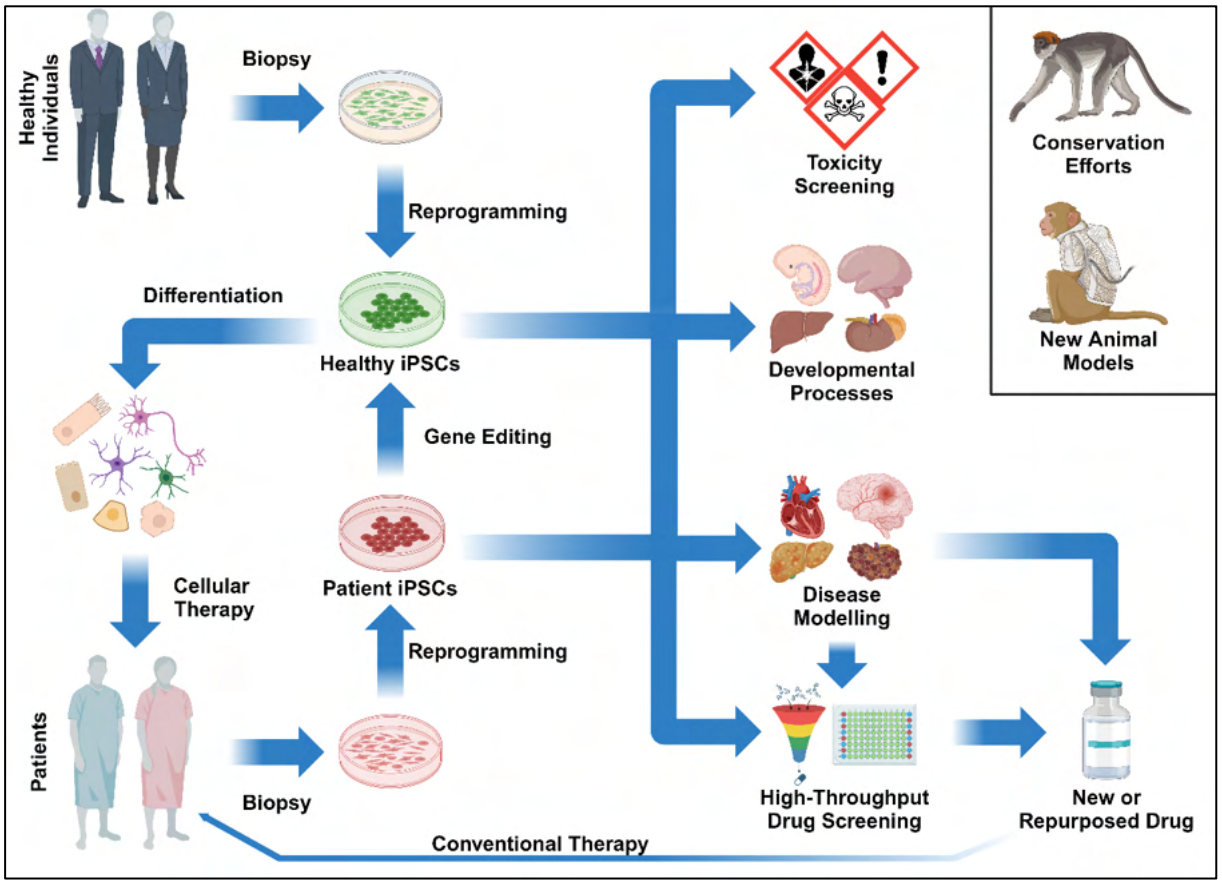

Figure 2: Applications of induced pluripotent stem cells. iPSCs can be reprogrammed from both healthy and diseased donors. Utilizing gene editing technologies (e.g. CRISPR/Cas9), patient iPSCs can be converted into healthy iPSCs. Both autologous gene edited iPSCs and allogenic iPSCs derived from certified healthy donors can be differentiated into terminally differentiated cells and used for cellular therapies in patients. Both healthy and patient iPSCs can also be used for research, especially in the areas of toxicity screening, developmental biology and disease modelling. Both the iPSCs and new insights from disease modelling research are utilized for high throughput drug screens in the search for new compounds or for secondary indications of already established drugs, which can then be used in conventional therapy of the investigated disease. iPSCs can also aid in the conservation efforts of endangered animals and in the establishment of new animal models (e.g. primate models). Figure created with BioRender.com.

Overall, advancement of iPSC technology has introduced a potent and innovative approach for both understanding and addressing diseases, as well as understanding not only human, but overall mammalian development.

II.II. Human Brain Development

II.II.I. General information about the human brain

The human brain is one of the most complex organs known to man and the largest mammalian brain in relation to the size of its bearer. The average adult human brain has a volume of 1350 cm^3, a total surface area of 1820 cm^2, contains approximately 100 billion neurons and an estimated 10 times this amount in glial cells – mainly astrocytes, oligodendrocytes and microglia[62-64].

Neurons, of which there are various types, are the information processing cells of the brain. A stereotypical neuron consists of soma, dendrites and axon, enabling the formation of synaptic connections with other neurons over long distances. Aside from some exceptions, inputs are generally collected by the dendrites and cell body, and output is distributed via the axon[65]. Signal transmission at the synapse is achieved via release of neurotransmitters at the presynaptic end and subsequent binding of said neurotransmitters at the postsynaptic end[66].

Astrocytes are the most abundant glial cell type of the central nervous system (CNS). While traditionally recognized as supportive cells for neurons, astrocytes play multifaceted roles in brain function and homeostasis. They i.a. influence neuronal survival, regulate cerebral blood flow, are essential components of the blood-brain barrier, clear neurotransmitters from the extracellular environment, contribute to the formation of neuronal circuits and influence synaptic formation, strength and turnover[67-70].

Oligodendrocytes are the myelinating cells of the CNS, capable of providing metabolic support to several axons at once and enwrapping them in myelin sheaths. Myelin is a modified and compacted plasma membrane that ensheaths the axons, insulating the axon and thereby enabling fast saltatory nerve conduction while ensuring axon integrity[71].

Microglia, which make up an estimated 10% of all brain cells, are the resident immune cells of the brain, protecting the CNS against invading pathogens and tissue damage, as well as removing dying neurons and ensuring homeostasis. Microglia originate from erythro-myeloid precursors within the embryonic yolk sac and migrate to the

developing brain early in its development. Unlike the developmentally similar macrophages, these cells are sustained through self-renewal processes and do not rely on bone marrow-derived progenitors for population maintenance. Their origination from the hematopoietic lineage also makes them the only major brain cell type derived from mesoderm, not ectoderm[70,72]. The structure of the nervous system and the main cellular compartments of the CNS are illustrated in Figure 3.

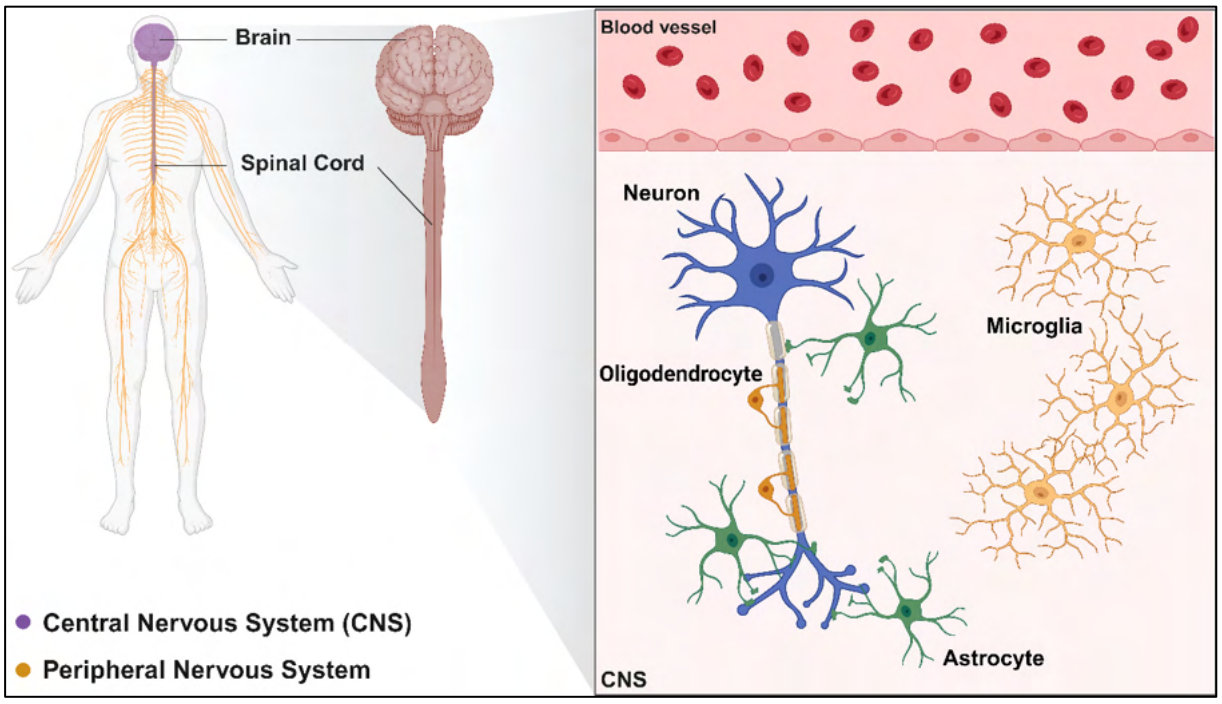

Figure 3: Schematic illustration of the nervous system and its main cellular components. The human nervous system is divided into two parts, the peripheral nervous system and the central nervous system (CNS). The CNS is divisible in two major parts – the brain and the spinal cord – which however are composed of the same cell types. The main cell types of the brain are neurons, astrocytes, oligodendrocytes and microglia.

II.II.II. Embryonic human brain development

Human brain development is a protracted process influenced by intrinsic and extrinsic factors, which starts at the third gestational week (GW) and ends in the earliest estimation in late adolescence, but potentially persists until end-of-life[73]. To achieve brain functionality, billions of cells have to be generated and orchestrated, which requires a complex series of dynamic and adaptive processes to occur within a tightly regulated genetic framework. The first step is the establishment of the three germinal layers – ecto-, meso- and endoderm - that will eventually give rise to all structures of the developing embryo in a process termed gastrulation, in GW2. During this establishment of the germ layers, ectodermal cells along the anterior-posterior midline

of the embryo are transformed into neuroepithelial cells (NECs)[73]. Next, in a process termed neurulation, the neural tube is formed. First, NECs form an area termed the neural plate at the end of GW3. Subsequently, the neural plate develops bilateral ridges, termed neural folds, at the junction to non-neural ectoderm, which start folding dorsally and inward, forming the hollow neural tube (Figure 4)[74]. The most anterior region of the neural tube will ultimately develop into the brain, while more posterior positioned cells will develop into the spinal column. Just before neural tube closure at the end of GW4, the anterior end expands to form three primary brain vesicles: prosencephalon (forebrain precursor), mesencephalon (midbrain precursor), and rhombencephalon (hindbrain precursor).

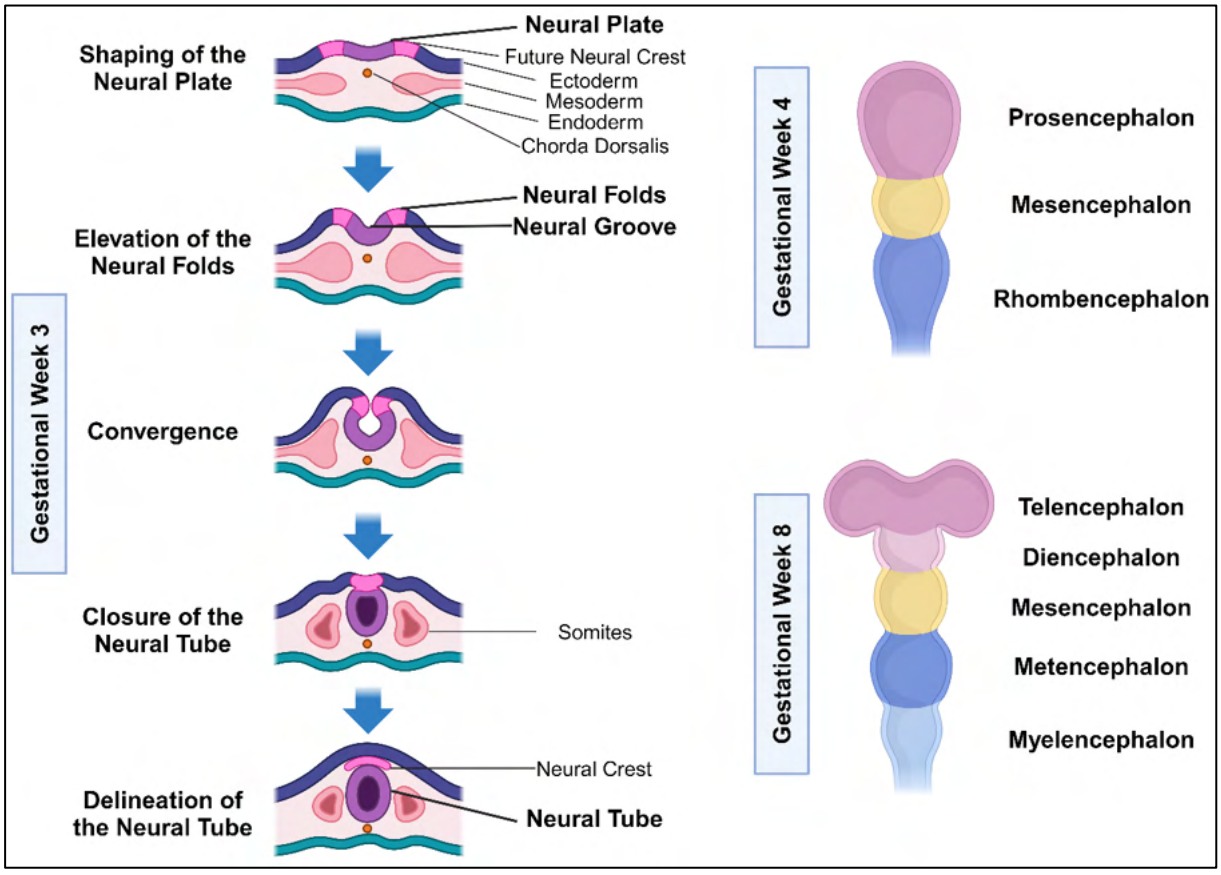

Figure 4: Schematic illustration of neurulation and establishment of brain vesicles. Neurulation starts in GW3 with the establishment of the neural plate along the midline of the embryo, dorsally of the chorda dorsalis. At the junction between neural and non-neural ectoderm, the neural ridges form and start elevating, folding dorsally and inward. The neural ridges converge and fuse, forming the hollow neural tube. The neural tube delineates from the rest of the ectoderm and wanders further ventrally. Cells originating from the fused tips of the neural folds form the neural crest and the body cavity is closed by non-neural ectoderm. After neurulation, the anterior region of the neural tube expands and forms the three primary brain vesicles – pros-, mes- and rhombencephalon – in GW4. The three primary brain vesicles then develop into the five secondary brain vesicles – tel-, di-, mes-, met- and myelencephalon – over the next four weeks. Figure created with BioRender.com.

This anterior-posterior regional patterning of the developing brain is regulated by WNT signalling, whereas dorsoventral patterning is regulated by gradients of bone morphogenic proteins (BMP) and WNT family members (WNT) signalling from the dorsal direction, and sonic hedgehog (SHH) signalling from the ventral direction. The established segments then subdivide into five secondary brain vesicles by the end of the embryonic period at GW8: the telencephalon and diencephalon from the prosencephalon, and the metencephalon and myelencephalon from the rhombencephalon. The mesencephalon remains undivided (Figure 4)[73,75].

II.II.III. Human neocortical development

Modern human brains have developed exceptional computational capabilities, enabling advanced cognitive functions which are closely tied to the massive expansion and enhanced connectivity of the human cerebral cortex[76]. The cerebral cortex, constituting more than half of the human brain's total volume, is a complex structure containing six layers of functionally diverse neurons and possesses a highly specialized regional organization. During embryonic and foetal development, cortical layering emerges in an inside-out manner as forebrain progenitors undergo proliferation and produce successive waves of neurons[77].

As described, the telencephalon starts off as a simple pseudostratified neuroepithelium at the anterior end of the neural plate. NECs exhibit polarity along their apicobasal axis, spanning the entire width of the neuroepithelium. Their basal membrane rests on the basal lamina, while the apical membrane faces the neural tube lumen[78]. From the end of gastrulation until around gestational day 42 in humans, the population of NECs undergoes symmetrical cell division, which produces two identical neural progenitor cells[79]. After this timepoint, neurogenesis begins, and NECs gradually transform into apical radial glia cells (aRGCs) by downregulating Golgi-derived apical trafficking and tight junctions and upregulating the expression of the master regulator of neurogenesis Paired Box 6 (*PAX6*) and glial markers such as Solute Carrier Family 1 Member 3 (*GLAST*) and Fatty Acid Binding Protein 7 (*BLBP*) while retaining their apicobasal polarity[80].

As neurogenesis begins, NECs transition from symmetric to asymmetric division, generating both an aRGC and a differentiating cell. In the neocortex, this differentiating cell constitutes either a neuron or a more fate-restricted progenitor known as an apical intermediate progenitor (aIP) and basal progenitor (BP)[78,81]. The nuclei of aRGCs and

aIPs remain in the proliferative zone adjacent to the ventricle, termed ventricular zone (VZ), and continue to divide, while BPs migrate basally. aIPs can undergo only one exhaustive division to produce two postmitotic neurons. BPs delaminate from the VZ and establish another proliferative zone adjacent to the VZ, the subventricular zone (SVZ), which is itself divided into an inner and outer SVZ (iSVZ/oSVZ) in gyrencephalic species like humans. Postmitotic neurons originating in the VZ and SVZ undergo radial and lateral-pial migration along the apicobasal process of aRGCs towards the developing neocortex[73,78].

BPs can be further classified into basal intermediate progenitors (bIPs) and basal radial glial cells (bRGCs), which can be generated either from NECs, aRGCs or BPs themselves. As bIPs migrate towards the SVZ, they downregulate astroglial markers and begin expressing the transcription factor TBR2[82]. Like aIPs, bIPs can divide once into two postmitotic neurons or undergo symmetric divisions to amplifying the number of progenitor cells and ultimately neurons[83,84].

Classical bRGCs possess a basal process inherited from the parent aRGC that contacts the basal lamina but lack an apical process. However, bRGCs exhibit a remarkable diversity. Some extend an apically directed process that does not reach the ventricle, while others lose basal contact and regrow a basal process that does not reach the basal lamina. Overall, bRGCs exist in various stages of extending processes in the apical, basal, or both directions[78]. Like aRGCs, bRGCs can be characterized by their expression of PAX6 and diverse astroglial markers, with about 50% also co-expressing TBR2[85].

Each of the BP types exhibits extensive self-renewal and proliferative capacities as well as the ability to directly generate neurons. All BP types have also been reported to have the ability to bidirectionally transition between BP types during proliferative divisions, however always enhancing the progenitor pool[78].

The last subtype of progenitor cell found during cortical development is the subapical progenitor (SAP). Unlike bRGCs, SAPs extend a process to the apical side and maintain contact with the ventricle. SAPs proliferate in an abventricular location, which means either in the basal VZ or in the SVZ. Little is known about the function of this cell type, but a role of SAPs in gyrification is assumed[86].

As already mentioned, the higher cognitive functions observed in humans are largely attributed to the massive expansion of the neocortex in comparison to other species. This expansion is the result of a vast increase in the numbers of neurons produced

during neocortical development, which in turn is the result of an increase in BPs. This increase of BPs can be observed in a variety of gyrencephalic species. While lissencephalic species like mice have a single SVZ, gyrencephalic species showcase the already mentioned partition of the SVZ in distinct iSVZ and oSVZ regions. The iSVZ corresponds to the SVZ in lissencephalic species and remains constant in thickness during neurogenesis, while the oSVZ consistently expands, harbouring up to four times as many progenitors as the VZ and iSVZ during the peak of neurogenesis[87]. It is important to note, that while in humans this hypertrophied oSVZ contributes to massive neuronal output, in other gyrencephalic species it might have other functions, as e.g in ferrets oSVZ bRGCs contribute more astrocytes to the cortex than neurons[78,88].
The structure of the developing neocortex and the differences between lissencephalic and gyrencephalic neocortex development are illustrated in Figure 5.

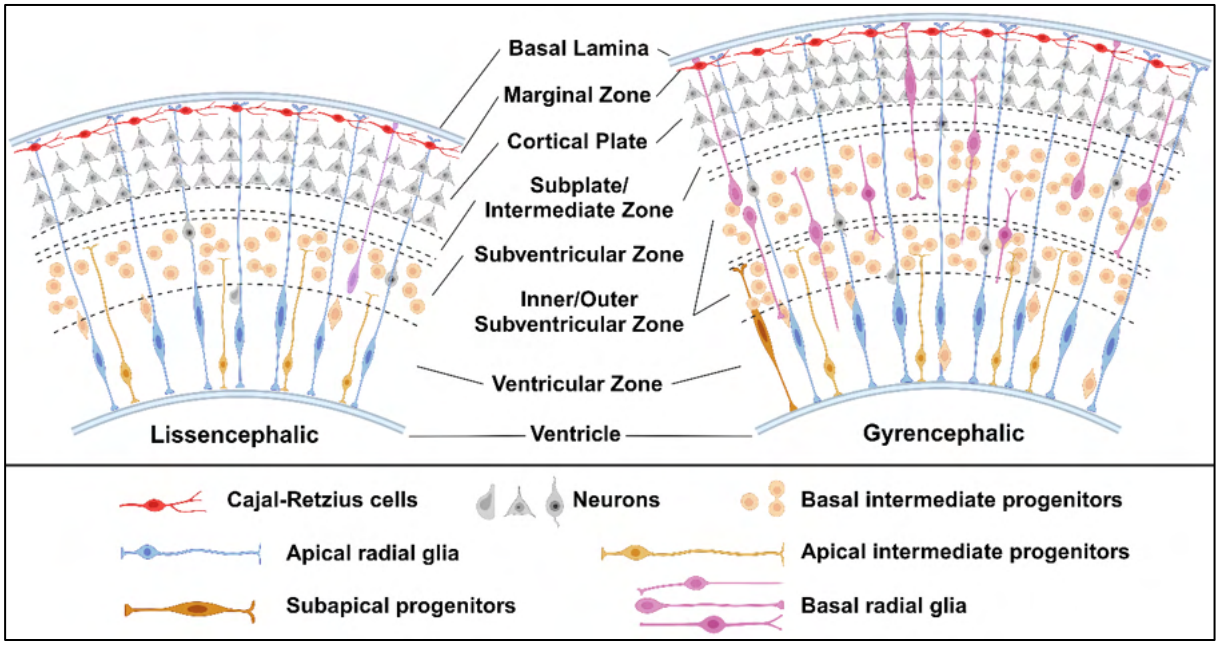

Figure 5: Schematic illustration of the structure and cellular makeup of the developing neocortex in lissencephalic and gyrencephalic species. Illustration representing the developing neocortex of a lissencephalic species, e.g. mouse (left), and a gyrencephalic species, e.g. human (right), and depicting the NPC types frequently observed in each of the germinal zones. Figure recreated from Florio and Huttner [78] using BioRender.com.

Another source of cortical neurons is located in the ventral telencephalon, in the regions termed medial, lateral and caudal ganglionic eminence, which will later become the basal ganglia. These areas are the source of inhibitory cortical interneurons, which migrate long distances while traversing the contour of the developing cortical mantle tangentially[89,90].

The migration of neurons into the developing neocortex results in the formation of a 6-layered structure. In this process, the first neurons to leave the proliferative zone form a structure called the preplate. When the preplate is formed, following migrating neurons split the preplate into two transient regions, the marginal zone (MZ) and the subplate (SP) and begin to form the cortical plate (CP) in an inside-out fashion. Inside-out means the deepest layer of the cortex, layer 6, is formed first and layer 5-1 are constructed afterward. The developmental cue for this orderly formation of the layers is produced by Cajal-Retzius cells in the MZ. These cells secrete Reelin, a protein involved in the signalling pathway which instructs neurons to halt migration and assume their positions in the cortex. Each successive wave of migrating neurons positions itself at the outermost layer of the developing cortex by bypassing the previous wave and halting their migration upon entering the Reelin signalling zone. Both MZ and SP mostly disappear by the end of the fetal developmental period[73,91].

After migration, neurons in their target region undergo differentiation processes enabling integration into local microcircuits between cortical layers, as well as long-range intra- and extra-cortical connections. These include axonal and dendritic outgrowth, synapse formation and stabilization, as well as long-range neural circuitry pathfinding in a remarkably accurate and efficient fashion[92,93].

After most of the neurogenesis occurred, neural progenitors switch to gliogenesis at mid-gestation, in which aRGCs detach from the apical surface, migrate basally and differentiate into glial precursors, first producing astrocytes and later on, roughly from the beginning of the postnatal period, oligodendrocytes[94].

II.III. Modelling brain development and disease using iPSCs

II.III.I. 2D Neural Modelling

As discussed earlier, the ability of iPSCs to differentiate into every cell type under the right conditions holds great potential to dissect the underlying pathophysiological mechanisms of diseases. So, to model neurological diseases, iPSC-based neural models have to start with neural induction, which means the commitment of iPSCs to the neuroectodermal lineage.

A widely used method to achieve this commitment is the “dual-SMAD inhibition”, or more precise the inhibition of TGFβ superfamily signalling, in particular BMP and Activin/NODAL signalling[95]. Utilizing two inhibitors, e.g dorsomorphin, an indirect inhibitor of SMAD1, SMAD5 and SMAD8 and SB-431542, an indirect inhibitor of

SMAD2 and SMAD3, iPSCs are directed towards the anterior neuroectodermal fate[96]. The anterior neuroectodermal fate, the forebrain fate, is the default direction of neuroectoderm in the absence of other developmental cues. However, utilizing the correct concentrations of morphogens, e.g. BMPs/WNTs/SHH for the dorsoventral axis and WNTs/Retinoic acid for the anterior-posterior axis, the derived NECs can be patterned into regional specific neural progenitor cells (NPCs), which in turn can give rise to every kind of neuron or glia.

In 2D cell culture, iPSC-derived forebrain NPCs arrange themselves in a characteristic rosette structure, termed neural rosette (NR), which mimics the apicobasal polarization of the neural tube. Furthermore, mitoses in the NR follow a sequence specific to NECs and aRGCs, termed interkinetic nuclear migration. NR cells also show other features of cortical NECs and aRGCs, like centrosomes localized to the apical end to extend cilia into the central lumen of each rosette and expression of cortical adherens junction proteins, e.g. ZO1 and N-cadherin, which are localized to the luminal surface[97].

During human cortical development, next to the NECs and aRGCs, there are abundant secondary populations of BPs found in the iSVZ and oSVZ. NRs also model this diversity of progenitor cells, as both bIPs and bRGCs can be identified basally of the aRGC-like cells. The NR thus is composed of polarized aRGC-like cells at the centre and BP-like cells located in an adjacent SVZ-like area[97-99]. Interestingly, when NRs are further differentiated without disturbance, these iPSC-derived cortical-like NPCs sequentially generate neurons with identities corresponding to all six layers of the neocortex[95,97].

The NPCs making up the NR can also be further expanded either in 2D or the NR can be detached and kept in suspension culture, forming spherical structures termed neurospheres (NS). Both expansion systems have advantages and disadvantages. Neurospheres are more work-intensive in propagation and grow slower, but also show higher and more homogenous expression of NPC specific gene expression and can be kept in culture for extended periods of time when compared to 2D expanded NPCs [100,101].

NPCs derived from both methods can be used for neurogenesis and the establishment of neuronal networks in 2D. To differentiate the NPCs, one can either omit the growth factors needed for retaining stemness in the NPCs – e.g. FGF2 and EGF[102] – or add neurotrophic factors to the culture. Neurotrophic factors, e.g. brain-derived growth factor (BDNF), neurotrophin 3 (NT-3), glia-derived growth factor (GDNF) and insulin-

like growth factor-1 (IGF1) have the added effect of promoting survival and differentiation of neurons, as well as being able to promote other cell fates, such as astrocyte or oligodendrocyte differentiation[103,104].

These simple 2D *in-vitro* models are already useful for modelling brain development and its diseases. However, while 2D differentiation techniques are straightforward and efficient for single-cell type differentiation, they often fall short in capturing the complexity of the human brain. This emphasizes the necessity for more physiologically relevant models that incorporate human-specific features of brain development[105].

II.III.II. 3D Neural Modelling

Modelling development and diseases of the brain is challenging due to its complex physiology. Achieving a deeper understanding of the human brain necessitates models capable of recreating at least parts of its complex architecture and functions. Recently, advancements in PSC-derived 3D brain organoid culture have enabled researchers to mimic diverse aspects of human brain physiology *in-vitro* and replicate fundamental disease processes.

Organoids are constructs commonly comprised of different types of cells in a dense 3D environment with direct cell–cell and cell–matrix contacts, reminiscent of a native tissue environment. This tissue-like environment in 3D cultures preserves cell phenotype and function more effectively than the rigid 2D culture environment[106].

In 2011, the first entirely 3D neural culture was realized by generating self-organizing optic cups from human PSCs. The generated organoids faithfully recapitulated the developing retina, demonstrating the capability of PSC-derived neural tissue to self-organize and develop organotypic tissue architecture in 3D culture[107]. Next, in 2013, was the establishment of unguided “cerebral” or “whole-brain” organoids with various regional identities by combining classical EB culture without patterning factors with Matrigel embedding, a technique which had recently been established to generate 3D intestinal tissues from adult intestinal stem cells, and agitation of the organoid culture[108,109]. Matrigel embedding provided a 3D environment for the cells to self-organize in and agitation of the organoids enhanced diffusion of nutrients and oxygen, which enabled formation of larger organoids[110]. In these large cerebral organoids, dorsal forebrain regions were shown to exhibit highly expanded progenitor zones, which displayed organisation reminiscent of a VZ and SVZ, as well as typical cellular behaviour as described before. Furthermore, neurons showed proper migration to the

basal surface where they organised into a preplate. Further along in their development, the generated neurons mimic cortical layering, differentiate and establish functional synapses (Figure 6)[109].

This same organization was also observed in organoids guided to a forebrain specific fate by Kadoshima et al. in the same year, again demonstrating the fidelity of organoid cultures to their developmental program[111]. Remarkably, the cytoarchitecture of cerebral organoids not only mirrors aspects of the human brain but also exhibits epigenomic and transcriptional programs resembling the fetal brain[112].

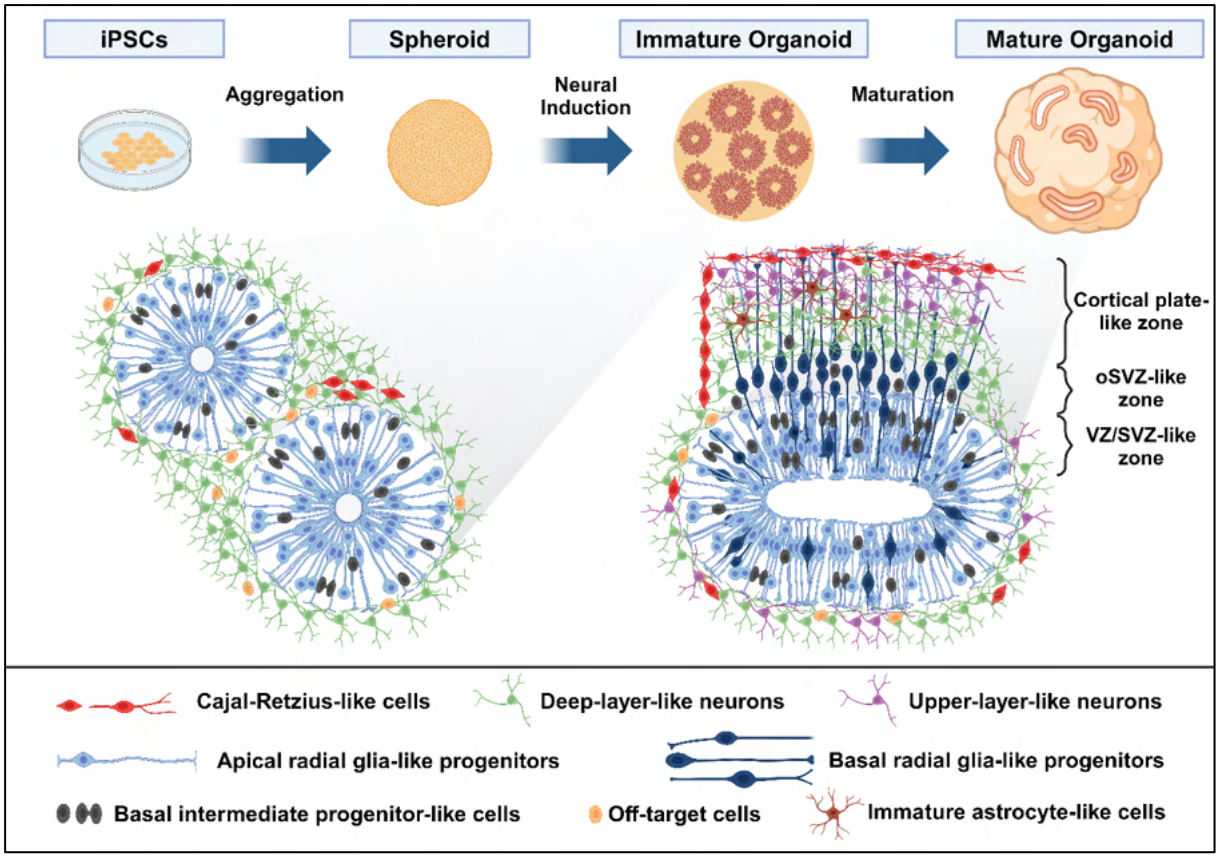

Figure 6: Schematic illustration of the progression of brain organoid maturation. iPSCs are aggregated to form a spheroid and patterned to induce neuroectodermal fate. In the immature organoid, neuroectodermal cells organize in rosettes and subsequently develop into mature brain organoids, which recapitulate the cellular diversity and cytoarchitectural organization of the developing human brain. The immature organoids (left) contain apical neuroepithelial stem cell-like and apical radial glia-like progenitors which form a ventricular (VZ)-like zone. Basal intermediate progenitor-like cells and deep-layer-like neurons surround this VZ-like zone. Mature organoids (right) display multiple progenitor zones, including a VZ-like zone and a subventricular (SVZ)-like zone, as well as an oSVZ-like zone containing basal radial glia-like progenitors. Mature brain organoids also mimic cortical layering, as neurons with distinct identity can be found basally of the progenitor zones, organizing into a cortical plate-like zone. Figure created with BioRender.com utilizing information from Di Lullo and Kriegstein [113] and Yang, et al. [114].

These initial protocols have been expanded on, some simplifying the protocol by e.g. omitting the Matrigel embedding step[115], but most concentrating on establishing guided methods to generate brain region specific organoids. These efforts have led to the development of protocols to specifically generate various brain regions, as well as protocols accelerating the emergence of astro- and oligodendrocytes, which arise late in development under normal conditions[104,116-118].

As mentioned before, PSC-derived neural models can be utilized for more than extending the findings previously obtained in animal models to the human setting. PSC models have revealed the extent to which cell diversity, as well as spatial and temporal patterning can be robustly recapitulated *in-vitro*, emphasizing the importance of intrinsic self-organization during development. The versatility and accessibility of PSC models makes them ideal to study developmental and disease mechanisms in an academic setting, providing a platform for questions not easily addressed by other model systems.

II.IV. Modelling neurological diseases using iPSCs

Disorders of the nervous system are the leading cause of healthy life-years lost due to ill-health, disability, or early death and the second leading cause of death globally, accounting for 9 million deaths per year. In 2016, there were 52.9 million children worldwide under the age of 5 with developmental disabilities. In Europe alone, brain disorders were estimated to cost 798 billion euro in 2010. Moreover, in 2019, the overall global societal cost of dementia was estimated at 1.3 trillion US-Dollar, which is equivalent to 1.5% of the global GDP[119].

Unravelling human brain development and dysfunction is a primary objective in neuro- and stem cell biology. Our previous knowledge largely stemmed from the analysis of pathological and post-mortem samples, supplemented by investigations into non-human primate development and mouse models of several neurological diseases. While these animal models, as well as primary and immortalized cell lines have been invaluable in beginning the process of dissecting the underlying developmental and pathophysiological mechanisms, they do not accurately reproduce the human brain physiology, genetics and developmental patterns.

As discussed in II.I.III., disease-specific iPSC models can and are being utilized to alleviate some of these hurdles, whether the disease is a defined genetic disorder or caused by pathogenic or environmental influences. iPSCs have been extensively used

to model neurodegenerative diseases such as Alzheimer‘s disease, frontotemporal dementia, amyotrophic lateral sclerosis, Parkinson‘s disease and Huntington‘s disease, but also for the modelling of neuropsychiatric and neurodevelopmental diseases like autism spectrum disorder, Rett´s disease and Nijmegen Breakage disease, as well as pathogen-caused neurological diseases like Congenital Zika[120-122]. Overall, utilization of patient-derived iPSCs, coupled with ongoing advancements in creating physiologically relevant 2D and 3D neural models, offers an unprecedented opportunity to investigate many human neurological diseases comprehensively for the first time.

II.IV.I. Cockayne Syndrome

Cockayne syndrome (CS), also called Neill-Dingwall-Syndrome, was first described by Edward Alfred Cockayne in 1936[123]. CS is a rare hereditary autosomal recessive disorder characterized by severe photosensitivity, failure to thrive, cachectic dwarfism, segmental progeria, vasculopathy, cataracts, dental caries and progressive multisystem degeneration. CS has a prevalence of 2.5 in 1 million births with no apparent overrepresentation in any specific population and a median life expectancy of 12 years. Particularly burdensome for CS patients are the various possible neurological afflictions such as intellectual disability, sensorineural hearing loss, progressive microcephaly, cerebellar hypoplasia, dys- and hypomyelination, dystrophic mineralization of neurons and vessels and segmental demyelinating peripheral neuropathy[124-127].

CS can be divided into five overlapping subtypes. In order of severity from light to severe, CS can be diagnosed as UV-sensitive syndrome (UVSS), late-onset type III, classical moderate type I, early-onset type II CS or very early-onset (fetal) cerebro-oculo-fascio-skeletal (COFS) syndrome[126].

CS can be caused by mutations in several genes, but the main cause are mutations in excision repair cross-complementing protein group 6 *ERCC6* (Cockayne Syndrome B Protein, CSB) and *ERCC8* (Cockayne Syndrome A Protein, CSA). Mutations in *ERCC6* account for two out of three cases of CS and generally cause more severe subtypes of CS. *ERCC6* encodes a 168 kDa protein of the SWI/SNF family of ATP-dependent chromatin remodelers, which functions as a facultative homodimer[126,128].

The first and most explored function of CSB is it role in transcription-coupled nucleotide excision repair (TC-NER). Mammalian cells have two DNA damage repair systems for

the removal of bulky DNA lesions, termed the global genome nucleotide excision repair (GG-NER) and TC-NER. The GG-NER directly scans genome-wide for e.g. UV-induced lesions, typically pyrimidine dimers, or bulky chemical adducts, while the TC-NER scans for an RNA-Polymerase II (RNAPII) stalled by such a lesion[129].

The loss of this specialized repair mechanism explains the photosensitivity found in CS patients. Loss of TC-NER may also account for part of the segmental progeria, as impaired TC-NER induces premature cell death in a p53-independent manner, but not all symptoms can be explained by the loss of this function[130-132].

Both CSA and CSB have also been implicated in the repair of oxidative damage-induced small non-helix-distorting DNA lesions. While oxidative lesions have been thought to mainly be repaired by base excision repair (BER) and mitochondrial (mt) BER, CS mutation carriers have also been shown to be more susceptible to cellular and mitochondrial oxidative damage. This susceptibility may be caused by a decreased activity of BER and mtBER repair factors, as CSB has been shown to colocalize with several BER-associated proteins, e.g. apurinic/apyrimidinic endonuclease 1 (*APE1*), poly-(ADP-ribose) polymerase (*PARP1*) and endonuclease VIII-like *(NEIL1*), and enhance their activity[133-135].

CSB also plays a crucial role not only in repairing single-strand lesions but also in addressing double-strand breaks (DSBs). DSBs can be repaired through two distinct pathways: non-homologous end joining (NHEJ) or homologous recombination (HR). NHEJ repairs DSBs without the use of a homologous sequence, rendering the mechanism more error-prone than HR. In the S/G2 phase of the cell cycle, HR is favoured, however the decision is dependent on CSB. CSB associates with DSBs, where it promotes the recruitment of BRCA1 DNA Repair Associated (*BRCA1*), an important factor for the initiation of HR. CSB simultaneously represses the recruitment of Tumor Protein P53 Binding Protein 1 (*TP53BP1*) and Replication Timing Regulatory Factor 1 (*RIF1*), factors favouring the initiation of NHEJ. CSB is also partially required for the phosphorylation of ATM Serine/Threonine Kinase (*ATM*), a factor necessary for the G2/M checkpoint activation. CSB depletion therefore leads to premature entry into mitosis[136,137].

Lastly, CSB has also been implicated in interstrand crosslinks repair (ICR). Interstrand crosslinks (ICL) are DNA lesions connecting the two strands of a DNA helix. It has been shown that CSB-deficient cells repair ICLs less efficiently than wild type cells. CSB interacts with DNA crosslink repair 1A (*DCLRE1A*), which stimulates its

recruitment to ICLs and enhances ICR. ICR seems to be especially impaired in differentiated cells, as has been shown in postmitotic neural cells[136,138,139].

The progressive symptoms of CS may potentially be attributed to the damage accumulated due to the failure or reduction of TC-NER, BER, ICR and HR activity. This damage accumulates more rapidly in non-proliferative tissues with high metabolic activity, such as the brain, which accrue damage throughout life and rely on functional repair mechanisms for maintenance[129].

Other than its function in repair mechanisms, CSB has also been found to be in involved in several other pathways and essential functions. For example, the severe growth retardation may result from alterations in hormonal axes supporting growth and metabolism. Dysfunction of TC-NER has been demonstrated to decrease the Growth Hormone/Insulin-like Growth Factor-1 (GH/IGF-1) hormonal axis. The accompanying reduction in proliferation and growth, and shift to protective maintenance, is a widely conserved mechanism observable in response to diverse genotoxic stresses[129,140]. This dysregulation of the GH/IGF-1 axis has also been identified in iPSC-derived CSB-deficient neurons[141]. Children with growth hormone deficiency, a disease resulting from impaired GH/IGF-1 axis, also show alterations of brain structure and cognitive impairment[142].

Furthermore, CSB deficiency has been found to selectively reduce autophagy, a crucial mechanism for cellular maintenance. Functioning autophagy is necessary for the disposal of defective or unnecessary cellular components. Scheibye-Knudsen and colleagues demonstrated that CSB-deficient cells accumulate defective mitochondria, potentially due to reduced recruitment of Sequestosome 1 (*p62*) and decreased ubiquitination. These mitochondria accumulate defects at an increased rate, likely due to the partially impaired mtBER. Consequently, there's an overall increase in both the number and the proportion of defective mitochondria, leading to enhanced glycolysis and oxygen consumption, thus directly elevating reactive oxygen species (ROS) production[143]. Mitochondrial dysfunction has been implicated in several neurodegenerative diseases and likely plays a role in the neurological phenotype found in CS patients[144].

The decrease in autophagy might be attributable to reduced cytoplasmic α-tubulin acetylation. This reduction may result from the missing interaction between CSB and histone deacetylase 6 (*HDAC6*), as well as the α-tubulin acetyltransferase (*ATAT1*). Reduced α-tubulin acetylation directly leads to destabilization of the tubulin network

and decreased efficiency of the cellular cargo system, as α-tubulin acetylation promotes motor protein binding and motility[145].

α-tubulin acetylation is also a prerequisite for the timely assembly and disassembly of primary cilia, and a decrease in acetylation may impact intraciliary transport. Primary cilia are essential cellular organelles for cell signalling and development, as well as overall homeostasis. Cilia dysfunction has various known detrimental effects and may contribute to several symptoms of CS, e.g. facial and dental deformities, ocular disorders, and microcephaly[146-150].

CSB-deficient cells also exhibit dysregulation of RNA Polymerase I transcription, as well as disturbed processing of pre-rRNA. This leads to an accumulation of ribosomal 18S-E intermediates and misfolded ribosomal proteins, which are susceptible to unfolding under stress. Together this might cause a malfunction of the global protein synthesis and a loss of proteostasis[151,152].

Another important function of CSB is its involvement in transcription regulation. CSB deficient cells show up to 50% reduced transcription and dysregulation of thousands of genes[136,153,154]. CSB can transiently interact with RNAPII, which enhances transcription elongation *in-vitro* by a factor of 3[155]. Additionally, CSB can be found at certain promoter and enhancer regions, suggesting a role in transcription initiation. Specifically, CSB is enriched in sites containing the 12-O-tetradecanoylphorbol-13-acetate (TPA) response elements, potentially guided there by bZIP transcription factors. In proximity to these elements, CSB influences gene expression and local chromatin structure[136,156].

As suggested by the last sentence and its protein family name, CSB also functions as a chromatin remodeler. While its activity is weak on its own, CSB can interact with various proteins that enhance its activity. For example, CSB can interact with certain proteins, e.g. nucleosome assembly protein 1 (*NAP1*)-like histone chaperones, resulting in a tenfold increase in its ATP-dependent chromatin remodelling activity[157].

This non-exhaustive enumeration of CSBs pleiotropic effects alone, taken together with the overall rarity and variability of this disease, showcases the difficulty in establishing universally valid assertions about CS. However, the identification of similarities and dissimilarities between the different types of CS is a prerequisite for the identification of targets for pharmaceutical intervention.

All the named functions likely contribute in varying degrees to the multi-organ symptoms found in CS patients. The contributors deemed most important for the CNS symptoms are summarized again in Figure 7.

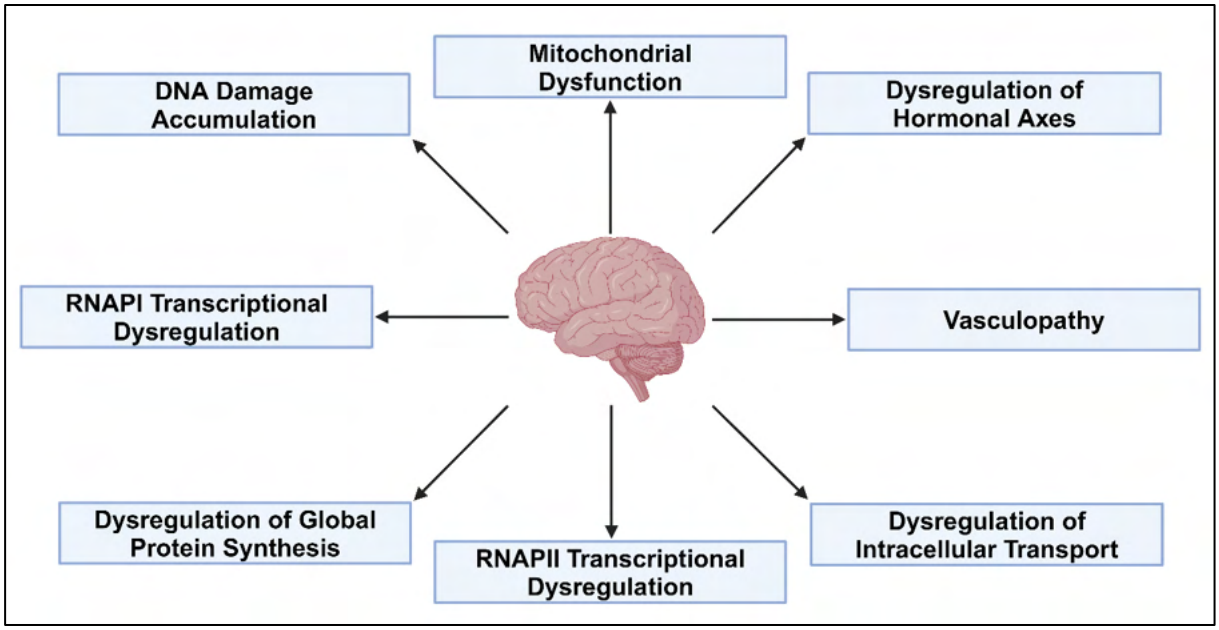

Figure 7: Main drivers of CS neurological symptoms. Figure created with BioRender.com.

II.IV.II. Cerebral malaria

Malaria is a disease caused by parasitic protozoans of the genus Plasmodium, in humans mainly by the four species Plasmodium (P.) falciparum, Plasmodium vivax Plasmodium ovale and Plasmodium malariae. Of the Malaria causing species, P. falciparum is considered the most dangerous and responsible for the high mortality rates associated with malaria[158].

A total of 247 million malaria cases were reported by 84 countries in 2021. In the same year, 619 000 deaths were associated with malaria. Globally, the reported cases of malaria have continuously decreased since 2000, however the decrease has stagnated and even reversed in some regions after 2014. Other regions, e.g. Argentina, El Salvador and Paraguay, are certified malaria-free for several years. 96 percent of malaria cases are concentrated in just 29 countries, 95 percent of which are located in the African region. Mortality rates follow a similar geographical pattern[159].

Infection usually occurs via a Plasmodium-carrying female mosquito of the Anopheles family. After infection, malaria can present either as simple malaria, characterized typically by fever or several episodes of fever, or one of several forms of severe

malaria. The most common forms of severe malaria are cerebral malaria (CM), severe malarial anaemia and malaria-associated acute respiratory distress syndrome[158,160].
CM is defined as a potentially reversible, diffuse encephalopathy causing a Glasgow coma score of 11/15 or less with no other causes of encephalopathy being identifiable. Other potential concomitant symptoms are retinopathy, headache, agitation, psychosis and seizures, as well as brainstem signs or focal neurological signs such as hemiplegia and cranial nerve palsies in rare and severe cases[161-163].
CM typically presents in the form of these serious neurological complications after infection with P. falciparum and is responsible for close to 20% of malaria-associated deaths in adults and 15% of deaths in children. The higher lethality of CM in adults is attributable to the development of multiple organ failure additionally to the neurological symptoms, which is rarely found in paediatric CM. While children exhibit higher survival rates, they are also more prone to the development of CM. An estimated 1% of patients infected with P. falciparum develop neurological symptoms, 90% of which are children. 10-20% of surviving patients display neurological sequelae upon discharge, indicating long-term damage of the CNS. The primary sequelae include cognitive and behavioural changes, motor abnormalities, and seizure disorders[158,164].
The exact etiology of CM is still elusive despite decades of research. Interestingly, the neuropathology is not directly caused by the pathogenic Plasmodium, as the parasite resides inside erythrocytes and does not enter the CNS but remains inside the vascular lumen[165].
There are two main hypotheses regarding the neuropathology of CM – the mechanical and cytokine storm hypothesis. The mechanical hypothesis is based on the intravascular sequestration (adhesion) of infected erythrocytes which results in e.g. vascular congestion, hypoperfusion and localized hypoxia[166]. Additionally, differences in local blood flow may contribute to increased intracranial pressure in CM. Sequestration of erythrocytes is facilitated by the parasite-encoded P. falciparum erythrocyte membrane protein-1 (*PfEMP-1*). PfEMP-1 is expressed on the surface of infected erythrocytes to prevent erythrocyte clearance via the spleen, but depending on the parasite strain, can also interact with various host adhesion receptors, such as Intercellular Adhesion Molecule 1 (*ICAM-1*), Vascular Cell Adhesion Molecule 1 (*VCAM-1*), Protein C Receptor (*EPCR*) and CD36 Molecule (*CD36*)[167-169]. The interaction between infected erythrocytes expressing distinct PfEMP-1 variants and their corresponding receptors triggers host signalling cascades including the activation

of inflammatory and coagulatory pathways, ultimately resulting in endothelial activation, disruption of BBB integrity and the onset of encephalopathy. Together, these factors ultimately lead to a breakdown of the BBB, brain haemorrhages, cerebral oedema and a localized pro-thrombotic state[165,170].

Several studies link the amount of infected erythrocyte sequestration in the brain vasculature to increased CM severity, however the extent to which this correlates with clinical symptoms and mortality remains a matter of debate.

Proponents of the "cytokine storm hypothesis" suggest that peripheral inflammation and elevated levels of various serum cytokines, including tumor necrosis factor-α (TNFα), interferon-γ (IFNγ), lymphotoxin-α (LTα), interleukin (IL) 1β, IL-2, IL-6, IL-8, and IL-10, are the main drivers of the CM pathology[171]. These cytokines released from immune cells then activate endothelial cells, prompting them to release chemokines such as C-C Motif Chemokine Ligand 2 (CCL2), CCL4, C-X-C Motif Chemokine 4 (CXCL4), CXCL8, and CXCL10[172]. These chemokines in turn lead to accumulation of immune cells, specifically monocytes, $CD8^+$/$CD4^+$ T-cells and natural killer cells. Accumulation of immune cells is followed by BBB disruption and perforin and granzyme-B-mediated endothelial cell apoptosis, which ultimately leads to immune cell invasion of the surrounding brain tissue, as well as extravasation of neurotoxic compounds[163,165,173].

Taken together, the pathogenesis of CM likely is a multifactorial process with parasite sequestration, peripheral and localized inflammation, endothelial dysfunction of cerebral microvasculature, invasion of immune cells and extravasation of neurotoxic molecules.

One of these compounds is the plasmodial metabolite Hemozoin (HMZ). HMZ, also called malarial pigment is an undegradable crystalline byproduct of the parasites haemoglobin degradation pathway and has immunomodulatory properties. During the initial cleavage in the haemoglobin degradation, heme is released, resulting in the oxidation of its ferrous iron (Fe^{2+}) into the reactive and harmful ferric iron (Fe^{3+}). To protect itself, the parasite crystallizes heme into HMZ through oxidation and dimerization[174].

HMZ has both pro- and anti-inflammatory properties, and its accumulation in tissues correlates with disease severity[175]. The accumulation of hemozoin has also been associated with severe malaria, indicating that its impact on the host immune response may negatively contribute to the development of malarial complications.

In CM, free extracellular HMZ deposits have been found alongside sequestered HMZ-containing infected erythrocytes. These free HMZ deposits frequently colocalize with platelets and fibrin and are more numerous in post-mortem brain tissue of CM patients than patients with other forms of severe malaria, potentially contributing to the vascular congestion, hypoperfusion and localized hypoxia associated with CM[176]. Additionally, HMZ was found in both intravascular and extravascular macrophages, potentially contributing to the local inflammatory response associated with the breakdown of the BBB[174]. Also potentially contributing to this breakdown, massive accumulation of HMZ can be found in the spleen of patients with CM and may influence the activation of pathogenic $CD8^+$ T-cells mentioned earlier. In a mouse model of CM, HMZ has also been shown to accumulate in brain tissue[177]. A dose- and time-dependent uptake and standalone toxicity of HMZ in the absence of other effectors was observed in astrocytes, neurons and microglia *in-vitro* indicating that HMZ can directly contribute to the pathogenesis of CM after disruption of the BBB[178,179]. All this information indicates, that understanding the role of HMZ in the pathogenesis of CM, as well as its exact neurotoxicity, could have significant implications for developing alternative therapeutic interventions aimed at minimizing its toxic effects within the CNS. The hallmarks of CM are summarized in Figure 8.

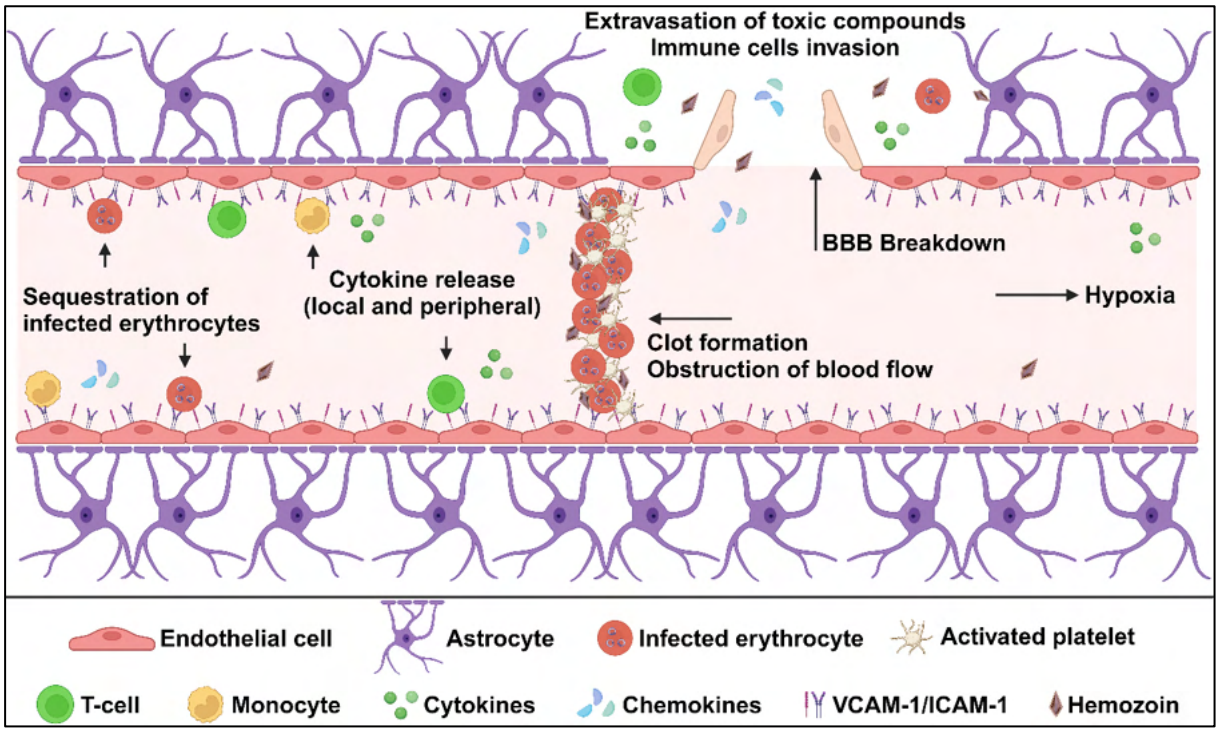

Figure 8: Series of events leading to P. falciparum-induced cerebral malaria. Sequestration of PfEMP-1-expressing infected erythrocytes onto the brain endothelium via parasite strain-specific adhesion molecules (e.g. VCAM-1 and ICAM-1) results in the

obstruction of blood flow, inducing inflammation and localized activation of endothelial cells (which might already be primed by peripheral proinflammatory cytokines). Activated endothelial cells secrete chemokines leading to accumulation of activated immune cells (e.g. Monocytes and T-cells) and subsequent localized release of proinflammatory cytokines. Localized inflammation activates platelets, which adhere to the sequestered infected erythrocytes, potentially leading to the formation of a clot, further obstructing blood flow. Obstructed blood flow causes downstream hypoxia and lack of nourishment. Heightened intracerebral inflammation, endothelial activation and physical obstruction of microvasculature might lead to breakdown of blood-brain barrier (BBB). Breakdown of BBB leads to invasion of immune cells into the brain parenchyma, as well as the extravasation of proinflammatory cytokines and toxic compounds such as Hemozoin. Hemozoin also accumulates on and exacerbates intravascular clot formation. Figure taken from Panda and Mahapatra [180] and modified. Figure was recreated using BioRender.com.

II.V. Objective

As mentioned in II.IV., diseases of the nervous system are the leading cause of healthy life-years lost and the second leading cause of death globally, thus carrying a massive physical, emotional, and economic impact on individuals, families, and society at large. Neurological diseases encompass a broad spectrum of disorders, from neurodevelopmental conditions like autism to neurodegenerative diseases such as Alzheimer's and Parkinson's. Improving the understanding of underlying pathomechanisms can potentially lead to early diagnosis, refined treatments, and possibly even to preventative strategies.

In this context, iPSCs offer an unprecedented opportunity to study and understand brain disorders, as their ability to self-renew and differentiate into every cell type provides a theoretically infinite source of disease-specific neural cells.

In this thesis, we concentrated on two diseases with strong neurological involvement, Cockayne Syndrome and Cerebral Malaria. The main goals for the investigation of CS were (1) the establishment of a patient-specific expandable 3D neurosphere protocol, (2) the establishment of a patient-specific 3D organoid protocol and (3) the execution of a transcriptomics analysis to identify early neurodevelopmental transcriptional dysregulation common to different severity grades of CS, potentially identifying new pathomechanisms underlying this devastating disease.

For CM, the main goals were (1) the establishment of an easy-to-use protocol for the generation of 2D neuronal networks, (2) the establishment of a HMZ treatment regimen for the modelling of CM *in-vitro* and (3) an initial assessment of the molecular changes in human neurons upon exposure to HMZ. The key findings of both publications are summarized in Figure 9.

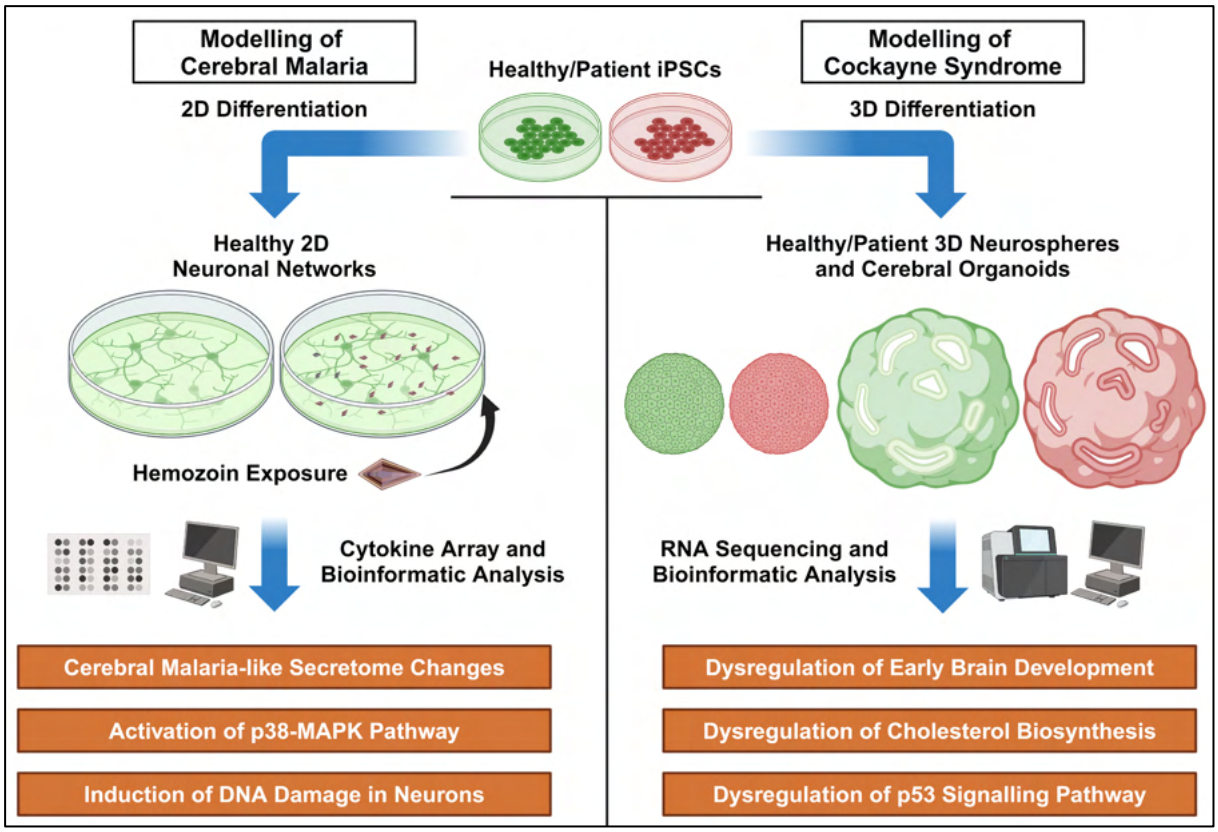

Figure 9: Graphical abstract summarizing the key findings from both publications presented in this thesis. Figure created with BioRender.com.

The thesis concludes with a discussion of our established iPSC models and the findings for both diseases in the context of recent literature, as well as an outlook into the necessary next steps in their research.

III. Publications

III.I. Cockayne Syndrome Patient iPSC-Derived Brain Organoids and Neurospheres Show Early Transcriptional Dysregulation of Biological Processes Associated with Brain Development and Metabolism

Leon-Phillip Szepanowski, Wasco Wruck, Julia Kapr, Andrea Rossi, Ellen Fritsche, Jean Krutmann and James Adjaye

Cells 2024, 13(7), 591

Abstract

Cockayne syndrome (CS) is a rare hereditary autosomal recessive disorder primarily caused by mutations in Cockayne syndrome protein A (CSA) or B (CSB). While many of the functions of CSB have been at least partially elucidated, little is known about the actual developmental dysregulation in this devasting disorder. Of particular interest is the regulation of cerebral development as the most debilitating symptoms are of neurological nature. We generated neurospheres and cerebral organoids utilizing Cockayne syndrome B protein (CSB)-deficient induced pluripotent stem cells derived from two patients with distinct severity levels of CS and healthy controls. The transcriptome of both developmental timepoints was explored using RNA-Seq and bioinformatic analysis to identify dysregulated biological processes common to both patients with CS in comparison to the control. CSB-deficient neurospheres displayed upregulation of the VEGFA-VEGFR2 signalling pathway, vesicle-mediated transport and head development. CSB-deficient cerebral organoids exhibited downregulation of brain development, neuron projection development and synaptic signalling. We further identified the upregulation of steroid biosynthesis as common to both timepoints, in particular the upregulation of the cholesterol biosynthesis branch. Our results provide insights into the neurodevelopmental dysregulation in patients with CS and strengthen the theory that CS is not only a neurodegenerative but also a neurodevelopmental disorder.

Author´s Contributions: (90%)

Conceptualisation, J.A., J.K. (Jean Krutmann), E.F. and **L.-P.S**.; formal analysis, **L.-P.S.** and W.W.; investigation, **L.-P.S.**, W.W., A.R. and J.K. (Julia Kapr); resources, J.A., J.K. (Jean Krutmann), E.F., A.R. and J.K. (Julia Kapr); data curation, **L.-P.S.** and W.W.; writing—original draft preparation, **L.-P.S.**; writing—review and editing, J.A. and W.W.; visualization, **L.-P.S.** and W.W.; supervision, J.A.; project administration, J.A., J.K. (Jean Krutmann) and E.F.; funding acquisition, J.A., J.K. (Jean Krutmann) and E.F. All authors have read and agreed to the published version of the manuscript.

Status: Published in Cells; Impact Factor 6.0; 5-Year-Impact Factor 6.7 (https://doi.org/10.3390/cells13070591)

cells

MDPI

Article

Cockayne Syndrome Patient iPSC-Derived Brain Organoids and Neurospheres Show Early Transcriptional Dysregulation of Biological Processes Associated with Brain Development and Metabolism

Leon-Phillip Szepanowski [1,2], Wasco Wruck [1], Julia Kapr [2], Andrea Rossi [2], Ellen Fritsche [2], Jean Krutmann [2] and James Adjaye [1,3,*]

[1] Institute for Stem Cell Research and Regenerative Medicine, University Hospital Düsseldorf, Moorenstrasse 5, D-40225 Duesseldorf, Germany; leon-phillip.szepanowski@iuf-duesseldorf.de (L.-P.S.)
[2] IUF—Leibniz Research Institute for Environmental Medicine, Auf'm Hennekamp 50, D-40225 Duesseldorf, Germany
[3] Zayed Centre for Research into Rare Diseases in Children (ZCR), University College London (UCL)—EGA Institute for Women's Health, 20 Guilford Street, London WC1N 1DZ, UK
* Correspondence: james.adjaye@med.uni-duesseldorf.de

Abstract: Cockayne syndrome (CS) is a rare hereditary autosomal recessive disorder primarily caused by mutations in Cockayne syndrome protein A (CSA) or B (CSB). While many of the functions of CSB have been at least partially elucidated, little is known about the actual developmental dysregulation in this devasting disorder. Of particular interest is the regulation of cerebral development as the most debilitating symptoms are of neurological nature. We generated neurospheres and cerebral organoids utilizing Cockayne syndrome B protein (CSB)-deficient induced pluripotent stem cells derived from two patients with distinct severity levels of CS and healthy controls. The transcriptome of both developmental timepoints was explored using RNA-Seq and bioinformatic analysis to identify dysregulated biological processes common to both patients with CS in comparison to the control. CSB-deficient neurospheres displayed upregulation of the VEGFA-VEGFR2 signalling pathway, vesicle-mediated transport and head development. CSB-deficient cerebral organoids exhibited downregulation of brain development, neuron projection development and synaptic signalling. We further identified the upregulation of steroid biosynthesis as common to both timepoints, in particular the upregulation of the cholesterol biosynthesis branch. Our results provide insights into the neurodevelopmental dysregulation in patients with CS and strengthen the theory that CS is not only a neurodegenerative but also a neurodevelopmental disorder.

Keywords: Cockayne syndrome; brain organoids; RNA-Seq; brain development; steroid biosynthesis

Citation: Szepanowski, L.-P.; Wruck, W.; Kapr, J.; Rossi, A.; Fritsche, E.; Krutmann, J.; Adjaye, J. Cockayne Syndrome Patient iPSC-Derived Brain Organoids and Neurospheres Show Early Transcriptional Dysregulation of Biological Processes Associated with Brain Development and Metabolism. *Cells* **2024**, *13*, 591. https://doi.org/10.3390/cells13070591

Received: 29 February 2024
Revised: 24 March 2024
Accepted: 26 March 2024
Published: 28 March 2024

1. Introduction

Cockayne syndrome (CS), first described by Edward Alfred Cockayne in 1936 [1], is a rare hereditary autosomal recessive disorder with a prevalence of 2.5 in 1 million births and no apparent overrepresentation in any specific population [2]. The median life expectancy of patients with CS is 12 years, but the time of death spans from neonatal to 55 years [2,3]. As a disease, CS is characterized by severe photosensitivity, failure to thrive, cachectic dwarfism, segmental progeria, vasculopathy, cataracts, dental caries and progressive multisystem degeneration. CS is also known for its various neurological afflictions like intellectual disability, sensorineural hearing loss, progressive microcephaly, cerebellar hypoplasia, dys- and hypomyelination, dystrophic mineralization of neurons and vessels and segmental demyelinating peripheral neuropathy [4,5].

The two main mutated genes in patients with CS are excision repair cross-complementing protein group 6 ERCC6 (Cockayne syndrome B protein, CSB), which two of three patients

exhibit a mutation in, and ERCC8 (Cockayne syndrome A protein, CSA), which comprise the remaining third [4].

The CSB protein is a crucial part of the transcription-coupled nucleotide excision repair mechanism (TC-NER), where it detects the DNA lesion-stalled RNA polymerase II (RNAPII) and initiates the repair process [6]. However, while the dysfunction of repair processes is associated with neurodegenerative diseases [7], loss of this repair mechanism cannot entirely explain the symptoms associated with patients with CS.

Additionally to its function in the TC-NER, CSB has been implicated as enhancing the efficacy of the base excision repair and mitochondrial base excision repair mechanism [8–10], is involved in the repair of double-strand breaks [11,12] and has been implicated in enhancing inter-strand crosslinks repair [13,14]. CSB has also been shown to be involved in transcription regulation. CSB-deficient cells show up to 50% reduced transcription and dysregulation of thousands of genes [15,16].

All these characteristics of CSB have been investigated employing mainly dermal fibroblasts of various patients with CS, Chinese hamster ovary- and mouse model-derived primary cells. Monotypic cell lines are typically well suited for initial gene function analyses and structure–function relationship studies but cannot fully illustrate the impact of a versatile protein such as CSB with multi-system manifestations. In 1997, the first mouse model of CS was described [17], enabling the investigation of primary cells of impacted tissues and whole organisms studies. Since then, mouse models of all CS-associated genes, *CSB*, *CSA*, *XPB*, *XPD* and *XPG*, have been established [18–22]. CS mouse models (except for *XPG*) generally exert a mild CS phenotype with reduced bodyweight, UV-sensitivity, mild neurodegenerative changes and a surprising increase in skin tumorigenesis, a symptom not found in human patients with CS. For the modelling of severe CS, CSA- or CSB-deficient mice can be crossed with mice lacking in other genes of the TC-NER machinery, e.g., *XPA* or *XPC* [19,23].

However, the discrepancy in the function of CS proteins and the need to combine two mutations to replicate specific characteristics emphasize the need for humanized models. The advent of induced pluripotent stem cells (iPSCs) enabled investigators to develop reliable human disease models to study the effects of mutations on human tissues. Several neurodegenerative and mental disorders e.g., Alzheimer, Parkinson's disease, schizophrenia and autism, have been the focal point of stem cell-based neurological research. However, this rare disease has only been subject of a few iPSC-based studies [24–29]. Some of these studies concentrated on CS patient-derived human dermal fibroblasts or SH-SY5Y cells and only incorporated CSB-deficient iPSC lines for singular experiments. Still, these studies have provided great insight into the transcriptional dysregulation in patients with CS. Several important pathways have been identified to be dysregulated in CS patient iPSC-derived neuronal networks e.g., axonogenesis, action potential of neurons, GH/IGF-1 signalling pathway, synaptic transmission, synaptogenesis and density of synapses [27]. In accordance with these enrichment clusters, a reduced synapse density, a reduced spike number and an altered network synchrony have been identified in iPSC-derived neuronal networks [27]. Two studies also identified dysregulation of miRNAs in CSB-deficient iPSCs and iPSC-derived neuronal networks [24,27]. A successful rescue attempt via CRISPR/Cas9 has demonstrated that restoration of one of two mutations in heterozygous mutants is sufficient to restore CSB function in CSB-deficient iPSCs and neural and mesenchymal stem cells [28]. Also, pharmacological intervention in iPSC-derived neurons has shown that TRKB agonists can increase arborization and neurite numbers in CSB-deficient iPSC-derived neurons [26].

All these studies have used iPSCs or iPSC-derived 2D and 2.5D neuronal models. So far, no one has utilised the approach of self-organising organoids, which better recapitulate the cellular heterogeneity, structure and functions of the primary tissues.

In this study, we sought to shed light on common transcriptional dysregulation associated with early cerebral development in patients with CS. However, as CS is a rare disease, obtaining patient material for reprogramming is difficult. We managed to acquire iPSC

lines derived from (i) two individuals with CS and (ii) a healthy control and differentiated them into expandable neural progenitor cells (NPCs) and cerebral organoids (COs). Next, we utilized next-generation sequencing (NGS) to analyse RNA transcription at the NPC stage and after 60 days of CO differentiation. Here, we compared NPCs and COs generated from CS patient-derived iPSCs with each other and an unaffected control. Comparative gene expression analysis revealed the dysregulation of several cellular pathways common between the two individuals. These included enrichment clusters which have been shown to be dysregulated in neurons, such as pathways associated with synaptogenesis, synaptic maintenance, axon guidance and the p53 signalling pathway but also pathways important for brain development and homeostasis, which have not been implicated in CS before. These included, e.g., the VEGFA-VEGFR2 signalling pathway, vesicle-mediated transport, and important metabolic pathways like steroid biosynthesis.

2. Materials and Methods

2.1. iPSC Culture Methods

The iPSC lines derived from patients with CS (CS789 and IUFi001) as well as the control line B4 used in this study have been previously described [30–32].

One clone per iPSC line was used for further investigation. iPSC lines were cultured in mTeSR Plus medium (StemCell Technologies, Vancouver, BC, Canada) supplemented with penicillin/streptomycin (P/S) (Gibco; Thermo Fisher Scientific, Inc., Waltham, MA, USA) on Matrigel-coated six-well plates (Corning, New York, NY, USA). The medium was changed every day, and cells were passaged at 70–80% confluency every 5–7 days using $PBS^{Ca-/Mg-}$ (Life Technologies; Thermo Fisher Scientific, Inc., Waltham, MA, USA) supplemented with 0,5 mM UltraPureTM EDTA (Gibco; Thermo Fisher Scientific, Inc., Waltham, MA, USA).

2.2. Generation of Neurospheres

For the generation of neurospheres, iPSCs were differentiated using a modified version of a protocol previously described in our workgroup [33–36].

Briefly, iPSCs were dissociated using TrypLE Express (Gibco; Thermo Fisher Scientific, Inc., Waltham, MA, USA) and seeded into ultra-low-attachment 96-well plates (NunclonTM SpheraTM, Thermo Fisher Scientific, Inc., Waltham, MA, USA) at 10,000 cells/well with mTeSR medium supplemented with 10 µM Y-27632 (Tocris Bioscience; Biotechne, Minneapolis, MN, USA). Neural induction was commenced at day 2 by replacing the medium with neural induction medium (NIM; 47.5% neurobasal A, 47.5% DMEM/F12, 2% B27 w/o vitamin A, 1% N2 supplement, 1% GlutaMAX, 1% penicillin/streptomycin; all from Gibco) supplemented with 10 µM SB-431542 (Torics Bioscience, Bristol, UK), 5 µM dorsomorphin (Tocris Bioscience) and 10 µM Y-27632. The medium was changed daily, and at day 6, Y-27632 was omitted. At day 8, the spheroids were transferred to poly-ornithine and laminin-coated (both Sigma-Aldrich; Merck KGaA, Darmstadt, Germany) six-well plates containing prewarmed neural differentiation medium (NDM; neurobasal A, 2% B27, 1% N2, 1% GlutaMAX, 1% P/S; all from Gibco) supplemented with 20 ng/mL of EGF and FGF2 (both PeproTech; Thermo Fisher Scientific, Inc., Waltham, MA, USA). The attached spheroids were further cultured in an incubator with 5% CO_2 and 37 °C with daily medium changes. On day 16, the neural rosettes were detached using STEMdiffTM Neural Rosette Selection Reagent (StemCell Technologies, Vancouver, BC, Canada) and transferred to non-adhesive 100 mm dishes containing NIM supplemented with 20 ng/mL FGF2 and EGF. From day 16 onwards, neurospheres were cultured in a shaking incubator (New Brunswick S41i, Eppendorf, Hamburg, Germany) under continuous agitation (60 rpm) with 5% CO_2 at 37 °C with daily medium change.

2.3. Generation of Organoids

For the generation of cerebral organoids, iPSCs were differentiated as described previously in our workgroup [33,35], with minor modifications. In short, iPSCs were

dissociated using TrypLE Express (Gibco; Thermo Fisher Scientific, Inc., Waltham, MA, USA) and seeded into ultra-low-attachment 96-well plates (NunclonTM SpheraTM, Thermo Fisher Scientific, Inc., Waltham, MA, USA) at 10,000 cells/well with mTeSR medium supplemented with 10 µM Y-27632 (Tocris Bioscience; Biotechne, Minneapolis, MN, USA). Neural induction was commenced on day 2 by replacing the medium with neural induction medium (NIM; 47.5% neurobasal A, 47.5% DMEM/F12, 2% B27 w/o vitamin A, 1% N2 supplement, 1% GlutaMAX, 1% penicillin/streptomycin; all from Gibco) supplemented with 10 µM SB-431542 (Tocris Bioscience), 5 µM dorsomorphin (Tocris Bioscience) and 10 µM Y-27632. The medium was changed daily, and on day 6, Y-27632 was omitted. On day 8, the spheroids were transferred to non-adhesive 100 mm dishes containing neural differentiation medium (NDM; neurobasal A, 2% B27, 1% N2, 1% GlutaMAX, 1% P/S, all from Gibco) supplemented with 20 ng/ml of EGF and FGF2 (both PeproTech; Thermo Fisher Scientific, Inc., Waltham, MA, USA). Organoids were further cultured in a shaking incubator (New Brunswick S41i, Eppendorf) under continuous agitation (60 rpm) with 5% CO_2 at 37 °C. The medium was changed daily until day 25. From day 25 to day 40, organoids were cultured in NDM supplemented with 20 ng/mL BDNF and NT-3 (both PeproTech; Thermo Fisher Scientific, Inc., Waltham, MA, USA). The medium was changed every 3 days. From day 40 onwards, the organoids were kept in NDM without further supplements with bi-weekly medium changes.

2.4. Neurosphere/Organoid Sectioning and Immunocytochemistry

Cerebral organoids were fixed in ice-cold 4% paraformaldehyde (PFA) for 1 h at room temperature, washed three times with PBS and dehydrated for 24 h in 30% sucrose/PBS at 4 °C.

Subsequently, the organoids were transferred to cryomolds containing Tissue-Tek OCT Compound 4583 embedding medium (Sakura Finetek, Umkirch, Germany), snap-frozen on liquid nitrogen and stored at −80 °C. The organoids were cut into 10 µm sections using a cryostat (CM1850, Leica, Nussloch, Germany) and captured on Superfrost Plus slides (Thermo Fisher Scientific, Inc., Waltham, MA, USA). For immunocytochemistry, cryosections were permeabilized with 0.5% Triton X-100 in PBS for 10 min and blocked with PBS containing 3% BSA and 0.1% Triton X-100 for 1 h. The samples were then incubated overnight at 4 °C with the following primary antibodies: mouse anti-βIII-tubulin (1:400, Cell Signalling Technologies #4466S, Danvers, MA, USA), rabbit anti-SOX2 (1:400, Cell Signalling Technologies #3579S), guinea pig anti-DCX (1:200, Merck Millipore #AB2253, Darmstadt, Germany), mouse anti-KI67 (1:400, Cell Signalling Technologies #9449S), rabbit anti-cleaved CASP3 (1:400, Cell Signalling Technologies #9664S), rabbit Nestin (1:1000, Merck Sigma-Aldrich #N5413, Darmstadt, Germany), mouse anti-MAP2 (Synaptic Systems, 1:500 #188011, Göttingen, Germany), guinea pig anti-NeuN (1:500, Synaptic Systems #266004), mouse anti-TAU (1:1000, Invitrogen, Thermo Fisher Scientific #MN1000), rabbit anti-S100B (1:100, Abcam #ab52642, Cambridge, UK), goat anti SOX1 (1:200, R&D Systems, Biotechne #AF3369, Minneapolis, MN, USA) and rabbit anti-gH2A.X (1:400, Cell Signalling Technologies #9718S). All antibodies are listed in Supplemental Table S1. The samples were washed three times with room-temperature (RT) PBS. The samples were further incubated with the appropriate secondary antibody conjugated with either Alexa-488, Alexa-555 or Alexa-647 (all 1:500, Invitrogen, Thermo Fisher Scientific) and the nuclear stain Hoechst 33258 (2 ug/mL, Sigma-Aldrich, Merck) for 2 h at RT. The slices were mounted with Fluoromount-G (Southern Biotech, Birmingham, AL, USA) and dried overnight at room temperature. Fluorescent images were obtained using an LSM 700 microscope (Carl Zeiss, Jena, Germany) and processed using ZEN 2012 software (version 1.1.2.0; Carl Zeiss) and ImageJ (FIJI version 2.14.0/1.54f; National Institutes of Health, Bethesda, MD, USA).

2.5. Image Analysis of Neurosphere and Organoid Histological Sections

Fluorescent images were obtained using an LSM 700 microscope (Carl Zeiss, Jena, Germany) and further analysed using ImageJ (FIJI version 2.14.0/1.54f; National Institutes of Health, Bethesda, MD, USA).

To determine the number of Hoechst-, SOX2-, KI67- and gH2A.X-positive cells, 3–4 random sections were chosen per organoid/neurosphere, and the number of positive nuclei was determined by manual counting. For cleaved CASP3, ImageJ was used to determine the integrated density, area and the background fluorescence of 3–4 random sections per organoid/neurosphere. These values were then used to calculate the corrected total cell fluorescence (CTCF).

2.6. Quantitative Reverse Transcription PCR (RT-qPCR)

Total RNA was extracted from iPSCs, 15–20 pooled day 30 neurospheres and 5–7 pooled day 60 organoids using TRIzol (Invitrogen; Thermo Fisher Scientific Inc., Waltham, MA, USA) and Direct-Zol RNA Mini Prep (Zymo Research, Freiburg, Germany). Extractions were performed according to the manufacturer's protocol. Moreover, 500 ng purified RNA was used for cDNA synthesis using a TaqMan reverse transcription reagent (Applied Biosystems; Thermo Fisher Scientific, Inc., Waltham, MA, USA).

The quantification of transcripts was performed by reverse transcription quantitative PCR (RT-qPCR) using the SYBR® Green RT-PCR assay (Applied Biosystems). Amplification, the detection of specific gene products and quantitative analysis were performed using the ViiA7 sequence detection system (Applied Biosystem). The expression levels were normalized relative to the expression of the housekeeping gene RPLP0 and analysed via the $2^{-\Delta\Delta CT}$ method. RT-qPCR data are depicted as mean values. Primers are listed in Supplemental Table S1.

2.7. Next-Generation Sequencing

Moreover, 1 µg RNA of each sample (n = 1 for each condition; 15–20 pooled day 30 neurospheres and 5–7 pooled day 60 organoids) was subjected to bulk next-generation sequencing (NGS) at BGI Genomics (BGI Group, Shenzhen, China). BGI performed the RNA-Seq (transcriptome) library preparation via the stranded mRNA enrichment method. Sequencing was performed on a DNBSeq PE100 platform with 20 M clean reads per sample.

FPKM (fragments per kilobase per million mapped fragments) and count values aligned by the BGI via the HISAT software (HISAT2 version 2.2.1) [37] to the reference genome GCF_000001405.38_GRCh38.p12 were imported into the R/Bioconductor environment [38]. Genes were considered expressed when the counts value was greater than the threshold of t = 5. Venn diagrams were generated based on expressed genes using the R package VennDiagram [39]. Dendrograms and heatmap were generated via the R methods "heatmap.2" and "hclust" from the R package gplots [40] or the R core functionality using Pearson's correlation as a similarity measure. Gene ontologies (GOs) were analysed via the GOstats R package [41]. KEGG pathways [42–45] were downloaded from the KEGG database in July 2020 and tested for the over-representation of genes via the R-built-in hypergeometric test. Dot plots of the most significantly over-represented pathways or GOs were generated via the R package ggplot2 [46]. Differentially expressed genes between two conditions were determined via the R-built-in Fisher's exact test using the criteria $p < 0.05$ and the ratio > 1.5 for upregulation or ratio < 2/3 for downregulation.

A comprehensive functional analysis of the clustered GO biological processes and pathways (KEGG pathways, Reactome gene sets, canonical pathways and CORUM) of gene sets based on a previous Venn analysis was performed using Metascape (http://metascape.org, accessed on 27 July 2022 and 3 March 2023) [47].

To identify the developmental age and enriched brain regions in the neurospheres and organoids, NGS datasets associated with foetal brain regions were downloaded from the Allen Brain Atlas (ABA) (https://www.brainspan.org/, accessed on 19 January 2022) [48]. Genes specific for brain regions were extracted from the ABA expression RPKM (reads

per kilobase per million mapped reads) data by first filtering only genes with a coefficient of variation (cv) greater than the median cv. Thereafter, for each brain region, the genes greater than the threshold t95 at the mean of the 95 quantiles of all samples were extracted. Heatmaps of enrichment in the ABA were made via the R package GSVA [49] (gene set variation analysis) and represent the GSVA enrichment scores of the dedicated brain regions. Brain regions are abbreviated by the following acronyms: occipital neocortex—Ocx, primary motor sensory cortex (samples)—M1C-S1C, amygdaloid complex—AMY, medial ganglionic eminence—MGE, posterior (caudal) superior temporal cortex (area 22c)—STC, upper (rostral) rhombic lip—URL, caudal ganglionic eminence—CGE, dorsal thalamus—DTH, anterior (rostral) cingulate (medial prefrontal) cortex—MFC, dorsolateral prefrontal cortex—DFC, orbital frontal cortex—OFC, lateral ganglionic eminence—LGE, inferolateral temporal cortex (area TEv, area 20)—ITC, hippocampus (hippocampal formation)—HIP, ventrolateral prefrontal cortex—VFC, and parietal neocortex—PCx.

2.8. Western Blotting

To harvest the total protein, 10–15 neurospheres and 4–6 organoids per cell line were rinsed twice with PBS and then lysed in RIPA buffer (Sigma-Aldrich; Merck KGaA, Darmstadt, Germany) supplemented with a protease inhibitor cocktail and phosphatase inhibitor cocktail (Roche, Mannheim, Germany). The protein content of lysates was quantified using the PierceTM Protein Assay Kit (Thermo Fisher Scientific Inc., Waltham, MA, USA). Furthermore, 20 µg of the protein samples were then heat-denatured and subsequently separated on a 4–12% Bis-Tris gel (Invitrogen; Thermo Fisher Scientific). The separated proteins were then transferred to a 0.45 µm nitrocellulose membrane via wet blotting for 3 h at 300 mA. The membranes were blocked in Tris-buffered saline/0.1% Tween-20 containing 5% skim milk and afterwards stained with the following antibodies: rabbit anti-CSB (1:1000, GeneTex Inc. #GTX104589, Irvine, CA, USA), rabbit anti-SQLE (1:1000, Proteintech #12544-1-AP, Rosemont, IL, USA), mouse anti-p53 (1:1000, Merck OP43) and mouse anti-β-actin (1:4000, Cell Signalling Technologies #4967S). All antibodies are listed in Supplemental Table S1. After incubation, the blots were washed three times with Tris-buffered saline/0.1% Tween-20 and subsequently stained with the appropriate secondary antibodies. Following three washing steps with Tris-buffered saline/0.1% Tween-20, the protein bands were visualized with ECL Western blotting detection reagents (Cytiva, Freiburg, Germany) in a UV chamber. The resulting bands were quantified using greyscale analysis with ImageJ (National Institutes of Health, Bethesda, MD, USA).

3. Results

3.1. Both Control and CSB-iPSCs Efficiently Differentiate into Neural Progenitors

For this project, we utilized two previously established iPSC lines generated from a patient with cerebro-oculo-fascio-skeletal syndrome (CS789), a patient with classical CS (IUFi001), as well as the established control line B4. The CS789 line carries a homozygous p.R683X mutation in exon 10 of the ERCC6 gene, leading to a stop codon and a predicted truncated protein. The IUFi001 line carries a compound mutation, p.K377X in exon 5 and p.R857X in exon 15 of the ERCC6 gene (Supplementary Figure S1) [30–32].

To investigate how CS affects early human neurodevelopment, we implemented our published suspension protocols for neurospheres (NS) (Figure 1A) and cerebral organoids (COs) (Figure 2A) [33,35]. The neurospheres were cultured for 30 days.

By day 30 of differentiation, immunocytochemical analysis revealed that control and CS NS were composed mostly of SRY-box transcription factor 2 (SOX2)+, SRY-box transcription factor 1 (SOX1)+ and Nestin+ neural progenitor cells (NPCs) organized in ventricular zone (VZ)-like structures surrounded by pan-neuronal marker tubulin beta 3 class III (TUBB3)+ early-born neurons (Figure 1B).

Cells **2024**, *13*, 591

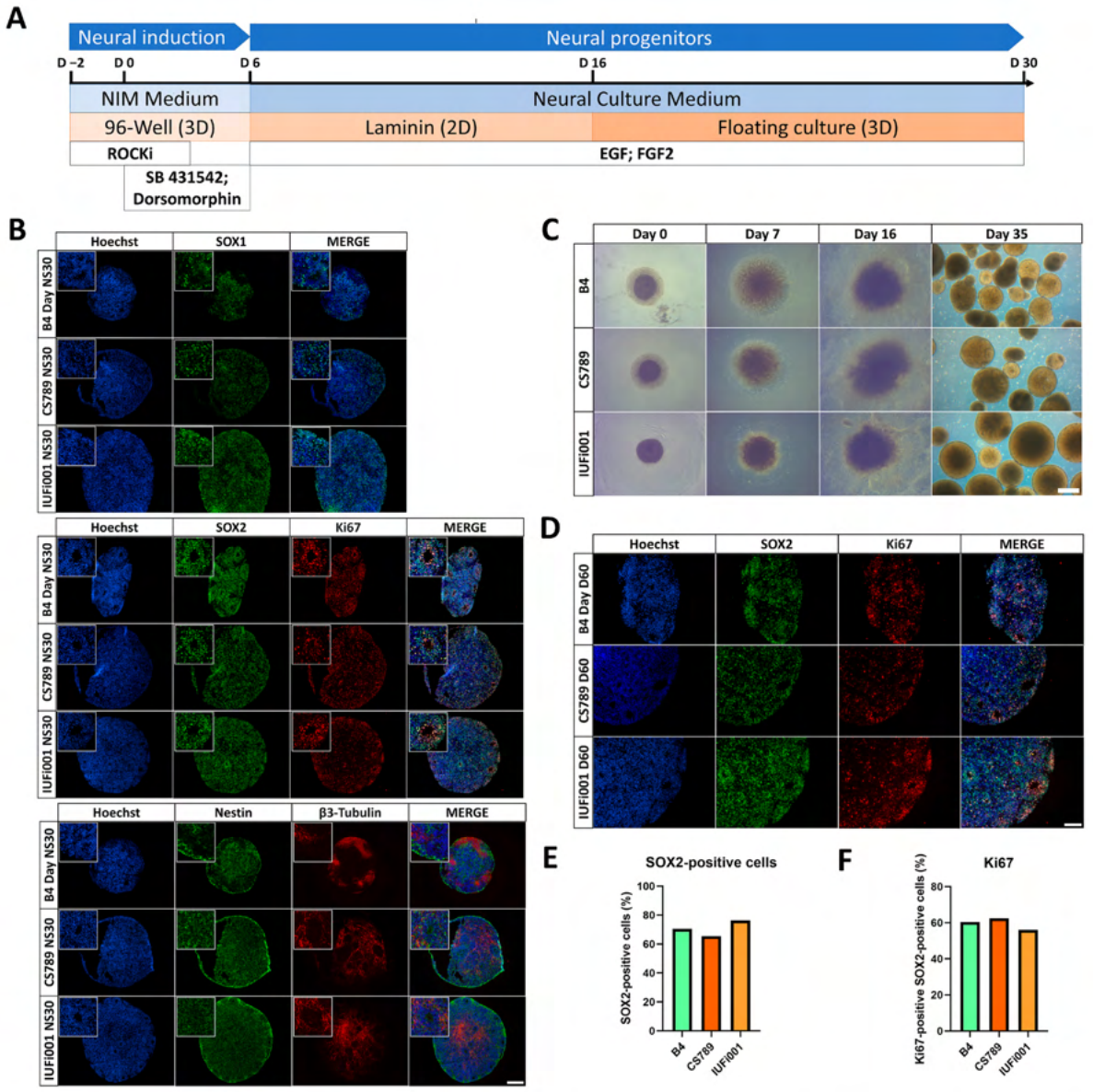

Figure 1. Generation and characterization of CS neurospheres. (**A**) Schematic outline of the protocol to generate iPSC-derived neurospheres. (**B**) Representative immunocytochemistry images of the distribution of cells expressing SOX1, SOX2, Ki67, Nestin and β3-Tubulin. 100× magnification, scale bar 200 µm. (**C**) Representative brightfield images of control and CS neurospheres at day 0, 7, 16 and 35 of differentiation. Scale bar, 200 µm. (**D**) Representative immunocytochemistry images of the distribution of cells expressing SOX2 and Ki67. 200× magnification, scale bar 100 µm. (**E**) Quantification of the SOX2-positive and Hoechst-positive cells in CTRL (B4), CS789 and IUFi001 neurospheres. (**F**) Quantification of the Ki67-positive cells within the SOX2-positive cells in CTRL (B4), CS789 and IUFi001 neurospheres. (**E**,**F**) Approximately ten random fields from three distinct neurospheres were analysed.

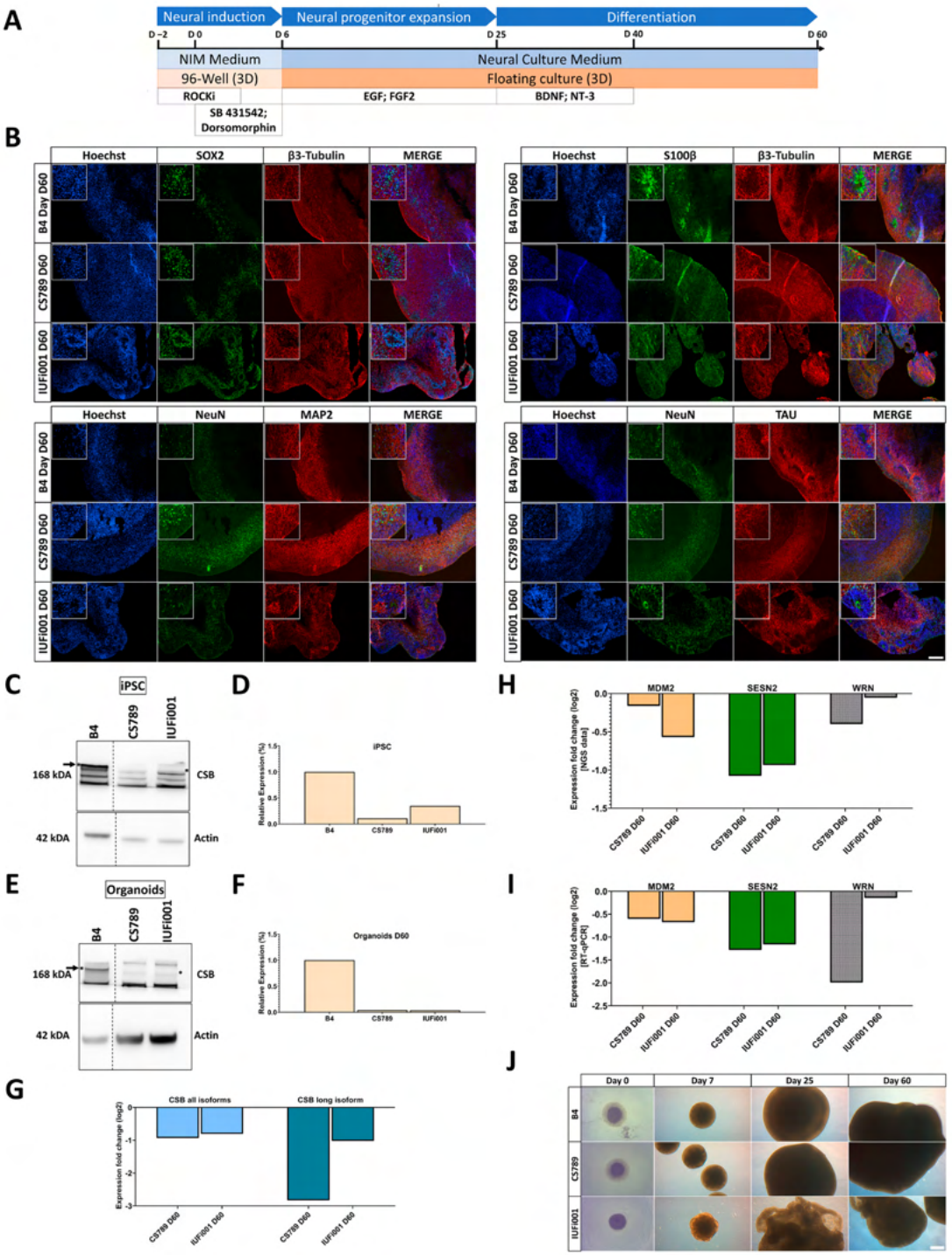

Figure 2. Generation and characterization of CS organoids. (**A**) Schematic outline of the protocol to generate iPSC-derived cerebral organoids. (**B**) Representative immunocytochemistry images of the distribution of cells expressing SOX2, β3-Tubulin, S100, NeuN, MAP2 and TAU. 100× magnification,

scale bar 200 µm. (**C**) Western blot analysis for full-length CSB and beta-actin at the iPSC stage. (**D**) Quantification of CSB Western blot analysis at the iPSC stage in CTRL (B4), CS789 and IUFi001. CSB expression of CS789 and IUFi001 is compared to CSB expression in CTRL (B4) (**E**). Western blot analysis for full-length CSB and beta-actin at day 60 of organoid differentiation. (**F**) Quantification of CSB Western blot analysis at iPSC stage in CTRL (**B**), CS789 and IUFi001. CSB expression of CS789 and IUFi001 is compared to CSB expression in CTRL (B4). (**G**) qRT-PCR analysis of full-length *CSB* mRNA expression and all isoform *CSB* mRNA expression in CS789 and IUFi001 organoids relative to control organoids. (**H**) Relative mRNA expression analysis of DNA damage-related genes *MDM2*, *SESN2* and *WRN* in CS789 and IUFi001 organoids compared to CTRL (B4). (**I**) qRT-PCR analysis of *MDM2*, *SESN2* and *WRN* mRNA expression in CS789 and IUFi001 organoids relative to CTRL (B4). (**J**) Representative brightfield images of control and CS organoids at day 0, 7, 25 and 53 of differentiation. Scale bar 200 µm. (**C**,**E**) Arrows indicate bands of interest. Asterisk (*) indicates height of bands of interest on the right side. Dotted lines indicate excision point of one sample. Full-length blots are presented in Supplementary Figure S3.

During differentiation, all cell lines behaved similarly with regards to attachment, the formation of rosettes and the generation of NS (Figure 1C). The manual assessment of SOX2+ nuclei (Figure 1D,E) and SOX2 and marker of proliferation Ki-67 (Ki-67) double-positive nuclei (Figure 1D,F) did not reveal differences in the number of SOX2+ NPCs and proliferating SOX2+ NPCs between all cell lines.

By comparing the B4, CS789 and IUFi001 NS RNA-Seq datasets with transcriptional datasets from the Allen Brain Atlas, we attempted to determine the developmental age of the NS (Supplementary Figure S2A) as described previously [33,50]. We observed that the transcriptomes of our day 30 NS are equivalent to 8–9 weeks post-conception foetal brains (Supplementary Figure S2B).

These results imply that control and CS patient-derived iPSCs can be efficiently differentiated into NS following our protocol. Patient-derived NS do not seem to exhibit changes in cyto-architecture, cellular makeup or proliferation in comparison to the control.

3.2. Both Control and CSB-iPSCs Efficiently Differentiate into Cerebral Organoids

To elucidate transcriptional regulation at advanced stages of early human neurodevelopment in patients with CS, we also cultured cerebral organoids for 60 days.

By day 60 of differentiation, immunocytochemical staining revealed that both CS and control lines share a common cyto-architecture. The outer layer (~300–500 nm) of these COs is composed of SOX2+ NPCs self-organized into VZ-like structures surrounded by early-born and mature neurons.

The mature neurons are microtubule-associated protein 2 (MAP2)+, microtubule-associated protein tau (TAU)+ and RNA binding fox-1 homolog 3 (NeuN)+ in the COs of all cell lines (Figure 2B). All neurons including the early-born neurons are stained with TUBB3. The staining of S100 calcium-binding protein B (S100B) reveals the presence of radial glial cells and/or early astrocyte progenitors in the COs of all three cell lines.

We performed a Western blot to detect CSB at the iPSC and day 60 CO stage (Figure 2C,E). This revealed markedly reduced levels of CSB in both patient-derived iPSC lines and COs in comparison to the control (Figure 2D,F). The full Western Blot can be found in Supplementary Figure S3. RT-qPCR revealed a ~50% translation reduction of all CSB isoforms in both patient-derived cell lines, a ~90% translation reduction of the full-length isoform in the CS789 line and a ~50% reduction in the IUFi001 line (Figure 2G).

Prior to NGS analysis, we performed RT-qPCR for the genes MDM2 proto-oncogene, E3 ubiquitin protein ligase (*MDM2*), sestrin-2 (*SESN2*) and Werner syndrome RecQ-like helicase (*WRN*), which were expected to be regulated in our patient-derived COs (Figure 2I). The dysregulation was later confirmed by the NGS data (Figure 2H).

Over the course of the CO differentiation, control and CS789 cell lines behaved similarly with respect to growth. The IUFi001 COs flattened and folded early in the differ-

entiation and were broken up into smaller organoids by the shear forces of the spinning incubator (Figure 2J). Still, except for the size, the cyto-architecture of the IUFi001 COs is comparable to the control and CS789 cell line.

By comparing the CO RNA-Seq datasets with datasets from the Allen Brain Atlas, we attempted to determine the developmental age of the COs (Supplementary Figure S2A). We observed that the transcriptomes of the day 60 COs are approximate to 13–21 weeks post-conception foetal brains (Supplementary Figure S2C).

Collectively, these results suggest that control and CS patient-derived iPSCs can efficiently differentiate into COs following our protocol. Patient-derived CS COs do not seem to exhibit major changes in cyto-architecture in comparison to the control and recapitulate aspects of early human neurodevelopment but present an expected dysregulation of damage-related gene expression.

3.3. CSB Neurospheres of Patients with Different Severity Show Distinct but Partially Overlapping Transcriptome Dysregulation

To gain insight into the early neurodevelopmental transcriptional differences between patients with CS and healthy individuals, we performed transcriptome analysis of the day 30 NS via RNA-Seq. Hierarchical clustering (Supplementary Figure S4A) and principal component analysis (Supplementary Figure S4B) of all datasets (iPSCs, neurospheres and organoids of B4, CS789 and IUFi001) revealed correct clustering of the respective timepoints to each other with no outliers.

Next, we compared the transcriptome of CS789 NS to control NS. We found that 641 genes are exclusively expressed in CS789 NS, 635 genes exclusively expressed in control NS and 14,001 genes expressed in both. Of these commonly expressed 14,001 genes, 2302 genes are upregulated and 430 genes downregulated in CS789 NS in comparison to the control (Figure 3A). With these identified differentially expressed genes (DEGs), we performed an enrichment analysis to identify the most dysregulated Kyoto Encyclopaedia of Genes and Genomes (KEGG) pathways in CS789 NS. The three most upregulated KEGG pathways are the following—*protein processing in endoplasmatic reticulum*, *adherens junction* and *Hippo signalling pathway* (Figure 3C). The three most downregulated KEGG pathways are *ribosome*, *oxidative phosphorylation* and *thermogenesis* (Figure 3D).

Subsequently, the transcriptome of the IUFi001 NS was compared to control NS. We identified 720 genes to be exclusively expressed in IUFi001 NS, 746 genes exclusively expressed in control NS and 13,890 genes expressed in both. Of the commonly expressed 13,890 genes, 1540 genes are upregulated and 723 genes downregulated in IUFi001 NS in comparison to the control (Figure 3B). The three most upregulated KEGG pathways in IUFi001 NS are the following—*protein processing in endoplasmatic reticulum*, *steroid biosynthesis* and *carbon metabolism* (Figure 3E). The three most downregulated KEGG pathways are *ribosome*, *oxidative phosphorylation* and *thermogenesis* (Figure 3F). Since we want to identify dysregulation common to all types of CS, we compared the 50 highest up- and downregulated KEGG pathways in both patient-derived NS in comparison to the control. The five most upregulated KEGG pathways common in CS789 and IUFi001 neurospheres are *protein processing in endoplasmatic reticulum*, *adherens junction*, *Hippo signalling pathway*, *RNA transport* and *Wnt signalling pathway* (Figure 3G).

The five most downregulated KEGG pathways common in CS789 and IUFi001 neurospheres are *ribosome*, *oxidative phosphorylation*, *thermogenesis*, *Parkinson's disease* and *Huntington's disease* (Figure 3H). The complete list of pathways common in the 50 most severely dysregulated KEGG pathways can be found in Supplemental Table S2.

These results indicate that while there are ample differences in gene expression between distinct individuals and severity grades of CS, there is also common dysregulation. And, while most symptoms manifest only postnatally in all but the most severe form of CS, this common dysregulation can already be detected in carriers of less severe forms at the NPC stage.

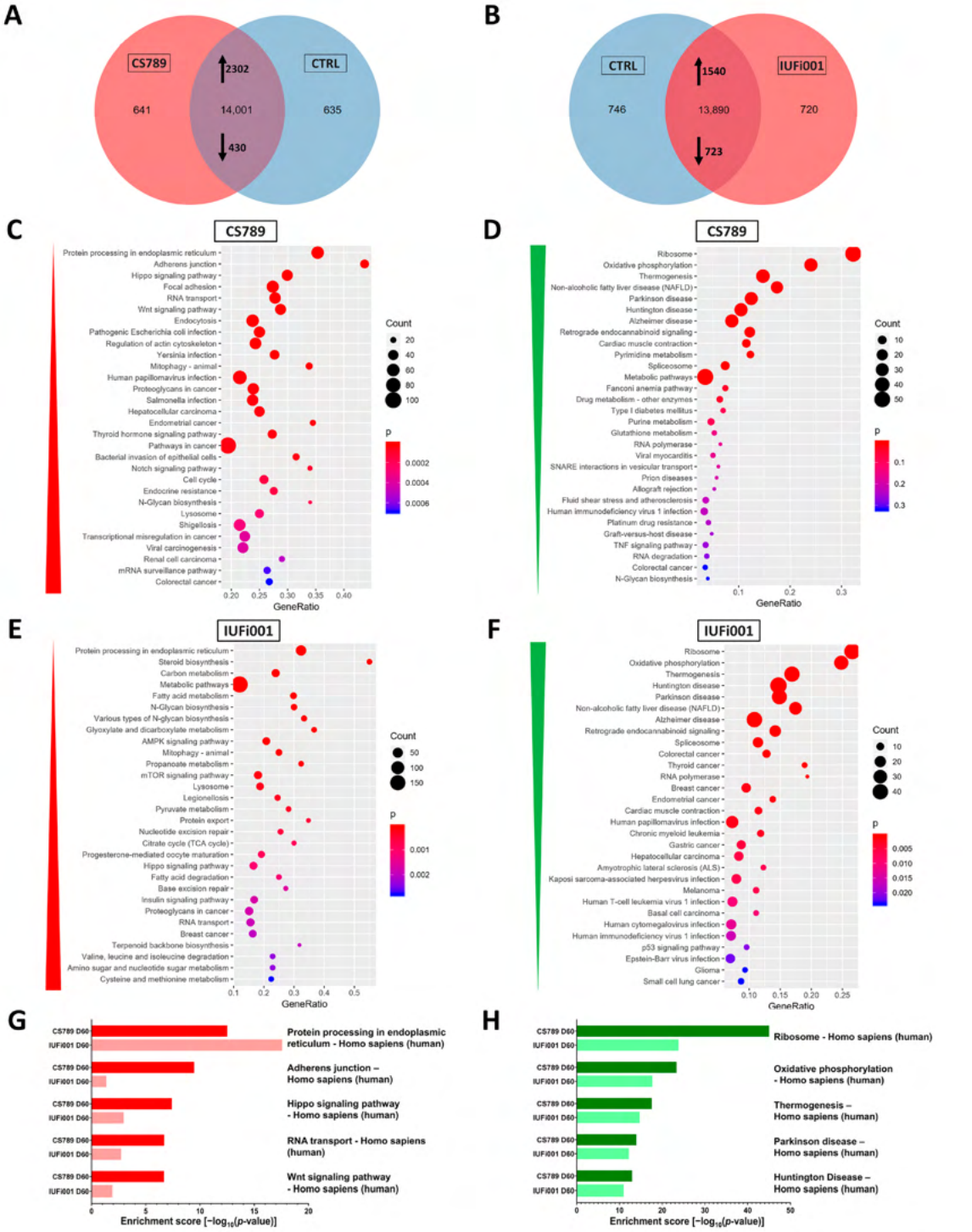

Figure 3. Global transcriptome and associated pathway analysis of control and CS neurospheres at day 30. (**A**) Venn diagram showing genes expressed only in CS789 neurospheres (641), in CTRL (B4)

neurospheres (635) and common to both (14,001) (detection p value < 0.05). (**B**) Venn diagram showing genes expressed only in IUFi001 neurospheres (720), in CTRL (B4) neurospheres (746) and common to both (13,890) (detection p value < 0.05). (**C**,**D**) Dot plots showing the top 30 differentially regulated KEGG pathways (**C**) in the 2302 significantly upregulated DEGs in day 30 CS789 neurospheres in comparison to CTRL (B4) (**D**) and in the 430 significantly downregulated DEGs in day 30 CS789 neurospheres in comparison to CTRL (B4). (**E**,**F**) Dot plots showing the top 30 differentially regulated KEGG pathways (**E**) in the 1540 significantly upregulated DEGs in day 30 IUFi001 neurospheres in comparison to CTRL (B4) (**F**) and in the 723 significantly downregulated DEGs in day 30 IUFi001 neurospheres in comparison to CTRL (B4). (**G**) Bar chart of the differentially upregulated KEGG pathways (top five ranked) common between day 30 CS789 and IUFi001 neurospheres in comparison to CTRL (B4) neurospheres. (**H**) Bar chart of the differentially downregulated KEGG pathways (top five ranked) common between day 30 CS789 and IUFi001 neurospheres in comparison to CTRL (B4) neurospheres.

3.4. CSB Organoids of Patients with Different Severity Show Distinct but Partially Overlapping Transcriptome Dysregulation

To investigate the molecular differences between patients with CS and healthy individuals at a more advanced stage of brain development (BD), we performed transcriptome analysis of the day 60 cerebral organoids.

We first compared the transcriptome of the CS789 COs to control COs. We identified 443 genes as exclusively expressed in CS789 COs, 1006 genes exclusively expressed in control COs and 14,030 genes expressed in both. Of these commonly expressed 14,030 genes, 373 genes are upregulated and 2163 downregulated in CS789 COs in comparison to the control (Figure 4A). We utilized the DEGs to perform an enrichment analysis to identify the most dysregulated KEGG pathways in CS789 COs. The three most upregulated KEGG pathways are *ribosome*, *steroid biosynthesis* and *terpenoid backbone biosynthesis* (Figure 4C). The three most downregulated KEGG pathways are *axon guidance*, the *Wnt signalling pathway* and *synaptic vesicle cycle* (Figure 4D).

Next, the transcriptome of the IUFi001 COs was compared to control COs. We identified 674 genes as exclusively expressed in IUFi001 COs, 610 genes exclusively expressed in control COs and 14,426 genes expressed in both. Of these 14,426 commonly expressed genes, 930 genes are upregulated, and 1687 downregulated in IUFi001 organoids in comparison to the control (Figure 4B). The three most upregulated KEGG pathways are *protein processing in endoplasmatic reticulum*, *metabolic pathways* and *pathways in cancer* (Figure 4E). The three most downregulated KEGG pathways are *axon guidance*, *the synaptic vesicle cycle* and *glutamatergic synapse* (Figure 4F).

We again compared the 50 highest up- and downregulated KEGG pathways in both patient-derived COs in comparison to the control. The five most upregulated KEGG pathways common in CS789 and IUFi001 COs are *steroid biosynthesis*, *p53 signalling pathway*, *breast cancer*, *terpenoid backbone biosynthesis* and *antigen processing and presentation*. (Figure 4G). The five most downregulated KEGG pathways common in CS789 and IUFi001 COs are *axon guidance*, *synaptic vesicle cycle*, *glutamatergic synapse*, *Wnt signalling pathway* and *signalling pathways regulating pluripotency of stem cells* (Figure 4H).

The complete list of pathways common in the 50 most severely dysregulated KEGG pathways can be found in Supplemental Table S2.

These results imply that while there are ample differences in gene expression between distinct individuals and severity grades of CS at the later stages of BD, there is also severe common dysregulation, especially the downregulation of genes important for BD and neuronal function. As with the neurospheres, this common dysregulation can already be detected in carriers of less severe forms of CS in the early stages of BD.

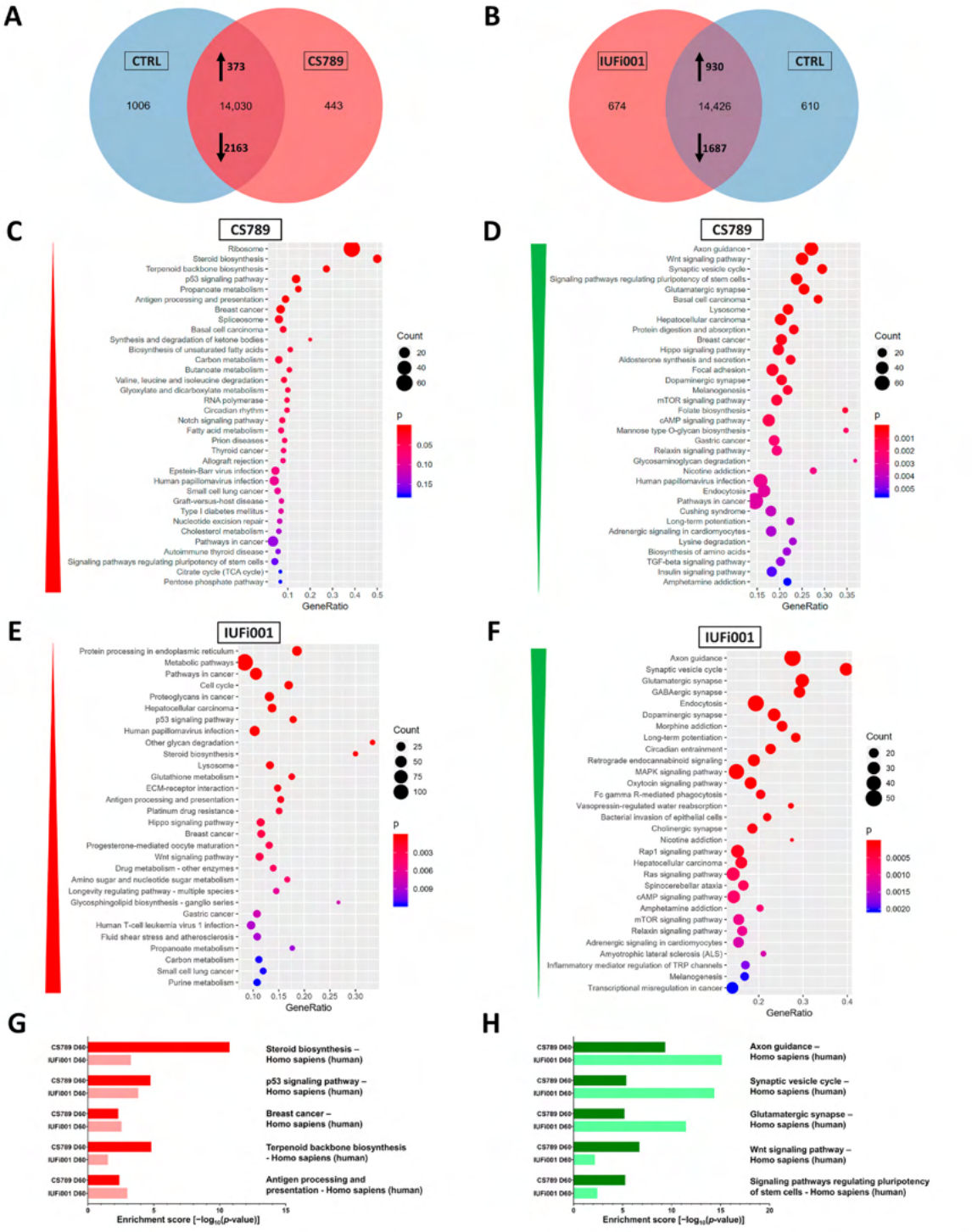

Figure 4. Global transcriptome and associated pathway analysis of control and CS organoids at day 60. (**A**) Venn diagram showing genes expressed only in CS789 organoids (443), in CTRL (B4) organoids (1006)

and common to both (14,030) (detection p value < 0.05). (**B**) Venn diagram showing genes expressed only in IUFi001 organoids (674), in CTRL (B4) organoids (610) and common to both (14,426) (detection p value < 0.05). (**C**,**D**) Dot plots showing the top 30 differentially regulated KEGG pathways (**C**) in the 373 significantly upregulated DEGs in day 60 CS789 organoids in comparison to CTRL (B4) (**D**) and in the 2163 significantly downregulated DEGs in day 60 CS789 organoids in comparison to CTRL (B4). (**E**,**F**) Dot plots showing the top 30 differentially regulated KEGG pathways (**E**) in the 930 significantly upregulated DEGs in day 60 IUFi001 organoids in comparison to CTRL (B4) (**F**) and in the 1687 significantly downregulated DEGs in day 60 IUFi001 organoids in comparison to CTRL (B4). (**G**) Bar chart of the differentially upregulated KEGG pathways (top five ranked) common between day 60 CS789 and IUFi001 organoids in comparison to CTRL (B4) organoids. (**H**) Bar chart of the differentially downregulated KEGG pathways (top five ranked) common between day 60 CS789 and IUFi001 organoids in comparison to CTRL (B4) organoids.

3.5. Non-Redundant Enrichment Analysis Reveals Dysregulation of VEGFA-VEGFR2 Signalling, Brain Development and Intracellular Transport in CSB Neurospheres

We performed an analysis of the dysregulated gene ontologies (GOs) in our CS NS in comparison to the control (Supplementary Figure S5). A variety of often related GOs were unveiled. To generate a clearer picture of the dysregulation in our CS neurospheres, the more extensive, upregulated gene sets (CS789 2302 genes; IUFi001 1540 genes) were subjected to Metascape-based analysis, which resulted in non-redundant enrichment clusters. An analysis of the downregulated gene sets can be found in Supplementary Figure S6.

For the CS789 NS, the three most enriched clusters were the *VEGFA-VEGFR2 signalling pathway*, *cell morphogenesis* and *head development* (Figure 5A). For the IUFi001 NS, the three most enriched clusters were *vesicle-mediated transport*, *intracellular protein transport* and *protein processing in endoplasmatic reticulum* (Figure 5B).

To pinpoint pathways of interest, we compared both gene sets employing Metascape-based analysis. The highest consensus can be observed in *vesicle-mediated transport*, *cell cycle*, the *VEGFA-VEGFR2 signalling pathway*, *intracellular protein transport* and *cellular responses to stress* (Figure 5C). A manual comparison of the singular analyses in Figure 5A,B revealed identical enrichment clusters to the Metascape-based comparison (Figure 5D).

Next, we chose the Reactome set *vesicle-mediated transport* and the GOs *intracellular protein transport* and *head development*, compared the corresponding gene lists of both patient-derived NS and extracted the genes similarly regulated in comparison to the control. This resulted in 165 genes for *intracellular protein transport*, 139 genes for *vesicle-mediated transport* and 82 genes for *head development*. The resulting gene sets were compared utilizing Pearson's heatmap analysis (Supplementary Figure S7). These gene sets were then reduced to the 40 highest dysregulated genes common between both patient-derived NS (Figure 5E–G).

These results imply that at the developmental stage of NPCs, there is severe dysregulation pertaining to distinct intracellular transport mechanisms, the coordination of cell cycles and protein metabolism common between distinct grades of severity in patients with CS.

3.6. Non-Redundant Enrichment Analysis Reveals Dysregulation of Neuron Projection Development, Brain Development and Distinct Synaptic Pathways in CSB Organoids

Furthermore, we performed an analysis of the dysregulated GOs in our CS COs in comparison to the control (Supplementary Figure S8). Again, a variety of often related GOs were unveiled. To produce a clearer picture of the dysregulation, the more extensive, downregulated gene sets (CS789 2163 genes; IUFi001 1687 genes) were subjected to Metascape-based analysis, which results in non-redundant enrichment clusters. An analysis of the upregulated gene sets can be found in Figure S9.

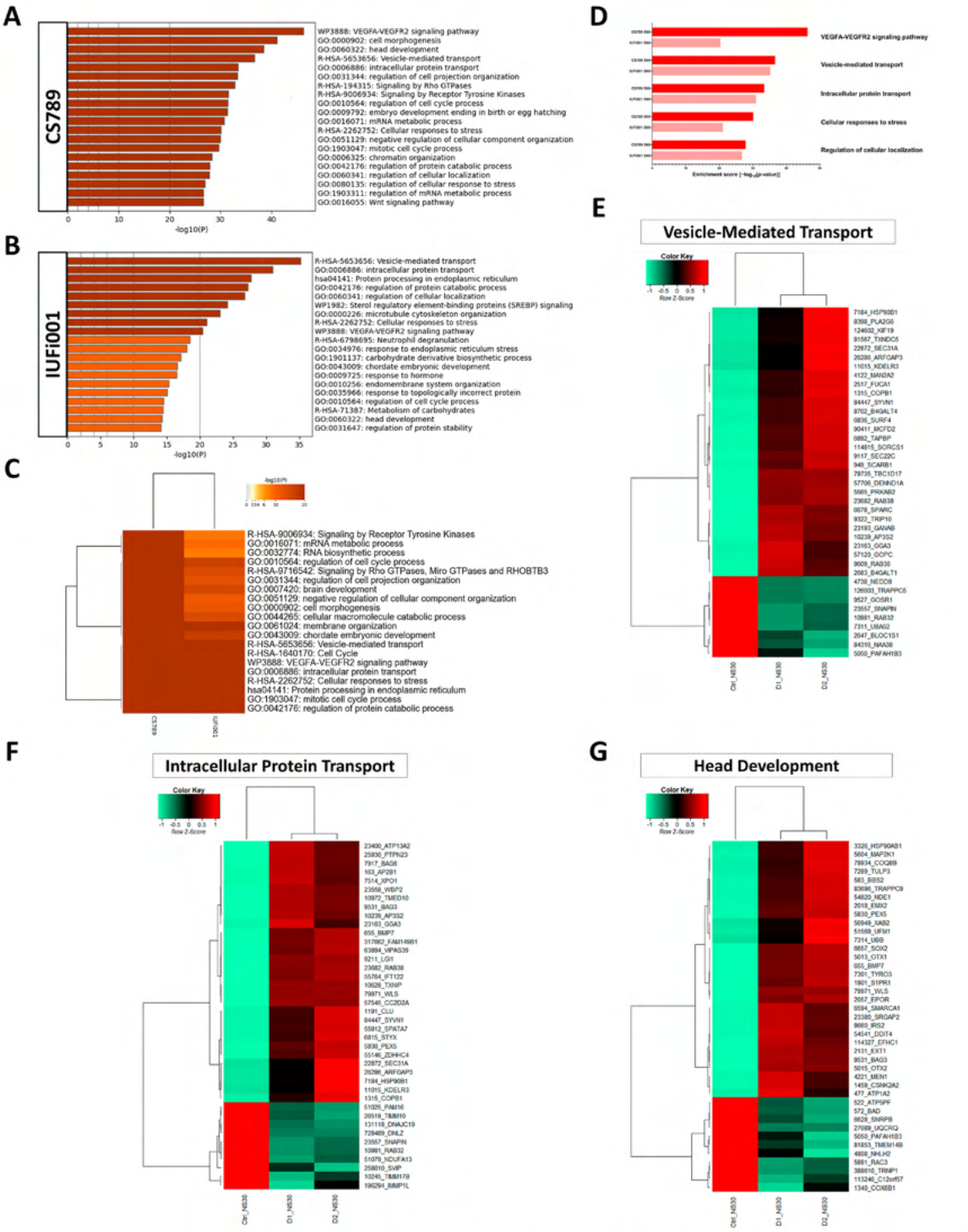

Figure 5. Comparative transcriptome and gene ontology analysis of upregulated DEGs in day 30 neurospheres. (**A**) Bar graph of the top 20 non-redundant enrichment clusters attributable to the

2302 DEGs upregulated in day 30 CS789 neurospheres in comparison to CTRL (B4). (**B**) Bar graph of the top 20 non-redundant enrichment clusters attributable to the 1540 DEGs upregulated in day 30 IUFi001 neurospheres. (**C**) Metascape-generated heatmap comparing upregulated gene sets employed in A and B revealed i.a. GOs involved in brain development, intracellular transport and cell cycle. (**D**) Bar chart of the differentially upregulated enrichment clusters (top five ranked) common between day 30 CS789 and IUFi001 neurospheres in comparison to CTRL (B4) neurospheres. (**E**) Pearson's heatmap depicting the 40 most dysregulated genes involved in vesicle-mediated transport common between day 30 CS789 and IUFi001 neurospheres in comparison to CTRL (B4). (**F**) Pearson's heatmap depicting the 40 most dysregulated genes involved in intracellular protein transport common between day 30 CS789 and IUFi001 neurospheres in comparison to CTRL (B4). (**G**) Pearson's heatmap depicting the 40 most dysregulated genes involved in head development common between day 30 CS789 and IUFi001 neurospheres in comparison to CTRL (B4).

For the CS789 COs, the three highest rated enrichment clusters were *neuron projection development*, *brain development* and *regulation of neuron projection development* (Figure 6A). For the IUFi001 COs, the three highest rated enrichment clusters were neuron *projection development*, *regulation of trans-synaptic signalling* and *brain development* (Figure 6B). To pinpoint pathways of interest, we compared both gene sets employing Metascape-based analysis. The highest consensus can be observed in *brain development*, *neuronal system*, *cell junction organization*, *regulation of trans-synaptic signalling* and *regulation of synapse structure or activity* (Figure 6C). A manual comparison of the singular analyses in Figure 6A,B revealed identical enrichment clusters to the Metascape-based comparison (Figure 6D).

Subsequently, we chose the GOs *neuron projection development*, *synaptic signalling* and *brain development*, compared the corresponding gene sets of both patient-derived COs and extracted the genes dysregulated in both patient-derived cell lines in comparison to the control. This resulted in 165 genes for *neuron projection development*, 131 genes for *synaptic signalling* and 117 genes for *brain development*. The resulting gene sets were compared utilizing Pearson's heatmap analysis (Supplementary Figure S10). These gene sets were then reduced to the 40 highest regulated genes common between both patient-derived COs (Figure 6E–G).

These results indicate that at the developmental stage of early BD, there is severe dysregulation pertaining to neuron projection development, synaptic function and maintenance and even overall BD.

3.7. Non-Redundant Enrichment Analysis of Genes Commonly Regulated at Both Timepoints Reveals Steroid Biosynthesis as Most Severely Affected

We were interested in the genes and associated pathways commonly dysregulated at both developmental timepoints. We pooled the RNA-Seq data of both patient-derived samples at the NS and CO stage and compared them to their respective control via Fisher´s exact test to determine the significantly regulated genes at both timepoints. Next, we compared the resulting gene sets to find genes commonly dysregulated between both timepoints.

The list of commonly dysregulated genes was then subjected to Metascape-based analysis (Figure 7A).

The highest commonly dysregulated enrichment cluster is the KEGG *pathway steroid biosynthesis* and partially overlapping with it, in sixth and eighth place, the Reactome set *activation of gene expression by SREBF (SREBP)* and the GO *fatty acid metabolism*. Other than that, there are three enrichment clusters we examined before, namely, the GOs *synaptic signalling* and *brain development*, as well as the Reactome set *COPII-mediated vesicle transport*.

Next, we investigated which of the commonly dysregulated genes are most severely regulated in both patient-derived lines at both timepoints in comparison to the control. We found that the genes MAGE family member A4 (*MAGEA4*), transmembrane protein 132C (*TMEM132C*), zinc finger protein 558 (*ZNF558*) and tripartite motif containing 4 (*TRIM4*) are the most severely and consistently regulated genes in all patient-derived samples (Supplementary Figure S11A,C,E,G).

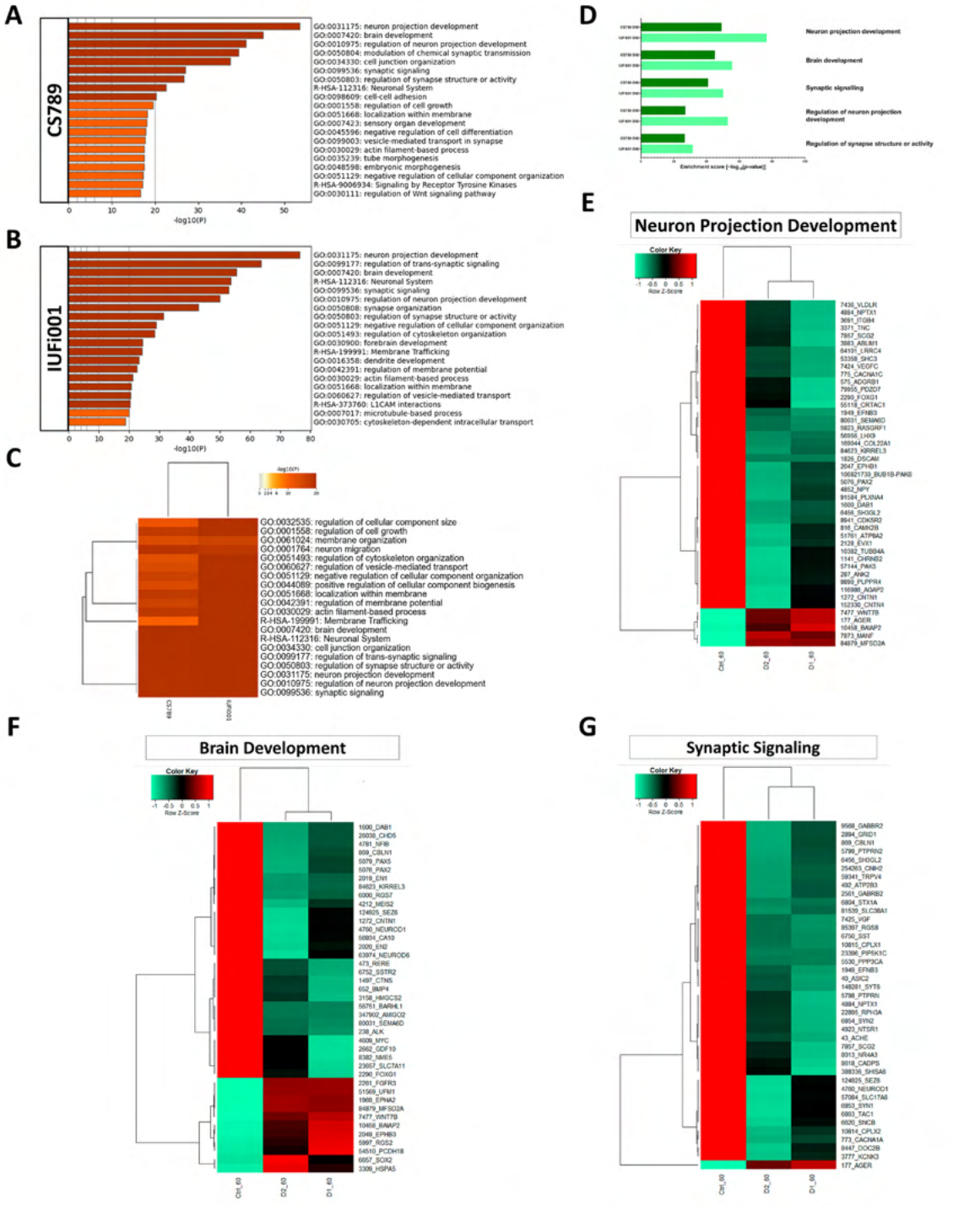

Figure 6. Comparative transcriptome and gene ontology analysis of downregulated DEGs in day 60 organoids. (**A**) Bar graph of the top 20 non-redundant enrichment clusters attributable to the 2163 DEGs downregulated in day 60 CS789 (D1) organoids in comparison to CTRL (B4). (**B**) Bar

graph of the top 20 non-redundant enrichment clusters attributable to the 1687 DEGs downregulated in day 60 IUFi001 organoids. (**C**) Metascape-generated heatmap comparing downregulated gene sets employed in A and B revealed i.a. GOs involved in brain development, cell junction organization, neuron projection development and synaptic signalling. (**D**) Bar chart of the differentially downregulated enrichment clusters (top five ranked) common between day 30 CS789 and IUFi001 neurospheres in comparison to CTRL (B4) neurospheres. (**E**) Pearson's heatmap depicting the 45 most dysregulated genes involved in neuron projection development common between day 60 CS789 and IUFi001 organoids in comparison to CTRL (B4). (**F**) Pearson's heatmap depicting the 40 most dysregulated genes involved in brain development common between day 60 CS789 and IUFi001 organoids in comparison to CTRL (B4). (**G**) Pearson's heatmap depicting the 40 most dysregulated genes involved in synaptic signalling common between day 60 CS789 and IUFi001 organoids in comparison to CTRL (B4).

After identifying these four genes, we ascertained our findings via RT-qPCR (Supplementary Figure S11B,D,F,H). We further investigated these four genes in another sets of day 60 COs, produced employing an altered media composition. In these COs, we detected the regulation *of MAGEA4*, *TMEM132C*, *ZNF558* and *TRIM4* akin to our initial dataset (Supplementary Figure S11I–L). We cultivated a small number of COs from the initial batch investigated in this work until day 120. The RT-qPCR of these samples also revealed the regulation of these four genes (Supplementary Figure S11M–P).

Following up on our initial Metascape-based analysis, we identified regulated genes involved in cholesterol biosynthesis (CB) in the KEGG pathway steroid biosynthesis at both timepoints. As CB requires the metabolite farnesyl pyrophosphate, we simultaneously investigated the mevalonate pathway branch of terpenoid backbone synthesis at both timepoints. While we found no significantly regulated genes in the NS, an analysis of the CO datasets revealed the regulation of hydroxymethylglutaryl-CoA synthase (*HMGCS*), hydroxymethylglutaryl-CoA reductase (*HMGCR*), one of the rate-limiting enzymes of CB, as well as isopentenyl-diphosphate delta-isomerase (*IDI*) and farnesyl diphosphate synthase (*FDPS*) (Supplementary Figure S12). An analysis of the CB branch of the KEGG pathway steroid biosynthesis indicated the second rate-limiting enzyme of CB squalene epoxidase (*SQLE*) and methylsterol mono-oxygenase (*MSMO1*) as regulated in both NS and COs. Furthermore, in the COs, the genes farnesyl-diphosphate farnesyltransferase 1 (*FDFT1*), 7-dehydrocholesterol reductase (*DHCR7*) and 24-dehydrocholesterol reductase (*DHCR24*) were found to be differentially regulated (Figure 7B,C). We validated these findings for the genes *HMGCR*, *SQLE*, *DHCR7* and *MSMO1* via RT-qPCR (Figure 7D–K).

We further analysed whether the regulation of *SQLE* translated to an increase in protein levels via Western blot. We found no difference in the NS but a nearly three-fold increase of SQLE in the COs (Figure 7N–P). The full Western blots can be found in Supplementary Figure S3.

Next, we analysed a pathway known to be dysregulated in CSB-deficient cells, the p53 signalling pathway. In the NS, we found the upregulation of zinc finger protein 385A (*ZNF385A*), P53-induced death domain protein 1 (*PIDD1*), shisa family member 5 (*SHISA5*), cyclin D1 (*CCND1*), sestrin 2 (*SESN2*) and sestrin 3 (*SESN3*), as well as the downregulation of SIVA1 apoptosis-inducing factor (*SIVA1*). In the COs, we found the downregulation of growth arrest and dNA-damage-inducible gamma (*GADD45G*), insulin-like growth factor binding protein 3 (*IGFBP3*), adhesion G protein-coupled receptor B1 (*ADGRB1*), *SESN2* and TSC complex subunit 2 (*TSC2*) as well as the upregulation of CD82 molecule (*CD82*) (Figure 7L,M). We further analysed the quantity of the p53 protein at both timepoints. Contrary to our expectations, we detected a decrease in p53 protein levels at both timepoints (Figure 7Q–S). The full Western Blots can be found in Supplementary Figure S3.

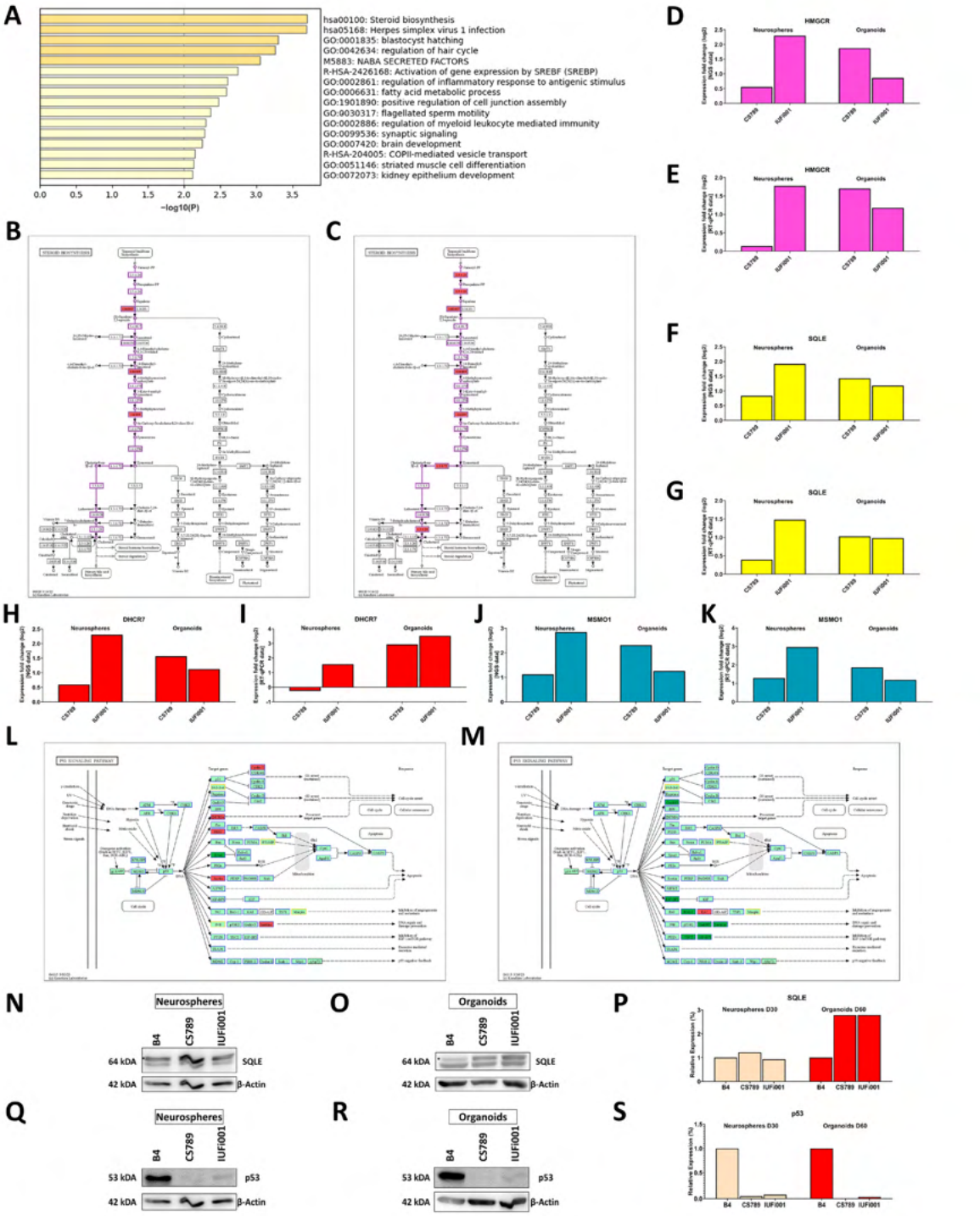

Figure 7. Metascape-based analysis of common genes dysregulated in day 30 CS neurospheres and day CS 60 organoids. (**A**) Bar graph of the 16 enrichment clusters attributable to the 181 DEGs regulated in

both day 30 CS NS and day 60 CS COs in comparison to CTRL (B4). (**B**,**C**) Schematic of the pathway steroid biosynthesis with the genes upregulated in CSB-deficient day 30 NS (**B**) and day 60 COs (**C**) indicated in red. (**D**,**F**,**H**,**J**) Relative mRNA expression analysis of *HMGCR* (**D**), *SQLE* (**F**), *DHCR7* (**H**) and *MSMO1* (**J**) in CS789 and IUFi001 organoids compared to CTRL (B4). (**E**,**G**,**I**,**K**) qRT-PCR analysis of *HMGCR* (**E**), *SQLE* (**G**), *DHCR7* (**I**) and *MSMO1* (**K**) mRNA expression in CS789 and IUFi001 organoids relative to CTRL (B4). (**L**,**M**) Schematic of p53 signalling pathway with genes upregulated in CSB-deficient day 30 NS (**L**) and day 60 COs (**M**) indicated in red and genes downregulated indicated in green. Genes which are not expressed are indicated in yellow. (**N**,**O**) Western blot analysis for SQLE in day 30 NS (**N**) and day 60 COs (**O**). (**P**) Quantification of SQLE Western blot analysis at the day 30 NS and day 60 CO stage in CTRL (B4), CS789 and IUFi001. SQLE expression of CS789 and IUFi001 is compared to SQLE expression in CTRL (B4) of the respective timepoint. (**Q**,**R**) Western blot analysis for p53 in day 30 NS (**Q**) and day 60 COs (**R**). (**S**) Quantification of p53 Western blot analysis at the day 30 NS and day 60 CO stage in CTRL (B4), CS789 and IUFi001. SQLE expression of CS789 and IUFi001 is compared to p53 expression in CTRL (B4) of the respective timepoint. (**N**,**O**) Asterisks (*) indicate bands of interest.

These results indicate the upregulation of CB during the early cerebral development of patients with CS. While we could identify the transcriptional upregulation of genes involved in CB in both day 30 NS and day 60 COs, this upregulation could only be confirmed on the translational level in the COs. Our results also confirm the dysregulation of the p53 signalling pathway in iPSC-derived NPCs and neurons during early human BD in patients with CS. Interestingly, this disruption of the p53 signalling pathway manifests in the altered expression of different genes between day 30 NS and day 60 COs. Unexpectedly, we detected a decrease in p53 protein levels at both timepoints.

4. Discussion

The major diagnostic criteria of CS are mostly symptoms of the central nervous system, e.g., progressive microcephaly, neurologic dysfunction and cerebellar atrophy. However, the mechanisms underlying these manifestations are still largely unknown due to the versatility of the causative protein and limitations of the available experimental models. To overcome this deficiency, we produced the first successful differentiation of CSB-deficient iPSC lines into cerebral organoids (COs). These COs enable us to model early developmental dysregulation in patients with CS and the effect of CSB deficiency on neural progenitor cells and neurons. The established model, however, does not include vascular cells or oligodendrocytes and is thus unable to reproduce neurological manifestations like hypomyelination and the dystrophic mineralization of vessels found in the central nervous system of patients with CS.

We employed two distinct, patient-derived, CSB-deficient iPSC lines, one generated from a donor with the most severe form of CS, cerebro-oculo-fascio-skeletal syndrome (COFS), and one generated from a donor with classical CS type I and differentiated them into neural progenitor cells (NPCs), in the form of neurospheres (NS) and COs. To elucidate the common dysregulation underlying aberrations in brain development (BD) found in different types of CS, we then subjected the mRNA of both developmental timepoints, day 30 NS and day 60 COs, to NGS and the resulting datasets to extensive bioinformatic analysis. The transcriptome of day 30 NS is estimated to correspond to 8–9 week post-conception foetal brains and the transcriptome of day 60 COs to 13–21 week post-conception foetal brains [33,50]. COs produced with this protocol have been shown to consist mostly of cells with forebrain identity. However, sub-populations of cells with midbrain and hindbrain identity are to be expected [33,51].

Transcriptome-based analysis of the differentially regulated KEGG pathways in the NS revealed several common pathways. The upregulated pathway *protein processing in endoplasmatic reticulum* and the downregulated pathway *ribosome* could indicate changes in the translational priming of NPCs. Ribosome biogenesis has been shown to be impaired in CSA- and CSB-deficient cells before due to a disturbance of RNA polymerase I tran-

scription and the processing of pre-rRNA [52,53]. A decrease in ribosome-related genes would be expected to result in a decrease in protein processing. This might indicate a compensatory mechanism to increase global protein production. However, it could also indicate the dysregulation of global protein synthesis, which has been implicated in the disease progression of schizophrenia patients [54].

Furthermore, our analysis indicated the *VEGFA-VEGFR2 signalling pathway* as modulated in our patient-derived cell lines. While known for its function in angiogenesis, VEGFA also has a direct impact on NPCs and neurons. VEGFA has been shown to increase the proliferation of primary embryonic cortical NPCs [55,56]. VEGFA has also been shown to decrease apoptosis in adult NPCs and to promote neuronal survival [57–61]. Additionally, VEGFA is surmised to be involved in dendrite outgrowth and axon guidance, two processes we found regulated in day 60 COs [56,58]. Overall, this increase in VEGFA-VEGFR2 signalling might present a compensatory mechanism to increase proliferation, which has been shown to be reduced in CSB-deficient NPCs [62] or a protective response to increased ambient stress, which can be observed in the form of *cellular responses to stress*.

We also provide an in-depth analysis of several regulated enrichment clusters in our patient-derived NS via heatmap analysis, namely, *vesicle-mediated transport*, *intracellular protein transport* and *head development*. Vesicular transport is an essential process by which membrane-bound vesicles are released from a donor compartment and transported to a specific cellular location. Disturbances of vesicle-mediated transport cause a multitude of disorders, several of which share symptoms with CS [63]. The following genes identified as regulated in our dataset have been associated with diseases caused by alterations in vesicle-mediated transport: LMAN1, SEC23A, SEC23B, SEC24B, SEC31A, GAK, VPS35L, DNM2, SBF1, BLOC1S1, COG1, COG4, SCYL1, MTM1, AP1S2, DENND5A and TRAPPC9 [64]. The dysregulation of a subpathway, namely COPII-mediated vesicle transport, is also observable between both investigated timepoints.

We were further interested in the GO *head development*. The observed upregulation of BD it encompasses could indicate a premature entry of NPCs into neurogenesis, a hallmark of microcephaly. One reason for this premature shift could be the increase in ambient cell stress observed in our analysis as DNA damage can promote accelerated neurogenesis [33,65–67]. Interestingly, patients with CS, except for patients with COFS, do not present microcephaly in prenatal development. Still, both of our patient-derived cell lines display similar regulation of BD at the NPC stage, indicating potential issues with developmental timing.

The highest upregulated KEGG pathway in day 60 COs, *steroid biosynthesis*, shows common dysregulation over both timepoints. *Steroid biosynthesis*, as well as the commonly dysregulated Reactome set *activation of gene expression by SREBF (SREBP)*, both encompass cholesterol biosynthesis (CB). Cholesterol is produced by neurons at early stages of BD. Cholesterol is necessary for the control of membrane fluidity and lipid raft structure and influences, e.g., neuronal receptor activity [68–70]. Correctly orchestrated CB is essential for BD and directly influences pathways dysregulated in our CSB-deficient lines as cholesterol is involved in synaptogenesis, stability and recycling of synaptic neurotransmitters and neurite outgrowth [69,71–74]. Cholesterol depletion, as well as accumulation, can lead to neuronal dysfunction and ultimately to neurodegeneration [73,75]. In a mouse model with a conditional knock-out of CB in radial glia cells, the affected pups exhibited a progressive loss of cortical neurons, as well as postnatal proliferation and migration deficits of cerebellar granule precursors [76]. Overall, diseases of cholesterol metabolism have a high overlap of symptoms with CS, with many manifesting with i.a. neurological symptoms like psychomotor impairment developmental delay and microcephaly [77].

We verified this upregulation of CB in the COs via RT-qPCR of the two rate-limiting enzymes *HMGCR* and *SQLE*, as well as *DHCR7* and *MSMO1*. On the protein level, we could detect a nearly 3-fold increase in the SQLE protein, reinforcing the hypothesis that CB is increased in CSB-deficient young neurons. Interestingly, while we could also detect an increase in *SQLE* transcription in our NS, this did not translate into an increase in the

SQLE protein. However, NPCs react differently to cholesterol depletion than neurons. In a mouse model with a conditional FDFT1 knock-out in VZ-NPCs, VEGF expression via a hypoxia-inducible factor-1 independent pathway was strongly upregulated. This increased angiogenesis and thus the influx of external cholesterol to the NPCs [78]. Fittingly, we also identified the upregulation of the VEGFA-VEGFR2 signalling pathway in our NS.

The p53 signalling pathway, reputed in its role as a tumour suppressor and its function in DNA damage response, cell cycle arrest, senescence and apoptosis, is also involved in BD. The deletion, mutation and inhibition of p53 can lead to female-biased neural tube defects [79]. However, deletions of effectors of p53 can lead to various brain malformations [80]. Due to the variety of potential outcomes, it is surmised that p53 stabilization has a controlled, dose- and time-dependent effect on distinct cell types during development [79]. In the context of CS, CSA and CSB have been shown to interact with p53 and regulate its degradation. Both proteins form a complex with p53 and MDM2, which facilitates ubiquitination and the subsequent degradation of p53 in an MDM2-dependent manner [81]. Due to decreased degradation, CSA- and CSB-deficient cells show elevated levels of p53 [82]. CSB also interacts directly with p53, competing with the essential factor E1A binding protein p300 (EP300) for its binding site. As CSB has a higher affinity for p53, this negatively modulates the function of p53 [83–85]. In summary, the regulation of the p53 signalling pathway was expected, due to a decrease in the degradation of p53 and absence of a negative regulator of p53 activity. This might have implications for BD as p53 is involved in the proliferation and differentiation of NPCs [86], and a controlled dose- and time-dependent stabilization of p53 is necessary for correct development.

Surprisingly, instead of the expected increase, we detected a decrease in the p53 protein levels at both timepoints. p53 protein levels have been revealed to be high during early embryogenesis and to decrease over the course of development until it plateaus at a low level in terminally differentiated cells [87–89]. This decrease in p53 protein levels we identified might be another manifestation of the dysregulation of BD we revealed in this work, further uncoupling the development of our CS-deficient cells from normal cerebral development. Another possibility would be the increased modification of p53, depleting the pool of unmodified p53 we examined, which would also directly impact BD.

The most significantly downregulated KEGG pathway in both patient-derived COs, *axon guidance*, has been shown to be dysregulated in human neuronal networks, as well as *axonogenesis*, which shows, in our analysis, as subpathway of *neuron projection development* [27]. In human neural cell lines, the ablation of CSB expression affected neuronal differentiation capabilities. The suppression of CSB led to a decrease in MAP2 expression, accompanied by reduced cell polarization. Together, this led to a decrease in neuritogenesis [16,90]. Alterations of neuritogenesis and axonal pathfinding may lead to pathological changes in neural circuitry.

The downregulated KEGG pathway *synaptic vesicle cycle* has been demonstrated to be dysregulated, as well as other pathways involved in synapse formation, activity and maintenance, whose dysregulation we could observe with the regulated *GOs regulation of trans-synaptic signalling*, *regulation of synapse structure* and *synaptic signalling* [27]. The correct function of synapse pathways are necessary for neuronal function and signal transmission, which both have been shown to be altered in CSB-deficient neural networks [27]. In CS patient cerebella, the downregulation of genes involved in synaptic exocytosis has been identified, which we also identified in our COs [16]. Our data also indicate the downregulation of synaptic endocytosis in our patient-derived COs. This alteration of synapse formation, activity and maintenance and the resulting changes likely contribute to the neurodevelopmental defects in patients with CS.

We further provide an analysis of several regulated enrichment clusters in our patient-derived COs via heatmap analysis, namely, the GOs *neuron projection development*, *synaptic signalling* and *brain development*.

Brain development, which was upregulated in NS, was found to be downregulated in day 60 COs. This was expected as CSB-deficient cells have been shown to exhibit the down-

regulation of thousands of genes, including brain-related genes, due to dysregulation of RNA polymerase II activity [15,16]. We found the brain development-related genes EPHA7, EPHB3, AFF2, NPY, WNT7B, TSPAN2, SRGAP2, UFM1, FUT10, POTEE, TRH and TPGS1 to be mostly upregulated in NS and downregulated in COs at both investigated timepoints.

However, the most significantly dysregulated genes are not associated with brain development. We found the genes *MAGEA4*, *TMEM132C*, *ZNF558* and *TRIM4* to be most severely regulated in all patient-derived samples. Other members of the MAGE-A family have been shown to potentially be involved in early BD [91]. *TMEM132C* has been revealed to be expressed in early NPCs and the developing cochlea and is differentially regulated in the dorsal forebrain and midbrain during murine development [92]. *TMEM132C* has also been shown to be differentially regulated in the NPCs of another disease with congenital cataracts and intellectual disability, Lowe syndrome [93]. Krüppel-associated box (KRAB) zinc finger protein *ZNF558*, has a role in mitochondrial maintenance and is thought to influence timing during early human BD [94]. *TRIM4* is a gene mainly known for its role in the ubiquitination of a variety of targets [95–97]. A genome-wide DNA methylation study found that the upregulation of *TRIM4* might be associated with neural tube defects [98].

So, while these four genes are not yet conclusively linked to BD, one can assume they might be associated. Interestingly, this dysregulation of all four genes seems to be traceable to later timepoints, indicating their involvement not only in early but at least also in mid-gestational BD.

To further decipher CS and find target genes utilizable in all forms of CS, a comparison between CSA- and CSB-deficient cerebral organoids is crucial. A comparison between CSA- and CSB-depleted SH-SY5Y cells showed significant overlap between the transcriptional dysregulation of both proteins but also regulation distinct to both. On the transcriptional and functional level, Wu et al. found CSB deficiency to inhibit neuritogenesis, while CSA deficiency even slightly increased the differentiation of the SH-SY5Y cells. This is a striking finding as patients with mutations in both genes show neurological symptoms and neurodegeneration [99]. As the symptoms of mutations in both proteins are largely convergent, but not identical, it would be interesting to identify the convergent and divergent mechanisms resulting in the subtle differences between both patient cohorts.

Due to the involvement of CSA and CSB in TC-NER, there has been an ongoing debate whether CS is a neurodegenerative or neurodevelopmental disorder. This work only concentrates on the neurodevelopmental effects of CS as we did not challenge the TC-NER via UV radiation or pharmacological intervention. We therefore expect the endogenous lesions warranting TC-NER to be menial. Nonetheless, the differences at steady-state are already sizeable, with the dysregulation of ribosome-related pathways in NPCs and the disruption of several pathways crucial for neuronal function and survival on the transcriptional level. Our findings are in line with a proposed hypothesis characterizing CS as a transcription syndrome, with many of the especially neurological symptoms being caused mainly by the dysregulation of RNAPI and RNAPII transcription rather than the inactivation of TC-NER [100].

5. Conclusions

In conclusion, this study is the first to produce CSB-deficient patient-derived 3D organoids. Our data provide new insights into the transcriptional dysregulation associated with brain development in patients with CS. We confirm the known dysregulation of neuron projection- and synapse-related pathways and expand this set with the dysregulation of the metabolic pathway steroid biosynthesis, as well as the dysregulation of lipid metabolism in NPCs and neurons in a 3D environment. Our data further provide substantiation to the theory that CS is not only a neurodegenerative but also a neurodevelopmental disorder, with a characteristic dysregulation of brain development at distinct stages. We also identified highly differentially regulated genes not previously highlighted in CSB-deficient neuronal cultures. These genes seem to be dysregulated at several stages of brain development, indicating them as potential target candidates for intervention.

Sadly, due to the rarity of CS and experimental limitations, only a small cohort was investigated. This increases the chance of a false-positive identification of differences. To mitigate this issue, future investigations should include more CS and control individuals, as well as optimally a CRISPR/Cas-mediated rescue of at least one CS cell line. Still, this work strengthens already established theories about the aetiology of CS and might provide leads for further research. As a future prospect, a deeper understanding of the underlying developmental dysregulation in the most devastating symptoms of CS can hopefully spur the development of therapeutic strategies.

Supplementary Materials: The following supporting information can be downloaded at: https://www.mdpi.com/article/10.3390/cells13070591/s1, Figure S1: Used cell lines and clinical information about Cockayne syndrome; Figure S2: Determination of developmental age of day 30 neurospheres and day 60 cortical organoids; Figure S3: Full Western blot for CSB, SQLE, p53 and beta-actin protein in Day 0 iPSCs, Day 30 NS and Day 60 COs; Figure S4: Quality control of next-generation sequencing data; Figure S5: Global transcriptome and associated gene ontology analysis of control and CS neurospheres on day 30; Figure S6: Comparative transcriptome and gene ontology analysis of downregulated DEGs in day 30 neurospheres; Figure S7: Analysis of select gene ontologies differentially regulated in day 30 neurospheres; Figure S8: Global transcriptome and associated gene ontology analysis of control and CS organoids on day 60; Figure S9: Comparative transcriptome and gene ontology analysis of upregulated DEGs in day 60 organoids; Figure S10: Analysis of select gene ontologies differentially regulated in day 60 organoids; Figure S11: RT-qPCR for MAGEA4, TMEM132C, ZNF558 and TRIM4 in Day 30 neurospheres, two sets of day 60 organoids and day 120 organoids; Figure S12: Analysis of the mevalonate pathway of the terpenoid backbone biosynthesis pathway in day 30 NS and day 60 COs; Supplementary Table S1: Primers and antibodies; Supplementary Table S2: Top 50 KEGG lists.

Author Contributions: Conceptualisation, J.A., J.K. (Jean Krutmann), E.F. and L.-P.S.; formal analysis, L.-P.S. and W.W.; investigation, L.-P.S., W.W., A.R. and J.K. (Julia Kapr); resources, J.A., J.K. (Jean Krutmann), E.F., A.R. and J.K. (Julia Kapr); data curation, L.-P.S. and W.W.; writing—original draft preparation, L.-P.S.; writing—review and editing, J.A. and W.W.; visualization, L.-P.S. and W.W.; supervision, J.A.; project administration, J.A., J.K. (Jean Krutmann) and E.F.; funding acquisition, J.A., J.K. (Jean Krutmann) and E.F. All authors have read and agreed to the published version of the manuscript.

Funding: This work was funded by the medical faculty of Heinrich Heine University Düsseldorf, the Leibniz Association (project-number K246/2019) and the German Research Foundation (project-number 417677437/GRK2578 "Impact of genotoxins on the differentiation efficacy of murine and human stem and progenitor cells and functional competence of thereof derived differentiated progeny"; Sub-project: 1a.)

Institutional Review Board Statement: The study was conducted in accordance with the Declaration of Helsinki, and approval for the use of iPSC lines was granted by the ethics committee of the medical faculty of Heinrich Heine University Duesseldorf (study number 5013, approved 9 June 2015).

Informed Consent Statement: Not applicable.

Data Availability Statement: The RNA-Seq datasets generated and analysed during the current study will be made available on NCBI GEO after the manuscript is accepted in a journal.

Acknowledgments: The authors are grateful to Kanehisa Laboratories for the permission to use their figures for terpenoid backbone biosynthesis, steroid biosynthesis and p53 signalling pathways for our figures. The figures were taken from https://www.genome.jp/kegg/ (accessed on 16 June 2023).

Conflicts of Interest: The authors declare no conflicts of interest. The funders had no role in the design of the study; in the collection, analyses or interpretation of data; in the writing of the manuscript; or in the decision to publish the results.

References

1. Cockayne, E.A. Dwarfism with retinal atrophy and deafness. *Arch. Dis. Child.* **1936**, *11*, 1. [CrossRef] [PubMed]
2. Licht, C.L.; Stevnsner, T.; Bohr, V.A. Cockayne syndrome group B cellular and biochemical functions. *Am. J. Hum. Genet.* **2003**, *73*, 1217–1239. [CrossRef]

3. Nance, M.A.; Berry, S.A. Cockayne syndrome: Review of 140 cases. *Am. J. Med. Genet.* **1992**, *42*, 68–84. [CrossRef] [PubMed]
4. Laugel, V. Cockayne syndrome: The expanding clinical and mutational spectrum. *Mech. Ageing Dev.* **2013**, *134*, 161–170. [CrossRef] [PubMed]
5. Weidenheim, K.M.; Dickson, D.W.; Rapin, I. Neuropathology of Cockayne syndrome: Evidence for impaired development, premature aging, and neurodegeneration. *Mech. Ageing Dev.* **2009**, *130*, 619–636. [CrossRef] [PubMed]
6. Marteijn, J.A.; Lans, H.; Vermeulen, W.; Hoeijmakers, J.H. Understanding nucleotide excision repair and its roles in cancer and ageing. *Nat. Rev. Mol. Cell Biol.* **2014**, *15*, 465–481. [CrossRef] [PubMed]
7. Gupta, S.; You, P.; SenGupta, T.; Nilsen, H.; Sharma, K. Crosstalk between different DNA repair pathways contributes to neurodegenerative diseases. *Biology* **2021**, *10*, 163. [CrossRef] [PubMed]
8. Muftuoglu, M.; de Souza-Pinto, N.C.; Dogan, A.; Aamann, M.; Stevnsner, T.; Rybanska, I.; Kirkali, G.; Dizdaroglu, M.; Bohr, V.A. Cockayne syndrome group B protein stimulates repair of formamidopyrimidines by NEIL1 DNA glycosylase. *J. Biol. Chem.* **2009**, *284*, 9270–9279. [CrossRef]
9. Thorslund, T.; von Kobbe, C.; Harrigan, J.A.; Indig, F.E.; Christiansen, M.; Stevnsner, T.; Bohr, V.A. Cooperation of the Cockayne syndrome group B protein and poly (ADP-ribose) polymerase 1 in the response to oxidative stress. *Mol. Cell. Biol.* **2005**, *25*, 7625–7636. [CrossRef]
10. Wong, H.-K.; Muftuoglu, M.; Beck, G.; Imam, S.Z.; Bohr, V.A.; Wilson, D.M., III. Cockayne syndrome B protein stimulates apurinic endonuclease 1 activity and protects against agents that introduce base excision repair intermediates. *Nucleic Acids Res.* **2007**, *35*, 4103–4113. [CrossRef]
11. Tiwari, V.; Baptiste, B.A.; Okur, M.N.; Bohr, V.A. Current and emerging roles of Cockayne syndrome group B (CSB) protein. *Nucleic Acids Res.* **2021**, *49*, 2418–2434. [CrossRef] [PubMed]
12. Batenburg, N.L.; Thompson, E.L.; Hendrickson, E.A.; Zhu, X.D. Cockayne syndrome group B protein regulates DNA double-strand break repair and checkpoint activation. *EMBO J.* **2015**, *34*, 1399–1416. [CrossRef] [PubMed]
13. Iyama, T.; Lee, S.Y.; Berquist, B.R.; Gileadi, O.; Bohr, V.A.; Seidman, M.M.; McHugh, P.J.; Wilson, D.M., 3rd. CSB interacts with SNM1A and promotes DNA interstrand crosslink processing. *Nucleic Acids Res.* **2015**, *43*, 247–258. [CrossRef] [PubMed]
14. Iyama, T.; Wilson, D.M., 3rd. Elements That Regulate the DNA Damage Response of Proteins Defective in Cockayne Syndrome. *J. Mol. Biol.* **2016**, *428*, 62–78. [CrossRef] [PubMed]
15. Balajee, A.S.; May, A.; Dianov, G.L.; Friedberg, E.C.; Bohr, V.A. Reduced RNA polymerase II transcription in intact and permeabilized Cockayne syndrome group B cells. *Proc. Natl. Acad. Sci. USA* **1997**, *94*, 4306–4311. [CrossRef]
16. Wang, Y.; Chakravarty, P.; Ranes, M.; Kelly, G.; Brooks, P.J.; Neilan, E.; Stewart, A.; Schiavo, G.; Svejstrup, J.Q. Dysregulation of gene expression as a cause of Cockayne syndrome neurological disease. *Proc. Natl. Acad. Sci. USA* **2014**, *111*, 14454–14459. [CrossRef] [PubMed]
17. van der Horst, G.T.; van Steeg, H.; Berg, R.J.; van Gool, A.J.; de Wit, J.; Weeda, G.; Morreau, H.; Beems, R.B.; van Kreijl, C.F.; de Gruijl, F.R. Defective transcription-coupled repair in Cockayne syndrome B mice is associated with skin cancer predisposition. *Cell* **1997**, *89*, 425–435. [CrossRef]
18. Van Der Horst, G.T.; Meira, L.; Gorgels, T.G.; De Wit, J.; Velasco-Miguel, S.; Richardson, J.A.; Kamp, Y.; Vreeswijk, M.P.; Smit, B.; Bootsma, D. UVB radiation-induced cancer predisposition in Cockayne syndrome group A (Csa) mutant mice. *DNA Repair* **2002**, *1*, 143–157. [CrossRef] [PubMed]
19. Jaarsma, D.; van der Pluijm, I.; van der Horst, G.T.; Hoeijmakers, J.H. Cockayne syndrome pathogenesis: Lessons from mouse models. *Mech. Ageing Dev.* **2013**, *134*, 180–195. [CrossRef]
20. Andressoo, J.-O.; Weeda, G.; de Wit, J.; Mitchell, J.R.; Beems, R.B.; van Steeg, H.; van der Horst, G.T.; Hoeijmakers, J.H. An Xpb mouse model for combined xeroderma pigmentosum and cockayne syndrome reveals progeroid features upon further attenuation of DNA repair. *Mol. Cell. Biol.* **2009**, *29*, 1276–1290. [CrossRef]
21. Andressoo, J.-O.; Mitchell, J.R.; de Wit, J.; Hoogstraten, D.; Volker, M.; Toussaint, W.; Speksnijder, E.; Beems, R.B.; van Steeg, H.; Jans, J. An Xpd mouse model for the combined xeroderma pigmentosum/Cockayne syndrome exhibiting both cancer predisposition and segmental progeria. *Cancer Cell* **2006**, *10*, 121–132. [CrossRef]
22. Harada, Y.-N.; Shiomi, N.; Koike, M.; Ikawa, M.; Okabe, M.; Hirota, S.; Kitamura, Y.; Kitagawa, M.; Matsunaga, T.; Nikaido, O. Postnatal growth failure, short life span, and early onset of cellular senescence and subsequent immortalization in mice lacking the xeroderma pigmentosum group G gene. *Mol. Cell. Biol.* **1999**, *19*, 2366–2372. [CrossRef] [PubMed]
23. Karikkineth, A.C.; Scheibye-Knudsen, M.; Fivenson, E.; Croteau, D.L.; Bohr, V.A. Cockayne syndrome: Clinical features, model systems and pathways. *Ageing Res. Rev.* **2017**, *33*, 3–17. [CrossRef]
24. Andrade, L.N.d.S.; Nathanson, J.L.; Yeo, G.W.; Menck, C.F.M.; Muotri, A.R. Evidence for premature aging due to oxidative stress in iPSCs from Cockayne syndrome. *Hum. Mol. Genet.* **2012**, *21*, 3825–3834. [CrossRef] [PubMed]
25. Kristensen, U.; Epanchintsev, A.; Rauschendorf, M.-A.; Laugel, V.; Stevnsner, T.; Bohr, V.A.; Coin, F.; Egly, J.-M. Regulatory interplay of Cockayne syndrome B ATPase and stress-response gene ATF3 following genotoxic stress. *Proc. Natl. Acad. Sci. USA* **2013**, *110*, E2261–E2270. [CrossRef] [PubMed]
26. Wang, Y.; Jones-Tabah, J.; Chakravarty, P.; Stewart, A.; Muotri, A.; Laposa, R.R.; Svejstrup, J.Q. Pharmacological bypass of Cockayne syndrome B function in neuronal differentiation. *Cell Rep.* **2016**, *14*, 2554–2561. [CrossRef] [PubMed]

27. Vessoni, A.T.; Herai, R.H.; Karpiak, J.V.; Leal, A.M.; Trujillo, C.A.; Quinet, A.; Agnez Lima, L.F.; Menck, C.F.; Muotri, A.R. Cockayne syndrome-derived neurons display reduced synapse density and altered neural network synchrony. *Hum. Mol. Genet.* **2016**, *25*, 1271–1280. [CrossRef] [PubMed]
28. Wang, S.; Min, Z.; Ji, Q.; Geng, L.; Su, Y.; Liu, Z.; Hu, H.; Wang, L.; Zhang, W.; Suzuiki, K. Rescue of premature aging defects in Cockayne syndrome stem cells by CRISPR/Cas9-mediated gene correction. *Protein Cell* **2020**, *11*, 1–22. [CrossRef]
29. Kapr, J.; Petersilie, L.; Distler, T.; Lauria, I.; Bendt, F.; Sauter, C.M.; Boccaccini, A.R.; Rose, C.R.; Fritsche, E. Human Induced Pluripotent Stem Cell-Derived Neural Progenitor Cells Produce Distinct Neural 3D In Vitro Models Depending on Alginate/Gellan Gum/Laminin Hydrogel Blend Properties. *Adv. Healthc. Mater.* **2021**, *10*, 2100131. [CrossRef]
30. Martins, S.; Hacheney, I.; Teichweyde, N.; Hildebrandt, B.; Krutmann, J.; Rossi, A. Generation of an induced pluripotent stem cell line (IUFi001) from a Cockayne syndrome patient carrying a mutation in the ERCC6 gene. *Stem Cell Res.* **2021**, *55*, 102456. [CrossRef]
31. Hofrichter, M. Establishment of a hiPSC-Based In Vitro Model to Study Environmental and Genetic Disturbances of Neurodevelopmental Processes. Inaugural-Dissertation, Heinrich-Heine-Universität Düsseldorf, Düsseldorf, Germany, 2016.
32. Wang, Y.; Adjaye, J. A cyclic AMP analog, 8-Br-cAMP, enhances the induction of pluripotency in human fibroblast cells. *Stem Cell Rev. Rep.* **2011**, *7*, 331–341. [CrossRef] [PubMed]
33. Martins, S.; Erichsen, L.; Datsi, A.; Wruck, W.; Goering, W.; Chatzantonaki, E.; de Amorim, V.C.M.; Rossi, A.; Chrzanowska, K.H.; Adjaye, J. Impaired p53-mediated DNA damage response contributes to microcephaly in Nijmegen Breakage Syndrome patient-derived cerebral organoids. *Cells* **2022**, *11*, 802. [CrossRef] [PubMed]
34. Martins, S.; Müller-Schiffmann, A.; Erichsen, L.; Bohndorf, M.; Wruck, W.; Sleegers, K.; Van Broeckhoven, C.; Korth, C.; Adjaye, J. IPSC-derived neuronal cultures carrying the Alzheimer's disease associated TREM2 R47H variant enables the construction of an Aβ-induced gene regulatory network. *Int. J. Mol. Sci.* **2020**, *21*, 4516. [CrossRef] [PubMed]
35. Sloan, S.A.; Andersen, J.; Pasca, A.M.; Birey, F.; Pasca, S.P. Generation and assembly of human brain region-specific three-dimensional cultures. *Nat. Protoc.* **2018**, *13*, 2062–2085. [CrossRef] [PubMed]
36. Liu, Y.; Liu, H.; Sauvey, C.; Yao, L.; Zarnowska, E.D.; Zhang, S.-C. Directed differentiation of forebrain GABA interneurons from human pluripotent stem cells. *Nat. Protoc.* **2013**, *8*, 1670–1679. [CrossRef]
37. Kim, D.; Langmead, B.; Salzberg, S.L. HISAT: A fast spliced aligner with low memory requirements. *Nat. Methods* **2015**, *12*, 357–360. [CrossRef]
38. Gentleman, R.C.; Carey, V.J.; Bates, D.M.; Bolstad, B.; Dettling, M.; Dudoit, S.; Ellis, B.; Gautier, L.; Ge, Y.; Gentry, J. Bioconductor: Open software development for computational biology and bioinformatics. *Genome Biol.* **2004**, *5*, R80. [CrossRef]
39. Chen, H.; Boutros, P.C. VennDiagram: A package for the generation of highly-customizable Venn and Euler diagrams in R. *BMC Bioinform.* **2011**, *12*, 35. [CrossRef]
40. Warnes, M.G.R.; Bolker, B.; Bonebakker, L.; Gentleman, R.; Huber, W.; Liaw, A. Package 'gplots'. In *Various R Programming Tools for Plotting Data*; R Foundation for Statistical Computing: Vienna, Austria, 2016.
41. Falcon, S.; Gentleman, R. Using GOstats to test gene lists for GO term association. *Bioinformatics* **2007**, *23*, 257–258. [CrossRef]
42. Kanehisa, M.; Furumichi, M.; Tanabe, M.; Sato, Y.; Morishima, K. KEGG: New perspectives on genomes, pathways, diseases and drugs. *Nucleic Acids Res.* **2017**, *45*, D353–D361. [CrossRef]
43. Kanehisa, M.; Goto, S. KEGG: Kyoto encyclopedia of genes and genomes. *Nucleic Acids Res.* **2000**, *28*, 27–30. [CrossRef] [PubMed]
44. Kanehisa, M. Toward understanding the origin and evolution of cellular organisms. *Protein Sci.* **2019**, *28*, 1947–1951. [CrossRef] [PubMed]
45. Kanehisa, M.; Furumichi, M.; Sato, Y.; Kawashima, M.; Ishiguro-Watanabe, M. KEGG for taxonomy-based analysis of pathways and genomes. *Nucleic Acids Res.* **2023**, *51*, D587–D592. [CrossRef] [PubMed]
46. Wickham, H. *ggplot2: Elegant Grophics for Data Analysis*; Springer: New York, NY, USA, 2009.
47. Zhou, Y.; Zhou, B.; Pache, L.; Chang, M.; Khodabakhshi, A.H.; Tanaseichuk, O.; Benner, C.; Chanda, S.K. Metascape provides a biologist-oriented resource for the analysis of systems-level datasets. *Nat. Commun.* **2019**, *10*, 1523. [CrossRef]
48. Jones, A.R.; Overly, C.C.; Sunkin, S.M. The Allen brain atlas: 5 years and beyond. *Nat. Rev. Neurosci.* **2009**, *10*, 821–828. [CrossRef] [PubMed]
49. Hänzelmann, S.; Castelo, R.; Guinney, J. GSVA: Gene set variation analysis for microarray and RNA-seq data. *BMC Bioinform.* **2013**, *14*, 7. [CrossRef] [PubMed]
50. Miller, J.A.; Ding, S.-L.; Sunkin, S.M.; Smith, K.A.; Ng, L.; Szafer, A.; Ebbert, A.; Riley, Z.L.; Royall, J.J.; Aiona, K. Transcriptional landscape of the prenatal human brain. *Nature* **2014**, *508*, 199–206. [CrossRef]
51. Lancaster, M.A.; Renner, M.; Martin, C.-A.; Wenzel, D.; Bicknell, L.S.; Hurles, M.E.; Homfray, T.; Penninger, J.M.; Jackson, A.P.; Knoblich, J.A. Cerebral organoids model human brain development and microcephaly. *Nature* **2013**, *501*, 373–379. [CrossRef] [PubMed]
52. Qiang, M.; Khalid, F.; Phan, T.; Ludwig, C.; Scharffetter-Kochanek, K.; Iben, S. Cockayne syndrome-associated CSA and CSB mutations impair ribosome biogenesis, ribosomal protein stability, and global protein folding. *Cells* **2021**, *10*, 1616. [CrossRef]
53. Alupei, M.C.; Maity, P.; Esser, P.R.; Krikki, I.; Tuorto, F.; Parlato, R.; Penzo, M.; Schelling, A.; Laugel, V.; Montanaro, L. Loss of proteostasis is a pathomechanism in Cockayne syndrome. *Cell Rep.* **2018**, *23*, 1612–1619. [CrossRef]

54. Topol, A.; English, J.; Flaherty, E.; Rajarajan, P.; Hartley, B.; Gupta, S.; Desland, F.; Zhu, S.; Goff, T.; Friedman, L. Increased abundance of translation machinery in stem cell–derived neural progenitor cells from four schizophrenia patients. *Transl. Psychiatry* **2015**, *5*, e662. [CrossRef]
55. Jin, K.; Zhu, Y.; Sun, Y.; Mao, X.O.; Xie, L.; Greenberg, D.A. Vascular endothelial growth factor (VEGF) stimulates neurogenesis in vitro and in vivo. *Proc. Natl. Acad. Sci. USA* **2002**, *99*, 11946–11950. [CrossRef]
56. Mackenzie, F.; Ruhrberg, C. Diverse roles for VEGF-A in the nervous system. *Development* **2012**, *139*, 1371–1380. [CrossRef] [PubMed]
57. Schänzer, A.; Wachs, F.P.; Wilhelm, D.; Acker, T.; Cooper-Kuhn, C.; Beck, H.; Winkler, J.; Aigner, L.; Plate, K.H.; Kuhn, H.G. Direct stimulation of adult neural stem cells in vitro and neurogenesis in vivo by vascular endothelial growth factor. *Brain Pathol.* **2004**, *14*, 237–248. [CrossRef] [PubMed]
58. Rosenstein, J.M.; Mani, N.; Khaibullina, A.; Krum, J.M. Neurotrophic effects of vascular endothelial growth factor on organotypic cortical explants and primary cortical neurons. *J. Neurosci.* **2003**, *23*, 11036–11044. [CrossRef] [PubMed]
59. Jin, K.L.; Mao, X.O.; Greenberg, D.A. Vascular endothelial growth factor: Direct neuroprotective effect in in vitro ischemia. *Proc. Natl. Acad. Sci. USA* **2000**, *97*, 10242–10247. [CrossRef] [PubMed]
60. Cui, W.; Li, W.; Han, R.; Mak, S.; Zhang, H.; Hu, S.; Rong, J.; Han, Y. PI3-K/Akt and ERK pathways activated by VEGF play opposite roles in MPP+-induced neuronal apoptosis. *Neurochem. Int.* **2011**, *59*, 945–953. [CrossRef] [PubMed]
61. Matsuzaki, H.; Tamatani, M.; Yamaguchi, A.; Namikawa, K.; Kiyama, H.; Vitek, M.P.; Mitsuda, N.; Tohyama, M. Vascular endothelial growth factor rescues hippocampal neurons from glutamate-induced toxicity: Signal transduction cascades. *FASEB J.* **2001**, *15*, 1218–1220. [CrossRef]
62. Sacco, R.; Tamblyn, L.; Rajakulendran, N.; Bralha, F.N.; Tropepe, V.; Laposa, R.R. Cockayne syndrome b maintains neural precursor function. *DNA Repair* **2013**, *12*, 110–120. [CrossRef]
63. Gissen, P.; Maher, E.R. Cargos and genes: Insights into vesicular transport from inherited human disease. *J. Med. Genet.* **2007**, *44*, 545–555. [CrossRef]
64. Yarwood, R.; Hellicar, J.; Woodman, P.G.; Lowe, M. Membrane trafficking in health and disease. *Dis. Models Mech.* **2020**, *13*, dmm043448. [CrossRef] [PubMed]
65. Li, R.; Sun, L.; Fang, A.; Li, P.; Wu, Q.; Wang, X. Recapitulating cortical development with organoid culture in vitro and modeling abnormal spindle-like (ASPM related primary) microcephaly disease. *Protein Cell* **2017**, *8*, 823–833. [CrossRef] [PubMed]
66. Gabriel, E.; Wason, A.; Ramani, A.; Gooi, L.M.; Keller, P.; Pozniakovsky, A.; Poser, I.; Noack, F.; Telugu, N.S.; Calegari, F. CPAP promotes timely cilium disassembly to maintain neural progenitor pool. *EMBO J.* **2016**, *35*, 803–819. [CrossRef] [PubMed]
67. Su, Y.; Ming, G.-l.; Song, H. DNA damage and repair regulate neuronal gene expression. *Cell Res.* **2015**, *25*, 993–994. [CrossRef] [PubMed]
68. Segatto, M.; Di Giovanni, A.; Marino, M.; Pallottini, V. Analysis of the protein network of cholesterol homeostasis in different brain regions: An age and sex dependent perspective. *J. Cell. Physiol.* **2013**, *228*, 1561–1567. [CrossRef] [PubMed]
69. Hussain, G.; Wang, J.; Rasul, A.; Anwar, H.; Imran, A.; Qasim, M.; Zafar, S.; Kamran, S.K.S.; Razzaq, A.; Aziz, N. Role of cholesterol and sphingolipids in brain development and neurological diseases. *Lipids Health Dis.* **2019**, *18*, 26. [CrossRef]
70. Zuo, H.; Wang, R.; Jiang, D.; Fang, D. Determining the composition of active Cholesterol in the plasma membrane of single cells by using Electrochemiluminescence. *ChemElectroChem* **2017**, *4*, 1677–1680. [CrossRef]
71. Goritz, C.; Mauch, D.H.; Pfrieger, F.W. Multiple mechanisms mediate cholesterol-induced synaptogenesis in a CNS neuron. *Mol. Cell. Neurosci.* **2005**, *29*, 190–201. [CrossRef]
72. Adibhatla, R.M.; Hatcher, J. Altered lipid metabolism in brain injury and disorders. In *Lipids in Health and Disease*; Springer: Dordrecht, The Netherland, 2008; pp. 241–268.
73. Martín, M.G.; Pfrieger, F.; Dotti, C.G. Cholesterol in brain disease: Sometimes determinant and frequently implicated. *EMBO Rep.* **2014**, *15*, 1036–1052. [CrossRef]
74. Mauch, D.H.; Nagler, K.; Schumacher, S.; Goritz, C.; Muller, E.-C.; Otto, A.; Pfrieger, F.W. CNS synaptogenesis promoted by glia-derived cholesterol. *Science* **2001**, *294*, 1354–1357. [CrossRef]
75. Djelti, F.; Braudeau, J.; Hudry, E.; Dhenain, M.; Varin, J.; Bieche, I.; Marquer, C.; Chali, F.; Ayciriex, S.; Auzeil, N. CYP46A1 inhibition, brain cholesterol accumulation and neurodegeneration pave the way for Alzheimer's disease. *Brain* **2015**, *138*, 2383–2398. [CrossRef] [PubMed]
76. Cunningham, D.; DeBarber, A.E.; Bir, N.; Binkley, L.; Merkens, L.S.; Steiner, R.D.; Herman, G.E. Analysis of hedgehog signaling in cerebellar granule cell precursors in a conditional Nsdhl allele demonstrates an essential role for cholesterol in postnatal CNS development. *Hum. Mol. Genet.* **2015**, *24*, 2808–2825. [CrossRef] [PubMed]
77. Jira, P. Cholesterol metabolism deficiency. In *Handbook of Clinical Neurology*; Elsevier: Amsterdam, The Netherlands, 2013; Volume 113, pp. 1845–1850.
78. Saito, K.; Dubreuil, V.; Arai, Y.; Wilsch-Bräuninger, M.; Schwudke, D.; Saher, G.; Miyata, T.; Breier, G.; Thiele, C.; Shevchenko, A. Ablation of cholesterol biosynthesis in neural stem cells increases their VEGF expression and angiogenesis but causes neuron apoptosis. *Proc. Natl. Acad. Sci. USA* **2009**, *106*, 8350–8355. [CrossRef]
79. Xiong, Y.; Zhang, Y.; Xiong, S.; Williams-Villalobo, A.E. A glance of p53 functions in brain development, neural stem cells, and brain cancer. *Biology* **2020**, *9*, 285. [CrossRef] [PubMed]

80. Xiong, S.; Van Pelt, C.S.; Elizondo-Fraire, A.C.; Liu, G.; Lozano, G. Synergistic roles of Mdm2 and Mdm4 for p53 inhibition in central nervous system development. *Proc. Natl. Acad. Sci. USA* **2006**, *103*, 3226–3231. [CrossRef] [PubMed]
81. Latini, P.; Frontini, M.; Caputo, M.; Gregan, J.; Cipak, L.; Filippi, S.; Kumar, V.; Vélez-Cruz, R.; Stefanini, M.; Proietti-De-Santis, L. CSA and CSB proteins interact with p53 and regulate its Mdm2-dependent ubiquitination. *Cell Cycle* **2011**, *10*, 3719–3730. [CrossRef] [PubMed]
82. Jaarsma, D.; van der Pluijm, I.; de Waard, M.C.; Haasdijk, E.D.; Brandt, R.; Vermeij, M.; Rijksen, Y.; Maas, A.; van Steeg, H.; Hoeijmakers, J.H. Age-related neuronal degeneration: Complementary roles of nucleotide excision repair and transcription-coupled repair in preventing neuropathology. *PLoS Genet.* **2011**, *7*, e1002405. [CrossRef] [PubMed]
83. Filippi, S.; Latini, P.; Frontini, M.; Palitti, F.; Egly, J.M.; Proietti-De-Santis, L. CSB protein is (a direct target of HIF-1 and) a critical mediator of the hypoxic response. *EMBO J.* **2008**, *27*, 2545–2556. [CrossRef] [PubMed]
84. Proietti-De-Santis, L.; Laugel, V.; Prantera, G. Cockayne syndrome. In *Chromatin Signaling and Neurological Disorders*; Elsevier: Amsterdam, The Netherlands, 2019; pp. 135–152.
85. Frontini, M.; Proietti-De-Santis, L. Cockayne syndrome B protein (CSB): Linking p53, HIF-1 and p300 to robustness, lifespan, cancer and cell fate decisions. *Cell Cycle* **2009**, *8*, 693–696. [CrossRef]
86. Armesilla-Díaz, A.; Bragado, P.; Del Valle, I.; Cuevas, E.; Lázaro, I.; Martin, C.; Cigudosa, J.; Silva, A. p53 regulates the self-renewal and differentiation of neural precursors. *Neuroscience* **2009**, *158*, 1378–1389. [CrossRef]
87. Molchadsky, A.; Rivlin, N.; Brosh, R.; Rotter, V.; Sarig, R. p53 is balancing development, differentiation and de-differentiation to assure cancer prevention. *Carcinogenesis* **2010**, *31*, 1501–1508. [CrossRef] [PubMed]
88. Louis, J.M.; McFarland, V.W.; May, P.; Mora, P.T. The phosphoprotein p53 is down-regulated post-transcriptionally during embryogenesis in vertebrates. *Biochim. Biophys. Acta (BBA)-Gene Struct. Expr.* **1988**, *950*, 395–402. [CrossRef]
89. Schmid, P.; Lorenz, A.; Hameister, H.; Montenarh, M. Expression of p53 during mouse embryogenesis. *Development* **1991**, *113*, 857–865. [CrossRef] [PubMed]
90. Ciaffardini, F.; Nicolai, S.; Caputo, M.; Canu, G.; Paccosi, E.; Costantino, M.; Frontini, M.; Balajee, A.; Proietti-De-Santis, L. The cockayne syndrome B protein is essential for neuronal differentiation and neuritogenesis. *Cell Death Dis.* **2014**, *5*, e1268. [CrossRef] [PubMed]
91. Gjerstorff, M.F.; Harkness, L.; Kassem, M.; Frandsen, U.; Nielsen, O.; Lutterodt, M.; Møllgård, K.; Ditzel, H.J. Distinct GAGE and MAGE-A expression during early human development indicate specific roles in lineage differentiation. *Hum. Reprod.* **2008**, *23*, 2194–2201. [CrossRef] [PubMed]
92. Wang, Y.; Herzig, G.; Molano, C.; Liu, A. Differential expression of the Tmem132 family genes in the developing mouse nervous system. *Gene Expr. Patterns* **2022**, *45*, 119257. [CrossRef] [PubMed]
93. Liu, H.; Barnes, J.; Pedrosa, E.; Herman, N.S.; Salas, F.; Wang, P.; Zheng, D.; Lachman, H.M. Transcriptome analysis of neural progenitor cells derived from Lowe syndrome induced pluripotent stem cells: Identification of candidate genes for the neurodevelopmental and eye manifestations. *J. Neurodev. Disord.* **2020**, *12*, 14. [CrossRef] [PubMed]
94. Johansson, P.A.; Brattås, P.L.; Douse, C.H.; Hsieh, P.; Adami, A.; Pontis, J.; Grassi, D.; Garza, R.; Sozzi, E.; Cataldo, R. A cis-acting structural variation at the ZNF558 locus controls a gene regulatory network in human brain development. *Cell Stem Cell* **2022**, *29*, 52–69.e58. [CrossRef] [PubMed]
95. Yan, J.; Li, Q.; Mao, A.-P.; Hu, M.-M.; Shu, H.-B. TRIM4 modulates type I interferon induction and cellular antiviral response by targeting RIG-I for K63-linked ubiquitination. *J. Mol. Cell Biol.* **2014**, *6*, 154–163. [CrossRef] [PubMed]
96. Han, D.; Wang, L.; Long, L.; Su, P.; Luo, D.; Zhang, H.; Li, Z.; Chen, B.; Zhao, W.; Zhang, N. The E3 Ligase TRIM4 Facilitates SET Ubiquitin-Mediated Degradation to Enhance ER-α Action in Breast Cancer. *Adv. Sci.* **2022**, *9*, 2201701. [CrossRef]
97. Huang, Y.; Li, S.; Jia, Z.; Li, S.; He, W.; Zhou, C.; Zhang, R.; Xu, R.; Sun, B.; Ali, D.W. TRIM4 interacts with TRPM8 and regulates its channel function through K423-mediated ubiquitination. *J. Cell. Physiol.* **2021**, *236*, 2934–2949. [CrossRef] [PubMed]
98. Zhang, H.; Guo, Y.; Gu, H.; Wei, X.; Ma, W.; Liu, D.; Yu, K.; Luo, W.; Ma, L.; Liu, Y. TRIM4 is associated with neural tube defects based on genome-wide DNA methylation analysis. *Clin. Epigenet.* **2019**, *11*, 17. [CrossRef] [PubMed]
99. Wu, Z.; Zhu, X.; Yu, Q.; Xu, Y.; Wang, Y. Multisystem analyses of two Cockayne syndrome associated proteins CSA and CSB reveal shared and unique functions. *DNA Repair* **2019**, *83*, 102696. [CrossRef] [PubMed]
100. Brooks, P. Blinded by the UV light: How the focus on transcription-coupled NER has distracted from understanding the mechanisms of Cockayne syndrome neurologic disease. *DNA Repair* **2013**, *12*, 656–671. [CrossRef] [PubMed]

Supplementary

A

	B4	CS789	IUFi001
Cell Type	Fetal Foreskin Fibroblast	Dermal Fibroblast	Dermal Fibroblast
Provided By	ISRM Düsseldorf	IUF - Leibniz Research Institute for Environmental Medicine	
Donor Age	Neonatal	10 months	3 years
Sex	♂	♂	♀
Reprogramming	Viral	Episomal	Episomal
***ERCC6* Mutation**	None	Exon 10/R683X	Exon 5/K377X; Exon15/R857X
CS Severity	None	COFS	CS Type I

B

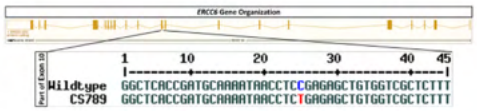

C

D

	Cerebrooculofacioskeletal (COFS) syndrome	Cockayne Syndrome Type II	Cockayne Syndrome Type I	Cockayne Syndrome Type III	UV-sensitive Syndrome
Onset	Fetal	At birth	First 2 years	3-4 years	Varying
Diagnosed at	Birth	Infancy	Childhood	Early teens	Childhood/Adulthood
Life Expectancy	Infancy	5-6 Years	16 years	30 years	Normal?
Suggestive Findings	Athrogryphosis Prenatal growth failure Prenatal Microcephaly Congenital Cataracts **or** Congenital Microphthalmia	**Major Criteria:** Postnatal growth failure; Progressive Microcephaly; Neurologic Dysfunction with developmental delay; White matter dysmyelination; Cerebellar Atrophy; Intracranial calcifications **Minor Criteria:** Cutaneous Photosensitivity; Demyelinating peripheral neuropathy; Pigmentary Retinopathy; Cataracts; Sensorineural Hearing loss; Enamel Hypoplasia; Tooth Anomalies; Cachectic Dwarfism			
Diagnosis	Multigene panel **or** Comprehensive genomic testing				

Supplementary Figure S1. Used cell lines and clinical information about Cockayne Syndrome (A) General information about the cell lines used in this work. (B) Schematic depiction of the ERCC6 mutation found in the CS789 iPSC line. (C) Schematic depiction of the ERCC6 mutation found in the IUFi001 iPSC line. (D) Table showing clinical features and diagnostic criteria of different types of Cockayne Syndrome.

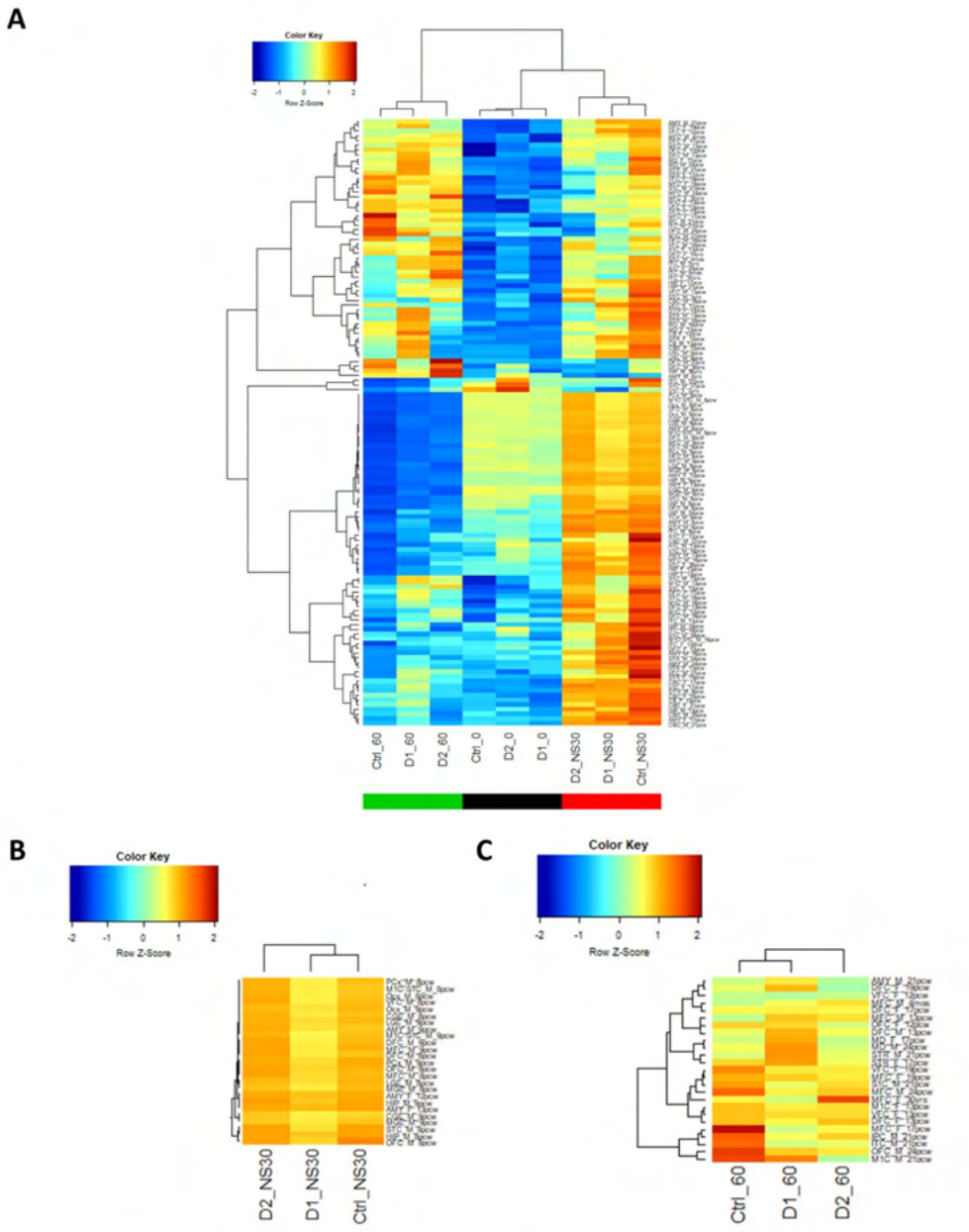

Supplementary Figure S2. Determination of developmental age of day 30 neurospheres and day 60 cortical organoids (A) Heat map of enrichment scores of transcriptomic data from control and CS iPSCs, neurospheres and organoids in comparison with the Allen Brain Atlas (ABA) human developmental Brain NGS data (https://www.brainspan.org/). (B) Region of highest consensus for the day 30 neurospheres extracted from A. (C) Region of highest consensus for the day 60 organoids extracted from A.

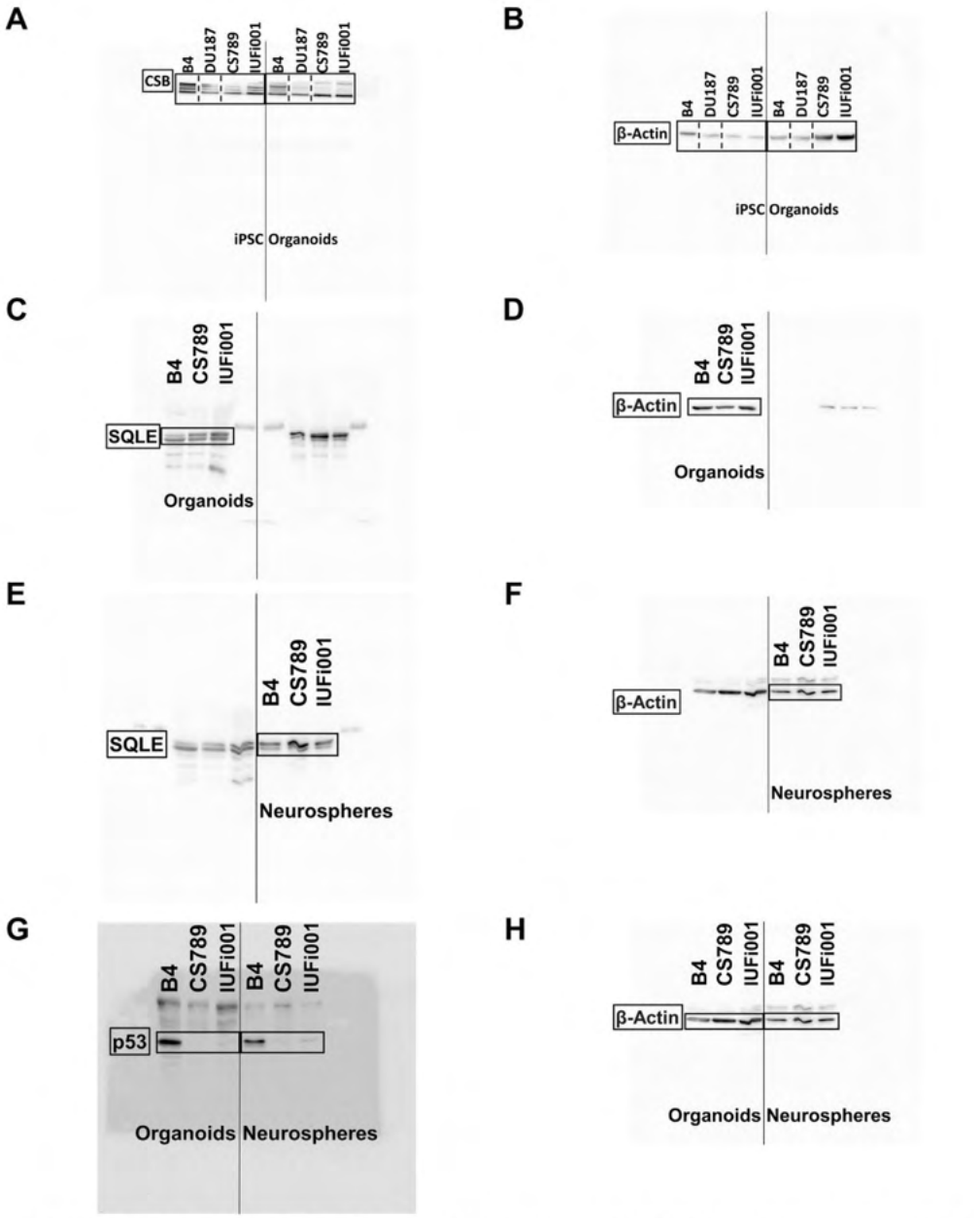

Supplementary Figure S3. Full Western Blot for CSB, SQLE, p53 and Beta-Actin protein in Day 0 iPSCs, Day 30 NS and Day 60 COs (A) Western Blot analysis for full-length CSB protein in B4, DU187, CS789 and IUFi001 iPSCs and COs. The cell line DU187 was not included in this article. (B) Western Blot for beta-Actin protein in B4, DU187, CS789 and IUFi001 iPSCs and COs. The cell line DU187 was not included in this article. (C) Western Blot analysis for SQLE protein in B4, CS789 and IUFi001 COs. (D) Western Blot analysis for beta-Actin protein in B4, CS789 and IUFi001 COs. (E) Western Blot analysis for SQLE protein in B4, CS789 and IUFi001 NS. (F) Western Blot analysis for beta-Actin protein in B4, CS789 and IUFi001 NS. (G) Western Blot analysis for p53 protein in B4, CS789 and IUFi001 NS and COs. (H) Western Blot analysis for beta-Actin protein in B4, CS789 and IUFi001 NS and COs. (B, D, F, H) Blot of the housekeeping gene used to quantify the respective blot in A, C, E and G on the left side of the figure. (Black outlines indicate parts of the image utilized to prepare the main figures. Dotted lines in A and B indicate where the DU187 line was excised from the image.)

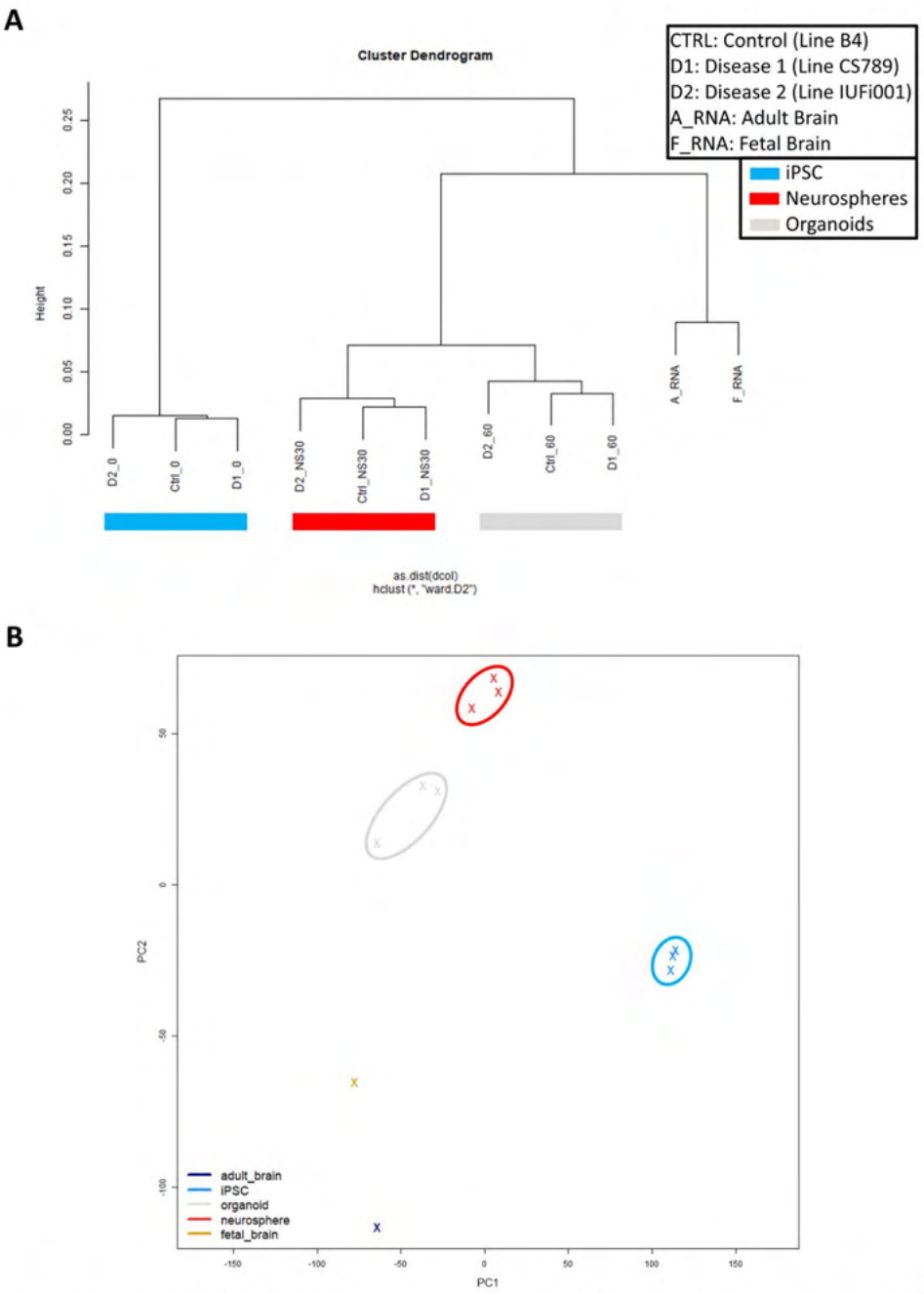

Supplementary Figure S4. Quality control of next generation sequencing data (A) Dendrogram obtained by hierarchical cluster analysis of NGS gene expression data for B4, CS789 and IUFi001 iPSCs, neurospheres and cerebral organoids. (B) Principal component analysis of NGS gene expression data for B4, CS789 and IUFi001 iPSCs, neurospheres and cerebral organoids.

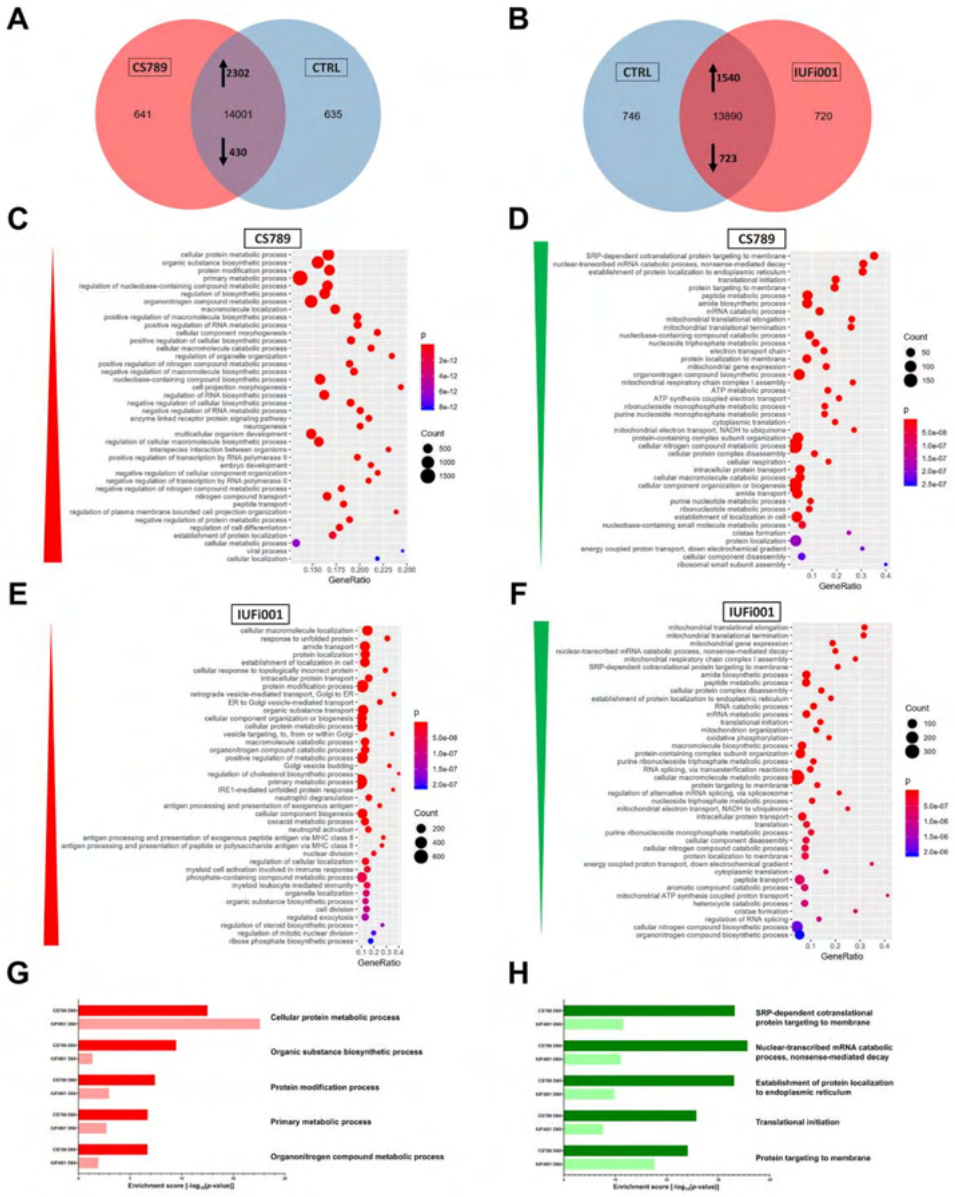

Supplementary Figure S5. Global transcriptome and associated Gene Ontology analysis of control and CS neurospheres at day 30 (A) Venn diagram showing genes expressed only in CS789 neurospheres (641), in CTRL (B4) neurospheres (635) and common to both (14001) (detection p value < 0.05). (B) Venn diagram showing genes expressed only in IUFi001 neurospheres (720), in CTRL (B4) neurospheres (746) and common to both (13890) (detection p value < 0.05). (C,D) Dot plots showing the Top 30 differentially regulated Gene Ontologies (c) in the 2302 significantly upregulated DEGs in day 30 CS789 neurospheres in comparison to CTRL (B4) (D) and in the 430 significantly downregulated DEGs in day 30 CS789 neurospheres in comparison to CTRL (B4). (E,F) Dot plots showing the Top 30 differentially regulated KEGG pathways (E) in the 1540 significantly upregulated DEGs in day 30 IUFi001 neurospheres in comparison to CTRL (B4) (F) and in the 723 significantly downregulated DEGs in day 30 IUFi001 neurospheres in comparison to CTRL (B4). (G) Bar chart of the differentially upregulated Gene Ontologies (Top 5 ranked) common between day 30 CS789 and IUFi001 neurospheres in comparison to CTRL (B4) neurospheres. (H) Bar chart of the differentially downregulated Gene Ontologies (Top 5 ranked) common between day 30 CS789 and IUFi001 neurospheres in comparison to CTRL (B4) neurospheres.

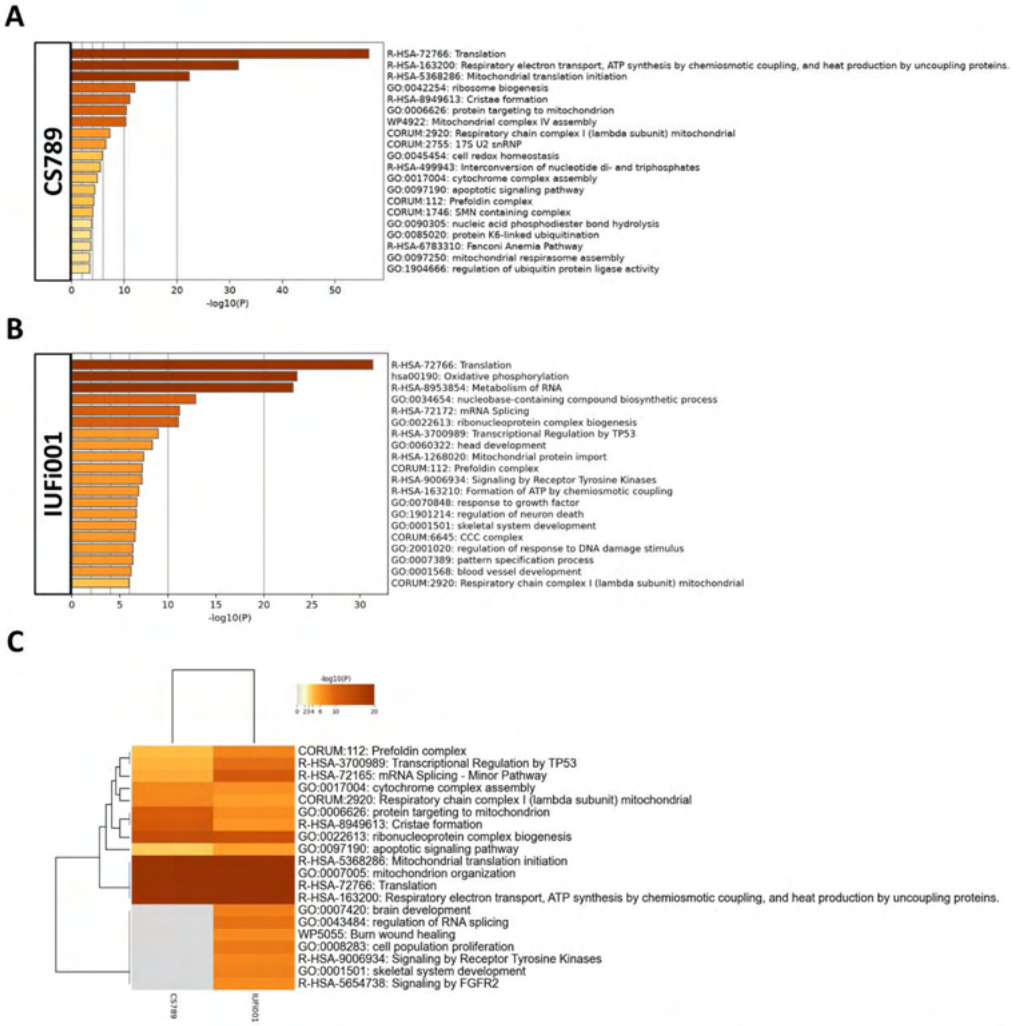

Supplementary Figure S6. Comparative transcriptome and Gene Ontology analysis of downregulated DEGs in day 30 neurospheres (A) Bar graph of the Top 20 non-redundant enrichment clusters attributable to the 430 DEGs upregulated in day 30 CS789 neurospheres in comparison to CTRL (B4). (B) Bar graph of the Top 20 non-redundant enrichment clusters attributable to the 723 DEGs downregulated in day 30 IUFi001 neurospheres. (C) Metascape-generated heatmap comparing downregulated gene-sets employed in A and B revealed i.a. GOs involved in mitochondrial translation initiation, mitochondrion organization and translation.

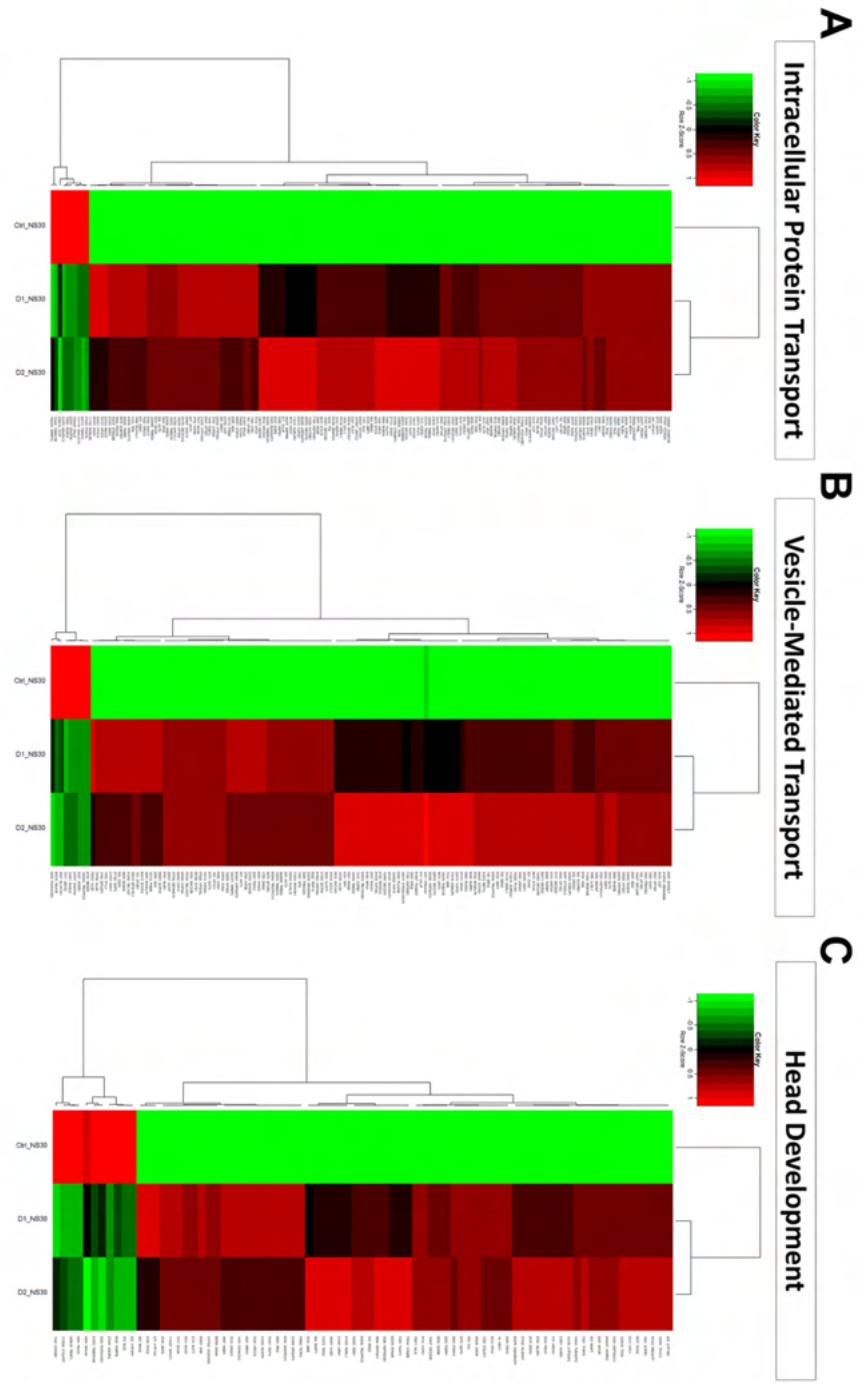

Supplementary Figure S7. Analysis of select Gene Ontologies differentially regulated in day 30 neurospheres (A) Pearson´s heatmap depicting all identified differentially regulated genes involved in intracellular protein transport common between day 30 CS789 (D1) and IUFi001 (D2) neurospheres in comparison to B4 (CTRL). (B) Pearson´s heatmap depicting all identified differentially regulated genes involved in vesicle-mediated transport common between day 30 CS789 (D1) and IUFi001 (D2) neurospheres in comparison to B4 (CTRL). (C) Pearson´s heatmap depicting all identified differentially regulated genes involved in head development common between day 30 CS789 (D1) and IUFi001 (D2) neurospheres in comparison to B4 (CTRL).

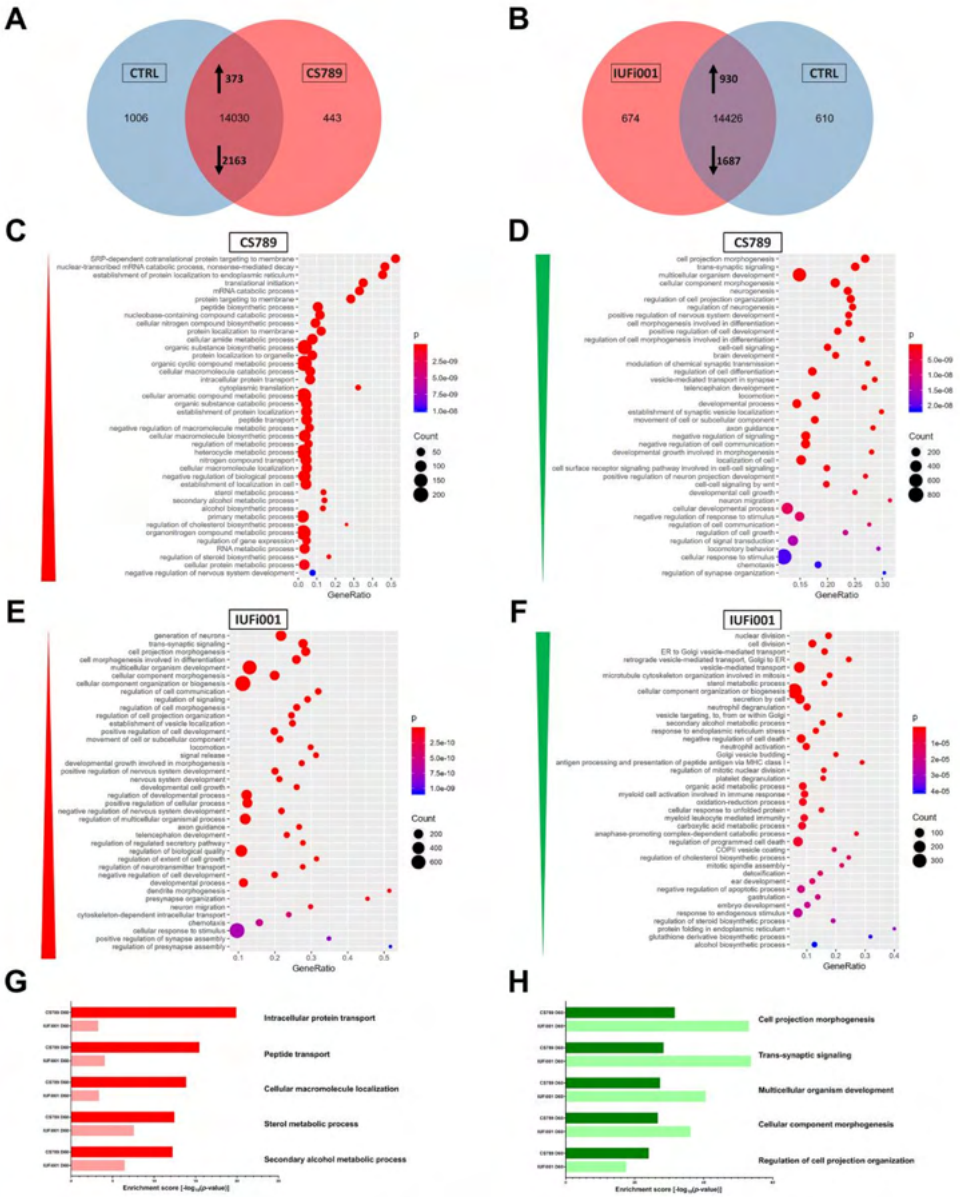

Supplementary Figure S8. Global transcriptome and associated Gene Ontology analysis of control and CS organoids at day 60 (A) Venn diagram showing genes expressed only in CS789 organoids (443), in CTRL (B4) organoids (1006) and common to both (14030) (detection p-value < 0.05). (B) Venn diagram showing genes expressed only in IUFi001 organoids (674), in CTRL (B4) organoids (610) and common to both (14426) (detection p value < 0.05). (C,D) Dot plots showing the Top 30 differentially regulated Gene Ontologies (C) in the 373 significantly upregulated DEGs in day 60 CS789 organoids in comparison to CTRL (B4) (D) and in the 2163 significantly downregulated DEGs in day 60 CS789 organoids in comparison to CTRL (B4). (E,F) Dot plots showing the Top 30 differentially regulated Gene Ontologies (E) in the 930 significantly upregulated DEGs in day 60 IUFi001 organoids in comparison to CTRL (B4) (F) and in the 1687 significantly downregulated DEGs in day 60 IUFi001 organoids in comparison to CTRL (B4). (G) Bar chart of the differentially upregulated Gene Ontologies (Top 5 ranked) common between day 60 CS789 and IUFi001 organoids in comparison to CTRL (B4) organoids. (H) Bar chart of the differentially downregulated Gene Ontologies (Top 5 ranked) common between day 60 CS789 and IUFi001 organoids in comparison to CTRL (B4) organoids.

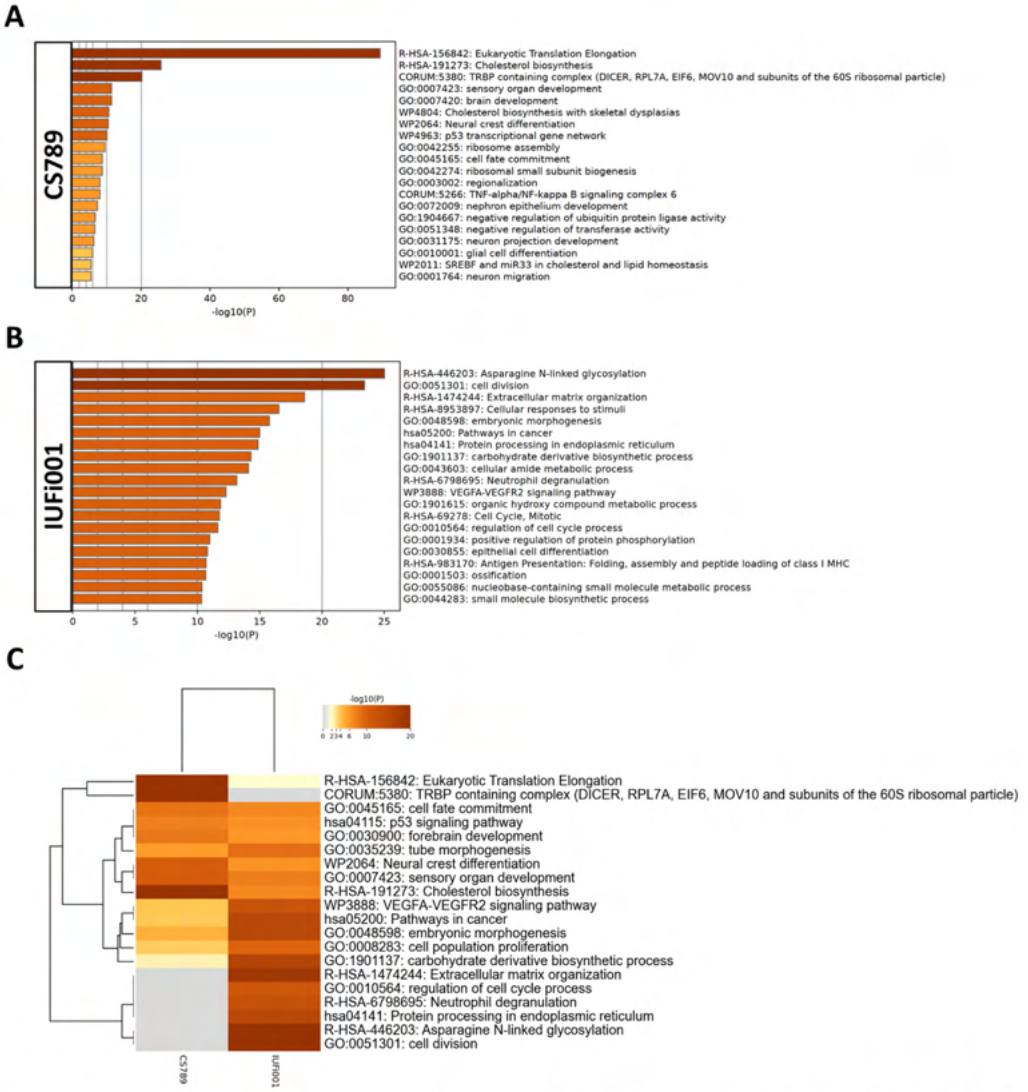

Supplementary Figure S9. Comparative transcriptome and Gene Ontology analysis of upregulated DEGs in day 60 organoids (A) Bar graph of the Top 20 non-redundant enrichment clusters attributable to the 373 DEGs upregulated in day 60 CS789 organoids in comparison to CTRL (B4). (B) Bar graph of the Top 20 non-redundant enrichment clusters attributable to the 930 DEGs upregulated in day 60 IUFi001 organoids. (C) Metascape-generated heatmap comparing upregulated gene-sets employed in A and B revealed i.a. GOs involved in forebrain development, p53-signalling pathway, cholesterol biosynthesis and VEGFA-VEGFR2 signalling pathway.

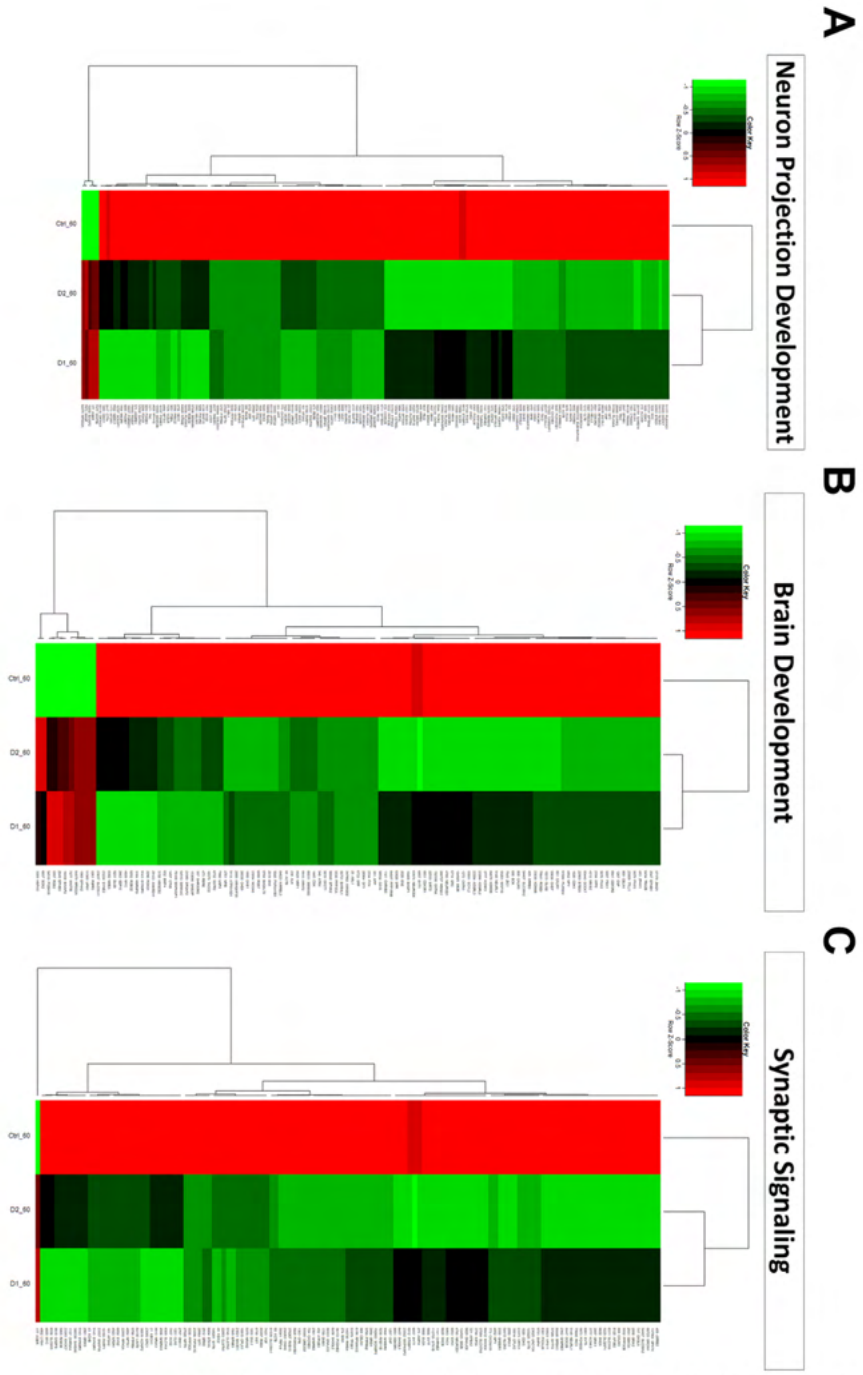

Supplementary Figure S10. Analysis of select Gene Ontologies differentially regulated in day 60 organoids (A) Pearson´s heatmap depicting all identified differentially regulated genes involved in neuron projection development common between day 60 CS789 (D1) and IUFi001 (D2) organoids in comparison to B4 (CTRL). (B) Pearson´s heatmap depicting all identified differentially regulated genes involved in brain development common between day 60 CS789 (D1) and IUFi001 (D2) organoids in comparison to B4 (CTRL). (C) Pearson´s heatmap depicting all identified differentially regulated genes involved in synaptic signalling common between day 60 CS789 (D1) and IUFi001 (D2) organoids in comparison to B4 (CTRL).

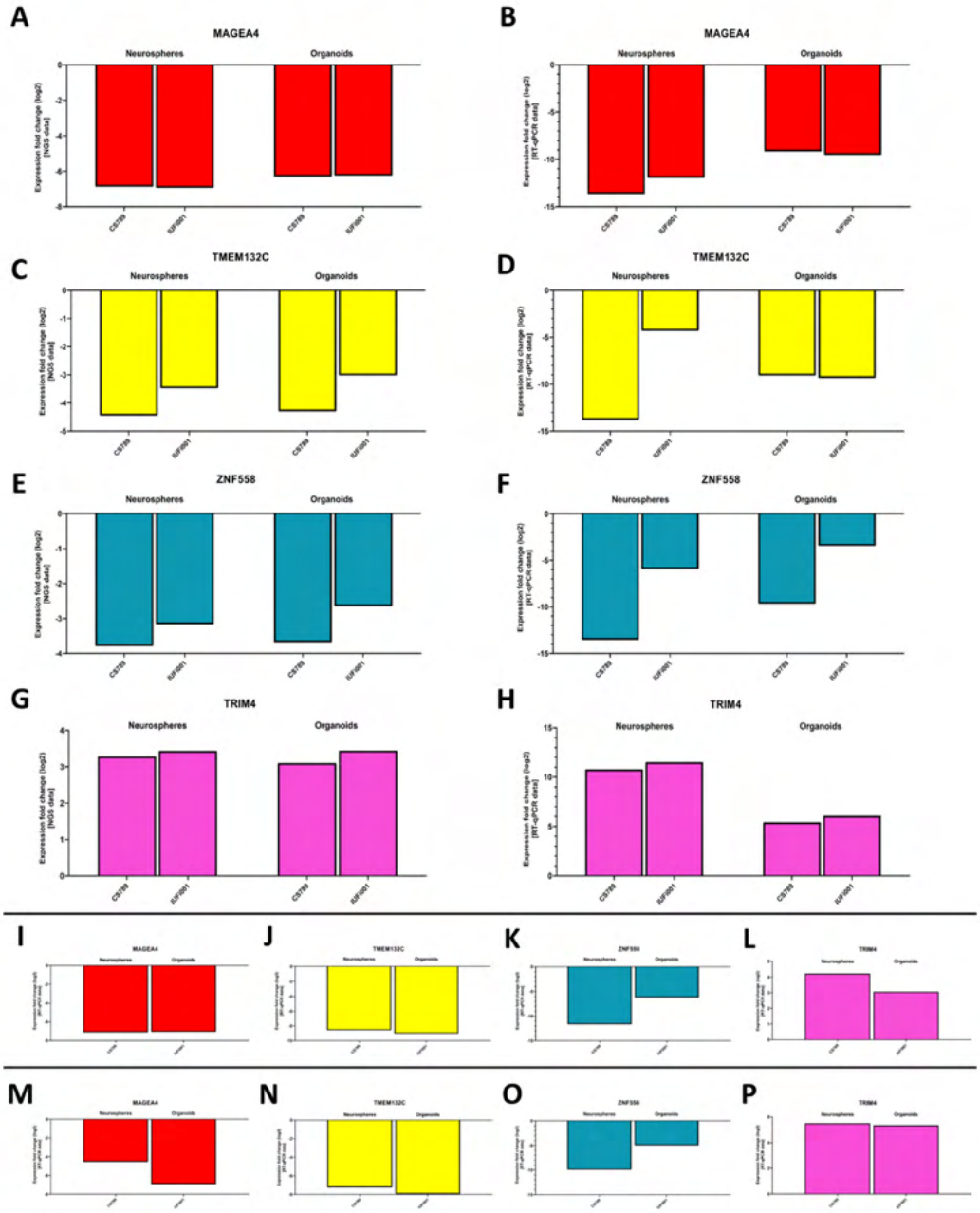

Supplementary Figure S11. RT-qPCR for MAGEA4, TMEM132C, ZNF558 and TRIM4 in Day 30 Neurospheres, two sets of Day 60 Organoids and Day 120 Organoids (A,C,E,G) Relative mRNA expression analysis of *MAGEA4* (A), *TMEM132C* (C), *ZNF558* (E), and *TRIM4* (G) in CS789 and IUFi001 day 30 neurospheres and day 60 organoids compared to CTRL (B4). (B,D,F,H) qRT-PCR analysis of *MAGEA4* (B), *TMEM132C* (D), *ZNF558* (F), and *TRIM4* (H) mRNA expression in CS789 and IUFi001 day 30 neurospheres and day 60 organoids relative to CTRL (B4). (I-L) RT-qPCR analysis of MAGEA4 (I), TMEM132C (J), ZNF558 (K) and TRIM4 (L) mRNA expression in a second set of day 60 CS789 and IUFi001 organoids relative to control organoids (B4). (M-P) RT-qPCR analysis of MAGEA4 (M), TMEM132C (N), ZNF558 (O) and TRIM4 (P) mRNA expression of day 120 CS789 and IUFi001 organoids relative to control organoids (B4).

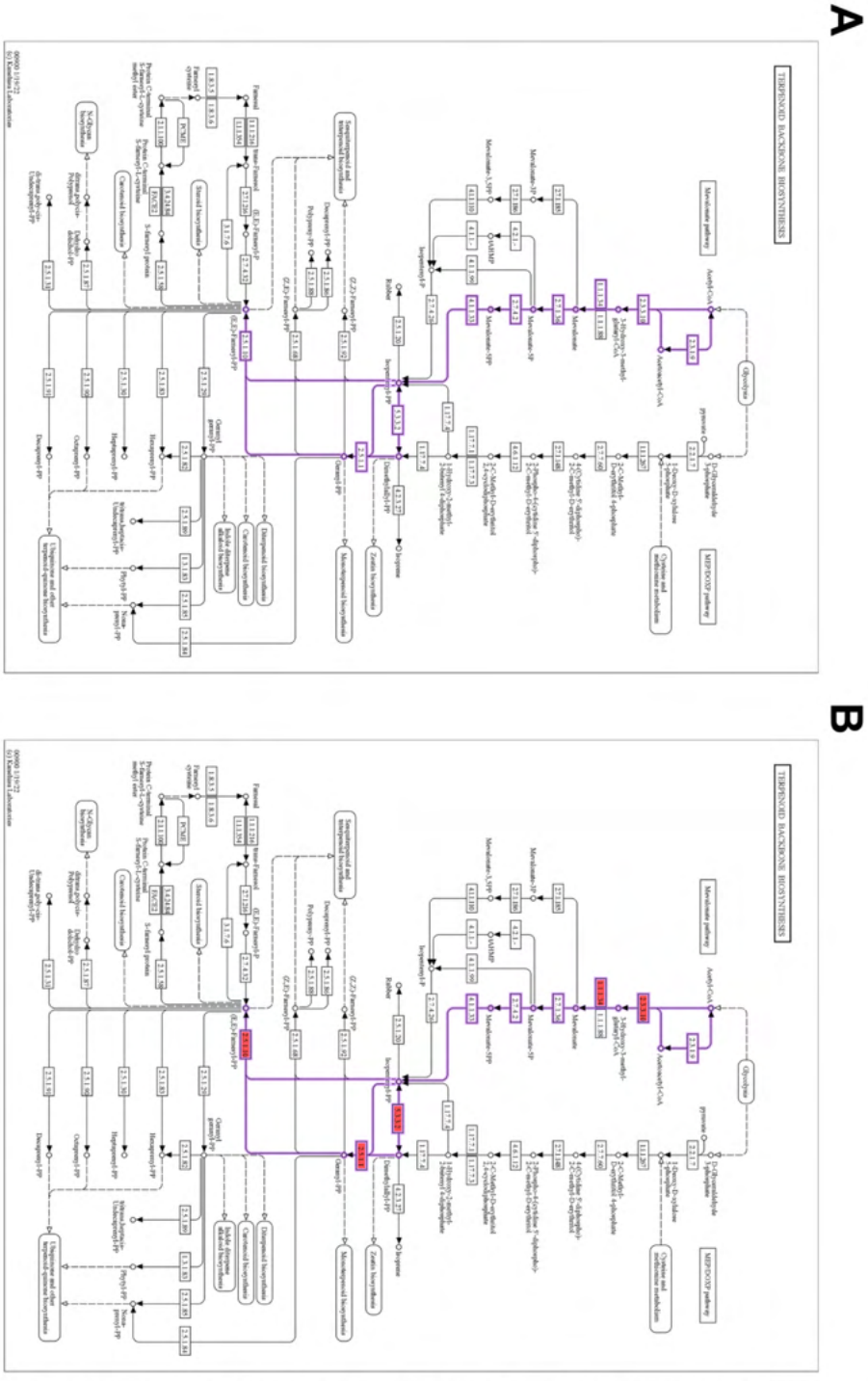

Supplementary Figure S12. Analysis of the Mevalonate pathway of the Terpenoid Backbone Biosynthesis pathway in day 30 NS and day 60 COs (A,B) Schematic of the pathway Terpenoid Back Biosynthesis with the Mevalonate pathway indicated in purple. The genes upregulated in CSB-deficient day 30 NS (A) and day 60 COs (B) are indicated in red.

Supplementary Table 1 Primers and Antibodies

Gene	Sequenz FWD	Sequenz REV
MDM2	AAACTGGGGAGTCTTGAGGG	TGCACATTTGCCTGCTCCTC
SESN2	ACAAGTGTTGTGGCCTTCCTGAAC	ATGGGTGAATGGCAAGTAGGAGGT
WRN	GCATGTGTTCGGAAGAGTGTTT	TGACATGGAAGAAACGTGGAA
HMGCR	CATCTGAAGGGTTCGCAGTG	TGACCTGGACTGGAAACGG
SQLE	GCCTGCCTTTCATTGGCTTC	TTCCTTTTCTGCGCCTCCTG
DHCR7	GCGCCAGAGACTGCAAATTC	ACTTCCCGATCCGAGGGTTA
MSMO1	TCATCATGAGTTTCAGGCTCCA	AATGGTCACCCATGCCCAAA
MAGEA4	CCAAGGAGAAGATCTGCCTGT	CAGGGACCAGAGGAGAGGAG
TMEM132C	CCCTTTACCCCAACGCAGAA	GTGCTGAATACAGCCTCCTGTT
ZNF558	CGGGATAAAGGAGGAGCGTC	GAAGGTTACCAAGCCCCGTA
TRIM4	AAAGCGATTCCAAGTGGCTGTA	CCAAGAACTGGCTGATGCTGT

Host	Antibody	Company	Ordering Number
Mouse	Map2	Synaptic Systems	188011
Guinea Pig	NeuN	Synaptic Systems	266004
Mouse	Tau	Invitrogen	MN1000
Rabbit	S100beta	Abcam	ab52642
Mouse	beta-3-Tubulin	Cell Signaling Technologies	4466S
Goat	SOX1	R&D Systems	AF3369
Rabbit	SOX2	Cell Signaling Technologies	3579S
Rabbit	CSB	GeneTex	GTX104508
Rabbit	SQLE	Proteintech	12544-1-AP
Mouse	Ki67	Cell Signaling Technologies	9449S
Mouse	p53	Merck	OP43

III.II. Hemozoin induces Malaria via activation of DNA damage, p38 MAPK and Neurodegenerative Pathways in Human iPSC-derived Neuronal Model of Cerebral Malaria

Abida Islam Pranty[#], **Leon-Phillip Szepanowski[#]**, Wasco Wruck, Akua Afriyie Karikari and James Adjaye

[#] Equal Contribution

Scientific Reports 2024

Abstract

Malaria caused by Plasmodium falciparum infection results in severe complications including cerebral malaria (CM), in which approximately 30% of patients end up with neurological sequelae. Sparse in vitro cell culture-based experimental models which recapitulate the molecular basis of CM in humans has impeded progress in our understanding of its etiology. This study employed healthy human induced pluripotent stem cells (iPSCs)-derived neuronal cultures stimulated with hemozoin (HMZ) - the malarial toxin as a model for CM. Secretome, qRT-PCR, Metascape, and KEGG pathway analyses were conducted to assess elevated proteins, genes, and pathways. Neuronal cultures treated with HMZ showed enhanced secretion of interferon-gamma (IFN-γ), interleukin (IL)1-beta (IL-1β), IL-8 and IL-16. Enrichment analysis revealed malaria, positive regulation of cytokine production and positive regulation of mitogen-activated protein kinase (MAPK) cascade which confirm inflammatory response to HMZ exposure. KEGG assessment revealed up-regulation of malaria, MAPK and neurodegenerative diseases-associated pathways which corroborates findings from previous studies. Additionally, HMZ induced DNA damage in neurons. This study has unveiled that exposure of neuronal cultures to HMZ, activates molecules and pathways similar to those observed in CM and neurodegenerative diseases. Furthermore, our model is an alternative to rodent experimental models of CM.

Author´s Contributions: (40%)

Conceptualisation, J.A., A.A.K., A.I.P. and **L.-P.S**.; formal analysis, A.I.P. **L.-P.S.** and W.W.; investigation, A.I.P., **L.-P.S.** and W.W.; resources, J.A; data curation, A.I.P., **L.-**

P.S. and W.W.; writing—original draft preparation, A.I.P., A.A.K. and **L.-P.S.**; writing—review and editing, J.A., A.A.K., A.I.P., **L.-P.S**. and W.W.; visualization, A.I.P., **L.-P.S.** and W.W.; supervision, J.A.; project administration, J.A.; funding acquisition, J.A. All authors have read and agreed to the published version of the manuscript.

Status: Published in Scientific Reports; Impact Factor 3.9; 5-Year-Impact Factor 4.3 (https://doi.org/10.1038/s41598-024-76259-3)

www.nature.com/scientificreports

scientific reports

Check for updates

OPEN

Hemozoin induces malaria via activation of DNA damage, p38 MAPK and neurodegenerative pathways in a human iPSC-derived neuronal model of cerebral malaria

Abida Islam Pranty[1,4], Leon-Phillip Szepanowski[1,4], Wasco Wruck[1], Akua Afriyie Karikari[3] & James Adjaye[1,2]✉

Malaria caused by *Plasmodium falciparum* infection results in severe complications including cerebral malaria (CM), in which approximately 30% of patients end up with neurological sequelae. Sparse in vitro cell culture-based experimental models which recapitulate the molecular basis of CM in humans has impeded progress in our understanding of its etiology. This study employed healthy human induced pluripotent stem cells (iPSCs)-derived neuronal cultures stimulated with hemozoin (HMZ) - the malarial toxin as a model for CM. Secretome, qRT-PCR, Metascape, and KEGG pathway analyses were conducted to assess elevated proteins, genes, and pathways. Neuronal cultures treated with HMZ showed enhanced secretion of interferon-gamma (IFN-γ), interleukin (IL)1-beta (IL-1β), IL-8 and IL-16. Enrichment analysis revealed malaria, positive regulation of cytokine production and positive regulation of mitogen-activated protein kinase (MAPK) cascade which confirm inflammatory response to HMZ exposure. KEGG assessment revealed up-regulation of malaria, MAPK and neurodegenerative diseases-associated pathways which corroborates findings from previous studies. Additionally, HMZ induced DNA damage in neurons. This study has unveiled that exposure of neuronal cultures to HMZ, activates molecules and pathways similar to those observed in CM and neurodegenerative diseases. Furthermore, our model is an alternative to rodent experimental models of CM.

Keywords iPSCs, Neurons, Hemozoin, Cerebral malaria, Neuro-inflammation, DNA damage

In spite of the significant efforts to combat malaria, the disease remains a public health problem globally. In 2022, there was an estimated 249 million malaria cases in 85 malaria endemic countries, which represents an increase of 2 million cases compared with 2021[1]. Also, the continuous importation of malaria to non-endemic regions consistently challenges elimination efforts, leading to the spread of drug-resistant parasites within and between countries[2]. *Plasmodium falciparum* and *vivax* are the most virulent of the five human parasite species. Nonetheless, *P. falciparum* is the species primarily implicated in severe and fatal forms of clinical malaria[3]. 1% of the *P. falciparum* infected children develop cerebral malaria (CM)[4]. Principal to the pathogenesis of *P. falciparum* infection is the toxin, hemozoin (HMZ), which is also referred to as the malaria pigment. *Falciparum* does not infiltrate the brain parenchyma but can cause severe damage to neurons, through the release of HMZ, which can induce reactive oxygen species (ROS) mediated macromolecular damage and inflammatory response[5,6]. Moreover, *P. falciparum* poses a challenge for experimental malaria investigations, due to its inability to infect model species like rodents[7]. A majority of falciparum malaria research is based on clinical studies, which limits access to certain tissues such as the brain. Human derived induced pluripotent stem cells (iPSCs) have emerged as a relevant tool for modelling several diseases *in-vitro*[8,9]. iPSCs can be used for extensive studies related to disease pathogenesis, the impact of exogenous factors and the molecular targets of disease-modulating

[1]Institute for Stem Cell Research and Regenerative Medicine, Medical Faculty, Heinrich-Heine University, 40225 Düsseldorf, Germany. [2]Zayed Centre for Research into Rare Diseases in Children (ZCR), University College London – EGA Institute for Women's Health, 20 Guilford Street, WC1N 1DZ London, United Kingdom. [3]Department of Biomedical Sciences, School of Allied Health Sciences, College of Health and Allied Sciences, University of Cape Coast, Cape Coast, Ghana. [4]These authors contributed equally: Abida Islam Pranty and Leon-Phillip Szepanowski. ✉email: james.adjaye@med.uni-duesseldorf.de; J.adjaye@ucl.ac.uk

treatments. With the lack of an appropriate experimental model for *P. falciparum*, and with the difficulty in studying the molecular-basis and mechanisms associated with malaria in human subjects, there is a pressing need for new models of falciparum malaria.

A major complication of *P. falciparum* infection is cerebral malaria (CM). Clinically, CM is characterized by lack of consciousness and coma, with high mortality rates[10]. Post-CM survivors sustain brain injuries and neurological sequelae including cognitive impairment, motor skill impairment, cortical blindness, seizures and attention deficit hyperactive disorder[10,11]. To date, the pathogenic mechanisms leading to CM remain an enigma as studies have been hampered by limited accessibility to human tissues and brain injury in human post-mortem tissues has provided limited cross-sectional data[12]. In a previous study using pooled transcriptome data from whole blood analysis of *P. falciparum* malaria patients, we discovered that falciparum malaria shared similar biological processes with neurodegenerative diseases[5]. Additionally, in our previous study we employed an iPSC-based model discovering that malaria was a significant pathway in constructing a network of genes associated with late onset Alzheimer's disease (LOAD)[13]. Both mild and severe forms of falciparum malaria have been previously linked to psychiatric disorders such as depression, irritability, anxiety, difficulties with concentration, disorientation and forgetfulness[14]. Deciphering the molecular changes that occur during the disease pathogenesis could unravel the link between falciparum malaria and neurodegenerative diseases.

In this study, we employed two healthy iPSC-line-derived neuronal cultures to characterize molecular changes that occur upon exposure of neuronal cultures to the parasite's most potent toxin- HMZ. After exposure to HMZ, qRT-PCR and secretome analysis revealed an increase in pro-inflammatory molecules and neurotrophins including interleukin-1-beta (IL-1β), IL-16, interferon-gamma (IFN-γ), monocyte chemotactic protein-1 (MCP-1), vascular endothelial growth factor (VEGF) and brain derived neurotrophic factor (BDNF). Pathway enrichment analysis using the Kyoto Encyclopedia of Genes and Genomes (KEGG) network revealed malaria, mitogen-activated protein kinase (MAPK), neurodegenerative and Alzheimer's disease (AD) pathways as upregulated in HMZ-exposed cells. This corroborates our previous study where neurodegenerative and AD pathways were elevated in falciparum malaria patients. Metascape assessment uncovered malaria, regulation of leukocyte proliferation, positive regulation of cytokine production and positive regulation of MAPK cascade, which are indicative of cellular inflammatory response to HMZ exposure. Furthermore, western blot analysis confirmed DNA damage in UM51-derived neurons, implicating HMZ as genotoxic. Investigations using HMC3 microglia cells revealed a similar pattern of inflammation and cellular injury. Taken together, the findings of this study consolidate the theory that CM and neurodegenerative diseases, such as AD, activate similar cellular mechanisms through inflammation, which could account for the neurological deficits observed in CM patients. It also demonstrates that iPSC-derived neuronal cultures could serve as a valuable model in research regarding CM.

Results

Generation of iPSC-derived neuronal networks to model cerebral malaria

The UM51 line was generated from SIX2-positive renal progenitor cells isolated from the urine of a 51-year-old healthy male of African origin[15], while healthy human fetal foreskin fibroblasts were reprogrammed to generate the B4-iPSC line (HFF1, ATCC, #ATCCSCRC-1041, http://www.atcc.org)[16] (Supplementary Table S1). To obtain neuronal networks, UM51 and B4 iPSCs were seeded as single cells for neural induction, then expanded as neural progenitor cells and further differentiated into neurons (Fig. 1a, Supplementary Fig. 1). A dose-response curve was prepared using ascending concentrations of HMZ on neuronal cultures to determine IC80 (cell survival rate) and the closest lower concentration examined (20 µM) was used for all following experiments (Supplementary Fig. 1). Subsequently, day 16 neuronal cultures from both cell lines were exposed to 20 µM hemozoin (HMZ) for 48 h to observe HMZ- induced effects in central nervous system (CNS) cell populations with the aim of modeling cerebral malaria using iPSC-derived neuronal cultures (Fig. 1a, Supplementary Fig. 1).

Bright field microscopy showed deposition of malaria pigments as brown crystals inside and/or around the neuronal cultures after 48 h of treatment (Fig. 1b, Supplementary Fig. 1). Neuronal features were confirmed in both control and HMZ-treated neuronal cultures by expression of neuronal markers Beta III tubulin (β3-Tubulin), tubulin associated unit (TAU), and microtubule- associated protein 2 (MAP2) (Fig. 1c, Supplementary Fig. 1).

HMZ activates inflammatory-associated pathways in iPSC-derived neuronal cultures

Supernatants from UM51 neuronal cultures were used to analyze the secretome profile of both HMZ-treated and control conditions (Supplementary Fig. 2). The resulting secretome profiles were further analyzed utilizing hierarchical clustering analysis (heatmap using Pearson correlation as similarity measure in Fig. 2a), which indicated induction of an inflammatory response upon treatment with 20 µM HMZ for 48 h. Secretome profiles from B4 neuronal cultures were analyzed using the same computational analyses, revealing a similar secretion pattern to that of UM51 neuronal cultures (Supplementary Fig. 3). Usually pro- and anti-inflammatory cytokines are involved not only in inflammatory response but also in immune-regulatory functions. Several crucial pro-inflammatory cytokines such as IL-8, IL1-B, IFN-G, IL-16 showed enhanced secretion, while anti-inflammatory cytokines such as IL-4, IL-13 showed reduced secretion (Fig. 2a) (Supplementary Fig. 2).

We further performed a Metascape-based analysis utilizing the list of up- and down-regulated cytokines obtained from the UM51 neuronal culture. The resulting enrichment clusters revealed malaria, positive regulation of cytokine production, positive regulation of MAPK cascade, and inflammatory responses to be activated by HMZ treatment (Fig. 2b). KEGG analysis revealed distinct regulated pathways upon HMZ exposure, which include malaria, ($p = 1.65 \times 10-7$, FDR = $2.59 \times 10-6$), MAPK signalling pathway ($p = 1.21 \times 10-9$, FDR = $2.84 \times 10-8$), pathways of neurodegeneration ($p = 0.0325$, FDR = 0.0588) and Alzheimer disease

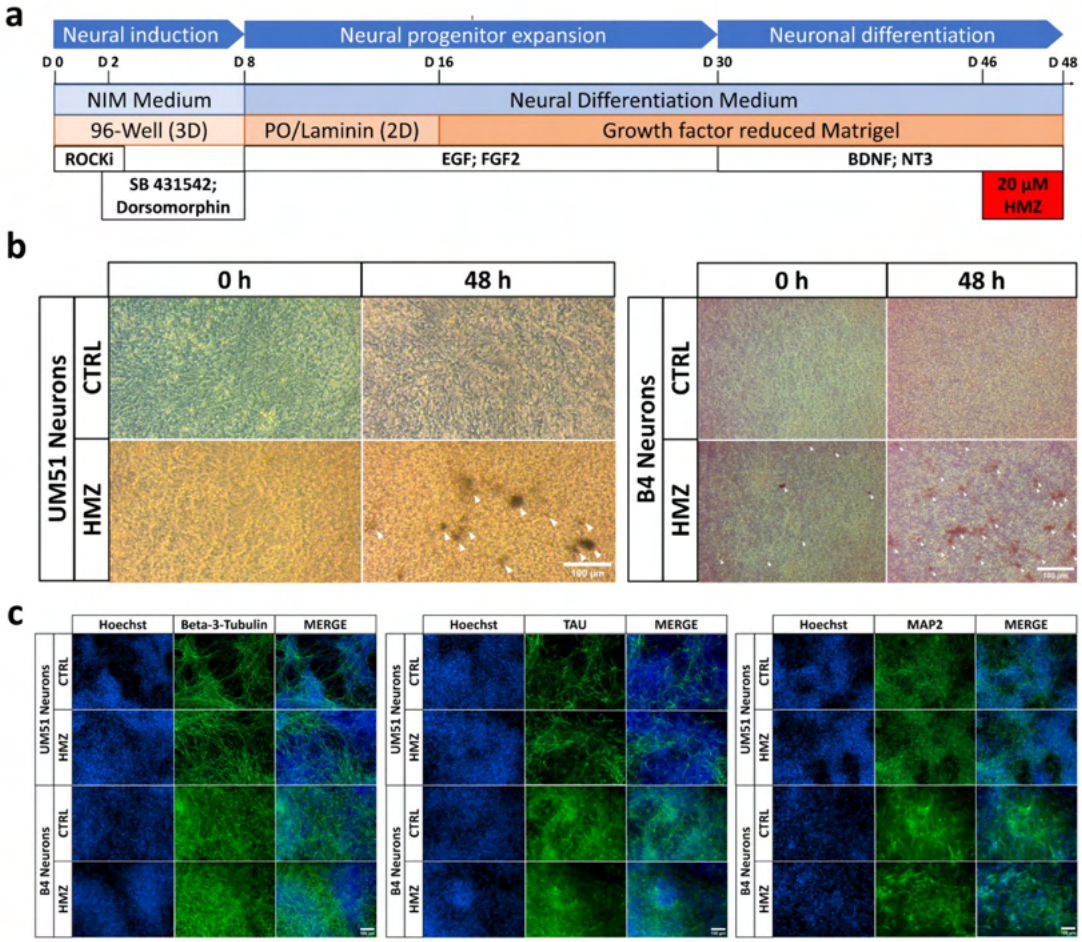

Fig. 1. Generation, characterization and utilization of iPSC-derived neuronal cultures for modelling cerebral malaria. (**a**) Schematic outline of the protocol used to generate iPSC-derived neuronal cultures. (**b**) Representative bright field images of control and HMZ-treated UM51- and B4 iPSC-derived neuronal cultures at 0 h and 48 h of exposure. Arrows depict the HMZ crystal deposition. Scale bar 100 µm. (**c**) Representative immunocytochemistry (ICC) images of β3-Tubulin-, TAU- and MAP2-positive cells in UM51- and B4-derived neuronal cultures after 48 h HMZ exposure in comparison to control. Scale bar 100 µm.

($p = 0.0446$, FDR = 0.0716) as upregulated pathways, and p53 signalling pathway ($p = 0.0069$, FDR = 0.0143) and apoptosis ($p = 0.0358$, FDR = 0.0576) as downregulated pathways (Fig. 2c, (Supplementary File 1).

Following the observations from the secretome profile, we performed qRT-PCR analysis to confirm mRNA expression of selected chemo- and cytokines in neuronal cultures of both cell lines (UM51 and B4) from treated and control conditions. We observed a significant increase in *TNF-α* mRNA expression and a non-significant increase in *IL-8* expression in the UM51 cultures. In contrast, the B4 cultures showed a non-significant increase in *TNF-α* and a significant increase in *IL-8* expression. Although *IL-6* expression levels were high in individual samples, no overall increase was observed in either cell line (Fig. 2d). Furthermore, immune-regulatory, and inflammation-associated chemokines such as monocyte chemoattractant protein-1 (MCP-1) and macrophage migration inhibitory factor (MIF) showed increased secretion upon HMZ treatment (Fig. 2a, Supplementary Fig. 2). Secretion of vascular endothelial growth factor (VEGF) and platelet derived growth factor subunit B (PDGFB), both belonging to the same protein family and reported to be associated with inflammation, were also enhanced[8] (Fig. 2a). Additionally, enhanced mRNA expression and protein secretion of brain derived neurotrophic factor (BDNF) was observed. BDNF has been reported to be involved in modulating neuro-inflammation by providing neuroprotection[17] (Fig. 2a and e). Next, we analyzed mRNA expression of selected genes associated with the mentioned pathways. Both UM51 and B4 neuronal cultures exhibited similar trends upon HMZ treatment in the neuronal cultures with a significant increase in *platelet and endothelial cell adhesion*

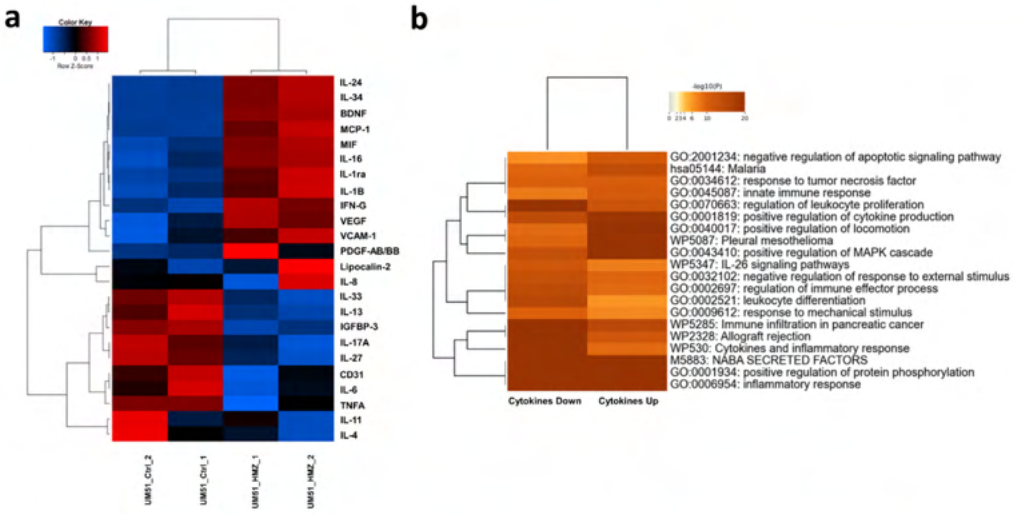

c

KEGG_Name (Upregulated)	p_hyper	q_hyper	Genes
Malaria	1.65E-07	2.59E-06	CCL2,CD40LG,HGF,ICAM1,IFNG,IL1B
MAPK signaling pathway	1.21E-09	2.84E-08	BDNF,CD14,CSF1,EGF,FGF19,FGF7,FLT3LG,HGF,IL1A,IL1B, PDGFA,PDGFB,VEGFA
Pathways of neurodegeneration	0.032533	0.058809507	AGER,BDNF,CSF1,DKK1,IL1A,IL1B
Alzheimer disease	0.044612	0.071617	AGER,CSF1,DKK1,IL1A,IL1B
KEGG_Name (Downregulated)	**p_hyper**	**q_hyper**	**Genes**
p53 signaling pathway	0.006855	0.014347	FAS,IGFBP3,THBS1
Apoptosis	0.0358292	0.057583	FAS,IL3,TNF

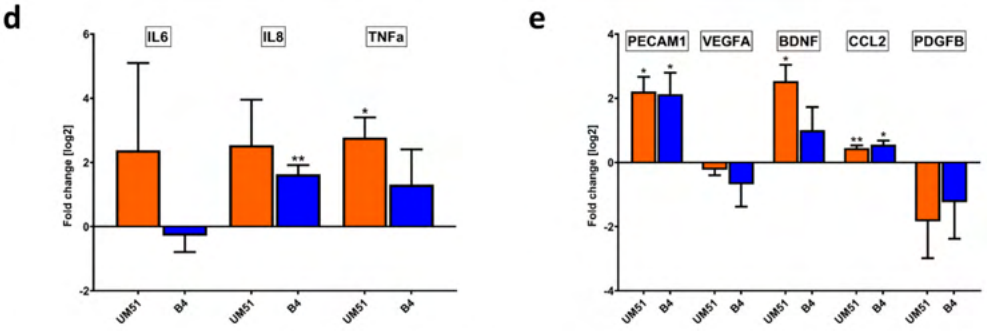

molecule 1 (PECAM1) and *C-C motif chemokine ligand 2* (*CCL2*) expression. *CCL2* and *PECAM1* encode for the MCP-1 and CD31 protein, respectively. Additionally, the mRNA expression of BDNF was significantly enhanced only in the UM51 cultures, while a non-significant increase was observed in the B4 cultures. Conversely, both *VEGFA* and *PDGFB* showed a non-significant decrease in mRNA expression levels upon HMZ exposure (Fig. 2e).

HMZ exposure induces DNA damage in UM51-derived neuronal cultures

We performed immunocytochemistry (ICC) and western blot (WB) analysis to evaluate the expression of the DNA damage marker- γH2AX (Fig. 3a,b). Both cell lines showed a similar trend with increased γH2AX levels in the WB analyses after HMZ exposure compared to the corresponding controls (Fig. 3b,c).

◂**Fig. 2**. Secretome analysis of neuronal cultures upon HMZ exposure reveals activation of inflammatory response, MAPK-signalling and neurodegenerative pathway. Cytokine array analyses was performed with supernatant derived from the UM51 neuronal cultures. (**a**) Pearson´s heatmap depicting selected chemo- and cytokines regulated in UM51 neuronal cultures after 48 h HMZ exposure in comparison to control. (**b**) Metascape-generated heatmap comparing the sets of up- and downregulated chemo- and cytokines derived from UM51 neuronal cultures after 48 h HMZ exposure reveals a secretome signature involved in i.a. Malaria, response to tumor necrosis factor and positive regulation of MAPK cascade. (**c**) Table depicting selected KEGG pathways including up-regulated malaria, MAPK signalling pathway, pathways of neurodegeneration, and Alzheimer disease. Down-regulated pathways include p53 signalling, and apoptosis upon HMZ exposure in comparison to control. Analysis was performed utilizing the list of up- and down-regulated cytokines obtained from the UM51 neuronal culture. (**d**) Relative mRNA expression analysis of *IL6*, *IL8* and *TNF-α* in UM51 and B4-derived neuronal cultures after 48 h HMZ exposure in comparison to control. (**e**) Relative mRNA expression analysis of *PECAM1*, *VEGFA*, *BDNF*, *CCL2* and *PDGFB* in UM51 and B4-derived neuronal cultures after 48 h HMZ exposure in comparison to control. (d, e) Values were normalized to *RPLP0* (housekeeping gene) and subsequently to controls. UM51 $n=3$; B4 Ctrl $n=2$; B4 HMZ $n=3$; blots depict mean and error bars depict SD of all experiments. Asterisk (*) depicts significance, which is indicated by $*p<0.05$; $**p<0.01$.

Manual counting of nuclei in ICC staining showed 30% γH2AX-positive cells after 48 h of HMZ exposure in the UM51 neuronal culture, while the control condition consisted of 6% γH2AX positive cells (Fig. 3a,d). On the contrary, B4 neuronal cultures showed almost no change in ICC staining analysis (Fig. 3a,d). Aligning with the observation from ICC, in WB analysis UM51 neurons showed stronger response to HMZ treatment than the B4 neurons with a 3.4-fold increase in γH2AX expression, while the B4 neurons showed only a 1.3-fold increase compared to their corresponding controls (Fig. 3b,c).

HMZ potentially activates p38 MAPK and not p53 signalling pathway in iPSC-derived neurons

As HMZ treatment on iPSC-derived neuronal cultures indicated p53 signalling pathway to be downregulated (Fig. 2c), and γH2AX levels were increased (Fig. 3), we investigated selected p53 signalling pathway-associated markers involved in DNA damage response and repair mechanisms (Supplementary Fig. 4)[18–20]. First, we analysed mRNA expression of the DNA damage and repair related genes in both UM51 and B4-derived neuronal cultures. We observed a trend toward downregulation of *p53* and *MDM2*, while *ATM, ATR, CHEK1*, and *CHEK2* were significantly upregulated compared to the corresponding controls. (Figure 4a and b).

In the WB analysis, p53 protein expression of the HMZ treated UM51 sample showed a slight increase, while the other p53 signalling-associated markers MDM2 (in both cell lines) and FAS (in UM51) showed a downregulated expression (Fig. 4c, d and f). All observations regarding these mentioned p53 signalling pathway-associated gene and protein expressions indicate a more vigorous response of the UM51 neuronal cultures upon HMZ exposure compared to B4 neuronal cultures (Fig. 4). This observation aligns with the observed higher DNA damage in the UM51 neuronal cultures compared to B4 (Fig. 3). Further experiments with immortalized HMC3 microglia-like cells also followed a similar trend with regards to p53 signalling pathway-associated markers and γH2AX expression after 48 h of HMZ exposure (Supplementary Fig. 5). Additionally, the change in total p38MAPK and phospho-p38MAPK protein expression might indicate MAPK signalling pathway activation after HMZ treatment in the iPSC-derived neuronal cultures (Figs. 2c and 4e).

Discussion

An acute neurological complication of *P. falciparum* infection is CM, which is marked by neurological sequela in some survivors. The molecular mechanisms that underlie CM remain an enigma, which can partly be attributed to the lack of a suitable model that captures the clinical outcomes observed in patients. In this study, we employed neuronal cultures derived from iPSC lines obtained from two healthy ethnically diverse males and HMZ, the malaria toxin, as an *in-vitro* model of CM. To evaluate the iPSC-derived neuronal cultures, we assessed their morphological characteristics and performed immunocytochemistry to confirm their neuronal identity by detecting the expression of pan-neuronal markers such as β3-tubulin and MAP2. TAU, MAP2 and β3-Tubulin-positive neuronal cultures were then stimulated with 20 µM HMZ for 48 h and deposition of the malarial toxin as brown crystals inside and/or around the neurons was observed. The deposition of HMZ as insoluble crystals into tissues is a common feature reported in both experimental and clinical malaria[21,22]. Indeed, the severity of falciparum infection is often correlated with the deposition of HMZ in organs[23] and HMZ granules have been previously linked to thrombosed micro-vessels in fatal CM induced hemorrhage[24].

Central to the progression of CM is neuro-inflammation. Notable inflammatory markers reported in CM include IL-1β, IL-6, IL-8, IFN-γ, TNF-α, PECAM-1, VCAM-1 and ICAM-1[25–27]. In this investigation, a secretome analysis using neuronal cell culture supernatant from UM51 cell line after HMZ treatment was conducted. Pearson´s heatmap analysis revealed an elevated IL-1β, IL-8 (partly), IL-16 and IFN-γ secretion. On the other hand, the levels of TNF-α, IL-6, IL-4 and IL-13 were lower in the HMZ treated cells. Interestingly, there was also a surge in the inflammatory-associated proteins: PDGFB, MIF, MCP-1 and VCAM-1. The increase in expression of these molecules is indicative of an inflammatory environment driven predominantly by a T helper type 1 (Th1) phenotype. Previous studies in clinical malaria have demonstrated that patients with CM had higher levels of pro-inflammatory Th1 cytokines as compared to severe malarial anemia patients[28,29], which could account in part for the acute injuries observed in CM. In addition, these Th1 cytokines and inflammation associated proteins may be crucial to the development of neurocognitive and psychiatric disorders in CM patients. For instance,

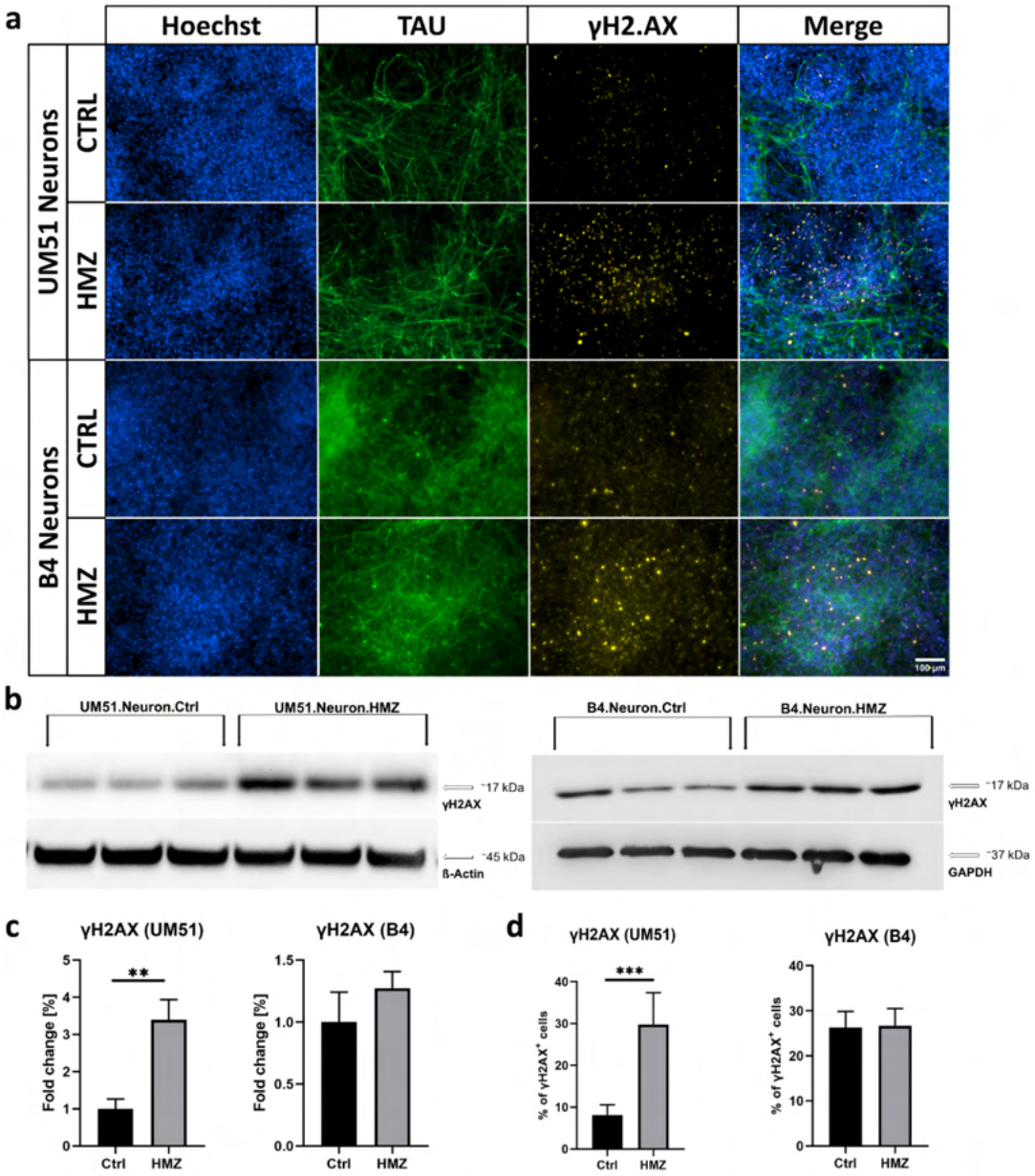

Fig. 3. HMZ exposure induces DNA damage in iPSC-derived neuronal cultures. All depicted results were recorded in UM51- and B4-derived neuronal cultures after 48 h HMZ exposure and compared to their corresponding controls. (**a**) Representative ICC images showing TAU- and γH2AX-positive cells. Scale bar 100 µm. (**b**) WB analysis for γH2AX. (**c**) Bar graphs showing γH2AX protein expression in fold change. Values were normalized to ß-Actin and GAPDH (housekeeping gene) and subsequently to control samples. (**d**) Manual ICC quantification of γH2AX-positive nuclei. (**c**, **d**) $n = 3$ for each condition, blots depict mean and error bars depict SD of all experiments. Asterisk (*) depicts significance, which is indicated by $^{**}p < 0.01$; $^{***}p < 0.001$. Approximately six random fields from three separate differentiations for each condition were manually analysed (**d**).

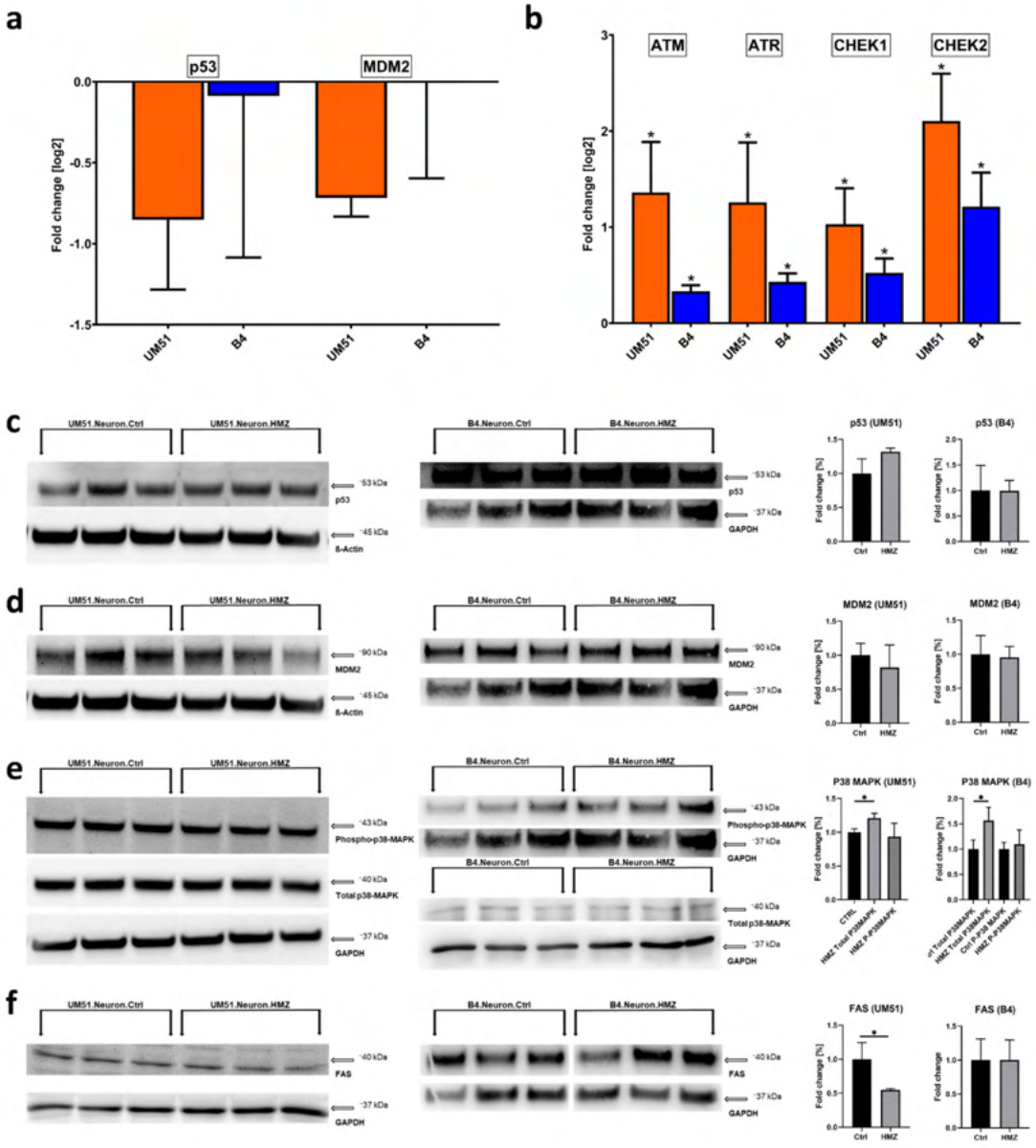

Fig. 4. HMZ exposure activates DNA damage responses. All depicted results were performed in UM51- and B4-derived neuronal cultures after 48 h HMZ exposure and compared to their corresponding controls. (**a**) Relative mRNA expression analysis of *p53* and *MDM2*. (**b**) Relative mRNA expression analysis of *ATM*, *ATR*, *CHEK1* and *CHEK2*. (**a**, **b**) Values were normalized to *RPLP0* (housekeeping gene) and subsequently to controls. (**c**–**f**) WB analyses and quantification of WB analyses for p53, MDM2, total p38MAPK, phospho-p38MAPK and FAS. Values were normalized to ß-Actin and GAPDH and subsequently to control samples. (a, b) UM51 $n = 3$; B4 Ctrl $n = 2$; B4 HMZ $n = 3$ (**c**–**f**) $n = 3$ for each condition. (**a**–**f**) Blots depict mean and error bars depict SD of all experiments. Asterisk (*) depicts significance, which is indicated by $^*p < 0.05$.

IL-8, IL-16 and MCP-1 have been implicated in neurocognitive symptoms in individuals with depression and anxiety[30], and IL-1β and IL-16 were associated with psychiatric symptoms in schizophrenia patients[31]. Again, in neurodegenerative research, IL-16 was reportedly increased in patients with cerebrovascular dementias and AD[32]. Although IL-16 has been associated with psychiatric disorders and AD, this is the first study to implicate the cytokine in an experimental CM model. The cytokine was found to be significantly higher in asymptomatic falciparum patients when compared to individuals infected with Chikungunya virus[33]. Hitherto, there have been no reports on this cytokine in CM studies involving humans, which necessitates further research to understand the relationship between IL-16 and neurological impairment in CM patients.

The pathogenesis of CM is characterized by persistent up-regulation of Th1 cytokines and inadequate production of anti-inflammatory cytokines including IL-4 and IL-13, which could possibly account for the observed lower levels of IL-4 and IL-13[34]. Instead of anti-inflammatory cytokines, the neurotrophic factor BDNF was elevated, which indicates a cellular response to remedy the highly inflammatory environment. In a study involving Ugandan children, McDonald et al., reported that lower BDNF levels were associated with poor prognosis in patients with CM, whereas higher levels of BDNF resulted in faster recovery from coma[35]. Using iPSC-derived brain organoids, Harbuzariu et al., discovered elevated levels of BDNF in response to heme injury[12]. Moreover, reduced BDNF expression has been linked to inflammation-induced apoptosis in neurons[36], signifying a protective role of this neurotrophin against neuronal damage.

Metascape-based analysis data, obtained from up- and down-regulated proteins identified in the secretome screening, revealed an enrichment of proteins associated with malaria, MAPK cascade and inflammatory processes. The results confirm that HMZ is capable of activating cellular processes involved in malaria infection, even in the absence of the parasite. It also implies that the molecules elevated in our in-vitro CM model are relevant in malaria pathogenesis. With reference to the KEGG analysis, there was an up-regulation of pathways associated with malaria, MAPK signalling, neurodegeneration, and AD, whereas p53 signalling and apoptosis pathways were down-regulated. The up-regulated pathways support data from previous studies that identified genes related to neurodegenerative and AD pathways in CM patients[5,37,38]. This signifies that CM and neurodegenerative diseases, especially AD, share similar cellular mechanisms with a common denominator being inflammation. In contrast, the down-regulated p53 and apoptotic pathways can be attributed to the significant concentration of BDNF in our assay. Indeed, it has been confirmed that BDNF inhibits pro-apoptotic signalling following brain injury[12]. Saba et al., confirmed that BDNF significantly decreased apoptosis in serum deprived astrocytes by reducing p53 and active Caspase-3 expression[39], hence the down-regulation of these pathways in our experiment.

Subsequent to secretome screening, the mRNA expression levels of pro-inflammatory cytokines associated with severe CM (TNF-α, IL-6, IL-8)[28] but had a reduced/marginal protein expression, were examined in both UM51 and B4 neuronal cultures. Our analysis revealed an upregulation of *TNF-α* and *IL-8* mRNA levels in UM51 and B4 cells respectively. Despite high *IL-6* expression levels in individual samples, there was no significant increase detected in either cell line. The relative lower levels of these pro-inflammatory cytokines could be attributed to the higher levels of BDNF. BDNF has been shown to have a negative correlation with TNF-α, IL-6 and IL-8[40,41], and it could also reverse the elevation of extracellular TNF-α and IL-6, after the exposure of neurons and microglia to lipopolysaccharide[36].

Additionally, we examined the mRNA expression of genes associated with the up-regulated KEGG pathways in both cell lines namely: *BDNF*, *CCL2* (MCP-1), *PECAM1*, *PDGFB* and *VEGF*. With the exception of the angiogenic factors, *PDGFB* and *VEGF*, we saw an increase in mRNA expression of the other molecules. It is noteworthy that PDGFB and VEGF were elevated in the secretome analysis, therefore the non-significant mRNA expression could imply a poor correlation between their mRNA levels and protein synthesis, a phenomenon commonly reported in eukaryotic cells in dynamic transitions such as stress response[42]. Collectively, these experiments provide evidence that CCL2, PECAM1, PDGF and VEGF, which are reported to modify cell junctions, increase endothelial permeability and enhance leukocyte trans-endothelial migration in inflammation[43–46] are key elements to HMZ induced cellular injury in CM. Ultimately, the significant expression of these factors represents inflammation and immune cell extravasation during CM pathogenesis.

A consequence of continuous inflammation is DNA damage. Therefore, in our successive experiments, we measured γH2AX, a reliable marker for DNA double strand breaks[47] in both UM51 and B4 neuronal cultures. Furthermore, we examined a selection of molecules involved in DNA damage and repair checkpoints including ATM, ATR, CHEK1 and CHEK2. Our analyses revealed a significant increase in γH2AX level, representing DNA damage in the UM51 neuronal cultures and only a slight increase in B4. This result is the first to confirm that HMZ induces DNA damage in neurons. The DNA checkpoint investigation revealed significant expression of *ATM*, *ATR*, *CHEK1* and *CHEK2* in both cultures, but more evident in UM51. Next, we measured downstream targets of the damage response pathway, p53 and p38 MAPK. We found the expression of *p53* transcripts to be lower in both cultures, but the expression of p53 protein to be slightly increased in UM51. We also detected lower protein levels of MDM2 (a negative regulator of p53) and FAS, a downstream target of p53. However, except for FAS, the changes were minimal. These results indicate that p53 pathway was not involved in the stress response in our experiments. On the contrary, we observed an up-regulation of total p38 MAPK in both cell lines, though there was no significantly higher expression of phosphorylated p38 MAPK. This is an indication that p38 pathway was activated in response to stress in our study. While phosphorylation is a key activator of p38 MAPK, other modifications such as acetylation and arginine methylation can also modulate its activity, enabling a fine-tuned response to different stimuli[48]. HMZ might therefore elicit phosphorylation-independent activation of p38 MAPK. Previous research has described an activation of the p38 MAPK pathway in response to DNA damage through ATM, when p53 pathway was deficient or compromised[49,50]. Moreover, p38 MAPK was found to mediate the release of lysozyme and upregulate other pro-inflammatory molecules in an experiment involving human adherent monocytes and natural HMZ[51]. Again, p38 MAPK was up-regulated in peripheral

blood mononuclear cells of patients infected with *P. falciparum*[52]. These observations suggest a vital role of p38 MAPK in facilitating cellular response to *P. falciparum* and HMZ. Therefore, future research should investigate the specific impact of HMZ on the p38-MAPK pathway.

As a subsequent goal, we examined the effect of HMZ on HMC3 microglia cells. There was an increase in the expression of known microglial activation markers-triggering receptor expressed on myeloid cells 2 (*TREM2*), ionized calcium binding adaptor molecule 1 (*IBA1*) and *CD45*. Compared to the control group, γH2AX levels in HMZ-treated microglia cells were higher, though the difference was not significant. HMC3 cells showed a significant rise in mRNA expression levels of DNA damage response molecules, including *ATM* and *CHEK2*. However, there were no changes in the expression levels of *ATR* and *CHEK1*. Once more, there was no significant increase in p53 levels in HMZ treated microglia cells. Thus, neurons and microglia cells show a similar response pattern to HMZ stimulation.

A limitation of this study is the lack of complete cellular components characteristic of the brain, which is comprised of neurons, glial cells and vascular units. This would have better captured the complexity of varying responses and interactions between different cell types in response to HMZ exposure in CM pathology. Future experiments using brain organoids could be a suitable approach in this regard. Additionally, including functional assays such as, multi-electrode arrays to measure action potentials, synaptic activity, and network dynamics, and/or calcium imaging to show intracellular signalling and network connectivity could be employed to improve the application of the model.

Conclusion

This study aimed at identifying molecules and pathways that mediate neuronal response to HMZ. Additional to the well-established cytokines identified in CM, we discovered IL-16, which has been implicated in other neurological diseases but not in CM. We also provide evidence for the first time that HMZ induces DNA damage in neurons. In summary, this study has demonstrated that HMZ can potently induce inflammatory responses in a comparable manner to clinical falciparum malaria. In addition, iPSC-derived neuronal cultures may provide a robust model for CM research. Also, given the increasing evidence of a link between neurodegenerative diseases and CM, further studies are required to validate this assertion, specifically with regards to the molecules that drive the pathogenesis and the phenotype of these diseases.

Methods and materials

Cell culture

iPSCs culture and NPC generation

Two healthy male-derived iPSC lines were used in this study. The UM51-hiPSC line was derived from SIX2-positive renal progenitor cells isolated from the urine of a 51-year-old healthy male of African origin (UM51)[15]. The other iPSC line (B4) was generated from healthy human fetal foreskin fibroblasts (HFF1, ATCC, #ATCCSCRC-1041, http://www.atcc.org)[16] (Supplementary Table S1). iPSCs were plated on Matrigel (Corning, New York, NY, USA)-coated culture dishes using mTeSR Plus medium (StemCell Technologies, Vancouver, Canada). Cultures were routinely tested for mycoplasma contamination. Cells were passaged by dissociation into small aggregates with ReLeSR (StemCell Technologies, Vancouver, Canada) every 5–7 days and split in a 1:5 ratio into fresh Matrigel-coated dishes. For neural progenitor cell (NPC) generation, iPSCs were split as single cells using accutase (Life Technologies, Waltham, MA, USA). In brief, at day 0, iPSC-colonies were dissociated with warm (37 °C) accutase, centrifuged at 200 rcf for 5 min, then resuspended in mTESR+with 10µM of ROCK inhibitor. 20,000 cells in 100 µL cell suspension were seeded per well of a 96 u-bottom well plate (Low attachment, U bottom) to form embryoid bodies (EBs). Seeded iPSCs were spinned down at 110 rcf for 3 min and incubated at 37 °C with 5% CO_2 for 24 h. At day 1, half of the medium volume was aspirated and replaced with neural induction medium (NIM) with 10µM of ROCK inhibitor. EBs were culture for 7 days (day 2–8) with NIM supplemented with 10 µM SB431542 and 5 µM Dorsomorphin (10µM of ROCK inhibitor until day 3). Medium was refreshed daily. On day 8, 20–30 EBs were plated per well of a Poly-Ornithine/Laminin (Sigma-Aldrich; Merck KGaA, Darmstadt, Germany) -coated 6-well plate to generate neural rosettes. EBs were cultured in neural differentiation medium (NDM) (Neurobasal A, 1% B27, 1% GlutaMAX, 1% P/S) supplemented with 20 ng/mL EGF and 20 ng/mL FGF2 and incubated at 37 °C with 5% CO_2 in static position. The medium was changed daily. At day 16, neural rosettes were selected using STEMdiff™ Neural Rosette Selection Reagent (StemCell Technologies, Vancouver, Canada) for 30 min–1 h at 37°. Warm accutase was used for 30 min at 37 °C to dissociate the neural rosettes. NPCs were further cultured in Growth-Factor Reduced (GFR) Matrigel (Corning, New York, NY, USA)-coated plates with NDM supplemented with 20 ng/mL EGF and 20 ng/mL FGF2. Accutase was used for splitting the NPCs. In parallel, early passages of NPCs were frozen in Cryostore CS10 (StemCell Technologies) for later usage.

Neuronal differentiation and hemozoin treatment

UM51- and B4 iPSC-derived NPCs were used for the neuronal differentiation. To initiate differentiation, NPCs were dissociated with warm accutase and plated on GFR Matrigel (Corning, New York, NY, USA)-coated plates. 500,000 cells/well in a 6-well plate and 80,000 cells/well in a 24 well plate were seeded to produce neuronal cultures. For cell adhesion, NDM supplemented with 20 ng/mL EGF and 20 ng/mL FGF2 was used for 24 h, which was then changed to NDM supplemented with 20 ng/mL BDNF and 20 ng/mL NT3 for the rest of the differentiation (Day 2–16). Cells were cultured until day 16 and medium was changed every 2–3 days. At day 16, neuronal cultures were exposed to 20 µM HMZ for 48 h.

Hemozoin (InvivoGen #tlrl-hz) was dissolved in PBS (pH 7.4) to obtain a stock concentration of 4.06 mM (5 mg/mL). To obtain a homogenous dispersion of hemozoin, the hemozoin-PBS suspension was sonicated for 5 min. For treatment, 20 µM hemozoin (HMZ) was added to the culture medium and incubated for 48 h.

Cell viability assay

To ascertain the appropriate concentration, we performed resazurin assay/alamar blue assay on B4 iPSC-derived neuronal cultures by exposing those to 0, 5 µM, 10 µM, 20 µM, 50 µM, 100 µM, 200 µM HMZ for 48 h. In brief, day 16 neurons were treated with the mentioned HMZ concentrations continuously for 48 h. 2 h before reaching the analysis time point, resazurin solution was added and incubated at 37 °C with 5% CO_2. After 2 h, 100 µl supernatant was transferred to a 96-well flat bottom plate in triplicate for each condition. Fluorescence was recorded using a plate reader with a 560 nm excitation/ 590 nm emission filter set. For the resazurin solution, a stock of 0.15 mg/mL resazurin in PBS was prepared, which was further diluted 1:10 with PBS before use. 100 µl diluted resazurin solution was added per well. 3 wells containing culture medium and diluted resazurin were prepared for background subtraction and instrument gain adjustment.

Based on Resazurin measurements of neuronal culture treated with varying doses of HMZ, IC50 plots were generated within the R environment employing the packages dr4pl and ggplot2[53,54] (Supplementary Fig. 1). The dr4pl method was parametrized to use a logistic model, the fitted curve was plotted using values from the model. Additionally, the IC50 was calculated via the logistic model in dr4pl.

Immunocytochemistry

Cells were fixed in 4% paraformaldehyde (PFA) (Polysciences, Warrington, FL, USA) for 10 min at room temperature (RT). After washing with 3 times with PBS, cells were directly used for staining. Fixed cells were permeabilized for 10 min using 0.1% Triton X-100 in PBS + Glycine (30 mM Glycine) at RT. After washing once with PBS, unspecific binding sites were blocked for 2 h at RT with 3% BSA in PBS + Glycine. Primary antibodies were diluted in 3% BSA in PBS + Glycine and incubated overnight at 4 °C (Supplementary Table S2). After washing three times with PBS, secondary antibodies diluted in 3% BSA/PBS/Glycine were added for 2 h and incubated at RT. Nuclei were stained with Hoechst 33,258. Stained cells were imaged using a Zeiss fluorescence microscope (LSM 700). Individual channel images were processed and merged with ImageJ software version 1.53c (U. S. National Institutes of Health, Bethesda, Maryland, USA). Cells were counted manually using the "Cell counter" function of ImageJ.

Secretome analysis

Human XL cytokine array

Cytokine arrays were used to analyse the secretome profiles of the UM51 and B4 iPSC-derived neuronal cultures upon HMZ exposure. After 48 h of HMZ treatment, the conditioned medium of the control and HMZ-treated neuronal cultures were stored at -20 °C. Relative expression levels of 105 soluble human proteins and cytokines were determined using the Human XL Cytokine Array Kit from R&D Systems. The cytokine array was performed following the manufacturer's guidelines. In brief, the membranes were blocked for 1 h on a rocking platform using the provided blocking buffer. Samples were prepared by diluting the desired quantity to a final volume of 1.5 mL with array buffer (array buffer 6). The sample mixtures were pipetted onto the blocked membranes and incubated overnight at 4 °C on a rocking platform. Membranes were washed three times with washing buffer for 10 min each at RT. Then, the membranes were incubated with detection antibody cocktail for 1 h at RT and washed three times. Afterwards, Streptavidin-HRP was added onto the membranes, and incubated for 30 min at RT. ECL detection reagent (Cytiva, Freiburg, Germany) was used to visualize bound proteins as spots, which were detected using a Fusion FX instrument (PeqLab, Erlangen, Germany) (Supplementary Fig. 2, Supplementary Fig. 3).

Image analysis of cytokine arrays

Images of the hybridized cytokine assays were scanned and analyzed via the FIJI/ImageJ software[55]. The grid on the cytokine array was detected semi-automatically employing pre-processing via Gaussian blur (size 4) and local maxima finding. The csv file containing the local maxima detected by FIJI/ImageJ was imported into the R programming environment and based on it corners were found and the grid between them interpolated making use of positions found as local maxima. Quantification of the spots at the grid locations was performed by the FIJI Microarray Profile plugin by Bob Dougherty and Wayne Rasband (https://www.optinav.info/MicroArray_Profile.htm, accessed on 21 December 2022), using integrated densities. Cytokine names were taken from proprietary lists of the manufacturer (Proteome Profiler Array from R & D Systems, Human XL Cytokine Array Kit, Catalog Number ARY022B) and assigned to the quantified spots by their grid positions.

Cytokine data analysis

The follow-up-processing of the quantified spots within the R/Bioconductor environment started with the Robust Spline Normalization from the R/Bioconductor package lumi[56,57]. The function heatmap.2 from the gplots package was applied to draw heatmaps using Pearson correlation as similarity measure[58]. Based on this cluster analysis via heatmap.2 genes were split into two clusters associated with up- and down-regulation by HMZ for subsequent analysis. Secretome profiles from B4 neuronal cultures were analyzed using the same computational analyses, demonstrating a similar secretion pattern to that of UM51 neuronal cultures, though at a lower intensity (Supplementary Fig. 3). In the supplementary file 2 conditional formatting indicates cytokines expressed in treatment („meanbgt", detection-p-value < 0.05) and control ("meanbgc", detection-p-value < 0.05) condition in red as well as differentially expressed cytokines by limma-p-value < 0.05 ("limmap") and limma-p-value adjusted for False-Discovery-Rate < 0.25 ("limmapa"). Ratios greater than 1.2 are also marked in red and

ratios less than 0.8333 are marked in green as was used for determination of up- and down-regulated cytokines. On the log-scale are just separated by positive (red) and negative (blue).

Metascape analysis

Comprehensive functional analysis of the clustered gene ontology (GO) biological processes and pathways (KEGG pathways, Reactome Gene Sets, Canonical pathways, and CORUM) of gene-sets based on data derived from the Human XL Cytokine Array was performed using Metascape[59] (http://metascape.org, accessed on 13 October 2023). Lists of up- and downregulated cytokines were treated as gene-sets for analytical purposes.

Pathway analysis

Cytokines were subjected to cluster analysis via the heatmap.2 function from the R package gplots using Pearson correlation as similarity measure and the default setting of hclust as hierarchical clustering method[58]. Cytokines from the two resulting clusters of HMZ-induced up- and down-regulation were analyzed for over-represented KEGG pathways in the follow-up analysis[60]. KEGG pathways were downloaded from the KEGG website in February 2023. The R-builtin hypergeometric test was employed to determine the p-value indicating the significance of the over-represented pathways. Malaria and p53 signalling (KEGG) pathway, shown in the Supplementary Fig. 4 were taken respectively from https://www.genome.jp/kegg-bin/show_pathway? hsa05144 and https://www.genome.jp/pathway/hsa04115.

Reverse transcriptase PCR (RT-PCR)

Control and HMZ-treated cells were lysed for 15 min in Trizol. RNA was isolated using the Direct-zol™ RNA Isolation Kit (Zymo Research, Freiburg, Germany) according to the user's manual, including the DNA digestion step. 500 ng of RNA was reverse transcribed using the TaqMan Reverse Transcription Kit (Applied Biosystems, Waltham, MA, USA). The primer sequences are shown in (Supplementary Table S3). Real-time PCRs were performed in technical and independent experiment triplicates ($n=3$) with Power Sybr Green Master Mix (Life Technologies, Darmstadt, Germany) on a VIIA7 (Life Technologies, Darmstadt, Germany) machine. Mean values were normalized to the ribosomal protein lateral stalk subunit P0 (RPLP0) and fold-change was calculated using the indicated controls. Changes in gene expression were presented in log2-scale. All values are depicted as mean with a 95% confidence interval (CI). Each singular value (Ctrl and HMZ) was compared to the mean of all corresponding control samples. The resulting values were used for statistical analysis. Statistical analysis was performed using Student's unpaired two-sample t-tests. For ease of reading, only values of the treated condition were presented.

Western blotting

Total protein from UM51- and B4-derived neuronal cultures was isolated using RIPA buffer (Sigma-Aldrich Chemicals, Taufkirchen, Germany), supplemented with protease and phosphatase inhibitors (Roche, Mannheim, Germany). Afterwards, Pierce BCA Protein Assay Kit (Thermo Fisher, Waltham, MA, USA) was used to determine protein concentration of the samples. 20 µg of the heat-denatured protein lysate of each sample was loaded on a 4–12% SDS-PAGE and then transferred via wet blotting onto a 0.45 µm nitro-cellulose membrane (GE Healthcare, Solingen, Germany). After 1 h of blocking with 5% milk in TBST, the membranes were stained with anti-γH2AX, anti-p53, anti-MDM2, anti-P38MAPK, anti-phospho-P38MAPK, anti-FAS, anti-Caspase 3, and anti-cleaved caspase 3 antibodies in the appropriate buffer (Supplementary Table S2). Incubation with primary antibodies was performed overnight at 4 °C. After washing the membranes three times with TBST, secondary antibody incubation was performed for 2 h at RT followed by washing with TBST (Supplementary Table S2). Anti-β-Actin and anti-GAPDH (glyceralde-hyde-3-phosphate dehydrogenase) were used as housekeeping proteins to normalize protein expression. ECL Western Blotting Detection Reagents (Cytiva, Freiburg, Germany) were used to visualize the stained protein bands and then detected in a Fusion FX instrument (PeqLab, Erlangen, Germany). Band intensity quantification and analysis was performed with Fusion Capt Advance software FX7 16.08 (PeqLab, Erlangen, Germany).

Statistical analysis

All obtained results were represented as mean ± standard deviation. Statistical analysis (Student's unpaired two-samples t-test) was performed utilizing GraphPad Prism v.8.0.2 (GraphPad Software, Boston, USA). A p-value of <0.05 was considered as statistically significant during analysis.

Data availability

Datasets resulting from the cytokine assay analyses in this study are available in the supplementary materials (Supplementary File 1, 2) data of this work.

Received: 13 March 2024; Accepted: 11 October 2024
Published online: 23 October 2024

References

1. World Health Organization. World malaria report 2023. (2023).
2. Arisco, N. J., Peterka, C. & Castro, M. C. Imported malaria definition and minimum data for surveillance. *Sci. Rep.* **12**, 17982. https://doi.org/10.1038/s41598-022-22590-6 (2022).
3. Gilson, R. C. et al. Growth of Plasmodium Falciparum in response to a rotating magnetic field. *Malar. J.* **17**, 190. https://doi.org/10.1186/s12936-018-2333-2 (2018).

4. Luzolo, A. L. & Ngoyi, D. M. Cerebral malaria. *Brain Res. Bull.* **145**, 53–58. https://doi.org/10.1016/j.brainresbull.2019.01.010 (2019).
5. Karikari, A. A., Wruck, W. & Adjaye, J. Transcriptome-based analysis of blood samples reveals elevation of DNA damage response, neutrophil degranulation, cancer and neurodegenerative pathways in Plasmodium Falciparum patients. *Malar. J.* **20**, 383. https://doi.org/10.1186/s12936-021-03918-5 (2021).
6. Polimeni, M. & Prato, M. Host matrix metalloproteinases in cerebral malaria: new kids on the block against blood-brain barrier integrity? *Fluids Barriers CNS* **11**, 1–1. https://doi.org/10.1186/2045-8118-11-1 (2014).
7. Jiménez-Díaz, M. B., Möhrle, J. J., Angulo-Barturen, I. & Demarta-Gatsi, C. Using Cryopreserved Plasmodium Falciparum sporozoites in a Humanized Mouse Model to study early malaria infection processes and test prophylactic treatments. *Microorganisms* **11**, 2209 (2023).
8. Pranty, A. I., Wruck, W. & Adjaye, J. Free bilirubin induces neuro-inflammation in an induced pluripotent stem cell-derived cortical organoid model of crigler-najjar syndrome. *Cells* 12 (2023). https://doi.org/10.3390/cells12182277
9. Harbuzariu, A. et al. Neuregulin-1/ErbB4 signaling modulates Plasmodium Falciparum HRP2-induced damage to brain cortical organoids. *iScience* **25**, 104407. https://doi.org/10.1016/j.isci.2022.104407 (2022).
10. Schiess, N. et al. Pathophysiology and neurologic sequelae of cerebral malaria. *Malar. J.* **19**, 266. https://doi.org/10.1186/s12936-020-03336-z (2020).
11. Idro, R., Marsh, K., John, C. C. & Newton, C. R. Cerebral malaria: mechanisms of brain injury and strategies for improved neurocognitive outcome. *Pediatr. Res.* **68**, 267–274. https://doi.org/10.1203/PDR.0b013e3181eee738 (2010).
12. Harbuzariu, A. et al. Modelling heme-mediated brain injury associated with cerebral malaria in human brain cortical organoids. *Sci. Rep.* **9**, 19162. https://doi.org/10.1038/s41598-019-55631-8 (2019).
13. Martins, S. et al. IPSC-derived neuronal cultures carrying the Alzheimer's disease associated TREM2 R47H variant enables the construction of an Aβ-Induced gene regulatory network. *Int. J. Mol. Sci.* **21**, 4516. https://doi.org/10.3390/ijms21124516 (2020).
14. Nevin, R. L. & Croft, A. M. Psychiatric effects of malaria and anti-malarial drugs: historical and modern perspectives. *Malar. J.* **15**, 332. https://doi.org/10.1186/s12936-016-1391-6 (2016).
15. Bohndorf, M. et al. Derivation and characterization of integration-free iPSC line ISRM-UM51 derived from SIX2-positive renal cells isolated from urine of an African male expressing the CYP2D6 *4/*17 variant which confers intermediate drug metabolizing activity. *Stem Cell. Res.* **25**, 18–21. https://doi.org/10.1016/j.scr.2017.10.004 (2017).
16. Wang, Y. & Adjaye, J. A cyclic AMP analog, 8-Br-cAMP, enhances the induction of pluripotency in human fibroblast cells. *Stem cell. Reviews Rep.* **7**, 331–341. https://doi.org/10.1007/s12015-010-9209-3 (2011).
17. Nociti, V. & Romozzi, M. The role of BDNF in multiple sclerosis neuroinflammation. *Int. J. Mol. Sci.* **24**https://doi.org/10.3390/ijms24098447 (2023).
18. Kanehisa, M., Furumichi, M., Sato, Y. & Kawashima, M. Ishiguro-Watanabe, M. KEGG for taxonomy-based analysis of pathways and genomes. *Nucleic Acids Res.* **51**, D587–D592 (2023).
19. Kanehisa, M. & Goto, S. KEGG: kyoto encyclopedia of genes and genomes. *Nucleic Acids Res.* **28**, 27–30 (2000).
20. Kanehisa, M. Toward understanding the origin and evolution of cellular organisms. *Protein Sci.* **28**, 1947–1951 (2019).
21. Frita, R., Carapau, D., Mota, M. M. & Hänscheid, T. *In Vivo Hemozoin Kinetics after Clearance of < i > Plasmodium berghei Infection in Mice. Malaria Research and Treatment 373086.* https://doi.org/10.1155/2012/373086*(2012).*
22. Eugenin, E. A., Martiney, J. A. & Berman, J. W. The malaria toxin hemozoin induces apoptosis in human neurons and astrocytes: potential role in the pathogenesis of cerebral malaria. *Brain Res.* **1720**, 146317–146317. https://doi.org/10.1016/j.brainres.2019.146317 (2019).
23. Pham, T. T., Lamb, T. J., Deroost, K. & Opdenakker, G. Van Den Steen, P. E. Hemozoin in Malarial complications: more questions than answers. *Trends Parasitol.* **37**, 226–239. https://doi.org/10.1016/j.pt.2020.09.016 (2021).
24. Greiner, J. et al. Correlation of hemorrhage, axonal damage, and blood-tissue barrier disruption in brain and retina of Malawian children with fatal cerebral malaria. *Front. Cell. Infect. Microbiol.* **5.** https://doi.org/10.3389/fcimb.2015.00018 (2015).
25. Newton, C. R. & Krishna, S. Severe falciparum malaria in children: current understanding of pathophysiology and supportive treatment. *Pharmacol. Ther.* **79**, 1–53. https://doi.org/10.1016/s0163-7258(98)00008-4 (1998).
26. Brown, H. et al. Cytokine expression in the brain in human cerebral malaria. *J. Infect. Dis.* **180**, 1742–1746. https://doi.org/10.1086/315078 (1999).
27. Akide Ndunge, O. B., Kilian, N. & Salman, M. M. Cerebral malaria and neuronal implications of Plasmodium Falciparum infection: from mechanisms to Advanced models. *Adv. Sci.* **9**, 2202944. https://doi.org/10.1002/advs.202202944 (2022).
28. Mandala, W. L. et al. Cytokine profiles in Malawian Children presenting with uncomplicated malaria, severe malarial Anemia, and cerebral malaria. *Clin. Vaccine Immunol.* **24**, e00533–e00516. https://doi.org/10.1128/CVI.00533-16 (2017).
29. Mahittikorn, A. et al. Increased interferon-γ levels and risk of severe malaria: a meta-analysis. *Sci. Rep.* **12**, 18917. https://doi.org/10.1038/s41598-022-21965-z (2022).
30. Pawlowski, T. et al. Depression and neuroticism in patients with chronic hepatitis C: correlation with peripheral blood mononuclear cells activation. *J. Clin. Virol.* **60**, 105–111. https://doi.org/10.1016/j.jcv.2014.03.004 (2014).
31. Cheng, X. et al. Correlation between elevated serum interleukin-1β, interleukin-16 levels and psychiatric symptoms in patients with schizophrenia at different stages. *BMC Psychiatr.* **23**, 396. https://doi.org/10.1186/s12888-023-04896-5 (2023).
32. Di Rosa, M. et al. Chitotriosidase and inflammatory mediator levels in Alzheimer's disease and cerebrovascular dementia. *Eur. J. Neurosci.* **23**, 2648–2656. https://doi.org/10.1111/j.1460-9568.2006.04780.x (2006).
33. Lobaloba Ingoba, L. et al. Diagnosis of chikungunya virus in febrile patients from a malaria holoendemic area. *Int. J. Infect. Dis.* **109**, 247–252. https://doi.org/10.1016/j.ijid.2021.06.043 (2021).
34. Waknine-Grinberg, J. H., McQuillan, J. A., Hunt, N., Ginsburg, H. & Golenser, J. Modulation of cerebral malaria by fasudil and other immune-modifying compounds. *Exp. Parasitol.* **125**, 141–146. https://doi.org/10.1016/j.exppara.2010.01.005 (2010).
35. McDonald, C. R. et al. Brain-derived neurotrophic factor is associated with disease severity and clinical outcome in ugandan children admitted to hospital with severe malaria. *Pediatr. Infect. Dis. J.* **36**, 146–150. https://doi.org/10.1097/INF.0000000000001382 (2017).
36. Calabrese, F. et al. Brain-derived neurotrophic factor: a bridge between inflammation and neuroplasticity. *Front. Cell. Neurosci.* **8**, 430. https://doi.org/10.3389/fncel.2014.00430 (2014).
37. Cabantous, S. et al. Understanding human cerebral malaria through a blood transcriptomic signature: Evidences for erythrocyte alteration, immune/Inflammatory dysregulation, and brain dysfunction. *Mediat. Inflamm.***2020** (3280689). https://doi.org/10.1155/2020/3280689 (2020).
38. Thiam, A. et al. Gene expression profiling in blood from cerebral malaria patients and mild malaria patients living in Senegal. *BMC Med. Genom.* **12**, 148. https://doi.org/10.1186/s12920-019-0599-z (2019).
39. Saba, J. et al. Astrocyte truncated tropomyosin receptor kinase B mediates brain-derived neurotrophic factor anti-apoptotic effect leading to neuroprotection. *J. Neurochem.* **146**, 686–702. https://doi.org/10.1111/jnc.14476 (2018).
40. Shkundin, A. & Halaris, A. IL-8 (CXCL8) correlations with psychoneuroimmunological processes and neuropsychiatric conditions. *J. Personalized Med.* **14**, 488 (2024).
41. Xia, F., Zeng, Q. & Chen, J. Circulating brain-derived neurotrophic factor dysregulation and its linkage with lipid level, stenosis degree, and inflammatory cytokines in coronary heart disease. *J. Clin. Lab. Anal.* **36**, e24546. https://doi.org/10.1002/jcla.24546 (2022).

42. Liu, Y., Beyer, A. & Aebersold, R. On the dependency of cellular protein levels on mRNA abundance. *Cell* **165**, 535–550. https://doi.org/10.1016/j.cell.2016.03.014 (2016).
43. Bazzari, A. H. & Bazzari, F. H. BDNF therapeutic mechanisms in neuropsychiatric disorders. *Int. J. Mol. Sci.* **23**, 8417 (2022).
44. Roberts, T. K. et al. CCL2 disrupts the adherens junction: implications for neuroinflammation. *Lab. Invest.* **92**, 1213–1233. https://doi.org/10.1038/labinvest.2012.80 (2012).
45. Yao, H., Duan, M. & Buch, S. Cocaine-mediated induction of platelet-derived growth factor: implication for increased vascular permeability. *Blood* **117**, 2538–2547. https://doi.org/10.1182/blood-2010-10-313593 (2011).
46. Zhang, Z. G. et al. VEGF enhances angiogenesis and promotes blood-brain barrier leakage in the ischemic brain. *J. Clin. Invest.* **106**, 829–838. https://doi.org/10.1172/JCI9369 (2000).
47. Mah, L. J., El-Osta, A. & Karagiannis, T. C. γH2AX: a sensitive molecular marker of DNA damage and repair. *Leukemia* **24**, 679–686. https://doi.org/10.1038/leu.2010.6 (2010).
48. Canovas, B. & Nebreda, A. R. Diversity and versatility of p38 kinase signalling in health and disease. *Nat. Rev. Mol. Cell. Biol.* **22**, 346–366. https://doi.org/10.1038/s41580-020-00322-w (2021).
49. Roy, S. et al. The role of p38 MAPK pathway in p53 compromised state and telomere mediated DNA damage response. *Mutat. Res. Genet. Toxicol. Environ. Mutagen.* **836**, 89–97. https://doi.org/10.1016/j.mrgentox.2018.05.018 (2018).
50. Reinhardt, H. C., Aslanian, A. S., Lees, J. A. & Yaffe, M. B. p53-deficient cells rely on ATM- and ATR-mediated checkpoint signaling through the p38MAPK/MK2 pathway for survival after DNA damage. *Cancer Cell.* **11**, 175–189. https://doi.org/10.1016/j.ccr.2006.11.024 (2007).
51. Polimeni, M. et al. Haemozoin induces early cytokine-mediated Lysozyme Release from Human monocytes through p38 MAPK- and NF-kappaB- dependent mechanisms. *PLoS One* **7**, e39497. https://doi.org/10.1371/journal.pone.0039497 (2012).
52. Hu, W. C. Human immune responses to Plasmodium falciparum infection: molecular evidence for a suboptimal THαβ and TH17 bias over ideal and effective traditional TH1 immune response. *Malar. J.* **12**, 392. https://doi.org/10.1186/1475-2875-12-392 (2013).
53. Hyowon An, J. T. L., Aubrey, G., Bailey,James, S. & Marron,Dirk, P. Dittmer Dr4pl: a stable convergence algorithm for the 4 parameter logistic model. *R J.* **11/2**, 171. https://doi.org/10.32614/RJ-2019-003 (2019).
54. Wickham, H. *Ggplot2: Elegant Graphics for data Analysis*212 (Springer, 2009).
55. Schneider, C. A., Rasband, W. S. & Eliceiri, K. W. NIH Image to ImageJ: 25 years of image analysis. *Nat. Methods* **9**, 671–675. https://doi.org/10.1038/nmeth.2089 (2012).
56. Gentleman, R. C. et al. Bioconductor: open software development for computational biology and bioinformatics. *Genome Biol.* **5**, R80. https://doi.org/10.1186/gb-2004-5-10-r80 (2004).
57. Du, P., Kibbe, W. A. & Lin, S. M. Lumi: a pipeline for processing Illumina microarray. *Bioinformatics* **24**, 1547–1548. https://doi.org/10.1093/bioinformatics/btn224 (2008).
58. Warnes, G. R. et al. *Gplots: Various R Programming Tools for Plotting Data*. http://CRAN.R-project.org/package=gplots (2015).
59. Zhou, Y. et al. Metascape provides a biologist-oriented resource for the analysis of systems-level datasets. *Nat. Commun.* **10**, 1523. https://doi.org/10.1038/s41467-019-09234-6 (2019).
60. Kanehisa, M., Furumichi, M., Tanabe, M., Sato, Y. & Morishima, K. KEGG: new perspectives on genomes, pathways, diseases and drugs. *Nucleic Acids Res.* **45**, D353–D361. https://doi.org/10.1093/nar/gkw1092 (2017).

Acknowledgements
The authors are grateful to Kanehisa Laboratories for the permission to use their figures for Malaria and p53 signalling pathways for the supplementary figures. The figures were taken from https://www.genome.jp/kegg/.

Author contributions
A.I.P. and L.P.S. designed and performed the experiments, processed and analyzed the data, and wrote and edited the manuscript. W.W. performed the bioinformatic analysis and data curation, helped with the figures, wrote the bioinformatic section in the Methods and Materials, and edited the manuscript. A.A.K. conceptualized the work, wrote and edited the manuscript. J.A. conceptualized and designed the work, edited the manuscript, acquired funding, and supervised the study. All authors have read and agreed to the submitted version of the manuscript.

Funding
Open Access funding enabled and organized by Projekt DEAL. J.A. acknowledges the medical faculty of Heinrich Heine University for financial support.

Declarations

Competing interests
The authors declare no competing interests.

Institutional Review Board Statement
The study and all the experimental protocols were conducted according to the guidelines set by the ethics committee of the medical faculty of Heinrich-Heine University, Germany (protocol code: 5704 and 5013).

Additional information
Supplementary Information The online version contains supplementary material available at https://doi.org/10.1038/s41598-024-76259-3.

Correspondence and requests for materials should be addressed to J.A.

Reprints and permissions information is available at www.nature.com/reprints.

Publisher's note Springer Nature remains neutral with regard to jurisdictional claims in published maps and institutional affiliations.

Supplementary Fig. 1:

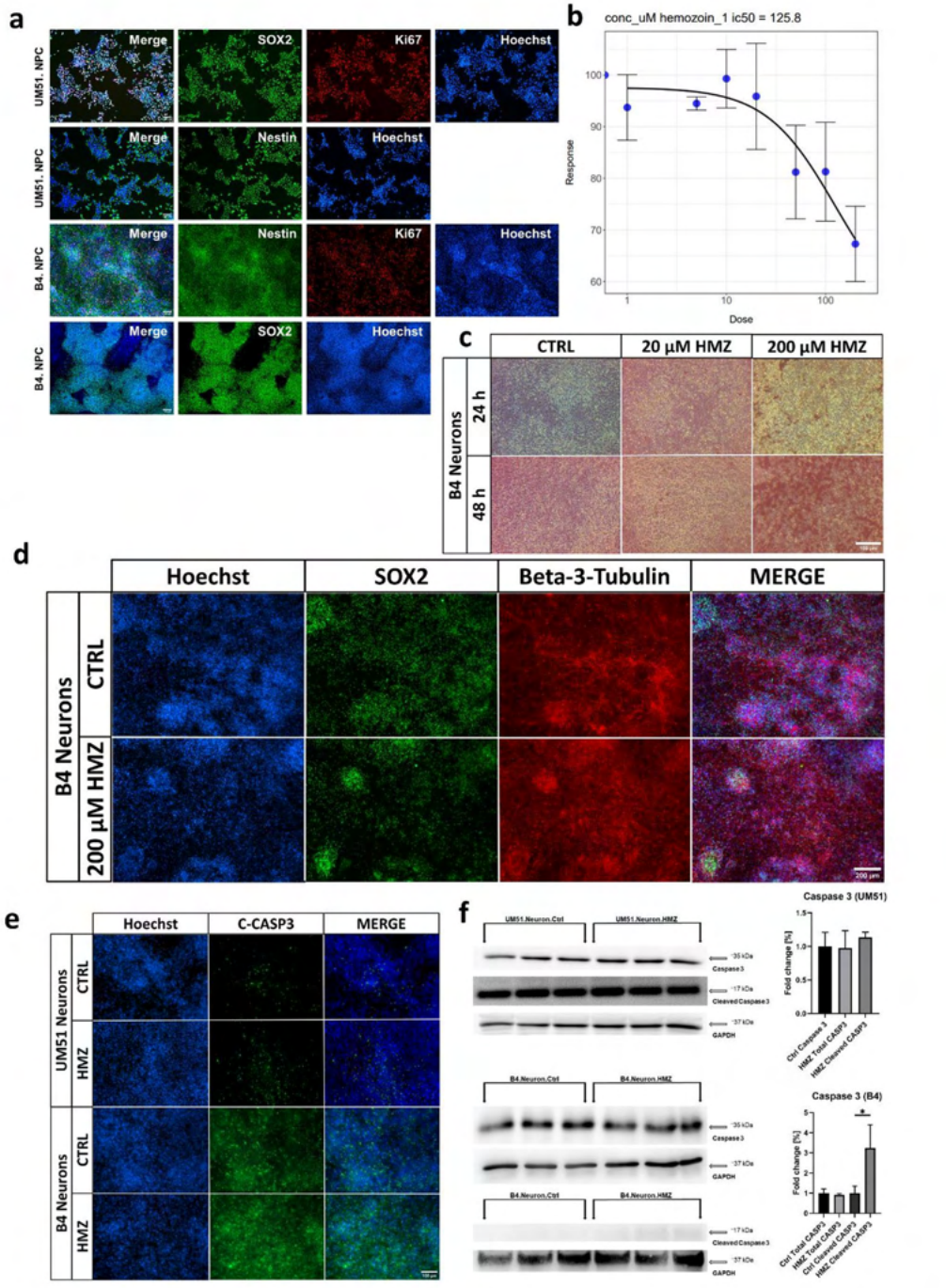

Supplementary Figure 1. Preliminary and optimal-dose experiments for HMZ treatments (a) Representative ICC images of Nestin-, SOX2- and KI67-positive cells in cultured neural progenitor cells. **(b)** Dose-response curve of B4-derived neuronal cultures treated with 0, 1, 5, 10, 20, 50, 100 and 200

µM HMZ. **(c)** Representative brightfield images of control, 20 µM and 200 µM HMZ-treated B4 iPSC-derived neuronal cultures at 24h and 48h of exposure. Scale bar 100 µm. **(d)** Representative ICC images of SOX2- and β3-Tubulin-positive cells in B4-derived neuronal networks after 48h of 200 µM HMZ exposure in comparison to control. Scale bar 200 µm. **(e)** Representative ICC images of Cleaved Caspase 3-positive cells in UM51- and B4-derived neuronal cultures after 48h exposure to 20 µM HMZ in comparison to control. Scale bar 100 µm. **(f)** WB analyses and quantification of WB analyses for total Caspase 3 and Cleaved Caspase 3 in in UM51- and B4-derived neuronal cultures after 48h HMZ exposure in comparison to control. n=3 for each condition, blots depict mean and error bars depict SD of all experiments. Asterisk (*) depicts significance, which is indicated by *p<0.05.

Supplementary Fig. 2:

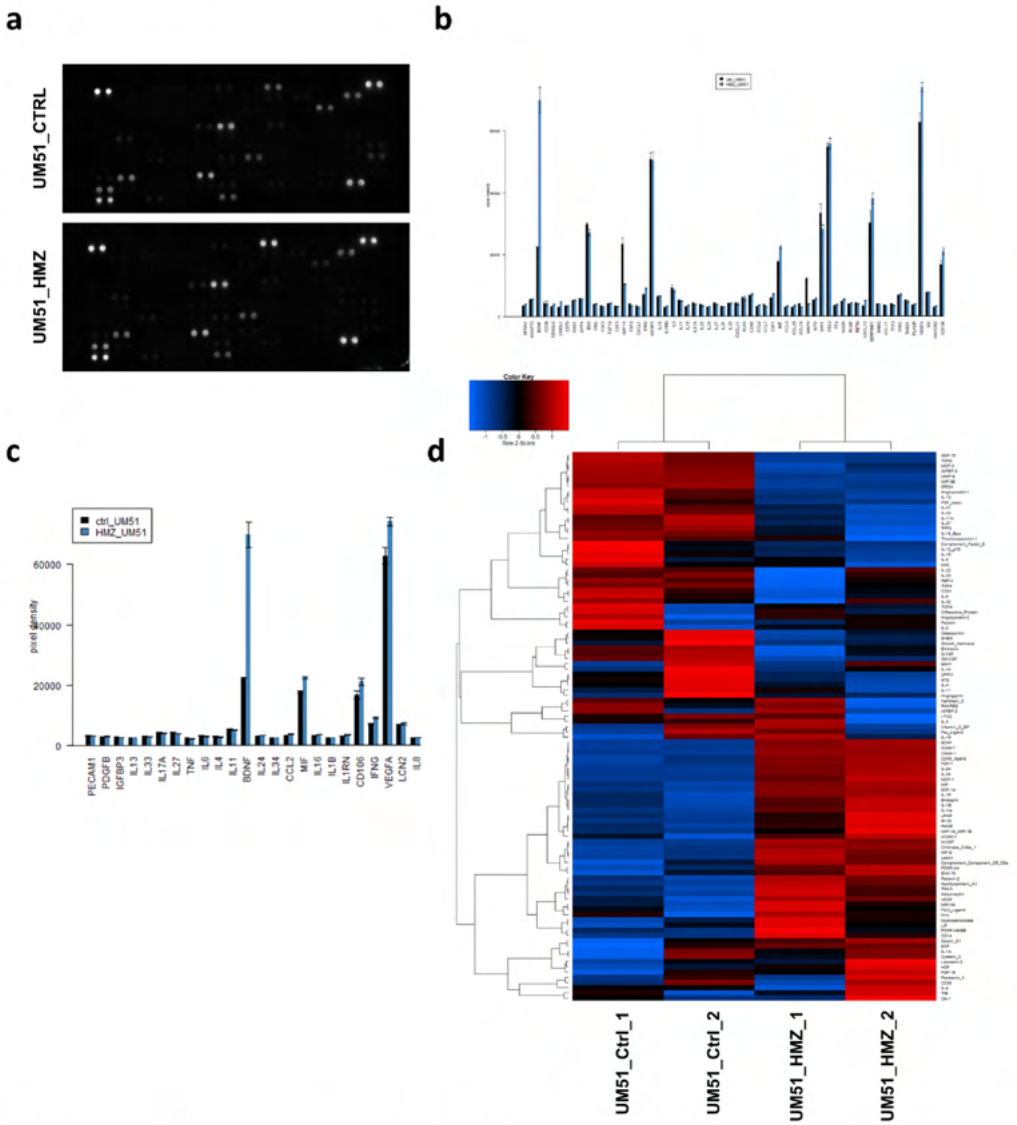

Supplementary Figure 2. UM51 neuronal culture cytokine array. (a) Cytokine array blots utilized for detecting altered secretomes in UM51 neuronal cultures after 48h 20 µM HMZ exposure in comparison to control. **(b)** Multibar plot showing all chemo- and cytokines with pixel density values over background

pixel density. **(c)** Multibar plot for selected chemo- and cytokines showcased as heatmap in Figure 2a. **(d)** Heatmap using Pearson correlation as similarity measure depicting all examined chemo- and cytokines. Error bars denote the standard error of the mean (b,c).

Supplementary Fig. 3:

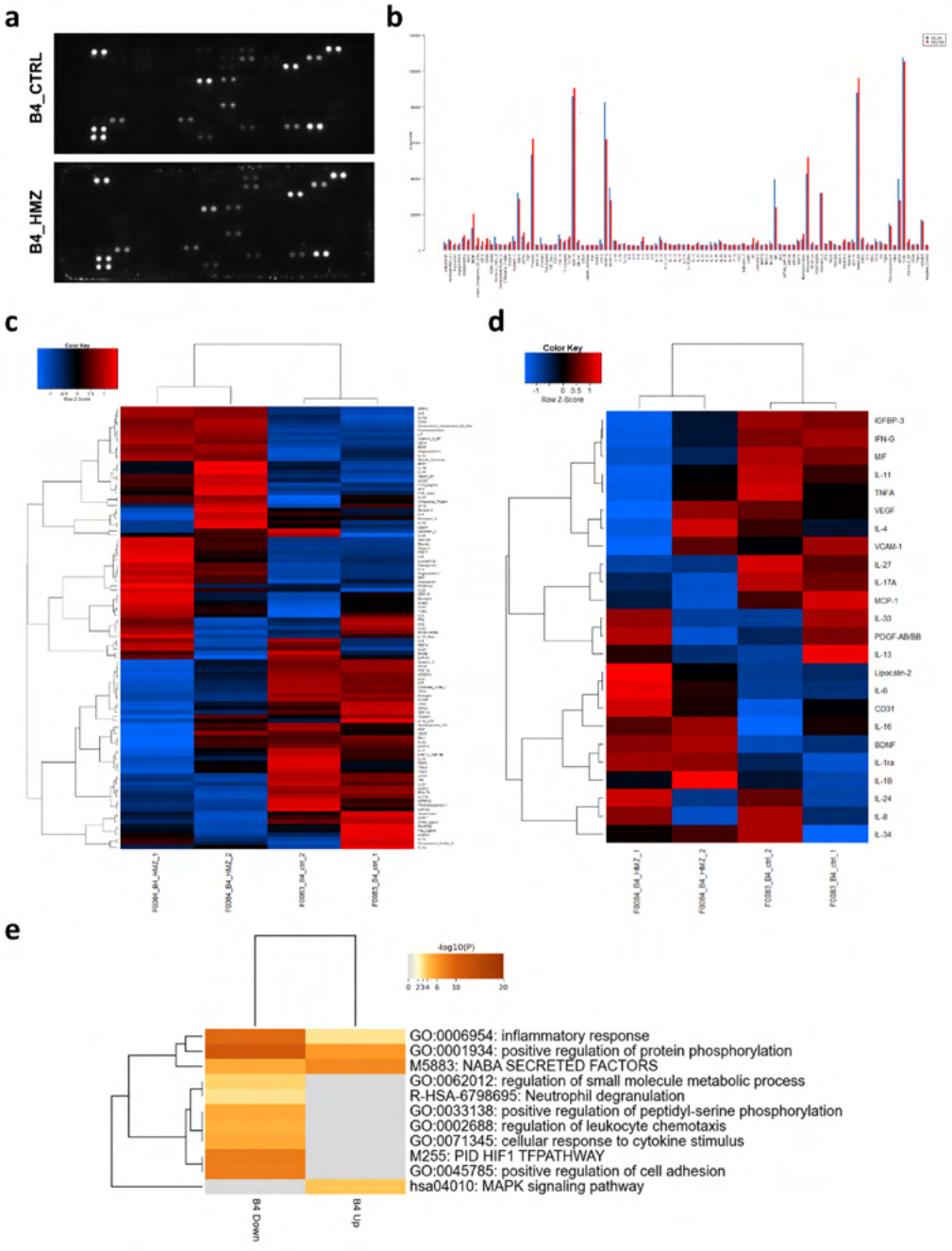

Supplementary Figure 3. Cytokine array of B4 neuronal cultures. (a) Cytokine array blots utilized for detecting altered secretomes in B4 neuronal cultures after 48h 20 µM HMZ exposure in comparison to control. **(b)** Multibar plot showing all chemo- and cytokines with pixel density values above background pixel density. **(c)** Pearson´s heatmap depicting all examined chemo- and cytokines. **(d)** Pearson´s heatmap depicting selected chemo- and cytokines regulated in B4 neuronal cultures after 48 h HMZ exposure in comparison to control. **(e)** Metascape-generated heatmap comparing the sets of up- and downregulated chemo- and cytokines derived from B4 neuronal cultures after 48 h HMZ exposure, revealing a secretome signature involved in i.a. inflammatory response and MAPK signalling pathway. Error bars denote the standard error of the mean (b).

Supplementary Fig. 4:

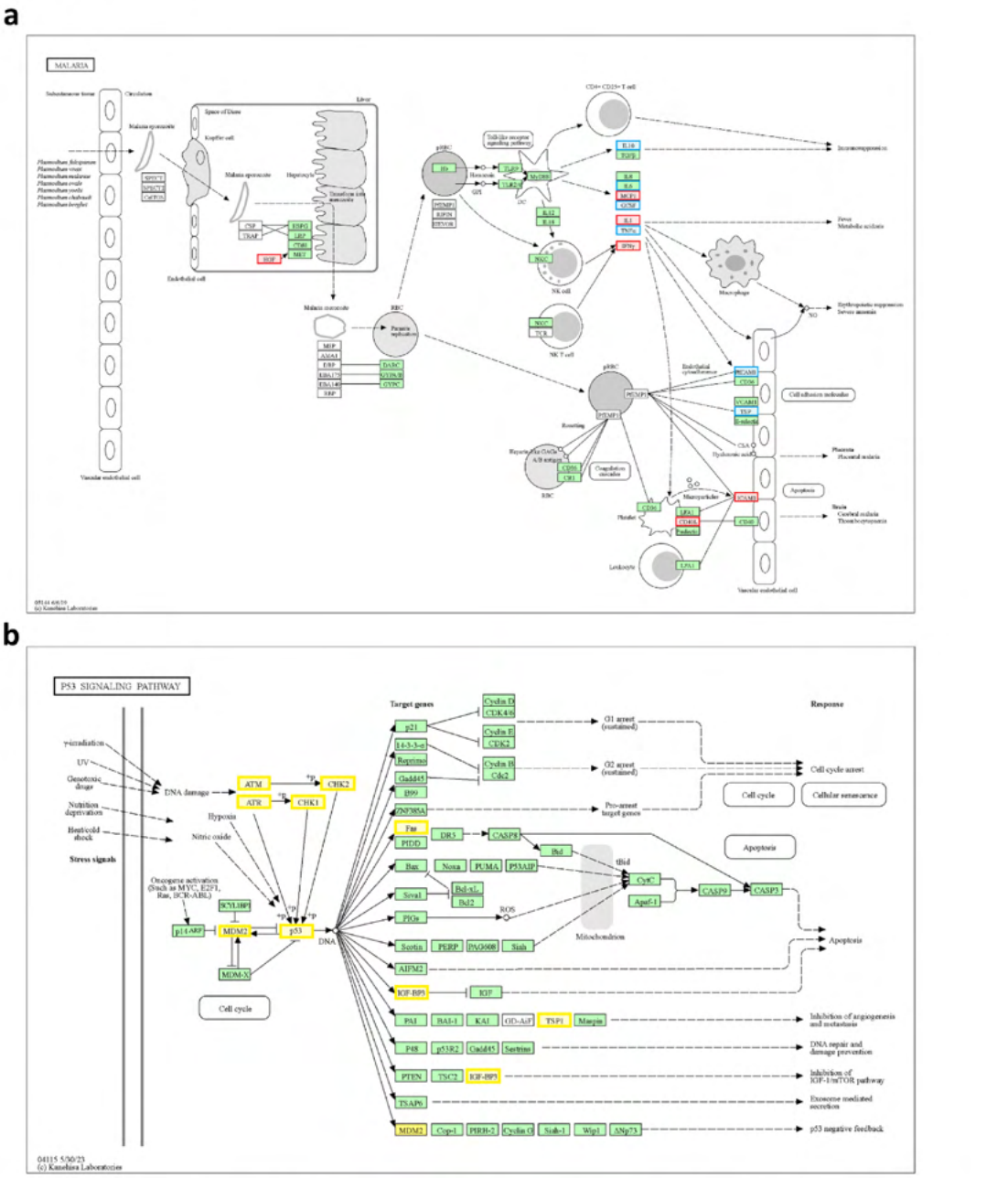

Supplementary Figure 4. Analysis of the KEGG pathways - Malaria and p53 signalling pathways in iPSC-derived neuronal cultures. (a) Schematic of the KEGG pathway Malaria. Cytokines upregulated in the secretome of UM51 neuronal cultures are marked in red, downregulated in blue. **(b)** Schematic of the KEGG pathway p53 signalling pathway. Regulated genes are highlighted in yellow, and non-regulated in grey.

Supplementary Fig. 5:

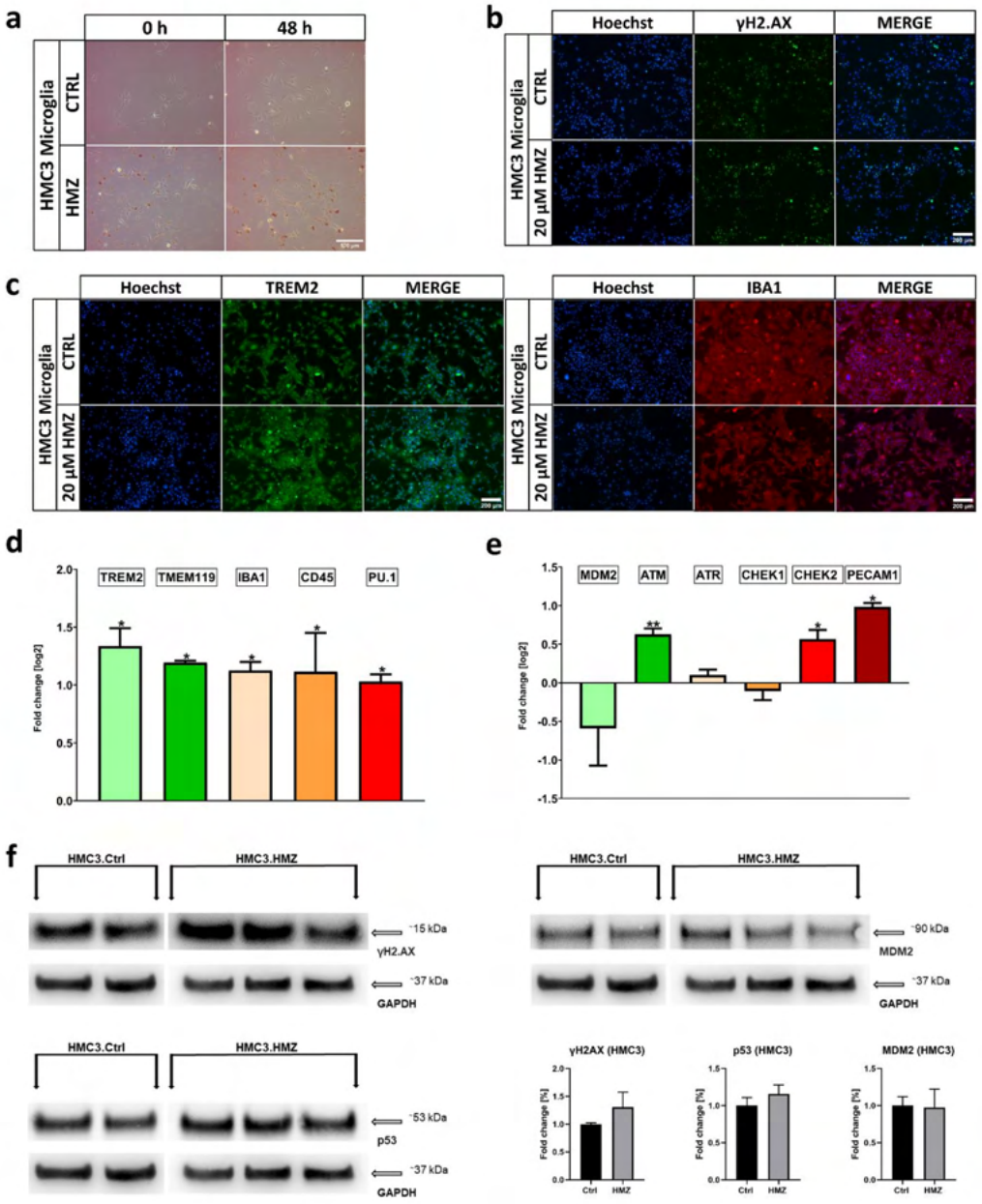

Supplementary Figure 5. HMC3 cells show signs of microglial activation and activation of DNA damage response. (a) Representative bright field images of control and 20 µM HMZ-treated HMC3 cells at 0h and 48h of exposure. Scale bar 100 µm. **(b,c)** Representative ICC images of γH2AX-, TREM2- and IBA1-positive HMC3 cells after 48h HMZ exposure in comparison to control. Scale bar 200 µm. **(d)** Relative mRNA expression analysis of *TREM2, TMEM119, IBA1, CD45* and *PU.1* in HMC3 cells after 48h HMZ exposure in comparison to control. **(e)** Relative mRNA expression analysis of *MDM2, ATM, ATR, CHEK1, CHEK2* and *PECAM1* in HMC3 cells after 48h HMZ exposure in comparison to control. **(f)** WB analyses and quantification of WB analyses for γH2AX, MDM2 and p53 after 48h HMZ exposure in comparison to control. Values were normalized to GAPDH and subsequently to control

samples. Ctrl n=2; HMZ n=3. (d,e) n=3; blots depict mean and error bars depict SD of all experiments. Asterisk (*) depicts significance, which is indicated by *p<0.05; **p<0.01.

Supplementary Table 1 Information of the used iPS-cell lines.

	Healthy Line (UM51)	Healthy Line (B4)
Sex	Male	Male
Age	51	Neonate
Ethnicity	African	N/A
Alternative name	ISRM-UM51	N/A
Cell source	Renal cells isolated from urine	Skin, fibroblast, foreskin
Method of reprogramming	Episomal-based plasmid	Retroviral transduction
Gene/locus	N/A	N/A
Associated Disease	None	None
Ethical Approval	Ethical committee of the medical faculty of Heinrich Heine University, Düsseldorf, Germany Approval number: 5704	Ethical committee of the medical faculty of Heinrich Heine University, Düsseldorf, Germany Approval number: 5013
Reference		
PMID	29035842	21120637

Supplementary Table 2 List of utilized antibodies.

Primary antibody	Application	Dilution	Company	Order No.
Anti-mouse ß3 tubulin (TUJ1)	IF	1:250	Cell Signaling	4466S
Anti-mouse TAU	IF	1:500	Invitrogen	MN1000
Anti-rabbit MAP2	IF	1:250	SySy	188002
Anti-mouse γH2A.X	IF, WB	1:200, 1:50	CST	9718S
Anti-mouse P53	WB	1:1000	CST	9283S
Anti-rabbit MDM2	WB	1:1000	CST	86934S
Anti-rabbit total P38MAPK	WB	1:1000	CST	9212S
Anti-rabbit Phospho-P38MAPK	WB	1:1000	CST	4511S
Anti-rabbit FAS (C18C12)	WB	1:1000	CST	4233T
Anti-mouse ß-Actin	WB	1:5000	CST	3700S
Anti-mouse GAPDH	WB	1:1000	Invitrogen	AM4300
Anti-rabbit SOX-2	IF	1:100	Sigma Aldrich	3579S
Anti-rabbit Nestin	IF	1:1000	Cell Signaling	N5413
Anti-mouse KI67	IF	1:200	CST	9449S
Anti-rabbit cleaved caspase 3	IF, WB	1:800, 1:1000	CST	9664S
Anti-rabbit total Caspase 3	WB	1:1000	CST	9662S
Anti-goat IBA1	IF	1:200	Biorbyt	orb19517
Anti-rabbit TREM2	IF	1:500	AvivaSysBio	OAAB02883

Secondary antibody	Application	Dilution	Company	Order No.
Alexa 488 goat anti rabbit IgG (H+L)	IF	1:600	ThermoFisher	A11008
Alexa 555 goat anti mouse IgG (H+L)	IF	1:600	ThermoFisher	A21424
Alexa 488 donkey anti goat IgG (H+L)	IF	1:600	ThermoFisher	A11055
Anti-rabbit IgG, HRP-linked Antibody	WB	1:1000	CST	7074S
ECL peroxidase labelled anti mouse antibody	WB	1:5000	GE	NA931V

Supplementary Table 3 List of used qRT-PCR primers.

Primer	Forward 5'→3'	Reverse 5'→3'
IL-6	GGTACATCCTCGACGGCATCT	GTGCCTCTT TGCTGCTTTCAC
IL-8	GTGCAGTTTTGCCAAGGAGT	ACTTCTCCACAACCCTCTGC
TNF- α	AGAACTCACTGGGGCCTACA	AGGAAGGCCTAAGGTCCACT
PECAM1	GAACCATGGAGGAGAGTGGC	AGAAACCCGCCCTGCATC
VEGFA	AAGGAGGAGGGCAGAATCATC	TGATGTTGGACTCCTCAGTG
BDNF	AACATGTCCATGAGGGTCCG	CAGTCTTTTTGTCTGCCGCC
CCL2	TCCCAAAGAAGCTGTGATCTTCAA	AGGGTGTCTGGGGAAAGCTA
PDGFB	AAGGCCATCAACATCACCGT	GGGTGCGGTTGTCTTTGAAC
P53	CAGGGCAGCTACGGTTTCC	CAGTTGGCAAAACATCTTGTTGAG
MDM2	AAACTGGGGAGTCTTGAGGG	TGCACATTTGCCTGCTCCTC
ATM	ACACTGCGCGTATAAGCCAATC	TTTTCAACCAGTTTTCCGTTACTTC
ATR	TGTTGGGCCCACTTTATGCAGC	TAGAGACGACCTGAGACGACGC
CHEK1	GGATCAGCTTTTCCCAGCCCAC	TTCTGTGAGGATCCTGGGGTGC
CHEK2	ACGGAGTTCACAACACAGCAGC	TCTACTAGTCGAAAGCGGCCCC
TREM2	CCCACCCACTTCCATCCTTC	CTCAGCCCTGGCAGAGTTTG
TREM19	CAAGGAACTGGTCCTGGGG	CAGGAGCAGCAACAGAAGGA
IBA1	GCTATGAGCCAAACCAGGGA	CTTCCAGTTTGGAGGGCAGA
CD45	ACAGCCAGCACCTTTCCTAC	GTGCAGGTAAGGCAGCAGA
PU1	CTGCAATGTCAAGGGAGGGG	GTCTTCTGATGGCTGAGGGG
RPLP0	TCGACAATGGCAGCATCTAC	ATCCGTCTCCACAGACAAGG

Supplementary Table 4 Downregulated KEGG Pathways

Please see the original publication.

Supplementary Table 5 Cytokine Array - Significantly Regulated Cytokines

Name	meanbgt	meanbgc	ratio	logratio	limmap	limmapa	SYMBOL
RAGE	1,0205E-05	2,0808E-10	0,90832043	-0,13872677	0,40600805	0,56652286	AGER
Angiopoietin-2	6,3251E-60	6,9841E-37	1,22818364	0,29652629	0,01410339	0,05547085	ANGPT2
Apolipoprotein_A-I	1,2801E-06	6,5933E-28	0,8516972	-0,23158749	0,21709592	0,38882851	APOA1
BDNF	8,532E-117	1,8294E-79	1,63425783	0,70863561	0,00074771	0,01121568	BDNF
Emmprin	3,682E-162	3,143E-154	1,16688866	0,22266691	0,23591884	0,40382395	BSG
Complement_Component_C5_C5a	1,4939E-34	1	2,49075933	1,31658563	0,00014734	0,00577837	C5
VCAM-1	4,354E-104	1,457E-99	0,95726915	-0,06300348	0,46177897	0,61841771	CD106
CD14	2,4457E-08	1	1,99996926	0,99997782	0,0002643	0,0063433	CD14
CD30	3,01E-26	0,99999499	2,15335213	1,10658426	0,0011233	0,01347962	CD30
CD40_ligand	0,99809423	7,4567E-16	0,55943792	-0,83795006	0,00229525	0,01967354	CD40LG
Chitinase_3-like_1	0,51091924	4,0969E-43	0,47854702	-1,06326742	0,00194049	0,01791223	CHI3L1
M-CSF	0,93875314	1,1367E-10	0,67432377	-0,56848665	0,00110097	0,01347962	CSF1
GM-CSF	1,3719E-17	4,4359E-08	1,20681936	0,27120974	0,02383913	0,07731609	CSF2
G-CSF	9,3097E-46	1,6504E-24	1,24412785	0,31513474	0,02828376	0,08702695	CSF3
Cystatin_C	0,00442633	1,2735E-50	0,62530157	-0,67737595	0,0141763	0,05547085	CST3
SDF-1A	0,03693045	2,3438E-24	0,68937105	-0,53664737	0,00624685	0,03569629	CXCL12
Dkk-1	1,527E-132	7,772E-133	0,89554027	-0,15916979	0,18750553	0,35860786	DKK1
DPPIV	4,3053E-71	2,3468E-47	1,29516977	0,37314122	0,00352702	0,02645265	DPP4
EGF	0,00015345	0,99995132	1,43052817	0,5165479	0,01006923	0,04663108	EGF
Endoglin	0,9466287	8,1831E-43	0,4611186	-1,11679024	0,00019261	0,00577837	ENG
FGF-19	3,9446E-24	3,8213E-59	0,71750508	-0,47893904	0,00747626	0,03926479	FGF19
Flt-3_Ligand	1,8569E-16	0,00078364	1,28218349	0,35860274	0,01433125	0,05547085	FLT3LG
Vitamin_D_BP	7,7364E-32	0,00271652	1,48505143	0,5705129	0,00070366	0,01121568	GC
GDF-15	7,726E-182	3,04E-178	1,05441657	0,07644495	0,39762984	0,56652286	GDF15
IFN-G	0,50153579	1,2529E-27	0,59239829	-0,75536063	0,0109441	0,04864047	IFNG
IGFBP-2	3,148E-166	4,593E-175	0,74898574	-0,41698983	0,01946193	0,06868917	IGFBP2
IGFBP-3	7,373E-132	3,578E-138	0,79652167	-0,32821448	0,02256285	0,07731609	IGFBP3
IL-11	6,3434E-12	9,2472E-42	0,75909848	-0,39764103	0,06136567	0,15667832	IL11
IL-1A	2,1416E-14	1,7107E-12	0,95829	-0,06146578	0,69726283	0,77664418	IL1A
IL-22	0,04807562	0,98769197	1,22535649	0,29320153	0,04653571	0,13108578	IL22
IL-27	1	0,00528959	0,60377546	-0,72791597	0,00338606	0,02645265	IL27
IL-31	0,8318258	0,02773356	0,8036947	-0,31528052	0,01728292	0,06284697	IL31
IL-32	0,03690461	1,0199E-25	0,82710196	-0,27386292	0,17815742	0,35631484	IL32
IL-5	4,0048E-46	2,1841E-12	1,41946555	0,50534784	0,00159879	0,01598791	IL5
Lipocalin-2	1,0443E-06	0,24212777	1,30595462	0,38510477	0,05918236	0,15438876	LCN2
LIF	1,1835E-39	0,99999978	2,17549493	1,12134366	2,9699E-05	0,00356388	LIF
MIF	1,494E-122	1,663E-142	0,6082475	-0,71726961	0,00408432	0,02689473	MIF
MMP-9	0,00401651	3,162E-27	0,82714242	-0,27379233	0,16837838	0,34836907	MMP9
Myeloperoxidase	1,4261E-66	1,3121E-32	1,44968574	0,53574019	0,00067252	0,01121568	MPO
uPAR	1,39E-131	3,083E-143	0,70418637	-0,50597078	0,00155406	0,01598791	PLAUR
Pentraxin_3	4,085E-139	2,187E-133	0,9972219	-0,00401353	0,93907482	0,95679351	PTX3
Resistin	7,9537E-07	0,00123985	1,07034999	0,09808262	0,17284465	0,35154844	RETN
Relaxin-2	0,49999786	0,01714714	1,25943832	0,33278047	0,75268057	0,82110608	RLN2
Serpin_E1	4,036E-187	5,256E-181	1,0952113	0,13120923	0,09462651	0,22710363	SERPINE1
SHBG	2,1707E-36	1,5474E-30	1,09320001	0,12855738	0,22737812	0,39694106	SHBG
Osteopontin	1,611E-158	1,153E-146	1,2138278	0,27956377	0,01479223	0,05547085	SPP1
Cripto-1	0,00512433	0,99999818	1,37162598	0,45588713	0,0101034	0,04663108	TDGF1
TFF3	0,00037934	5,4896E-30	0,72057394	-0,47278161	0,00425833	0,02689473	TFF3
TfR	0,04262428	5,0762E-12	0,78731635	-0,34498465	0,00523491	0,03140947	TFRC
Thrombospondin-1	4,6404E-93	1,1302E-92	0,91611293	-0,12640265	0,10724626	0,25234415	THBS1
BAFF	2,5531E-19	1,7639E-13	1,154845	0,20769923	0,13204393	0,30471677	TNFSF13B
VEGF	8,756E-192	4,62E-190	0,97923097	-0,0302789	0,68004853	0,77664418	VEGFA

Supplementary Material 1 Original Western Blots

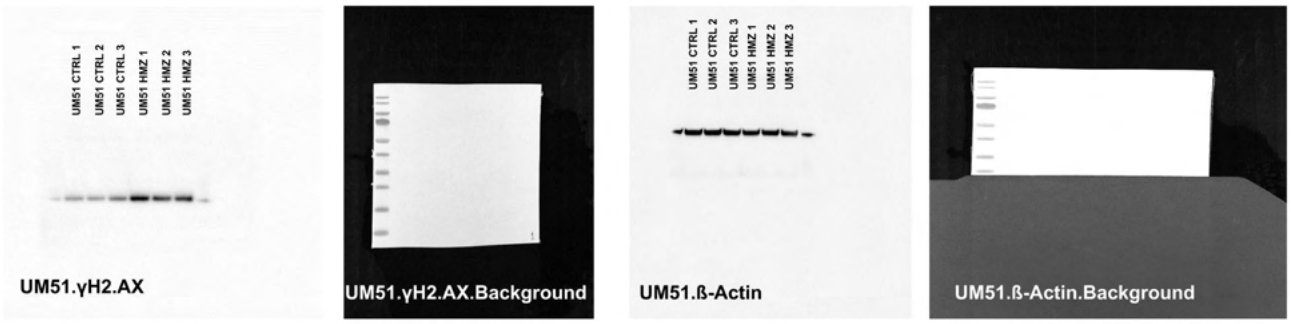

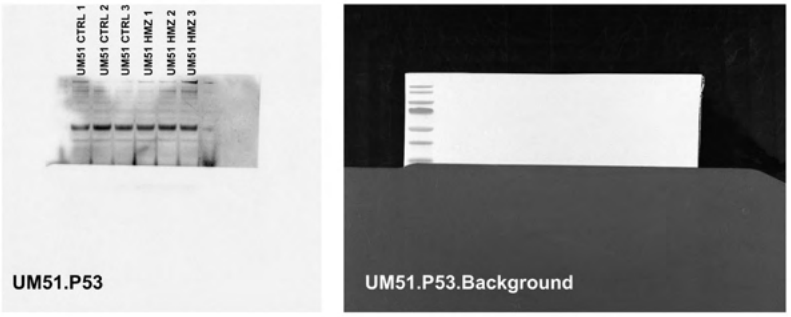

The whole blot membranes for main figure 3,4. The stainings were done on the same membrane for γH2AX and P53.

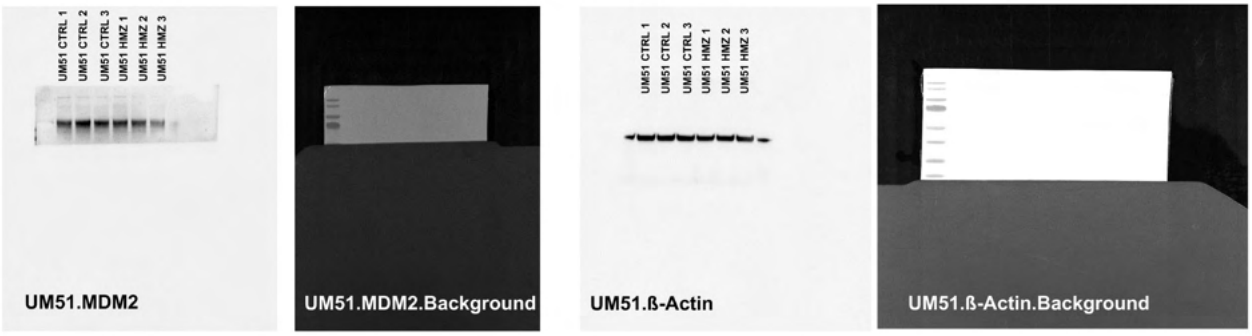

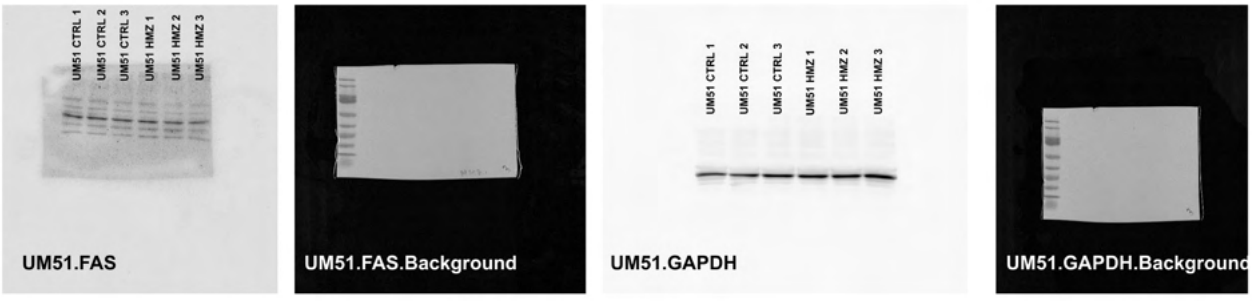

The whole blot membranes for main figure 4.

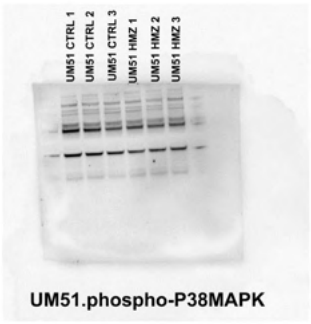

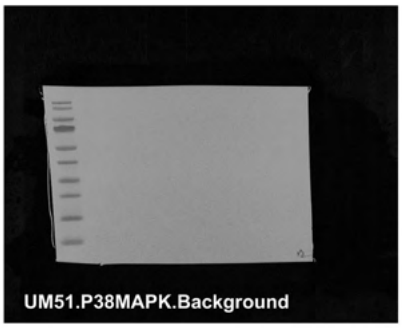

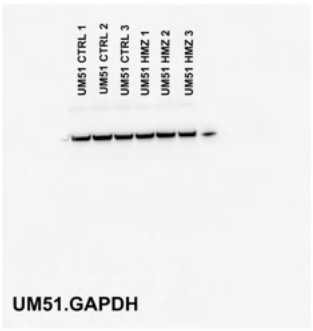

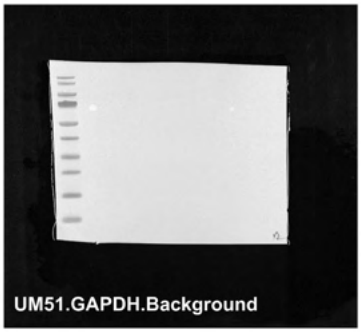

The whole blot membranes for main figure 4.

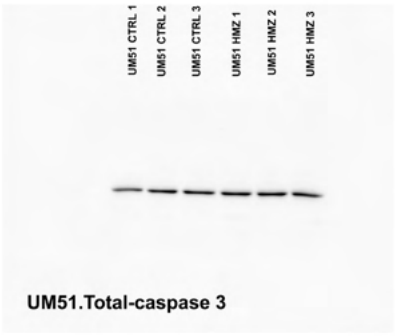

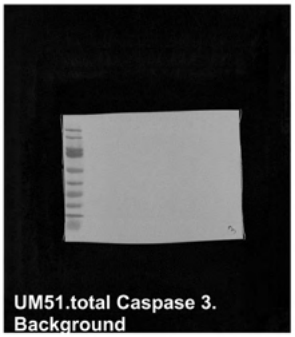

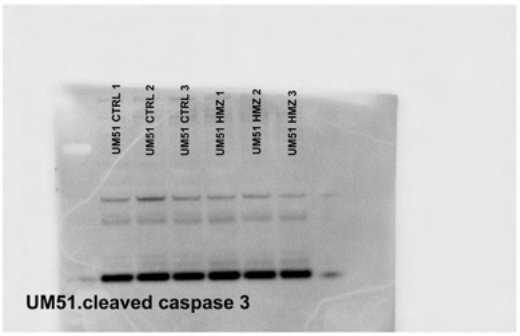

The whole blot membranes for supplementary figure 1. Cleaved caspase 3 was stained first, then the membrane was stripped and further used for total caspase 3.

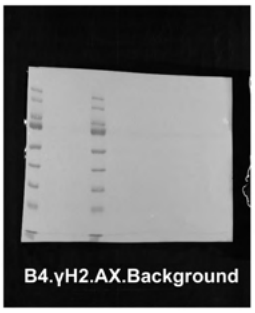

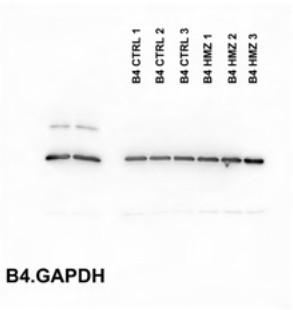

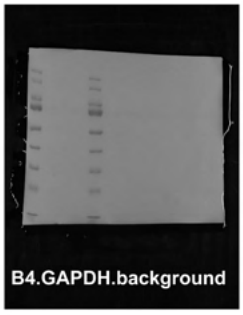

The whole blot membranes for main figure 3.

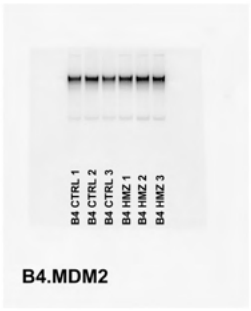

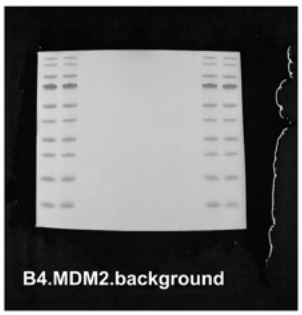

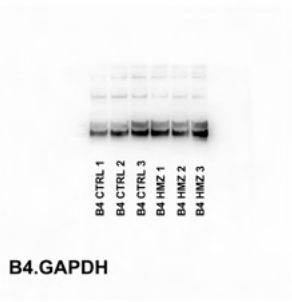

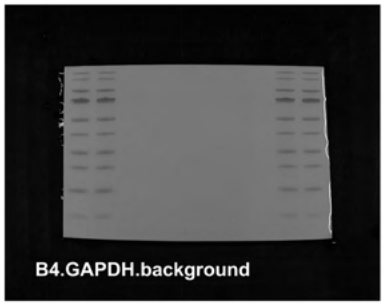

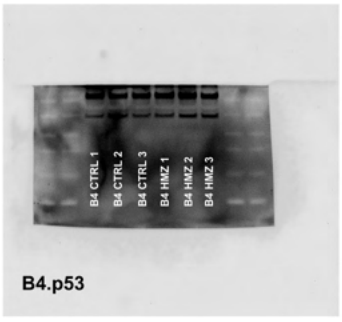

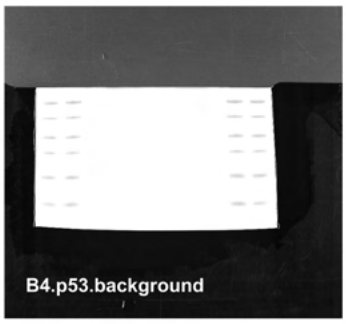

The whole blot membranes for main figure 4. The stainings were done on the same membrane for MDM2 and p53.

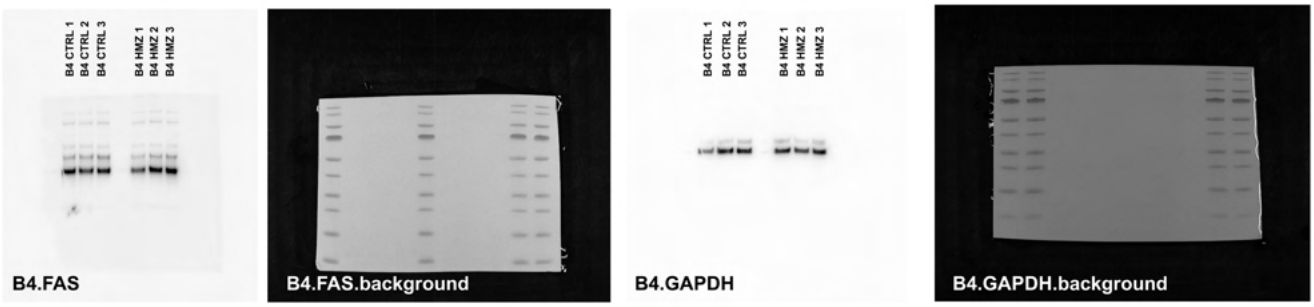

The whole blot membranes for main figure 4.

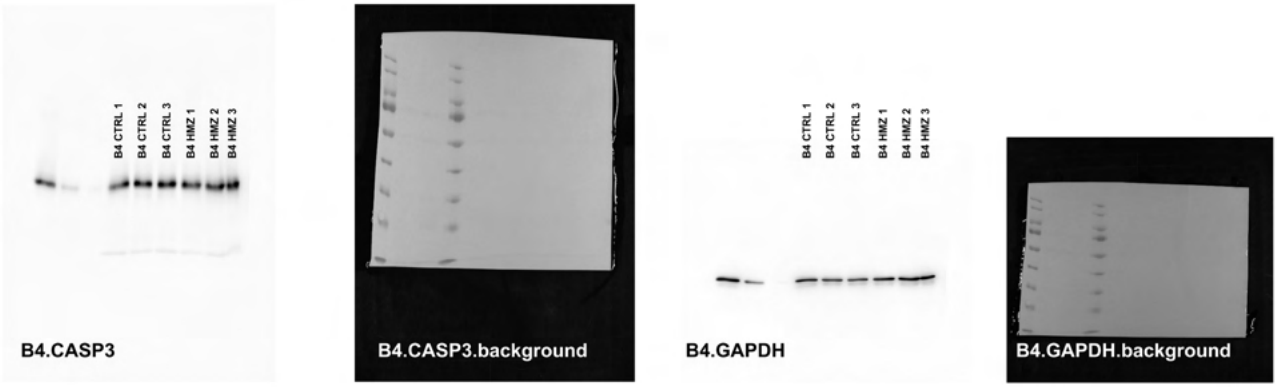

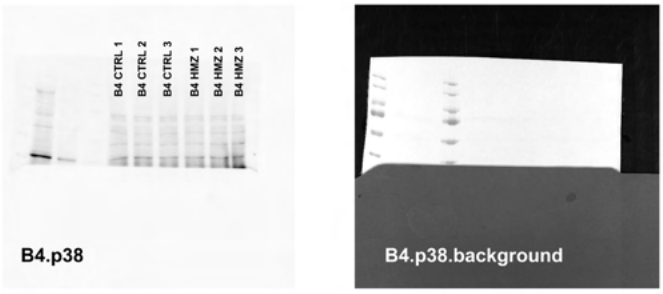

The whole blot membranes for main figure 4 and supplementary figure 1. The stainings were done on the same membrane for total p38 and CASP3.

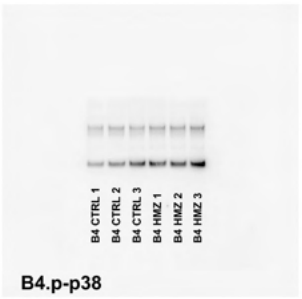

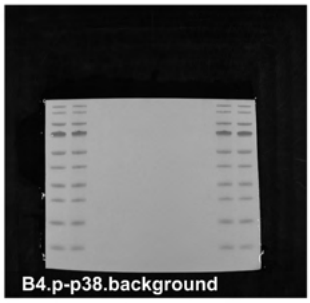

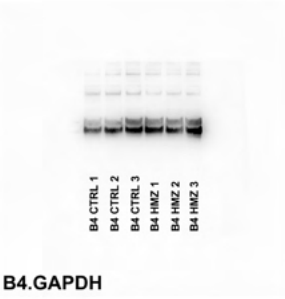

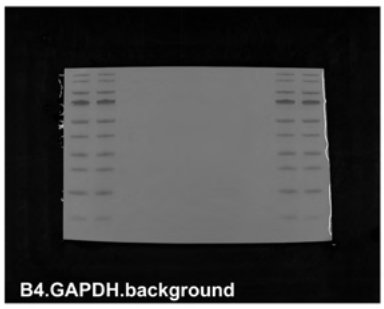

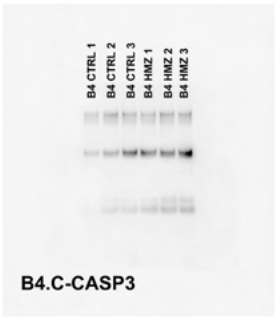

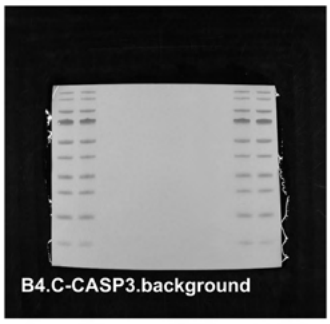

The whole blot membranes for main figure 4 and supplementary figure 1. The stainings were done on the same membrane for p-p38 and C-CASP3.

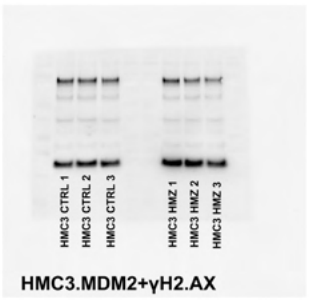

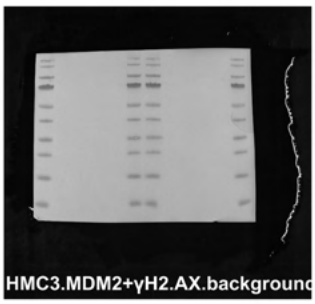

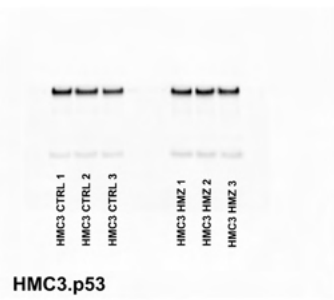

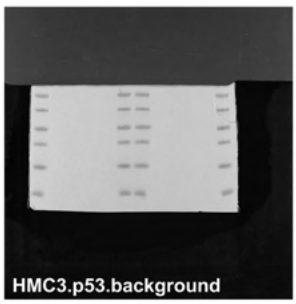

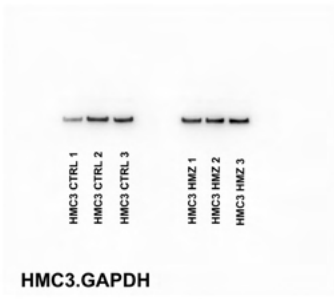

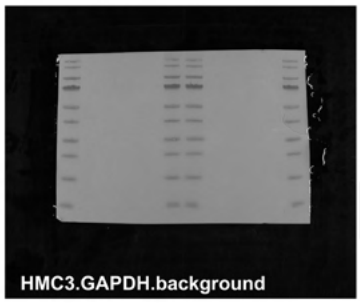

The whole blot membranes for supplementary figure 4. The stainings were done on the same membrane for all proteins.

IV. Concluding remarks

Neurological diseases have an extensive impact on individuals and society, affecting millions of people worldwide. For individuals, these conditions – whether neurodevelopmental or neurodegenerative - often lead to progressive cognitive, motor, and sensory impairments with significant reduction in the quality of life. For society, the cost of care, lost productivity, and the need for long-term support of patients place an immense strain on healthcare systems and economies. Therefore, addressing neurological diseases through research into the underlying pathomechanisms should not only be a medical priority but also presents a critical socioeconomic issue. However, neurological research has always been hampered by the inaccessibility of disease models accurately recapitulating the given disease phenotype. This shortcoming has been partially remedied since the advent of iPSCs in 2006, as they enable researchers to create patient-specific neural cells which accurately model the genetic and phenotypic characteristics of many neurological diseases.

The work in hand sought to utilize this advantage of iPSCs to model two diseases with pronounced neurological involvement: the rare disease Cockayne Syndrome (CS) and Cerebral Malaria (CM), a severe potential complication of the tropical disease Malaria. The focus for Cockayne Syndrome was on the establishment of 3D neural models from iPSCs derived from patients with distinct severity grades of CS, aiming to identify similarities common to all forms of this devastating disease. For Cerebral Malaria, we concentrated on the establishment of a fast and easy-to-use 2D model to assess the impact of Hemozoin in CM and provide a tool for other researchers to unravel the pathomechanisms underlying this deadly complication of Malaria.

IV.I. Modelling Cockayne Syndrome using patient-derived iPSCs

Cockayne Syndrome is a rare disease, which previously mostly has been investigated due to the involvement of the two main proteins involved in its etiology – CSA and CSB – in the transcription-coupled nucleotide repair mechanism. However, due to the involvement of both proteins in other crucial cellular mechanisms, their potential involvement in cellular aging - evidenced by the segmental progeria in affected patients – and the newfound accessibility of patient-specific cells due to reprogramming technology, research into this debilitating disease has seen a renaissance.

In III.I. we performed transcriptome analysis of neurospheres (NS) and the first generated brain organoids derived from two patients with varying severity levels of CS and compared them to a healthy control.

Our analysis provides evidence for many pathways thought to be drivers of the CS neurological symptoms (summarized in Figure 7). In neurospheres, which means spheres consisting of neural progenitor cells (NPCs), we found prominent dysregulation of the RNAPI transcription associated pathways *protein processing in endoplasmatic reticulum* and *ribosome*, indicating protein biosynthesis as dysregulated at this early developmental stage prone to disturbance. RNAPI transcriptional dysregulation has been shown to negatively influence the stability of the proteome in CS patients and in conjunction with the elevated reactive oxygen species present in CS patients, leads to endoplasmatic reticulum (ER) stress. Chemical chaperones, e.g. 4-phenyl butyric acid or tauroursodeoxycholic acid (TUDCA), have been shown to be able to alleviate ER stress and while not administrable this early in development, might be a feasible addition to other treatment options in the management of CS symptoms. TUDCA has the additional benefit of reducing ROS, preserving mitochondrial function and inciting an anti-neuroinflammatory response[151,152,181]. Further research should be conducted to ascertain these effects in human CS-patient derived NPCs and other neural cells employing the cell culture models established in this work.

We further found modulation of *VEGFA/VEGFR2 signalling pathway* in NS. Vascular Endothelial Growth Factor A (*VEGFA*) and its receptor Vascular Endothelial Growth Factor Receptor 2 (*VEGFR2*) play critical roles in angiogenesis and the maintenance of vascular homeostasis[182]. Little is known about the exact dysregulation pertaining to this pathway in CS patients. VEGF normally is expressed upon hypoxic stress, which occurs upon deprivation of oxygen, and activates the transcriptional program to induce vascularization through stabilization of hypoxia inducible factor 1α (*HIF1α*). However, CSB-deficient cells fail to induce *VEGF* transcription, even though HIF1α is stabilized. This is hypothesized to occur because CSB-deficient terminally differentiated cells exhibit markedly increased levels of p53 expression. Both p53 and HIF1α require the co-activator E1A Binding Protein P300 (*p300*) to activate their translational program, but the abnormally high levels of p53 sequester most of the p300, inhibiting hypoxic response. CSB also is required to separate p53 and p300, so CSB deficiency may impede hypoxic response in two ways[183]. As we found p53 protein levels to be reduced

in both of our patient-derived NS, p300 might be available in our developmentally young samples to activate angiogenesis-related pathways like *VEGFA/VEGFR2 signalling pathway*. However, as already discussed in III.I, VEGFA has diverse functions in NPCs. VEGFA is suggested to e.g. increase proliferation and survival of NPCs and is directly upregulated in response to cholesterol deprivation, a pathway we found to be dysregulated in both the NS and organoids[184-187]. As CS patients frequently show pathological changes of the brain vasculature, which could potentially be one cause of e.g. the brain calcifications found in these patients, further research into the *VEGFA-VEGFR2 signalling pathway* in brain and endothelial cells might provide important insights into the etiology of the neurological symptoms and how to attenuate them[188,189]. The further development of our protocol to produce vascularized brain organoids would constitute an adequate first step to decipher this scarcely investigated symptom. Similarly, investigation into CS-deficient kidney cells, especially vascularized kidney organoids, would potentially provide interesting insights into this pathway, as CS patients frequently display renal hypertension, a disease caused by the narrowing of kidney arteries, as well as other renal complications[190].

We further found dysregulation of *intracellular protein transport* and *vesicle-mediated transport* pathways in NS, as well as the subpathway *COPII-mediated vesicle transport* in both NS and organoids. Both pathways might be dysregulated due to the disruption of the microtubule network mentioned in II.IV.I. The instability of the microtubule network due to reduced α-tubulin acetylation impairs the binding and motility of motor proteins, potentially hampering protein and vesicular transport. Consequently, proteins and lipids may not reach the target area in a timely manner, disrupting cell signalling, membrane integrity, and overall metabolic balance of the cell[145,191]. Moreover, impaired vesicular transport affects the endocytic and exocytic pathways, two pathway we found to be dysregulated in the brain organoids, which are essential for the uptake of nutrients and secretion of waste products, as well as the secretion and recycling of signalling molecules[192,193]. The accumulation of vesicles and misdirected transport can lead to cellular stress, potentially further exacerbating the neurodegeneration observed in CS patients[194].

The defect α-tubulin acetylation has been partially rescued in CSB-deficient human fibroblasts, C. elegans and mouse skin employing the pan-histone deacetylase (HDAC) inhibitor suberoylanilide hydroxamic acid, also known as Vorinostat, which has already been approved for clinical use. This points to HDAC inhibition as an additional

potential therapeutic option for CS patients[145]. With regards to translational aspects, four HDAC inhibitors, Vorinostat, Romidepsin, Panobinostat, and Belinostat, have been approved for human use and could be investigated for repurposed use in CS patients[195]. Nevertheless, the potential benefits of HDAC inhibition for CS first need to be validated through preclinical studies using patient-derived neural cells.

In the brain organoids, we observed severe dysregulation of the pathway *neuron projection development*. As discussed in III.I, CSB-deficient cells have been shown to exhibit a decrease in neuritogenesis, partially due to a decrease in MAP2 expression, which is accompanied by reduced cell polarization[196,197]. This defect has been partially remedied *in-vitro* via overexpression of Synaptotagmin 9 (*SYT9*), a key component of the exocytic machinery controlling neurotrophin release, implicating the involvement of disturbed intracellular transport in this complication. Neuritogenesis has also been partially restored via administration of BDNF, as well as administration of the BDNF pharmacological analogues amitriptyline and 7,8-dihydroxyflavone (Tropoflavin), revealing another crucial growth factor as potentially dysregulated in CS patients[196]. Amitriptyline is a tricyclic antidepressant approved for human use and as such could potentially be used as a repurposed drug for CS. However, due to its extensive side effect profile, especially potential exacerbation of the glaucoma found in CS patients, further research using advanced iPSC-based cell culture models and CS mouse models should first be performed[198].

Tropoflavin is a naturally occurring flavone found to act as a potent and selective agonist of the main BDNF receptor tropomyosin receptor kinase B (*TRKB*)[199,200]. It has been shown to be both orally bioavailable, able to penetrate the blood-brain barrier and demonstrated therapeutic efficacy in animal models of several CNS disorders, i.a. depression, amyotrophic lateral sclerosis, Rett syndrome and Alzheimer's disease[200-204]. Additionally, tropoflavin has been shown to modulate mitochondrial gene expression, possesses potent TRKB-independent antioxidant activity and has been shown to be protective against both glutamate-induced excitotoxicity and oxidative stress, potentially providing secondary benefits for CS patients[205-207]. A prodrug of tropoflavin with improved potency and pharmacokinetics, R13, has been designed and displayed therapeutic efficacy in a mouse model of Alzheimer's disease[208]. Due to this variety of potentially beneficial effects of tropoflavin for CS patients, investigations should be performed in CS patient-derived iPSC models to ascertain its effectiveness in restoring neuritogenesis, as well as eventual other benefits.

We further found dysregulation of the pathway *steroid biosynthesis*, with particular involvement of the subpathway *cholesterol biosynthesis* in both NS and organoids.

CS-patient derived cells have previously been shown to exhibit abnormal lipid metabolism[209,210]. Lipid metabolism dysfunctions have been proposed to be involved in other neurodegenerative diseases, e.g. amyotrophic lateral sclerosis, where aberrant lipid metabolism is proposed to underlie disruption of essential functions also found in CS, like mitochondrial dysfunction, impaired neuronal transport, cytoskeletal defects and reduced neurotransmitter release. Coherently, cholesterol, the main sterol lipid im mammals, is known to play a crucial role in various cellular processes, including membrane structure, signal transduction, and neural development[211].

Cholesterol is the only integral lipid for the formation and maintenance of myelin sheaths around neuronal axons. Brain cholesterol is produced locally and can only sparsely be substituted from peripheral tissues. Accordingly, disorders which interfere with sterol synthesis or intracellular trafficking of cholesterol cause hypomyelination and neurodegeneration, both of which are prominent features in CS patients[212,213]. As discussed in III.I., cholesterol is also a critical component of cell membranes and involved in the formation of lipid rafts, which are necessary for cell signalling and neuronal function. Impaired cholesterol biosynthesis can disrupt these lipid rafts, leading to altered cellular signalling and impaired neuronal development[214-216]. Furthermore, cholesterol is a precursor for steroid hormones, which are vital for brain development and function[217]. Thus, alterations of cholesterol biosynthesis might exacerbate the dysregulation of various hormonal axes found in CS patients.

Taken together, the disruption in cholesterol biosynthesis in CS may therefore contribute to the severe neurodevelopmental and neurodegenerative symptoms observed in CS patients. Confirming and subsequently understanding the link between cholesterol metabolism and CS may open new avenues for therapeutic interventions aimed at restoring normal lipid metabolism and improving neurological outcomes in CS patients.

Overall, this thesis only concentrates on the neurodevelopmental effects of CS, without challenging the usual focus of CS research – TC-NER. However, our findings are in line with the mechanisms thought to be the main drivers of CS neurological symptoms, with the dysregulation of RNAPI transcription-associated and vasculature-associated pathways in NPCs, the disruption of several pathways crucial for neuronal function and

survival in cerebral organoids and metabolic changes in both NPCs and cerebral organoids.

Due to the very low prevalence of CS and, thus, availability of samples, as well as experimental, temporal and financial limitations, only a few individuals were investigated, which increases the chance of a false-positive identification of differences. Therefore, future investigations should include more CS and especially control individuals, as well as optimally a CRISPR/Cas-mediated rescue, as is recommended for such studies[218]. Furthermore, to find target genes utilizable in all forms of CS, as well as potential therapeutic options universal for all types of CS, a comparison between CSA- and CSB-deficient iPSC-derived organoids is essential. As the symptoms of mutations in both proteins are largely convergent, but not identical, it would be valuable to explore the shared and distinct mechanisms underlying the subtle differences observed between the two patient cohorts.

Nonetheless, the work in hand strengthens already established theories about the etiology of CS and might provide leads for further research. Especially the potential dysregulation of lipid metabolism has not been a focus of CS research until now, which might be due to the rarity of CS brain samples and the isolation of the brain from the rest of the body´s cholesterol distributing system. With numerous approved medications targeting cholesterol metabolism and transport, this might present a promising avenue to improve the management of CS-associated neurological symptoms.

IV.II. Modelling Cerebral Malaria using iPSCs

Cerebral malaria (CM) is a potentially life-threatening neurological complication caused by Plasmodium falciparum infection, which is transmitted to humans by infected Anopheles mosquitoes. It predominantly affects children under the age of five in sub-Saharan Africa. As a disease, CM is characterized by the sequestration of infected erythrocytes in the microvasculature of the brain, leading to an intense inflammatory response, the disruption of the blood-brain barrier (BBB) and cerebral oedema[158,164].

Modelling CM has posed a challenge to researchers, as P. falciparum is unable to infect rodents and access to non-post-mortem human brain tissue is limited[219]. This limitation can be circumvented via the use of iPSCs, which can provide a theoretically unlimited source of human neural cells.

For the work in hand, we established an iPSC-based 2D neural model termed neuronal networks. This was a deliberate choice to (i) establish an easy-to-use model which can be used by other researchers and (ii) due to the properties of hemozoin (HMZ), the agent employed to model CM-associated brain injury. HMZ is an undegradable crystalline byproduct of the parasites metabolism and is usually present as crystals of varying sizes[174]. Due to their size, these HMZ crystals were expected to have low penetrance into 3D cell culture models, a known limitation with some chemicals. To circumvent this issue and enable the HMZ to affect not just the outermost neurons of a 3D culture, we opted to establish a 2D culture model.

Subsequently, the neuronal networks were exposed to 20 µM HMZ for 48h to model brain injury in CM after BBB breakdown and decipher the reaction of human neurons to this chemical. As expected, inflammation-associated pathways were found to be activated and the secretome of HMZ-exposed neurons was significantly altered. Secretion of the known CM-associated pro-inflammatory cytokines IL-1β, IL-8 and IFN-γ was increased, while the anti-inflammatory cytokines IL-4 and IL-13 were found to be reduced.

Elevated levels of IL-1β, IL-8 and IFN-γ have previously been detected in patients suffering from CM, indicating its involvement in the inflammatory response associated with the disease. All three cytokines are essential for the recruitment and activation of immune cells to sites of infection and inflammation[220,221]. Especially IFN-γ is a potent cytokine which can exacerbate the inflammatory milieu by promoting the production of other pro-inflammatory cytokines and chemokines, thereby potentiating the immune response[222]. This neuron-driven heightened inflammation and immune activation may contribute to the neuronal damage and the neurological symptoms associated with CM, especially to the seizures, as findings suggest that cytokines can increase seizure susceptibility[223]. Elevation of IL-1β and IFN-γ secretion aligns with a known consequence of HMZ exposure, the activation of the NLR Family Pyrin Domain Containing 3 (NLRP3) inflammasome. The assembly of the NLRP3 inflammasome leads to proximity-induced autocatalytic activation of Caspase-1. Once activated, Caspase-1 cleaves pro-IL-1β and pro-IL-18 into their biologically active forms. IL-18, a co-stimulatory cytokine, mediates adaptive immunity and can induce the production of IFN-γ[222,224]. Unfortunately, the levels of IL-18 were not investigated as it was not included in the Proteome Profiler Human XL Cytokine Array Kit used in the work at hand[225,226].

IL-4 is a cytokine known for its role in regulating immune responses, in particular for inhibiting inflammatory responses, such as proinflammatory responses governed by IFN-γ[227]. In the context of CM, IL-4 is thought to exert a protective effect by reducing excessive inflammation. In a mouse model of experimental CM, IL-4 treatment significantly reduced parasitaemia, CM pathology, and mortality[228]. A meta-analysis found IL-4 blood levels to be reduced in patients with overall severe malaria, not just CM, indicating a role in overall malaria disease progression[229].

Similarly, IL-13 is generally considered an anti-inflammatory cytokine, but under certain conditions, such as allergic diseases and asthma, IL-13 can also contribute to inflammation by promoting eosinophil recruitment or enhancing the expression of adhesion molecules on endothelial cells[230,231]. However, in neurons, IL-13 has been revealed to be neuroprotective[232]. In patients with severe malarial anaemia, IL-13 has been demonstrated to be significantly elevated and might contribute to disease severity, but its exact role in severe malaria and especially CM is severely underinvestigated[233]. Like the closely related IL-4, IL-13 might exert a protective effect by reducing excessive inflammation, but may still potentially be detrimental to CM patients, as its precise mode of action depends on the balance of other cytokines and immune factors present.

Interestingly, we observed a decrease in secreted IL-6 and TNF-α in our neuronal networks. Elevated levels of these proinflammatory cytokines have been shown in the plasma and cerebrospinal fluid of CM patients[234-237]. Additionally, post-mortem examinations of CM patients have revealed higher expression levels of TNF-α in brain tissue[238]. However, another study demonstrated that levels of serum IL-6 and TNF-α were only raised significantly in CM patients with multiple vital organ dysfunction, not in patients with CM alone, indicating both cytokines as not necessarily involved in the neurological symptoms[239]. This discrepancy might occur because cytokines are often produced locally and, therefore, may not be detectable in the bloodstream except during severe disease exacerbations, such as in cases of multiple organ dysfunction[240]. Overall, CNS glial cells play a more prominent role in the inflammatory response to pathogen-associated molecules like HMZ. These glial cells are more likely to produce TNF-α and IL-6 upon HMZ exposure, with neurons responding indirectly to the inflammatory environment rather than producing these potent proinflammatory cytokines themselves[241].

Intriguingly, we also observed an increase in secerned IL-16, a cytokine not previously indicated in the etiology of CM. IL-16 is mainly known as a potent chemoattractant of CD4 expressing cells, so its main target are $CD4^+$T-cells, which in turn are necessary for a robust $CD8^+$T-cell immune response[242,243]. As mentioned in II.IV.II., T-cells play a crucial role in the pathogenesis and excessive immune response found in CM. $CD8^+$T-cell contribution might even be a main driver of CM, as mice with impaired CD8+T-cell immune response were found to be protected from experimental CM[244,245]. However, increased influx of $CD4^+$T-cell subpopulations might also play a beneficial role in CM by modulating the immune response to prevent excessive inflammation[246,247].

Similarly, we detected modulation of the IL-26 signalling pathway. IL-26 belongs to the IL-10 family and is produced by various immune cells, including T-cells, and can induce the production of both pro- and anti-inflammatory cytokines and chemokines, e.g. IL-8 and IL-10[248]. As such, excessive IL-26 signalling might exacerbate recruitment and activation of immune cells but can potentially also attenuate inflammation in CM. Understanding the precise role of IL-26 signalling in CM could provide new insights into the balance between protective immunity and harmful inflammation in CM.

We further found increased expression of Platelet Endothelial Cell Adhesion Molecule (*PECAM1*)*, BDNF* and C-C Motif Chemokine Ligand 2 (*CCL2*) in the HMZ exposed neuronal networks. PECAM-1 is a cell adhesion molecule that is primarily expressed on endothelial cells, platelets, and various immune cells and known best for its role in leukocyte transmigration, angiogenesis, and maintaining vascular integrity. By facilitating the transmigration of leukocytes across the endothelium, PECAM-1 might play a role in CM associated neuroinflammation. For example, in a model of NeuroAIDS, it is hypothesized that soluble PECAM-1 accumulates within the CNS vasculature, altering PECAM-1 facilitated interactions between endothelial and immune cells. These changes may enhance the transmigration of HIV-infected leukocytes into the CNS and alter BBB permeability, thereby contributing to the pathogenesis of NeuroAIDS[249]. However, soluble adhesion molecules secerned by neurons might also have completely different functionality, as e.g. a soluble isoform of Cell Adhesion Molecule 1 (*CADM1*) is involved in the directional neurite extension of superior cervical ganglion neurons[250].

CCL2, also known as Monocyte Chemoattractant Protein-1 (MCP-1), is a potent chemokine capable of recruiting and activating immune cells and has been associated

with disease severity in CM patients[251]. Endothelial cells derived from CM patients have been shown to produce significantly higher levels of MCP-1 in response to TNF-α stimulation compared to endothelial cells from patients with uncomplicated malaria[252]. Our research indicated both increased secretion and significantly upregulated expression of CCL2 in HMZ-exposed neuronal networks. Interestingly, there may be a direct link between the increase in CCL2 and the increase in PECAM-1. Leukocytes from HIV-infected patients treated *in-vitro* with CCL2 were found to cleave PECAM-1 into its soluble form, suggesting a similar mechanism could be at play in CM[249].

BDNF, as mentioned before, is a growth factor involved in the survival, growth, and maintenance of neurons. Brain insults have previously been shown to transiently increase local BDNF expression and secretion[253-256]. In a study investigating BDNF plasma levels in Ugandan children with severe malaria, higher plasma BDNF concentrations at presentation were associated with shorter time in coma, reduced chance of disability, as well as reduced probability of death[257]. In a mouse model of CM, a decrease in BDNF mRNA in several brain regions directly correlates to symptom progression[258]. In summary, the increase in BDNF expression and secretion we observed in the neuronal networks is in line with both early chemical insult to CNS neurons and the changes associated with CM, supporting its implicated role as a potential compensatory or survival mechanism.

As outlined, the observed changes in both secretome and gene expression of the HMZ-exposed neuronal networks align in large parts with characteristic changes found in CM. This indicates that the established model is capable of recapitulating parts of CM pathology, even while employing only HMZ instead of actual parasite-infected erythrocytes. As such, the model might present a valuable and easy-to-use tool for understanding CM pathology and testing potential therapeutic interventions.

We further investigated how the inflammatory environment produced by HMZ exposure influenced the neuronal networks. As DNA damage can be a consequence of enhanced inflammation, we investigated the amount of γ-H2A.X Variant Histone (*γH2AX*)-positive foci, a reliable marker for DNA double-strand breaks, in the nuclei of HMZ exposed neurons, as well as expression of the DNA damage response-associated genes ATM Serine/Threonine Kinase (*ATM*), ATR Serine/Threonine Kinase (*ATR*), Checkpoint Kinase 1 (*CHEK1*) and Checkpoint Kinase 2 (*CHEK2*)[259]. While γH2AX-positive foci were only increased in one of two examined cell lines,

expression of the DNA damage associated transcripts were significantly increased in both, nonetheless indicating DNA damage as increased in both cell lines. As the investigated DNA damage response-associated genes are direct effectors of Tumor Protein P53 (*p53*), we further investigated changes in p53 expression and translation, as well as changes in its direct negative effector MDM2 Proto-Oncogene (*MDM2*)[260]. Expression and protein levels of both genes were found to not be affected by the HMZ-induced inflammation, indicating activation of a p53-independent DNA damage response.

The p38 mitogen-activated protein kinase (MAPK) pathway is another pathway involved in the cellular response to various stress signals, e.g. ultraviolet (UV) radiation, oxidative stress, pro-inflammatory cytokines and DNA damage. The p38 pathway is integrated with other key DNA damage response pathways, including the ATM and ATR pathways, and can induce cell cycle arrest and cell death[261-263]. In both investigated neuronal networks, p38-MAPK protein levels were found to be increased, indicating p38-MAPK signalling as involved in the neuronal response to HMZ injury. Involvement of the p38-MAPK pathway has been shown in HMZ-exposed immune cells before, but not in neurons[264,265]. Interestingly, p38-MAPK is directly involved in the modulation of NLRP3-inflammasome activity, which is known to be upregulated in response to HMZ exposure. p38-MAPK signalling can both increase or decrease NLRP3-mediated inflammation[266,267]. In primary cortical neurons and brain tissue under ischemic conditions, MAPK signalling was shown to increase expression and activation of NLRP1 and NLRP3 inflammasomes[268]. As such, deciphering the role of p38-MAPK in the HMZ-induced chemical insult of neurons and other brain cells might provide further insight into the etiology of CM and might constitute a promising target for therapeutic intervention. p38 inhibition is already being investigated as a potential strategy in diseases such as Alzheimer´s Disease, rheumatoid arthritis and diverse cardiovascular diseases[269].

Interestingly, the neuronal networks produced for this study exhibited significant differences in their responses to HMZ exposure. The UM51 cell line, derived from a male of African descent, exhibited a strong reaction to the insult, whereas the B4 cell line, derived from a Caucasian male, demonstrated a comparatively muted response. For future experiments, it would be interesting to include a broader range of cell lines from individuals of both African and Caucasian descent. This would allow for a more

comprehensive investigation into whether ethnicity directly influences the strength of the immune response to malaria-derived molecules.

In conclusion, the established iPSC-derived 2D neuronal network model offers a practical approach to investigating part of the complex CM pathology. The observed inflammatory responses and cytokine profiles in response to HMZ exposure closely mirror those seen in patients with CM, indicating the models potential for further research. The differential responses observed between cell lines of different ethnic backgrounds highlight the importance of including diverse genetic backgrounds in future studies to better understand the role of ethnicity in immune responses to malaria-derived molecules. Additionally, the detected involvement of the p38 MAPK pathway in the neuronal response to HMZ-induced injury might open new avenues for exploring therapeutic interventions. Overall, the established model might not only provide insights into the molecular mechanisms underlying CM but also serve as a tool for testing potential treatments, ultimately contributing to the development of more effective therapies for this life-threatening condition.

V. Appendix

V.I. Additional publications

V.I.I. Forskolin induces FXR expression and enhances maturation of iPSC-derived hepatocyte-like cells

Christiane Loerch, Leon-Phillip Szepanowski, Julian Reiss, James Adjaye, Nina Graffmann

Frontiers in Cell and Developmental Biology (Front. Cell Dev. Biol.), 2024

Abstract

The generation of iPSC-derived hepatocyte-like cells (HLCs) is a powerful tool for studying liver diseases, their therapy as well as drug development. iPSC-derived disease models benefit from their diverse origin of patients, enabling the study of disease-associated mutations and, when considering more than one iPSC line to reflect a more diverse genetic background compared to immortalized cell lines. Unfortunately, the use of iPSC-derived HLCs is limited due to their lack of maturity and a rather fetal phenotype. Commercial kits and complicated 3D-protocols are cost- and time-intensive and hardly useable for smaller working groups. In this study, we optimized our previously published protocol by fine-tuning the initial cell number, exchanging antibiotics and basal medium composition and introducing the small molecule forskolin during the HLC maturation step. We thereby contribute to the liver research field by providing a simple, cost- and time-effective 2D differentiation protocol. We generate functional HLCs with significantly increased HLC hallmark gene (ALB, HNF4α, and CYP3A4) and protein (ALB) expression, as well as significantly elevated inducible CYP3A4 activity.

Status: Published in Frontiers in Cell and Developmental Biology; Impact Factor 4.6 (https://doi.org/10.3389/fcell.2024.1383928)

VI. References

1 Banaszynski, L. A., Allis, C. D. & Lewis, P. W. Histone variants in metazoan development. *Developmental cell* **19**, 662-674 (2010).

2 Till, J. E. & McCulloch, E. A. A direct measurement of the radiation sensitivity of normal mouse bone marrow cells. *Radiation research* **14**, 213-222 (1961).

3 Kolios, G. & Moodley, Y. Introduction to stem cells and regenerative medicine. *Respiration* **85**, 3-10 (2012).

4 Tarkowski, A. K. Experiments on the development of isolated blastomeres of mouse eggs. *Nature* **184**, 1286-1287 (1959).

5 Rossant, J. Stem cells from the mammalian blastocyst. *Stem cells* **19**, 477-482 (2001).

6 P De Miguel, M., Fuentes-Julián, S. & Alcaina, Y. Pluripotent stem cells: origin, maintenance and induction. *Stem cell reviews and reports* **6**, 633-649 (2010).

7 Friedenstein, A., Chailakhjan, R. & Lalykina, K. The development of fibroblast colonies in monolayer cultures of guinea-pig bone marrow and spleen cells. *Cell Proliferation* **3**, 393-403 (1970).

8 Zhou, T. *et al.* Challenges and advances in clinical applications of mesenchymal stromal cells. *Journal of hematology & oncology* **14**, 1-24 (2021).

9 Sousa, B. R. *et al.* Human adult stem cells from diverse origins: an overview from multiparametric immunophenotyping to clinical applications. *Cytometry Part A* **85**, 43-77 (2014).

10 Majo, F., Rochat, A., Nicolas, M., Jaoudé, G. A. & Barrandon, Y. Oligopotent stem cells are distributed throughout the mammalian ocular surface. *Nature* **456**, 250-254 (2008).

11 Bentzinger, C. F., Wang, Y. X., von Maltzahn, J. & Rudnicki, M. A. The emerging biology of muscle stem cells: Implications for cell-based therapies. *Bioessays* **35**, 231-241 (2013).

12 Xu, H. & Liang, H. The regulation of totipotency transcription: Perspective from in vitro and in vivo totipotency. *Frontiers in Cell and Developmental Biology* **10**, 1024093 (2022).

13 Liu, G., David, B. T., Trawczynski, M. & Fessler, R. G. Advances in pluripotent stem cells: history, mechanisms, technologies, and applications. *Stem cell reviews and reports* **16**, 3-32 (2020).

14 Martin, G. R. Isolation of a pluripotent cell line from early mouse embryos cultured in medium conditioned by teratocarcinoma stem cells. *Proceedings of the National Academy of Sciences* **78**, 7634-7638 (1981).

15 Evans, M. J. & Kaufman, M. H. Establishment in culture of pluripotential cells from mouse embryos. *nature* **292**, 154-156 (1981).

16 Thomson, J. A. *et al.* Embryonic stem cell lines derived from human blastocysts. *science* **282**, 1145-1147 (1998).

17 Gurdon, J. B. The developmental capacity of nuclei taken from intestinal epithelium cells of feeding tadpoles. *Development* **10**, 622-640 (1962).

18 Wilmut, I., Schnieke, A. E., McWhir, J., Kind, A. J. & Campbell, K. H. Viable offspring derived from fetal and adult mammalian cells. *Nature* **385**, 810-813 (1997).

19 Liu, Z. *et al.* Cloning of macaque monkeys by somatic cell nuclear transfer. *Cell* **172**, 881-887. e887 (2018).

20 Miller, R. A. & Ruddle, F. H. Pluripotent teratocarcinoma-thymus somatic cell hybrids. *Cell* **9**, 45-55 (1976).

21 Tada, M., Tada, T., Lefebvre, L., Barton, S. C. & Surani, M. A. Embryonic germ cells induce epigenetic reprogramming of somatic nucleus in hybrid cells. *The EMBO journal* (1997).

22 Cowan, C. A., Atienza, J., Melton, D. A. & Eggan, K. Nuclear reprogramming of somatic cells after fusion with human embryonic stem cells. *Science* **309**, 1369-1373 (2005).

23 Mitsui, K. *et al.* The homeoprotein Nanog is required for maintenance of pluripotency in mouse epiblast and ES cells. *Cell* **113**, 631-642 (2003).

24 Schöler, H., Balling, R., Hatzopoulos, A. K., Suzuki, N. & Gruss, P. Octamer binding proteins confer transcriptional activity in early mouse embryogenesis. *The EMBO journal* **8**, 2551-2557 (1989).

25 Yuan, H., Corbi, N., Basilico, C. & Dailey, L. Developmental-specific activity of the FGF-4 enhancer requires the synergistic action of Sox2 and Oct-3. *Genes & development* **9**, 2635-2645 (1995).

26 Takahashi, K. & Yamanaka, S. Induction of pluripotent stem cells from mouse embryonic and adult fibroblast cultures by defined factors. *cell* **126**, 663-676 (2006).

27 Morita, S., Kojima, T. & Kitamura, T. Plat-E: an efficient and stable system for transient packaging of retroviruses. *Gene therapy* **7**, 1063-1066 (2000).

28 Tokuzawa, Y. *et al.* Fbx15 is a novel target of Oct3/4 but is dispensable for embryonic stem cell self-renewal and mouse development. *Molecular and cellular biology* **23**, 2699-2708 (2003).

29 Takahashi, K. *et al.* Induction of pluripotent stem cells from adult human fibroblasts by defined factors. *cell* **131**, 861-872 (2007).

30 Karagiannis, P. *et al.* Induced pluripotent stem cells and their use in human models of disease and development. *Physiological reviews* **99**, 79-114 (2019).

31 Zhu, Z. & Huangfu, D. Human pluripotent stem cells: an emerging model in developmental biology. *Development* **140**, 705-717 (2013).

32 Zhang, X. *et al.* Pax6 is a human neuroectoderm cell fate determinant. *Cell stem cell* **7**, 90-100 (2010).

33 Itskovitz-Eldor, J. *et al.* Differentiation of human embryonic stem cells into embryoid bodies comprising the three embryonic germ layers. *Molecular medicine* **6**, 88-95 (2000).

34 Sharon, N., Mor, I., Golan-Lev, T., Fainsod, A. & Benvenisty, N. Molecular and functional characterizations of gastrula organizer cells derived from human embryonic stem cells. *Stem cells* **29**, 600-608 (2011).

35 Maury, Y., Gauthier, M., Peschanski, M. & Martinat, C. Human pluripotent stem cells for disease modelling and drug screening. *Bioessays* **34**, 61-71 (2012).

36 Tropel, P. *et al.* High-efficiency derivation of human embryonic stem cell lines following pre-implantation genetic diagnosis. *In Vitro Cellular & Developmental Biology-Animal* **46**, 376-385 (2010).

37 Mateizel, I., Spits, C., De Rycke, M., Liebaers, I. & Sermon, K. Derivation, culture, and characterization of VUB hESC lines. *In Vitro Cellular & Developmental Biology-Animal* **46**, 300-308 (2010).

38 Wu, S. M. & Hochedlinger, K. Harnessing the potential of induced pluripotent stem cells for regenerative medicine. *Nature cell biology* **13**, 497-505 (2011).

39 Soldner, F. *et al.* Parkinson's disease patient-derived induced pluripotent stem cells free of viral reprogramming factors. *Cell* **136**, 964-977 (2009).

40 Gore, A. *et al.* Somatic coding mutations in human induced pluripotent stem cells. *Nature* **471**, 63-67 (2011).

41 Kim, K. *et al.* Epigenetic memory in induced pluripotent stem cells. *Nature* **467**, 285-290 (2010).

42 Kajiwara, M. *et al.* Donor-dependent variations in hepatic differentiation from human-induced pluripotent stem cells. *Proceedings of the National Academy of Sciences* **109**, 12538-12543 (2012).

43 Mekhoubad, S. *et al.* Erosion of dosage compensation impacts human iPSC disease modeling. *Cell stem cell* **10**, 595-609 (2012).

44 Avior, Y., Sagi, I. & Benvenisty, N. Pluripotent stem cells in disease modelling and drug discovery. *Nature reviews Molecular cell biology* **17**, 170-182 (2016).

45 Shi, Y., Inoue, H., Wu, J. C. & Yamanaka, S. Induced pluripotent stem cell technology: a decade of progress. *Nature reviews Drug discovery* **16**, 115-130 (2017).

46 Urbach, A., Schuldiner, M. & Benvenisty, N. Modeling for Lesch-Nyhan disease by gene targeting in human embryonic stem cells. *Stem cells* **22**, 635-641 (2004).

47 Mali, P. *et al.* RNA-guided human genome engineering via Cas9. *Science* **339**, 823-826 (2013).

48 Jinek, M. *et al.* RNA-programmed genome editing in human cells. *elife* **2**, e00471 (2013).

49 Cong, L. *et al.* Multiplex genome engineering using CRISPR/Cas systems. *Science* **339**, 819-823 (2013).

50 Hockemeyer, D. & Jaenisch, R. Induced pluripotent stem cells meet genome editing. *Cell stem cell* **18**, 573-586 (2016).

51 Vincent, F. *et al.* Developing predictive assays: the phenotypic screening "rule of 3". *Science translational medicine* **7**, 293ps215-293ps215 (2015).

52 Lee, G. *et al.* Large-scale screening using familial dysautonomia induced pluripotent stem cells identifies compounds that rescue IKBKAP expression. *Nature biotechnology* **30**, 1244-1248 (2012).

53 Wainger, B. J. *et al.* Effect of ezogabine on cortical and spinal motor neuron excitability in amyotrophic lateral sclerosis: a randomized clinical trial. *JAMA neurology* **78**, 186-196 (2021).

54 McNeish, J., Gardner, J. P., Wainger, B. J., Woolf, C. J. & Eggan, K. From dish to bedside: lessons learned while translating findings from a stem cell model of disease to a clinical trial. *Cell stem cell* **17**, 8-10 (2015).

55 Lund, R. J., Närvä, E. & Lahesmaa, R. Genetic and epigenetic stability of human pluripotent stem cells. *Nature Reviews Genetics* **13**, 732-744 (2012).

56 Meissner, T., Strominger, J. & Cowan, C. The universal donor stem cell: removing the immune barrier to transplantation using CRISPR/Cas9 (TRAN1P. 946). *The Journal of Immunology* **194**, 140.128-140.128 (2015).

57 Kim, J. Y., Nam, Y., Rim, Y. A. & Ju, J. H. Review of the current trends in clinical trials involving induced pluripotent stem cells. *Stem cell reviews and reports*, 1-13 (2022).

58 Sayed, N., Liu, C. & Wu, J. C. Translation of human-induced pluripotent stem cells: from clinical trial in a dish to precision medicine. *Journal of the American College of Cardiology* **67**, 2161-2176 (2016).

59 Kimbrel, E. A. & Lanza, R. Current status of pluripotent stem cells: moving the first therapies to the clinic. *Nature reviews Drug discovery* **14**, 681-692 (2015).

60 Zhang, J. *et al.* Induced pluripotent stem cell-derived mesenchymal stem cells hold lower heterogeneity and great promise in biological research and clinical applications. *Frontiers in Cell and Developmental Biology* **9**, 716907 (2021).

61 Friedrich Ben-Nun, I. *et al.* Induced pluripotent stem cells from highly endangered species. *Nature methods* **8**, 829-831 (2011).

62 Pakkenberg, B. & Gundersen, H. J. G. Neocortical neuron number in humans: effect of sex and age. *Journal of comparative neurology* **384**, 312-320 (1997).

63 Herculano-Houzel, S. The human brain in numbers: a linearly scaled-up primate brain. *Frontiers in human neuroscience* **3**, 857 (2009).

64 Budday, S., Steinmann, P. & Kuhl, E. Physical biology of human brain development. *Frontiers in cellular neuroscience* **9**, 257 (2015).

65 Holcomb, P. S., Deerinck, T. J., Ellisman, M. H. & Spirou, G. A. Construction of a polarized neuron. *The Journal of Physiology* **591**, 3145-3150 (2013).

66 Holz, R. W. & Fisher, S. K. Synaptic transmission and cellular signaling: an overview. *Basic Neurochemistry*, 235-257 (2012).

67 Keaney, J. & Campbell, M. The dynamic blood–brain barrier. *The FEBS journal* **282**, 4067-4079 (2015).

68 Takano, T. *et al.* Astrocyte-mediated control of cerebral blood flow. *Nature neuroscience* **9**, 260-267 (2006).

69 Haim, L. B. & Rowitch, D. H. Functional diversity of astrocytes in neural circuit regulation. *Nature Reviews Neuroscience* **18**, 31-41 (2017).

70 Domingues, H. S., Portugal, C. C., Socodato, R. & Relvas, J. B. Oligodendrocyte, astrocyte, and microglia crosstalk in myelin development, damage, and repair. *Frontiers in cell and developmental biology* **4**, 71 (2016).

71 Fields, R. D. Myelin—more than insulation. *Science* **344**, 264-266 (2014).

72 Sousa, C., Biber, K. & Michelucci, A. Cellular and molecular characterization of microglia: a unique immune cell population. *Frontiers in immunology* **8**, 245768 (2017).

73 Stiles, J. & Jernigan, T. L. The basics of brain development. *Neuropsychology review* **20**, 327-348 (2010).

74 Copp, A. J., Greene, N. D. & Murdoch, J. N. The genetic basis of mammalian neurulation. *Nature Reviews Genetics* **4**, 784-793 (2003).

75 Stiles, J. *The fundamentals of brain development: Integrating nature and nurture*. (Harvard University Press, 2008).

76 Vanderhaeghen, P. & Polleux, F. Developmental mechanisms underlying the evolution of human cortical circuits. *Nature Reviews Neuroscience* **24**, 213-232 (2023).

77 Agirman, G., Broix, L. & Nguyen, L. Cerebral cortex development: an outside-in perspective. *FEBS letters* **591**, 3978-3992 (2017).

78 Florio, M. & Huttner, W. B. Neural progenitors, neurogenesis and the evolution of the neocortex. *Development* **141**, 2182-2194 (2014).

79 Wodarz, A. & Huttner, W. B. Asymmetric cell division during neurogenesis in Drosophila and vertebrates. *Mechanisms of development* **120**, 1297-1309 (2003).

80 Paridaen, J. T. & Huttner, W. B. Neurogenesis during development of the vertebrate central nervous system. *EMBO reports* **15**, 351-364 (2014).

81 Götz, M. & Huttner, W. B. The cell biology of neurogenesis. *Nature reviews Molecular cell biology* **6**, 777-788 (2005).

82 Englund, C. *et al.* Pax6, Tbr2, and Tbr1 are expressed sequentially by radial glia, intermediate progenitor cells, and postmitotic neurons in developing neocortex. *Journal of Neuroscience* **25**, 247-251 (2005).

83 Haubensak, W., Attardo, A., Denk, W. & Huttner, W. B. Neurons arise in the basal neuroepithelium of the early mammalian telencephalon: a major site of neurogenesis. *Proceedings of the National Academy of Sciences* **101**, 3196-3201 (2004).

84 Hansen, D. V., Lui, J. H., Parker, P. R. & Kriegstein, A. R. Neurogenic radial glia in the outer subventricular zone of human neocortex. *Nature* **464**, 554-561 (2010).

85 Betizeau, M. *et al.* Precursor diversity and complexity of lineage relationships in the outer subventricular zone of the primate. *Neuron* **80**, 442-457 (2013).

86 Pilz, G.-A. *et al.* Amplification of progenitors in the mammalian telencephalon includes a new radial glial cell type. *Nature communications* **4**, 2125 (2013).

87 Smart, I. H., Dehay, C., Giroud, P., Berland, M. & Kennedy, H. Unique morphological features of the proliferative zones and postmitotic compartments of the neural epithelium giving rise to striate and extrastriate cortex in the monkey. *Cerebral cortex* **12**, 37-53 (2002).

88 Reillo, I., de Juan Romero, C., García-Cabezas, M. Á. & Borrell, V. A role for intermediate radial glia in the tangential expansion of the mammalian cerebral cortex. *Cerebral cortex* **21**, 1674-1694 (2011).

89 Corbin, J. G., Nery, S. & Fishell, G. Telencephalic cells take a tangent: non-radial migration in the mammalian forebrain. *Nature neuroscience* **4**, 1177-1182 (2001).

90 Nery, S., Fishell, G. & Corbin, J. G. The caudal ganglionic eminence is a source of distinct cortical and subcortical cell populations. *Nature neuroscience* **5**, 1279-1287 (2002).

91 Valiente, M. & Marín, O. Neuronal migration mechanisms in development and disease. *Current opinion in neurobiology* **20**, 68-78 (2010).

92 Douglas, R. J. & Martin, K. A. Neuronal circuits of the neocortex. *Annu. Rev. Neurosci.* **27**, 419-451 (2004).

93 Fame, R. M., MacDonald, J. L. & Macklis, J. D. Development, specification, and diversity of callosal projection neurons. *Trends in neurosciences* **34**, 41-50 (2011).

94 Tabata, H. Diverse subtypes of astrocytes and their development during corticogenesis. *Frontiers in neuroscience* **9**, 136043 (2015).

95 Suzuki, I. K. & Vanderhaeghen, P. Is this a brain which I see before me? Modeling human neural development with pluripotent stem cells. *Development* **142**, 3138-3150 (2015).

96 Chambers, S. M. *et al.* Highly efficient neural conversion of human ES and iPS cells by dual inhibition of SMAD signaling. *Nature biotechnology* **27**, 275-280 (2009).

97 Shi, Y., Kirwan, P., Smith, J., Robinson, H. P. & Livesey, F. J. Human cerebral cortex development from pluripotent stem cells to functional excitatory synapses. *Nature neuroscience* **15**, 477-486 (2012).

98 Zhang, S.-C., Wernig, M., Duncan, I. D., Brüstle, O. & Thomson, J. A. In vitro differentiation of transplantable neural precursors from human embryonic stem cells. *Nature biotechnology* **19**, 1129-1133 (2001).

99 Elkabetz, Y. *et al.* Human ES cell-derived neural rosettes reveal a functionally distinct early neural stem cell stage. *Genes & development* **22**, 152-165 (2008).

100 Sun, T. *et al.* A comparison of proliferative capacity and passaging potential between neural stem and progenitor cells in adherent and neurosphere cultures. *International Journal of Developmental Neuroscience* **29**, 723-731 (2011).

101 Zhou, S. *et al.* Neurosphere based differentiation of human iPSC improves astrocyte differentiation. *Stem Cells International* **2016** (2016).

102 Bressan, R. B. *et al.* EGF–FGF2 stimulates the proliferation and improves the neuronal commitment of mouse epidermal neural crest stem cells (EPI-NCSCs). *Experimental cell research* **327**, 37-47 (2014).

103 Peteri, U. K. *et al.* Generation of the Human Pluripotent Stem-Cell-Derived Astrocyte Model with Forebrain Identity. *Brain Sci* **11**, doi:10.3390/brainsci11020209 (2021).

104 Shaker, M. R. *et al.* Rapid and Efficient Generation of Myelinating Human Oligodendrocytes in Organoids. *Front Cell Neurosci* **15**, 631548, doi:10.3389/fncel.2021.631548 (2021).

105 Jorfi, M., D'Avanzo, C., Kim, D. Y. & Irimia, D. Three-dimensional models of the human brain development and diseases. *Advanced healthcare materials* **7**, 1700723 (2018).

106 Strobel, H. A., Moss, S. M. & Hoying, J. B. Methods for vascularization and perfusion of tissue organoids. *Mammalian Genome* **33**, 437-450 (2022).

107 Eiraku, M. *et al.* Self-organizing optic-cup morphogenesis in three-dimensional culture. *Nature* **472**, 51-56 (2011).

108 Sato, T. *et al.* Single Lgr5 stem cells build crypt-villus structures in vitro without a mesenchymal niche. *Nature* **459**, 262-265 (2009).

109 Lancaster, M. A. *et al.* Cerebral organoids model human brain development and microcephaly. *Nature* **501**, 373-379 (2013).

110 Kelava, I. & Lancaster, M. A. Stem cell models of human brain development. *Cell stem cell* **18**, 736-748 (2016).

111 Kadoshima, T. *et al.* Self-organization of axial polarity, inside-out layer pattern, and species-specific progenitor dynamics in human ES cell–derived neocortex. *Proceedings of the National Academy of Sciences* **110**, 20284-20289 (2013).

112 Luo, C. *et al.* Cerebral organoids recapitulate epigenomic signatures of the human fetal brain. *Cell reports* **17**, 3369-3384 (2016).

113 Di Lullo, E. & Kriegstein, A. R. The use of brain organoids to investigate neural development and disease. *Nature Reviews Neuroscience* **18**, 573-584 (2017).

114 Yang, Q., Hong, Y., Zhao, T., Song, H. & Ming, G.-l. What makes organoids good models of human neurogenesis? *Frontiers in Neuroscience* **16**, 872794 (2022).

115 Pasca, A. M. *et al.* Functional cortical neurons and astrocytes from human pluripotent stem cells in 3D culture. *Nat Methods* **12**, 671-678, doi:10.1038/nmeth.3415 (2015).

116 Sebastian, R., Pavon, N. S., Song, Y., Diep, K. T. & Pak, C. in *Stem Cell-Based Neural Model Systems for Brain Disorders* 169-183 (Springer, 2023).

117 Valiulahi, P. *et al.* Generation of caudal-type serotonin neurons and hindbrain-fate organoids from hPSCs. *Stem Cell Reports* **16**, 1938-1952 (2021).

118 Sozzi, E., Nilsson, F., Kajtez, J., Parmar, M. & Fiorenzano, A. Generation of human ventral midbrain organoids derived from pluripotent stem cells. *Current protocols* **2**, e555 (2022).

119 Organization, W. H. *Intersectoral global action plan on Epilepsy and other neurological disorders 2022–2031*. (World Health Organization, 2023).

120 Shpichka, A. *et al.* Organoids in modelling infectious diseases. *Drug Discovery Today* **27**, 223-233 (2022).

121 Levy, R. J. & Paşca, S. P. What have organoids and assembloids taught us about the pathophysiology of neuropsychiatric disorders? *Biological Psychiatry* **93**, 632-641 (2023).

122 Martins, S. *et al.* Impaired p53-mediated DNA damage response contributes to microcephaly in Nijmegen Breakage Syndrome patient-derived cerebral organoids. *Cells* **11**, 802 (2022).

123 Cockayne, E. A. Dwarfism with retinal atrophy and deafness. *Archives of disease in childhood* **11**, 1 (1936).

124 Licht, C. L., Stevnsner, T. & Bohr, V. A. Cockayne syndrome group B cellular and biochemical functions. *The American Journal of Human Genetics* **73**, 1217-1239 (2003).

125 Nance, M. A. & Berry, S. A. Cockayne syndrome: review of 140 cases. *American journal of medical genetics* **42**, 68-84 (1992).

126 Laugel, V. Cockayne syndrome: the expanding clinical and mutational spectrum. *Mech Ageing Dev* **134**, 161-170, doi:10.1016/j.mad.2013.02.006 (2013).

127 Weidenheim, K. M., Dickson, D. W. & Rapin, I. Neuropathology of Cockayne syndrome: Evidence for impaired development, premature aging, and neurodegeneration. *Mechanisms of ageing and development* **130**, 619-636 (2009).

128 Christiansen, M., Thorslund, T., Jochimsen, B., Bohr, V. A. & Stevnsner, T. The Cockayne syndrome group B protein is a functional dimer. *The FEBS journal* **272**, 4306-4314 (2005).

129 Marteijn, J. A., Lans, H., Vermeulen, W. & Hoeijmakers, J. H. Understanding nucleotide excision repair and its roles in cancer and ageing. *Nat Rev Mol Cell Biol* **15**, 465-481, doi:10.1038/nrm3822 (2014).

130 Apostolou, Z., Chatzinikolaou, G., Stratigi, K. & Garinis, G. A. Nucleotide Excision Repair and Transcription-Associated Genome Instability. *Bioessays* **41**, e1800201, doi:10.1002/bies.201800201 (2019).

131 Ljungman, M. & Lane, D. P. Transcription—guarding the genome by sensing DNA damage. *Nature Reviews Cancer* **4**, 727-737 (2004).

132 Fousteri, M. & Mullenders, L. H. Transcription-coupled nucleotide excision repair in mammalian cells: molecular mechanisms and biological effects. *Cell Res* **18**, 73-84, doi:10.1038/cr.2008.6 (2008).

133 Muftuoglu, M. *et al.* Cockayne syndrome group B protein stimulates repair of formamidopyrimidines by NEIL1 DNA glycosylase. *Journal of Biological Chemistry* **284**, 9270-9279 (2009).

134 Thorslund, T. *et al.* Cooperation of the Cockayne syndrome group B protein and poly (ADP-ribose) polymerase 1 in the response to oxidative stress. *Molecular and cellular biology* **25**, 7625-7636 (2005).

135 Wong, H.-K. *et al.* Cockayne syndrome B protein stimulates apurinic endonuclease 1 activity and protects against agents that introduce base excision repair intermediates. *Nucleic acids research* **35**, 4103-4113 (2007).

136 Tiwari, V., Baptiste, B. A., Okur, M. N. & Bohr, V. A. Current and emerging roles of Cockayne syndrome group B (CSB) protein. *Nucleic Acids Res* **49**, 2418-2434, doi:10.1093/nar/gkab085 (2021).

137 Batenburg, N. L., Thompson, E. L., Hendrickson, E. A. & Zhu, X. D. Cockayne syndrome group B protein regulates DNA double-strand break repair and checkpoint activation. *EMBO J* **34**, 1399-1416, doi:10.15252/embj.201490041 (2015).

138 Iyama, T. *et al.* CSB interacts with SNM1A and promotes DNA interstrand crosslink processing. *Nucleic Acids Res* **43**, 247-258, doi:10.1093/nar/gku1279 (2015).

139 Iyama, T. & Wilson, D. M., 3rd. Elements That Regulate the DNA Damage Response of Proteins Defective in Cockayne Syndrome. *J Mol Biol* **428**, 62-78, doi:10.1016/j.jmb.2015.11.020 (2016).

140 Niedernhofer, L. J. *et al.* A new progeroid syndrome reveals that genotoxic stress suppresses the somatotroph axis. *Nature* **444**, 1038-1043, doi:10.1038/nature05456 (2006).

141 Vessoni, A. T. *et al.* Cockayne syndrome-derived neurons display reduced synapse density and altered neural network synchrony. *Human molecular genetics* **25**, 1271-1280 (2016).

142 Zhou, Z. *et al.* Alterations in brain structure and function associated with pediatric growth hormone deficiency: a multi-modal magnetic resonance imaging study. *Frontiers in Neuroscience* **16**, 1043857 (2023).

143 Scheibye-Knudsen, M. *et al.* Cockayne syndrome group B protein prevents the accumulation of damaged mitochondria by promoting mitochondrial autophagy. *J Exp Med* **209**, 855-869, doi:10.1084/jem.20111721 (2012).

144 Norat, P. *et al.* Mitochondrial dysfunction in neurological disorders: Exploring mitochondrial transplantation. *NPJ Regenerative medicine* **5**, 22 (2020).

145 Majora, M. *et al.* HDAC inhibition improves autophagic and lysosomal function to prevent loss of subcutaneous fat in a mouse model of Cockayne syndrome. *Science translational medicine* **10** (2018).

146 Hampl, M. *et al.* Role of Primary Cilia in Odontogenesis. *J Dent Res* **96**, 965-974, doi:10.1177/0022034517713688 (2017).

147 Farooq, M. *et al.* RRP7A links primary microcephaly to dysfunction of ribosome biogenesis, resorption of primary cilia, and neurogenesis. *Nat Commun* **11**, 5816, doi:10.1038/s41467-020-19658-0 (2020).

148 Grisanti, L., Revenkova, E., Gordon, R. E. & Iomini, C. Primary cilia maintain corneal epithelial homeostasis by regulation of the Notch signaling pathway. *Development* **143**, 2160-2171, doi:10.1242/dev.132704 (2016).

149 Wang, S. F. *et al.* Review of Ocular Manifestations of Joubert Syndrome. *Genes* **9**, doi:10.3390/genes9120605 (2018).

150 Brugmann, S. A. *et al.* A primary cilia-dependent etiology for midline facial disorders. *Hum Mol Genet* **19**, 1577-1592, doi:10.1093/hmg/ddq030 (2010).

151 Qiang, M. *et al.* Cockayne syndrome-associated CSA and CSB mutations impair ribosome biogenesis, ribosomal protein stability, and global protein folding. *Cells* **10**, 1616 (2021).

152 Alupei, M. C. *et al.* Loss of proteostasis is a pathomechanism in Cockayne syndrome. *Cell Reports* **23**, 1612-1619 (2018).

153 Balajee, A. S., May, A., Dianov, G. L., Friedberg, E. C. & Bohr, V. A. Reduced RNA polymerase II transcription in intact and permeabilized Cockayne syndrome group B cells. *Proceedings of the National Academy of Sciences* **94**, 4306-4311 (1997).

154 Wang, Y. *et al.* Dysregulation of gene expression as a cause of Cockayne syndrome neurological disease. *Proceedings of the National Academy of Sciences* **111**, 14454-14459 (2014).

155 Selby, C. P. & Sancar, A. Cockayne syndrome group B protein enhances elongation by RNA polymerase II. *Proceedings of the National Academy of Sciences* **94**, 11205-11209 (1997).

156 Lake, R. J. *et al.* The sequence-specific transcription factor c-Jun targets Cockayne syndrome protein B to regulate transcription and chromatin structure. *PLoS Genet* **10**, e1004284 (2014).

157 Cho, I., Tsai, P. F., Lake, R. J., Basheer, A. & Fan, H. Y. ATP-dependent chromatin remodeling by Cockayne syndrome protein B and NAP1-like histone chaperones is required for efficient transcription-coupled DNA repair. *PLoS Genet* **9**, e1003407, doi:10.1371/journal.pgen.1003407 (2013).

158 Luzolo, A. L. & Ngoyi, D. M. Cerebral malaria. *Brain research bulletin* **145**, 53-58 (2019).

159 Organization, W. H. *World malaria report 2022*. (World Health Organization, 2022).

160 Kotlyar, S. *et al.* Spleen volume and clinical disease manifestations of severe Plasmodium falciparum malaria in African children. *Transactions of the Royal Society of Tropical Medicine and Hygiene* **108**, 283-289 (2014).

161 Newton, C. R. & Warrell, D. A. Neurological manifestations of falciparum malaria. *Annals of neurology* **43**, 695-702 (1998).

162 Gitau, E. & Newton, C. Blood–brain barrier in falciparum malaria. *Tropical Medicine & International Health* **10**, 285-292 (2005).

163 Polimeni, M. & Prato, M. Host matrix metalloproteinases in cerebral malaria: new kids on the block against blood–brain barrier integrity? *Fluids and Barriers of the CNS* **11**, 1-24 (2014).

164 Storm, J. & Craig, A. G. Pathogenesis of cerebral malaria—inflammation and cytoadherence. *Frontiers in cellular and infection microbiology* **4**, 100 (2014).

165 Schiess, N. *et al.* Pathophysiology and neurologic sequelae of cerebral malaria. *Malaria journal* **19**, 1-12 (2020).

166 MacPherson, G., Warrell, M., White, N., Looareesuwan, S. & Warrell, D. Human cerebral malaria. A quantitative ultrastructural analysis of parasitized erythrocyte sequestration. *The American journal of pathology* **119**, 385 (1985).

167 Avril, M., Bernabeu, M., Benjamin, M., Brazier, A. J. & Smith, J. D. Interaction between endothelial protein C receptor and intercellular adhesion molecule 1 to mediate binding of Plasmodium falciparum-infected erythrocytes to endothelial cells. *MBio* **7**, 10.1128/mbio. 00615-00616 (2016).

168 Shabani, E., Hanisch, B., Opoka, R. O., Lavstsen, T. & John, C. C. Plasmodium falciparum EPCR-binding PfEMP1 expression increases with malaria disease severity and is elevated in retinopathy negative cerebral malaria. *BMC medicine* **15**, 1-14 (2017).

169 Storm, J. *et al.* Cerebral malaria is associated with differential cytoadherence to brain endothelial cells. *EMBO Molecular Medicine* **11**, e9164 (2019).

170 Clemens, R. *et al.* Activation of the coagulation cascade in severe falciparum malaria through the intrinsic pathway. *British journal of haematology* **87**, 100-105 (1994).

171 Mandala, W. L. *et al.* Cytokine profiles in Malawian children presenting with uncomplicated malaria, severe malarial anemia, and cerebral malaria. *Clinical and vaccine immunology* **24**, e00533-00516 (2017).

172 Dunst, J., Kamena, F. & Matuschewski, K. Cytokines and chemokines in cerebral malaria pathogenesis. *Frontiers in cellular and infection microbiology* **7**, 324 (2017).

173 Schmid, U. *et al.* The deubiquitinating enzyme cylindromatosis dampens CD8+ T cell responses and is a critical factor for experimental cerebral malaria and blood–brain barrier damage. *Frontiers in immunology* **8**, 27 (2017).

174 Pham, T.-T., Lamb, T. J., Deroost, K., Opdenakker, G. & Van den Steen, P. E. Hemozoin in malarial complications: more questions than answers. *Trends in parasitology* **37**, 226-239 (2021).

175 Deroost, K. *et al.* Hemozoin induces hepatic inflammation in mice and is differentially associated with liver pathology depending on the Plasmodium strain. *PloS one* **9**, e113519 (2014).

176 Grau, G. E. *et al.* Platelet accumulation in brain microvessels in fatal pediatric cerebral malaria. *The Journal of infectious diseases* **187**, 461-466 (2003).

177 Deroost, K. *et al.* Improved methods for haemozoin quantification in tissues yield organ-and parasite-specific information in malaria-infected mice. *Malaria journal* **11**, 1-11 (2012).

178 Velagapudi, R., Kosoko, A. M. & Olajide, O. A. Induction of neuroinflammation and neurotoxicity by synthetic hemozoin. *Cellular and Molecular Neurobiology* **39**, 1187-1200 (2019).

179 Eugenin, E. A., Martiney, J. A. & Berman, J. W. The malaria toxin hemozoin induces apoptosis in human neurons and astrocytes: potential role in the pathogenesis of cerebral malaria. *Brain research* **1720**, 146317 (2019).

180 Panda, C. & Mahapatra, R. K. An update on cerebral malaria for therapeutic intervention. *Molecular Biology Reports* **49**, 10579-10591 (2022).

181 Khalaf, K., Tornese, P., Cocco, A. & Albanese, A. Tauroursodeoxycholic acid: a potential therapeutic tool in neurodegenerative diseases. *Translational Neurodegeneration* **11**, 33 (2022).

182 Abhinand, C. S., Raju, R., Soumya, S. J., Arya, P. S. & Sudhakaran, P. R. VEGF-A/VEGFR2 signaling network in endothelial cells relevant to angiogenesis. *Journal of cell communication and signaling* **10**, 347-354 (2016).

183 Vélez-Cruz, R. & Egly, J.-M. Cockayne syndrome group B (CSB) protein: at the crossroads of transcriptional networks. *Mechanisms of ageing and development* **134**, 234-242 (2013).

184 Saito, K. *et al.* Ablation of cholesterol biosynthesis in neural stem cells increases their VEGF expression and angiogenesis but causes neuron apoptosis. *Proceedings of the National Academy of Sciences* **106**, 8350-8355 (2009).

185 Jin, K. *et al.* Vascular endothelial growth factor (VEGF) stimulates neurogenesis in vitro and in vivo. *Proceedings of the National Academy of Sciences* **99**, 11946-11950 (2002).

186 Mackenzie, F. & Ruhrberg, C. Diverse roles for VEGF-A in the nervous system. *Development* **139**, 1371-1380 (2012).

187 Schänzer, A. *et al.* Direct stimulation of adult neural stem cells in vitro and neurogenesis in vivo by vascular endothelial growth factor. *Brain pathology* **14**, 237-248 (2004).

188 Brooks, P. Blinded by the UV light: how the focus on transcription-coupled NER has distracted from understanding the mechanisms of Cockayne syndrome neurologic disease. *DNA repair* **12**, 656-671 (2013).

189 Hayashi, M., Miwa-Saito, N., Tanuma, N. & Kubota, M. Brain vascular changes in Cockayne syndrome. *Neuropathology* **32**, 113-117 (2012).

190 Stern-Delfils, A. *et al.* Renal disease in Cockayne syndrome. *European Journal of Medical Genetics* **63**, 103612 (2020).

191 Gissen, P. & Maher, E. R. Cargos and genes: insights into vesicular transport from inherited human disease. *Journal of medical genetics* **44**, 545-555 (2007).

192 Grant, B. D. & Donaldson, J. G. Pathways and mechanisms of endocytic recycling. *Nature reviews Molecular cell biology* **10**, 597-608 (2009).

193 Bhuin, T. & Roy, J. K. Rab proteins: the key regulators of intracellular vesicle transport. *Experimental cell research* **328**, 1-19 (2014).

194 Martinez-Vicente, M. & Cuervo, A. M. Autophagy and neurodegeneration: when the cleaning crew goes on strike. *The Lancet Neurology* **6**, 352-361 (2007).

195 Yoon, S. & Eom, G. H. HDAC and HDAC inhibitor: from cancer to cardiovascular diseases. *Chonnam medical journal* **52**, 1 (2016).

196 Wang, Y. *et al.* Pharmacological bypass of Cockayne syndrome B function in neuronal differentiation. *Cell reports* **14**, 2554-2561 (2016).

197 Ciaffardini, F. *et al.* The cockayne syndrome B protein is essential for neuronal differentiation and neuritogenesis. *Cell death & disease* **5**, e1268-e1268 (2014).

198 Thour, A. & Marwaha, R. in *StatPearls [Internet]* (StatPearls Publishing, 2023).

199 Liu, X. *et al.* Biochemical and biophysical investigation of the brain-derived neurotrophic factor mimetic 7, 8-dihydroxyflavone in the binding and activation of the TrkB receptor. *Journal of Biological Chemistry* **289**, 27571-27584 (2014).

200 Liu, X. *et al.* Optimization of a small tropomyosin-related kinase B (TrkB) agonist 7, 8-dihydroxyflavone active in mouse models of depression. *Journal of medicinal chemistry* **55**, 8524-8537 (2012).

201 Liu, X. *et al.* A synthetic 7, 8-dihydroxyflavone derivative promotes neurogenesis and exhibits potent antidepressant effect. *Journal of medicinal chemistry* **53**, 8274-8286 (2010).

202 Johnson, R. A. *et al.* 7, 8-dihydroxyflavone exhibits therapeutic efficacy in a mouse model of Rett syndrome. *Journal of applied physiology* (2012).

203 Castello, N. A. *et al.* 7, 8-Dihydroxyflavone, a small molecule TrkB agonist, improves spatial memory and increases thin spine density in a mouse model of Alzheimer disease-like neuronal loss. *PloS one* **9**, e91453 (2014).

204 Korkmaz, O. T. *et al.* 7, 8-Dihydroxyflavone improves motor performance and enhances lower motor neuronal survival in a mouse model of amyotrophic lateral sclerosis. *Neuroscience letters* **566**, 286-291 (2014).

205 Chen, J. *et al.* Antioxidant activity of 7, 8-dihydroxyflavone provides neuroprotection against glutamate-induced toxicity. *Neuroscience letters* **499**, 181-185 (2011).

206 Li, T. *et al.* Mitochondriomics reveals the underlying neuroprotective mechanism of TrkB receptor agonist R13 in the 5× FAD mice. *Neuropharmacology* **204**, 108899 (2022).

207 Zhang, R. *et al.* Preventive effect of 7, 8-dihydroxyflavone against oxidative stress induced genotoxicity. *Biological and Pharmaceutical Bulletin* **32**, 166-171 (2009).

208 Chen, C. *et al.* The prodrug of 7, 8-dihydroxyflavone development and therapeutic efficacy for treating Alzheimer's disease. *Proceedings of the National Academy of Sciences* **115**, 578-583 (2018).

209 Ferreri, C. *et al.* Effects of oxygen tension for membrane lipidome remodeling of cockayne syndrome cell models. *Cells* **11**, 1286 (2022).

210 Sanchez-Roman, I. *et al.* Two Cockayne Syndrome patients with a novel splice site mutation–clinical and metabolic analyses. *Mechanisms of Ageing and Development* **175**, 7-16 (2018).

211 Tracey, T. J., Steyn, F. J., Wolvetang, E. J. & Ngo, S. T. Neuronal lipid metabolism: multiple pathways driving functional outcomes in health and disease. *Frontiers in molecular neuroscience* **11**, 10 (2018).

212 Saher, G. *et al.* High cholesterol level is essential for myelin membrane growth. *Nature neuroscience* **8**, 468-475 (2005).

213 Saher, G. & Stumpf, S. K. Cholesterol in myelin biogenesis and hypomyelinating disorders. *Biochimica Et Biophysica Acta (BBA)-Molecular and Cell Biology of Lipids* **1851**, 1083-1094 (2015).

214 Segatto, M., Di Giovanni, A., Marino, M. & Pallottini, V. Analysis of the protein network of cholesterol homeostasis in different brain regions: an age and sex dependent perspective. *Journal of Cellular Physiology* **228**, 1561-1567 (2013).

215 Hussain, G. *et al.* Role of cholesterol and sphingolipids in brain development and neurological diseases. *Lipids in health and disease* **18**, 1-12 (2019).

216 Zuo, H., Wang, R., Jiang, D. & Fang, D. Determining the composition of active Cholesterol in the plasma membrane of single cells by using Electrochemiluminescence. *ChemElectroChem* **4**, 1677-1680 (2017).

217 Martín, M. G., Pfrieger, F. & Dotti, C. G. Cholesterol in brain disease: sometimes determinant and frequently implicated. *EMBO reports* **15**, 1036-1052 (2014).

218 Polit, L. D. *et al.* Recommendations, guidelines, and best practice for the use of human induced pluripotent stem cells for neuropharmacological studies of neuropsychiatric disorders. *Neuroscience Applied*, 101125 (2023).

219 Jiménez-Díaz, M.-B., Möhrle, J. J., Angulo-Barturen, I. & Demarta-Gatsi, C. Using Cryopreserved Plasmodium falciparum Sporozoites in a Humanized Mouse Model to Study Early Malaria Infection Processes and Test Prophylactic Treatments. *Microorganisms* **11**, 2209 (2023).

220 Newton, C. R. & Krishna, S. Severe falciparum malaria in children: current understanding of pathophysiology and supportive treatment. *Pharmacology & therapeutics* **79**, 1-53 (1998).

221 Akide Ndunge, O. B., Kilian, N. & Salman, M. M. Cerebral malaria and neuronal implications of plasmodium falciparum infection: From mechanisms to advanced models. *Advanced Science* **9**, 2202944 (2022).

222 Bhat, M. Y. *et al.* Comprehensive network map of interferon gamma signaling. *Journal of cell communication and signaling* **12**, 745-751 (2018).

223 Galic, M. A., Riazi, K. & Pittman, Q. J. Cytokines and brain excitability. *Frontiers in neuroendocrinology* **33**, 116-125 (2012).

224 Okamura, H., Kashiwamura, S.-i., Tsutsui, H., Yoshimoto, T. & Nakanishi, K. Regulation of interferon-γ production by IL-12 and IL-18. *Current opinion in immunology* **10**, 259-264 (1998).

225 Kelley, N., Jeltema, D., Duan, Y. & He, Y. The NLRP3 inflammasome: an overview of mechanisms of activation and regulation. *International journal of molecular sciences* **20**, 3328 (2019).

226 Tiemi Shio, M. *et al.* Malarial hemozoin activates the NLRP3 inflammasome through Lyn and Syk kinases. *PLoS pathogens* **5**, e1000559 (2009).

227 Berger, A. Th1 and Th2 responses: what are they? *Bmj* **321**, 424 (2000).

228 Wu, X. *et al.* IL-4 treatment mitigates experimental cerebral malaria by reducing parasitemia, dampening inflammation, and lessening the cytotoxicity of T cells. *The Journal of Immunology* **206**, 118-131 (2021).

229 Kotepui, K. U., Thirarattanasunthon, P., Rattaprasert, P. & Kotepui, M. A systematic review and meta-analysis of blood interleukin-4 levels concerning malaria infection and severity. *Malaria Journal* **21**, 217 (2022).

230 Pope, S. M. *et al.* IL-13 induces eosinophil recruitment into the lung by an IL-5–and eotaxin-dependent mechanism. *Journal of Allergy and Clinical Immunology* **108**, 594-601 (2001).

231 Bochner, B. S., Klunk, D. A., Sterbinsky, S. A., Coffman, R. L. & Schleimer, R. P. IL-13 selectively induces vascular cell adhesion molecule-1 expression in human endothelial cells. *Journal of immunology (Baltimore, Md.: 1950)* **154**, 799-803 (1995).

232 Li, S. *et al.* Interleukin-13 and its receptor are synaptic proteins involved in plasticity and neuroprotection. *Nature Communications* **14**, 200 (2023).

233 Ndoricyimpaye, E. L. *et al.* Integrated Analysis of Cytokine Profiles in Malaria Patients Discloses Selective Upregulation of TGF-β1, β3, and IL-9 in Mild Clinical Presentation. *International Journal of Molecular Sciences* **23**, 12665 (2022).

234 Gimenez, F., Barraud de Lagerie, S., Fernandez, C., Pino, P. & Mazier, D. Tumor necrosis factor α in the pathogenesis of cerebral malaria. *Cellular and Molecular Life Sciences CMLS* **60**, 1623-1635 (2003).

235 Esamai, F. *et al.* Cerebral Malaria in Children: Serum and Cerebrospinal Fluid TNF-α and TGF-β Levels and Their Relationship to Clinical Outcome. *Journal of tropical pediatrics* **49**, 216-223 (2003).

236 Lyke, K. *et al.* Serum levels of the proinflammatory cytokines interleukin-1 beta (IL-1β), IL-6, IL-8, IL-10, tumor necrosis factor alpha, and IL-12 (p70) in Malian children with severe Plasmodium falciparum malaria and matched uncomplicated malaria or healthy controls. *Infection and immunity* **72**, 5630-5637 (2004).

237 Stins, M. F. *et al.* Elevated brain derived neurotrophic factor in plasma and interleukin-6 levels in cerebrospinal fluid in meningitis compared to cerebral malaria. *Journal of the Neurological Sciences* **450**, 120663 (2023).

238 Brown, H. *et al.* Cytokine expression in the brain in human cerebral malaria. *The Journal of infectious diseases* **180**, 1742-1746 (1999).

239 Day, N. P. *et al.* The prognostic and pathophysiologic role of pro-and antiinflammatory cytokines in severe malaria. *The Journal of infectious diseases* **180**, 1288-1297 (1999).

240 Sullivan, K. E. *et al.* Measurement of cytokine secretion, intracellular protein expression, and mRNA in resting and stimulated peripheral blood mononuclear cells. *Clinical Diagnostic Laboratory Immunology* **7**, 920-924 (2000).

241 Rauf, A. *et al.* Neuroinflammatory markers: key indicators in the pathology of neurodegenerative diseases. *Molecules* **27**, 3194 (2022).

242 Cruikshank, W. W., Kornfeld, H. & Center, D. M. Interleukin-16. *Journal of leukocyte biology* **67**, 757-766 (2000).

243 Laidlaw, B. J., Craft, J. E. & Kaech, S. M. The multifaceted role of CD4+ T cells in CD8+ T cell memory. *Nature Reviews Immunology* **16**, 102-111 (2016).

244 Kuehlwein, J. M. *et al.* Protection of Batf3-deficient mice from experimental cerebral malaria correlates with impaired cytotoxic T-cell responses and immune regulation. *Immunology* **159**, 193-204 (2020).

245 Shaw, T. N. *et al.* Perivascular arrest of CD8+ T cells is a signature of experimental cerebral malaria. *PLoS pathogens* **11**, e1005210 (2015).

246 Blanc, A.-L. *et al.* Suppression of CD4+ effector responses by naturally occurring CD4+ CD25+ Foxp3+ regulatory T cells contributes to experimental cerebral malaria. *Infection and Immunity* **84**, 329-338 (2016).

247 Kumar, R., Loughland, J. R., Ng, S. S., Boyle, M. J. & Engwerda, C. R. The regulation of CD4+ T cells during malaria. *Immunological reviews* **293**, 70-87 (2020).

248 Hör, S. *et al.* The T-cell lymphokine interleukin-26 targets epithelial cells through the interleukin-20 receptor 1 and interleukin-10 receptor 2 chains. *Journal of Biological Chemistry* **279**, 33343-33351 (2004).

249 Eugenin, E. *et al.* Shedding of PECAM-1 during HIV infection: a potential role for soluble PECAM-1 in the pathogenesis of NeuroAIDS. *Journal of leukocyte biology* **79**, 444-452 (2006).

250 Hagiyama, M., Ichiyanagi, N., Kimura, K. B., Murakami, Y. & Ito, A. Expression of a soluble isoform of cell adhesion molecule 1 in the brain and its involvement in directional neurite outgrowth. *The American journal of pathology* **174**, 2278-2289 (2009).

251 Royo, J. *et al.* Changes in monocyte subsets are associated with clinical outcomes in severe malarial anaemia and cerebral malaria. *Scientific reports* **9**, 17545 (2019).

252 Wassmer, S. C. *et al.* Vascular endothelial cells cultured from patients with cerebral or uncomplicated malaria exhibit differential reactivity to TNF. *Cellular microbiology* **13**, 198-209 (2011).
253 Kokaia, Z. *et al.* Brain insults in rats induce increased expression of the BDNF gene through differential use of multiple promoters. *European Journal of Neuroscience* **6**, 587-596 (1994).
254 Lindvall, O., Kokaia, Z., Bengzon, J., Elme, E. & Kokaia, M. Neurotrophins and brain insults. *Trends in neurosciences* **17**, 490-496 (1994).
255 Rudge, J. S. *et al.* Endogenous BDNF protein is increased in adult rat hippocampus after a kainic acid induced excitotoxic insult but exogenous BDNF is not neuroprotective. *Experimental neurology* **149**, 398-410 (1998).
256 Kokaia, Z., Andsberg, G., Yan, Q. & Lindvall, O. Rapid alterations of BDNF protein levels in the rat brain after focal ischemia: evidence for increased synthesis and anterograde axonal transport. *Experimental neurology* **154**, 289-301 (1998).
257 McDonald, C. R. *et al.* Brain-derived neurotrophic factor is associated with disease severity and clinical outcome in Ugandan children admitted to hospital with severe malaria. *The Pediatric Infectious Disease Journal* **36**, 146-150 (2017).
258 Linares, M. *et al.* Brain-derived neurotrophic factor and the course of experimental cerebral malaria. *brain research* **1490**, 210-224 (2013).
259 Mah, L., El-Osta, A. & Karagiannis, T. γH2AX: a sensitive molecular marker of DNA damage and repair. *Leukemia* **24**, 679-686 (2010).
260 Wang, H., Guo, M., Wei, H. & Chen, Y. Targeting p53 pathways: mechanisms, structures, and advances in therapy. *Signal transduction and targeted therapy* **8**, 92 (2023).
261 Im, J.-S. & Lee, J.-K. ATR-dependent activation of p38 MAP kinase is responsible for apoptotic cell death in cells depleted of Cdc7. *Journal of biological chemistry* **283**, 25171-25177 (2008).
262 Kim, J. & Wong, P. K. Loss of ATM impairs proliferation of neural stem cells through oxidative stress-mediated p38 MAPK signaling. *Stem cells* **27**, 1987-1998 (2009).
263 Wood, C. D., Thornton, T. M., Sabio, G., Davis, R. A. & Rincon, M. Nuclear localization of p38 MAPK in response to DNA damage. *International journal of biological sciences* **5**, 428 (2009).
264 Khadjavi, A., Valente, E., Giribaldi, G. & Prato, M. Involvement of p38 MAPK in haemozoin-dependent MMP-9 enhancement in human monocytes. *Cell Biochemistry and Function* **32**, 5-15 (2014).
265 Polimeni, M. *et al.* Haemozoin induces early cytokine-mediated lysozyme release from human monocytes through p38 MAPK-and NF-kappaB-dependent mechanisms. *PLoS One* **7**, e39497 (2012).
266 Rajamäki, K. *et al.* p38δ MAPK: a novel regulator of NLRP3 inflammasome activation with increased expression in coronary atherogenesis. *Arteriosclerosis, Thrombosis, and Vascular Biology* **36**, 1937-1946 (2016).
267 Shin, J. N. *et al.* p38 MAPK activity is required to prevent hyperactivation of NLRP3 inflammasome. *The Journal of Immunology* **207**, 661-670 (2021).
268 Fann, D. Y.-W. *et al.* Evidence that NF-κB and MAPK signaling promotes NLRP inflammasome activation in neurons following ischemic stroke. *Molecular neurobiology* **55**, 1082-1096 (2018).
269 Lee, J. K. & Kim, N.-J. Recent advances in the inhibition of p38 MAPK as a potential strategy for the treatment of Alzheimer's disease. *Molecules* **22**, 1287 (2017).

VII. Eidesstattliche Erklärung

Ich versichere an Eides statt, dass die Dissertation von mir selbstständig und ohne unzulässige fremde Hilfe unter Beachtung der „Grundsätze zur Sicherung guter wissenschaftlicher Praxis an der Heinrich-Heine-Universität Düsseldorf“ erstellt worden ist.

Einzelne Teile des Textes können Übereinstimmungen mit den von mir verfassten und in diese Arbeit eingepflegten Originalpublikationen aufweisen.

Diese Arbeit wurde weder bei einer anderen akademischen Institution eingereicht noch habe ich erfolglose Promotionsversuche unternommen.

Ort, Datum: _____

Unterschrift: _____

Leon-Phillip Szepanowski

Gewidmet

Ellen und Klaus Szepanowski

Alfred und Wilma Laqua

und Fabian Szepanowski